Multidisciplinary Fusion: Structural Geology, Remote Sensing and Geotechnical Analysis for Geothermal Exploration and Natural Hazard Assessment in Southwestern British Columbia, Canada

by

Mahmud Muhammad

M.Sc. (Geoscience), University of Nevada Las Vegas, 2016
B.Sc. (Geology), Salahaddin University-Erbil, 2010

Thesis Submitted in Partial Fulfillment of the
Requirements for the Degree of
Doctor of Philosophy

in the
Department of Earth Sciences
Faculty of Science

© Mahmud Muhammad 2024
SIMON FRASER UNIVERSITY
Summer 2024

Declaration of Committee

Name:	**Mahmud Muhammad**
Degree:	**Doctor of Philosophy (Earth Sciences)**
Title:	**Multidisciplinary Fusion: Structural Geology, Remote Sensing and Geotechnical Analysis for Geothermal Exploration and Natural Hazard Assessment in Southwestern British Columbia, Canada**
Committee:	**Chair: Shahin Dashtgard**
	Professor, Earth Sciences

Glyn Williams-Jones
Supervisor
Professor, Earth Sciences

Doug Stead
Committee Member
Professor Emeritus, Earth Sciences

Giacomo Falorni
Committee Member
Technical Director
TRE Altamira

Sergio Sepúlveda
Examiner
Professor, Earth Sciences

Scott McDougall
External Examiner
Associate Professor, Earth, Ocean and Atmospheric Sciences
University of British Columbia

Abstract

Southwestern British Columbia is characterized by notable geologic and physiographic features, including the Jurassic-Tertiary Coast Mountain batholith (Coast Plutonic Complex) and the Quaternary Garibaldi Volcanic Belt (GVB). This volcanic belt stretches from northwestern Washington to southern British Columbia and concludes at the Nootka fault. The region's young and complex geology and challenging climate present opportunities for resource exploration, such as geothermal energy, alongside natural hazard risks like landslides and volcanic activity. To balance these opportunities and challenges, existing technologies and innovative workflows are necessary for effective resource utilization and hazard mitigation. This thesis combines structural geology, remote sensing, and geotechnical analysis to identify challenges, opportunities, and solutions for geothermal exploration as well as monitoring and mitigating landslides in southwestern British Columbia, particularly at the Mount Meager Volcanic Complex (MMVC) and Mount Currie escarpment.

At MMVC, detailed surface structural geology mapping, paleomagnetic analysis, and radiometric dating were used to investigate the volcanic rocks' kinematic history and structural features including faults and folds. The study also established the relationships between various deformation stages and proposed a structural model explaining deformation of the MMVC over the past 5 million years. The research identified potential sites for geothermal exploration and highlighted geological structures that could trigger earthquakes, landslides, or volcanic activity.

At Mount Currie, the study revealed that the escarpment, which extends east-northeast to west-southwest, likely formed as a gravitational collapse fault due to compression at the mountain crest. This faulting is shaped more by local stress patterns than direct seismic activity and is influenced by the surrounding thrust faults, Owl Creek, and Miller Creek, as well as crustal rebound caused by glacial unloading. A critical block on the NE-3 peak of the Mount Currie ridge was identified as particularly vulnerable, with an estimated 14.4 million cubic meters of bedrock potentially at risk of displacement should it fail.

Finally, this study introduced cutting-edge optical flow algorithm workflows, presented as the open-source Python package AkhDefo, enabling the processing of various datasets,

including live-streamed webcam footage, satellite optical, and radar backscatter imagery. In summary, this study provides valuable insights into the geology and geohazards of southwestern British Columbia and offers new approaches to resource exploration and natural hazard management.

Keywords: Q̓welq̓welústen (Mount Meager); Mount Currie; Landslides; Geothermal; AkhDefo; Garibaldi Volcanic Belt; Remote Sensing; Structural Geology

Dedication

To my beloved parents, who have remained close in my heart despite the physical distance during my studies over the past decade, I dedicate this work to you in gratitude and love. Your unwavering support, encouragement, and faith in my journey have been my guiding light. Though we've been apart, your presence has been felt in every milestone reached, and I thank you for the sacrifices you've made to help me pursue my dreams.

To all those who have endured the devastation of wars, displacement, and loss, we stand in unwavering Solidarity. To those affected by the Kurdish genocide during the Anfal Campaign and the Halabja tragedy, and to the people suffering in Iraq, Syria, Ukraine, Gaza, and every part of the world due to unjust wars driven by greed and selfish political agendas, I honor your resilience and courage. I mourn the lives needlessly lost and recognize the enduring strength of those who continue to fight for justice, peace, and the fundamental right to live with dignity. Your struggles remind me of the urgent need to rise above division and conflict, advocating for a world where compassion and humanity prevail over the darkness of oppression.

To the stateless people whose land and rights have been taken away, especially my beloved and fellow Kurdish people, I dedicate this work in recognition of your unbreakable spirit and resilience. Despite the relentless challenges and injustice, you face, your courage and unwavering hope continue to shine brightly. Your strength in the pursuit of a rightful home and your determination to preserve your heritage and identity inspire us all to fight for a future where justice and self-determination prevail.

To the spirit of coexistence in Canada and in goodwill to the nation that has given me the opportunity to resettle, study, and pursue my dreams, I extend my deepest gratitude. Thank you, Canada, for welcoming me and for allowing me to flourish in a society where diversity and acceptance prevail.

Acknowledgements

I would like to take this opportunity to express my profound gratitude to all those who have supported me throughout PhD journey. Firstly, I extend my whole-hearted thanks to my senior supervisor, Dr. Glyn, for his academic and personal mentorship. I also wish to acknowledge my co-supervisor, Dr. Stead, for his invaluable guidance and professional advice.

I am deeply appreciative of the collaboration with esteemed colleagues outside SFU, including Dr. Giacomo Falorni and Dr. Riccardo Tortini from TRE-ALTAMIRA, and Dr. René W. Barendregt from the University of Lethbridge. My sincere thanks go to Nupoint Systems Inc. for their generous donation of the ground-based camera and weather system, and to Weir-Jones Engineering for their installation and ongoing maintenance.

I also wish to thank to the Lílwat Nation, Energex Renewable Energy, the pilots of No Limits Helicopter Adventures and the Meager Creek Development Corporation for their technical and logistical support.

I am grateful to Simon Fraser University and particularly Department of Earth Sciences Faculty and Staff, Geoscience BC, and Natural Resources Canada for their support, particularly Dr. Steve Grasby, who led the Garibaldi Geothermal Volcanic Belt Assessment Project and provided helicopter support for geological fieldwork on Meager. Additionally, I thank Mitacs and the Canadian Space Agency for providing a stipend during my studies. I am also thankful to the Geological Society of America for giving me Richard B and Cynthia Waitt Research Award based on excellence of field geology mapping aspect of my project.

I extend heartfelt thanks to the graduate students from both SFU and UBC who contributed to the fieldwork: Davide Donati, A. Borch, B. Coughlan, J. Connelly, M. Harris, and S. Leiter. I am also grateful to my coworkers and lab mates in the Physical Volcanology Group at SFU: Juan Anzieta, Sarah Aufrere, Yannick Le Moigne, Princess Cosalan, Antonina Calahorrano, Benjamin Coughlan, Yuyen Pan, Sarai Montañez, Cassia Snyder, and Zina Boileau.

Finally, I would like to thank my family for their unconditional support and deeply appreciate my friend Bestoon Shakor for always being there whenever I needed help, company, and support.

Table of Contents

List of Tables

List of Figures

Chapter 1.   Introduction

Southwestern British Columbia hosts distinct geologic and physiographic features, notably the ~1700 km-long Coast Mountain batholith (also known as the Coast Plutonic Complex) and the Quaternary-aged Garibaldi Volcanic Belt (GVB). This extensively glaciated volcanic belt extends from northwestern Washington to southern British Columbia and terminates in the north at the Nootka fault and represents the northern extent of the Cascade Volcanic Arc (Gehrels et al., 2009; Russell et al., 2023) (Fig. 1.1).

The region has also experienced widespread tectonism with three Cenozoic stages of uplift from north to south (Parrish, 1982). First, intense post-orogenic uplift of the eastern and central Coast Mountain batholith. Second, Middle Cenozoic uplift of the Coast Mountains starts from Mount Waddington to southeast Alaska. Third, Pliocene to Recent > 3 km of uplift (<5 Ma) in the southern Coast Mountains encompasses the current GVB which includes, Mount Currie (non-volcanic mountain) and the Mount Meager Volcanic Complex (MMVC). Two critical geologic events that may have contributed to the rapid uplift of the southern Coast Mountains include: 1) the interruption of calc alkaline volcanic activity of the Pemberton Volcanic Belt > 7 Ma and in the Garibaldi Volcanic Belt < 2 Ma; 2) Plate boundary reorganization and change in relative velocity between the Explorer and North America plate at about 5 Ma; which was subsequently followed by westward migration of the volcanic arc centres into a NW trending current Garibaldi Volcanic Belt (Parrish, 1982). Although neotectonic activity is still not well constrained in the GVB, the recent geothermal research initiative led by Natural Resources Canada (NRCan) and several western Canadian universities including Simon Fraser University involved preliminary structural geology and paleomagnetic studies on the North Lillooet Ridge, north of the Mount Meager Volcanic Complex (Harris et al., 2020; Muhammad et al., 2021). The current preliminary interpretation suggests that this region, particularly MMVC was tectonically active at least between 300-700 ka or between 2-1.2 Ma (Muhammad et al., 2021).

The GVB is the site of geologically recent volcanic activity (e.g., 2360 BP eruption of the Mount Meager Volcanic Complex; Hickson et al., 1999), with frequent shallow earthquakes (Friele et al., 2008), and numerous thermal springs. Additionally, the identification of active fumaroles on Job Glacier in 2016 (Venugopal et al., 2017, 2020;

Grasby et al., 2021; Roberti et al., 2021a). Starting in the 1970s, the Mount Meager Volcanic Complex became the focus of geothermal exploration aimed at production of renewable energy (Fairbank et al., 1980, 1981; Ghomshei et al., 1986, 1992, 2004, 2009; Roberti et al., 2021a) where exploration drilling identified ground water above 200°C. Intermittent geothermal studies have continued to the present (Grasby and Hutcheon, 2001; Harris et al., 2020; Grasby et al., 2021; Muhammad et al., 2021).

The presence of geothermal systems can result in widespread hydrothermal alteration that can weaken the crystalline basement and recent volcanic rocks. Finally, the region has experienced multiple ice-ages and periods of deglaciation. Glaciers destabilize volcanic edifices in many ways. They abrade and fracture already weak, highly fractured flows and pyroclastic deposits and remove support from the base of over-steepened slopes, changing the stress regime and further decreasing their stability (Huggel, 2009; McColl et al., 2010; Grämiger et al., 2017). This unloading at the base of large slopes, when coupled with the often-extensive hydrothermal alteration of volcanic massifs, can trigger large landslides capable of traveling tens of kilometers and impacting population centres, roads, railways, pipelines, and rivers.

Increasing summer temperatures can accelerate snowmelt that can infiltrate slopes and trigger landslides. Large amounts of water from melting ice easily enters the fractured rocks and may be stored in the porous and permeable rocks of the volcanic edifice (Delcamp et al., 2016) increasing pore water pressure, which in turn causes instability (Terlien, 1998). The saturated, weakened, and altered rocks may deform by creep processes (Cecchi et al., 2004; Capra, 2006; Pola et al., 2014; Heap et al., 2015), inducing gravitational stress that can culminate in collapse (van Wyk de Vries and Francis, 1997; Cecchi et al., 2004); in the event of a deep-seated collapse of a volcanic flank, this pore water can transform a simple rockslide into a mobile debris avalanche or debris flow (Roverato et al., 2011; Capra et al., 2013; Roberti, 2018). In fact, most modern and historical landslides at Mount Meager are related to glacial retreat, water infiltration along with the debutressing effect, and the intense alteration produced by the hydrothermal system beneath the mountain complex. For instance, both the 1998 and 2010 landslide events are believed to be at least in part linked to specific climatic triggers (Bovis and Jakob, 2000; Friele et al., 2008; Hetherington, 2014).

Glacial retreat and thinning may even increase the chances of new eruptions. Many researchers have examined the relationship between deglaciation and volcanic eruptions (Rampino et al., 1979; Jellinek et al., 2004; Huybers and Langmuir, 2009), between eruptions and large-scale collapses of volcanic edifices (Voight et al., 1981, 2002; Siebert, 1984; Glicken, 1996), and the influence of deglaciation as a mass wasting trigger in volcanic environments (Holm et al., 2004; Capra, 2006; Capra et al., 2013).
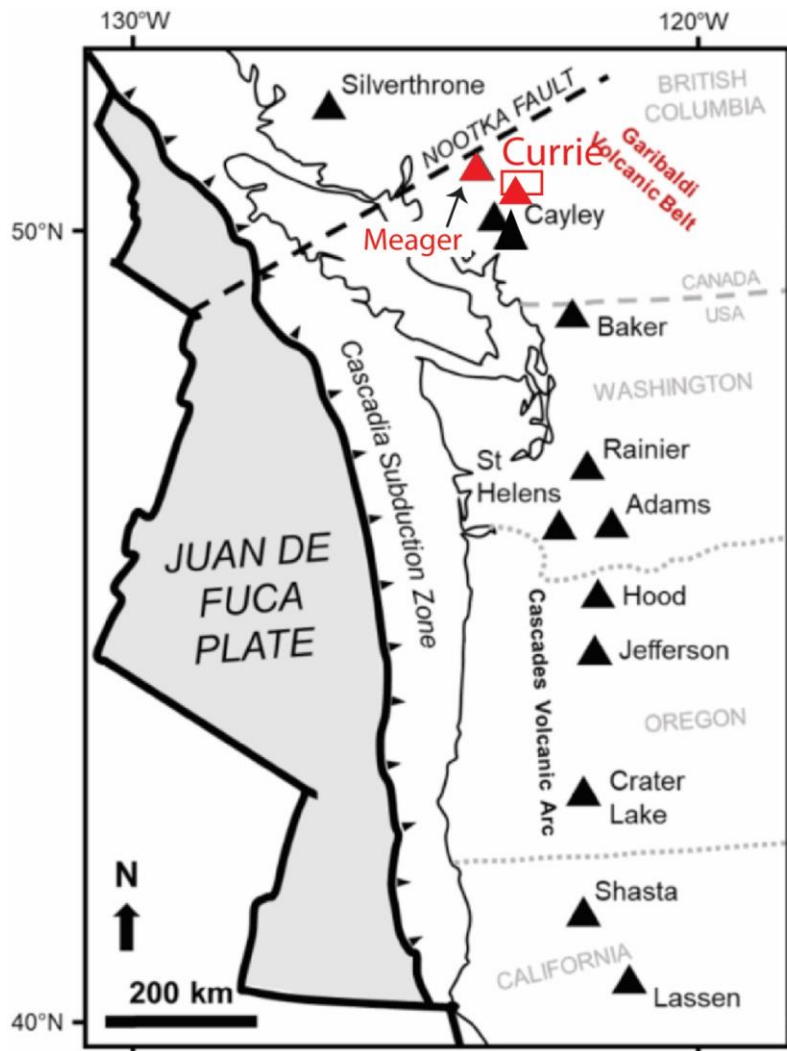
Figure 1.1.   **Physiographic map of western North America showing locations of both Mount Meager and Mount Currie relative to the Garibaldi Volcanic Belt (GVB) and Southwestern British Columbia, Canada.**

1.1. Objectives:

Often exploration for natural resources is conducted in regions of complex tectonic and climatic conditions. One such example is geothermal exploration within the southwestern British Columbia particularly at MMVC which comprises the northern end of the GVB. The lack of sufficient surface structural geology knowledge has hindered efficient exploitation of the geothermal resource buried beneath MMVC. Additionally, the risk of natural hazards in the region such as the 2010 MMVC landslide, the largest historical landslide in Canada, necessitates understanding the baseline natural hazards within the MMVC. At the GVB, including the MMVC, tectonics dictates the current physiography of mountain ranges, while climate, deglaciation, and hydrothermal systems can exacerbate rock slope instability.

Utilizing the existing geothermal resource at MMVC requires a thorough understanding of structural geology parameters including sequence of deformation, kinematic history and kinematic compatibility of structures such as faults and folds to pinpoint hydrothermal fluid pathways and delineate the geothermal reservoir boundaries. Additionally, to sustain the development of the geothermal resource and mitigate threats to infrastructure requires a proper natural hazard monitoring program to differentiate anthropological triggered hazards due to exploitation versus the existing and naturally triggered hazards due to past geological conditions. In this study, I thus take a multi-disciplinary approach to enhance the surface structural geology knowledge at MMVC and study the rock slope-instability within two distinctive geologic settings in the southwestern British Columbia.

The first case study focuses on the active ice-clad volcanic system, Qẃelqẃelústen (Angelbeck et al., 2024) or the Mount Meager Volcanic Complex, which is characterized by the presence of an extensive hydrothermal system. In contrast, the second case study focuses on a steep-slope mountain scarp structure on Mount Currie which, while not affected by extensive hydrothermal alteration, is still impacted by deglaciation and rapid uplift in the region. Additionally, this study uses a newly developed workflow tested on other well studied landslides such as the May 20th, 2017, Mud Creek landslide in California, USA and the Morenny Rock-Glacier, Tien Shan Mountains in Kazakhstan. These landslides were instrumental in validating the landslide monitoring methods developed here. Although a range of questions will develop through studying these

mountain complexes, the main purpose of this study is to define the key geological and geotechnical parameters that can enhance geothermal exploration and influence slope instability and landslides in the region. Some of the goals of this work include but are not limited to:

1. Developing a state of art technique and methodology to monitor slope instability via optical and radar imagery (Chapters 2 and 5).
2. Understanding the geological challenges for geothermal exploration and documenting surface structural geology knowledge at MMVC (Chapter 3).
3. Understanding the importance of geological factors that shaped the physiography of mountains and their influence on rock-slope instability and landslides in southwestern British Columbia (Chapter 4).

1.2. Background and Methods

This thesis employs a range of methods and tools including traditional field geology investigations, analysis of rock samples for determining the absolute ages of geological units through techniques like paleomagnetic and radiometric dating, and the use of remote sensing data from ground and satellite optical imagery as well as satellite radar imagery. Additionally, it involves the development of cutting-edge open-source software for processing both optical and radar images to monitor land deformation. Below, I provide a summary of the methodologies and techniques utilized throughout the thesis.

1.2.1. Methods for Landslide Analysis

Methods for landslide and slope instability analysis depend on site condition and type of failure (Stead et al., 2001; Gupte, 2006); therefore, it is essential to first classify and define the term landslides. The proposed definition of landslide by the world landslide inventory is a "movement of a mass of rock, earth, or debris down a slope (Benko, 1997; Hungr et al., 2014). Landslides have been classified according to 1) type and speed of movement and 2) type of material involved (Varnes, 1978; Cruden and Varnes, 1996; Benko, 1997; Hungr et al., 2014).

Table 1.1.   Classification of Landslides (after Varnes, 1978 and Benko, 1997).

Type of Movement	Type of Material		
	Bedrock	Engineering soils	
		Predominately	
		Coarse	Fine
Fall	Rock Fall	Debris Fall	Earth Fall
Topple	Rock Topple	Debris Topple	Earth Topple
Slide	Rockslide	Debris Slide	Earth Slide
Spread	Rock Spread	Debris Spread	Earth Spread
Flow	Rock Flow	Debris Flow	Earth Flow

Fall: Related to very rapid to extremely rapid movement of rock mass in response to gravitational movement of masses on very steep slopes. The rock mass may detach partially and fall freely through the air; subsequently bouncing, rolling, or simultaneously bouncing and rolling determined by the steepness of the slope angle below the unstable rock mass (Benko, 1997; Highland, 2004; Hungr et al., 2014; Li and Mo, 2019). The detached rock mass can move a great distance due to its high kinetic energy. Such rapid movement can be associated with other types of movement including toppling and sliding (Fig. 1.2).

Topple: Characterized by downslope overturning of rock mass through rotation or flexure of interrelating blocks of rock. This movement is controlled by gravity, or forces exerted by neighboring blocks or fluids within discontinuities. Additionally, toppling can progress to or develop into rockslides and rock falls depending on plane of failure, geometry of the unstable section and direction of discontinuities (Fig. 1.2).

Sliding: The rock mass moves along a single or several surface ruptures which separate the displaced mass from the underlying material. Sliding can occur in multiple ways such as rotational sliding and transitional sliding (Cruden and Varnes, 1996; Benko, 1997; Li and Mo, 2019) (Fig. 1.2). In the case of rotational sliding, the geometry of the failure surface is curved and concave with minimal amount of internal deformation and this type of failure is typical for homogenous material. By contrast, in transitional sliding, the geometry of the failure surface is planar or undulant. These types of failure surfaces follow discontinuities, contacts between different rock types, and weak layers or weathering interfaces.

Spreads: This type of movement may occur when bedrock is overlying a softer material (Fig. 1.2). The softer base causes the above bedrock mass to fracture and eventually separate at an extremely slow rate (Cruden and Varnes, 1996; Benko, 1997; Li and Mo, 2019). In such cases, the main movement is controlled by extensional modes either by shear or tensile fractures. Groundwater level and permeability of the unconsolidated base material controls the stability of the overlying bedrock mass.

Flows: This type is characterized by continuous movement, and it does not have a distinct failure surface. Flow can occur within both unconsolidated material and bedrock. Flow within bedrock contains deformation distributed along various macro and micro fractures rather than concentrating along a single fracture plane. Additionally, flow within bedrock may result in plastic deformation such as folding, bending, and bulging. Slow flow in bedrock is also known as Sackung or deep-seated gravitational collapse in high mountains regions (Fig. 1.2).

Modelling of landslides and unstable slopes in the last three decades has improved with advances in the computing capacity of personal computers (Stead et al., 2006) and led to the development of many software suites (e.g., Rocscience and Itasca). Performing numerical modelling of rock slope stability is useful either to predict future slope behavior or when investigating a range of slope failure mechanisms (Stead and Coggan, 2012).
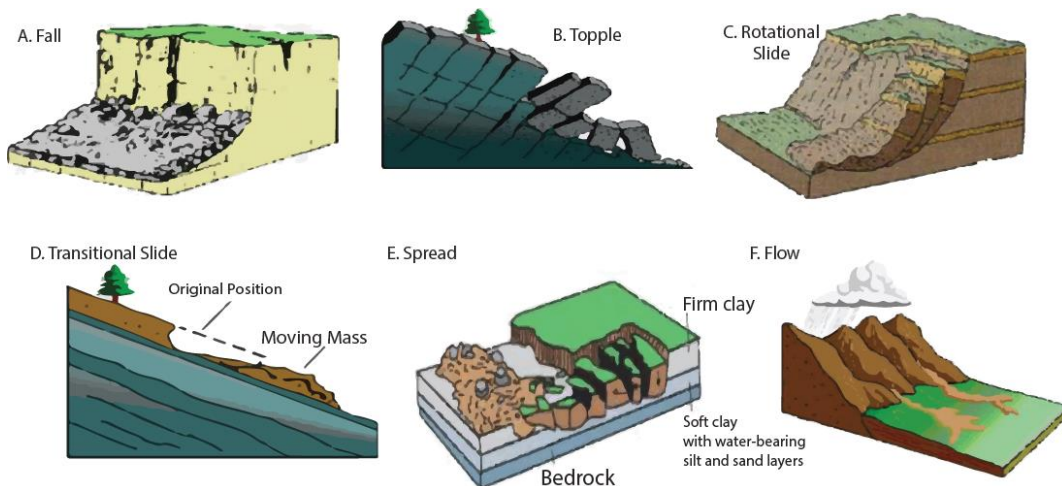
Figure 1.2.   Examples of main types of Landslide mechanism (modified from Highland, 2004)

There are several steps and methodologies for conducting slope instability analysis. These include geotechnical kinematic analysis, limit equilibrium analysis, and numerical modeling. The first two methods will be discussed and applied in Chapter 4. Although numerical modeling is beyond the scope of this thesis, it was recommended for future research as it addresses the limitations of the other techniques.

Geotechnical Kinematic analysis and Limit Equilibrium Analysis (LEA)

Geotechnical kinematic analysis of slope stability involves studying the orientation of discontinuities in terms of dip and dip direction. The processes include projecting three-dimensional data into a two-dimensional representation by plotting discontinuity data on stereographic projections. Detailed explanation of the stereographic techniques and their application in geotechnical kinematic analysis exist elsewhere in the published literature (Hoek and Bray, 1981; Goodman and Shi, 1985; Stead and Coggan, 2006; Hoek and Brown, 2019). Additionally, advances in computing technology have led to sophisticated computer software such as DIPS (Hoek and Bray, 1981; Goodman and Shi, 1985; Hoek and Brown, 2019, 2019) to perform kinematic analysis of discontinuities.

Nevertheless, classical stereographic analysis is the first step in most investigations of rock-slope stability, and helps in assessing different kinematic failure mechanisms, including planar, wedge, and toppling instability. However, it is essential that overreliance on orientation data alone be avoided, and full use of these techniques be made (Stead and Coggan, 2012). The more advanced stage is the determination of the critical key blocks that may control the rock slope stability which was known as block theory or wedge stability (Goodman and Shi, 1985; Goodman, 1995; Yeung et al., 2003). Block theory is a geometric analysis method used to identify potentially hazardous blocks within geological materials intersected by discontinuities in three dimensions. It is particularly applicable to hard, blocky rock, where blocks of varying sizes may pose a load or hazard risk in excavations or foundations (Goodman and Shi, 1985; Goodman, 1995; Yeung et al., 2003).

A discontinuous rock mass is made up of both discontinuities and intact rock blocks, with the blocks being enclosed by these discontinuities. When the intact rock is strong and the stress levels are insufficient to cause failure, the behavior of the discontinuous rock mass is primarily governed by the discontinuities. These discontinuities intersect,

creating rock blocks of varying sizes and shapes, and the stability of these blocks needs to be evaluated to determine the overall stability of the rock mass.

Current limit equilibrium-based methods for wedge stability analysis have some limitations: (1) they do not account for dynamic equilibrium, (2) most are unable to address rotational modes, and (3) none are capable of managing complex rotational modes, such as torsional sliding (Yeung et al., 2003). Addressing the first limitation, analytical studies have demonstrated that the accurate failure mode of a rectangular block on an inclined plane can be determined by considering the dynamic equilibrium of the block, which involves incorporating inertial forces into the equilibrium equations (Yeung et al., 2003). Regarding the second and third limitations, rotational failure modes are challenging to analyze and are therefore often overlooked in practice (Goodman and Shi, 1985; Yeung et al., 2003).

In Chapter 4, we used RocSlope3 software (Rocscience Inc., 2024) which is designed based on the model of block theory (wedge stability). By default, RocSlope3 only considers sliding failure mechanisms along wedges and cannot deal with complex movements such as rotation of blocks or simultaneous sliding and rotation of blocks. As such RocSlope3 performs LEA through evaluating the safety factors of numerous blocks, within highly jointed rock masses where failures are dictated by structural conditions in which it considers sliding modes only and the mode must be assumed a priori. We specifically applied RocSlope3 software to major structures such as regional faults and large-scale linear features on Mount Currie. Further details of the analysis such as factors of safety, volume and key block identification are discussed in Chapter 4.

The popularity of the limit equilibrium analysis technique for rock-slope instability analysis is largely related to its simplicity and large amount of research which has highlighted its application. The condition of early failure in limit equilibrium analysis is presumed along a continuous slip surface of a known or assumed shape. Hence, the factor of safety is calculated for the slope stability in regard to the shear strength as the ratio of the total force available to resist failure to the total force tending to induce failure (Benko, 1997). In general, all limit equilibrium analysis codes use the common concept of comparison of resisting forces/moments mobilized and the disturbing forces/moments (Goodman and Shi, 1985; Reid et al., 2001; Stead et al., 2001; Eberhardt, 2008).

1.2.2. Remote Sensing

The remote sensing approaches used in this thesis involve processing ground and satellite optical and radar imagery using an open-source software called AkhDefo, developed as part of this PhD (Muhammad et al., 2022), in addition to the existing well-documented software and techniques such as SqueeSAR (Ferretti et al., 2011), ISCE2 (Rosen et al., 2012), Mintpy (Yunjun et al., 2019) and LiDAR-based Digital Elevation Change Detection (Warrick et al., 2019).

Radar Remote Sensing Imagery

Radar remote sensing is considered as an active remote sensing system, using the microwave domain of the electromagnetic spectrum. The currently available radar systems operate across different microwave wavelength bands such as P, L, S, C and X (Table 1.1) (Ferretti et al., 2007; Rosenqvist and Killough, 2018). In radar remote sensing, the choice of wavelength determines the size of an object that can be captured accurately and hence affects the spatial resolution of the image. Objects smaller than the radar wavelength will be invisible or transparent to the radar, although they may cause some attenuation of the signal (Ferretti et al., 2007).

Table 1.2.   **Most widely used Radar wavelength resolutions.**

Wavelength band	Wavelength in centimeter
P-band	~69.0 cm
L-band	~23.5 cm
S-band	~9.4 cm
C-band	5.6 cm
X-band	3.1 cm

Radar imagery can also provide information about the motion of the land surface through a technique called Interferometric Synthetic Aperture Radar (InSAR). The radar satellite transmits signals to the ground and receives the backscatter radar reflection (Ferretti et al., 2007) and this process is repeated every time the satellite passes over the area of interest. Hence, ground displacement with centimetric resolution can be measured through the comparison of two images or millimeter resolution using stacks of images captured at different times over the same area of interest. The comparison between radar images creates a new radar product called an interferogram through the signal phase difference between repeated measurements, and includes various components such as topography, atmosphere, and ground motion. After removing the topography and atmospheric effects (Ferretti et al., 2007; TRE ALTAMIRA, 2018), it is possible to retain the phase difference related to ground motion which leads to the formation of a new product called differential interferogram.

Unlike optical satellites, which capture images with a near-vertical incidence angle, SAR satellites utilize a side-look configuration (Figs. 1.2 and 1.3). SAR satellites orbit the Earth in a sun-synchronous LEO ("Low Earth Orbit"; any orbit around the Earth with an orbital period of less than about two hours) polar orbit with north-south (descending geometry) and south-north (ascending geometry) transit. A sun-synchronous orbit is a near-polar orbit around Earth and allows the satellite to pass over the same part of the Earth at approximately the same local solar time on each orbit. The orbit is designed so that the satellite always crosses the equator at the same local solar time. This means the lighting conditions remain consistent, which is particularly useful for imaging, mapping, and reconnaissance satellites (https://earthobservatory.nasa.gov/features/OrbitsCatalog).

InSAR measures displacement along the line of sight (LOS) and has less sensitivity to N-S displacement due to the SAR satellite orbit geometry (Fig. 1.2) (TRE ALTAMIRA, 2018). To estimate vertical and east-west displacement from the LOS of InSAR measurements, SAR images of different geometries (Ascending and Descending) can thus be processed with areas of interest by two mirroring views (Fig. 1.2) with the same revisit time (TRE ALTAMIRA, 2018). SAR geometry also can lead to some distortions, particularly in high topographic terrains with steep slopes (Fig. 1.3). The possible geometrical distortions include layover, shadow, and foreshortening.

Foreshortening occurs when the radar signal hits a steep slope that faces the radar. The slope appears compressed in the radar image, making it look shorter than it actually is. Layover occurs when the radar signal reaches the top of a tall feature (like a mountain or building) before it reaches the base. This causes the top of the feature to appear closer to the radar than the base, resulting in a reversal of the normal order of objects. This leads to a distortion where the object appears to be leaning towards the radar. Shadowing can occur when the slope of the terrain faces away from the satellite and the slope angle is greater than the radar incident angle; in other words some areas are not visible in the radar signal and result in dark areas (shadows) in the image (Fig. 1.3) (Ferretti et al., 2007; TRE ALTAMIRA, 2018).
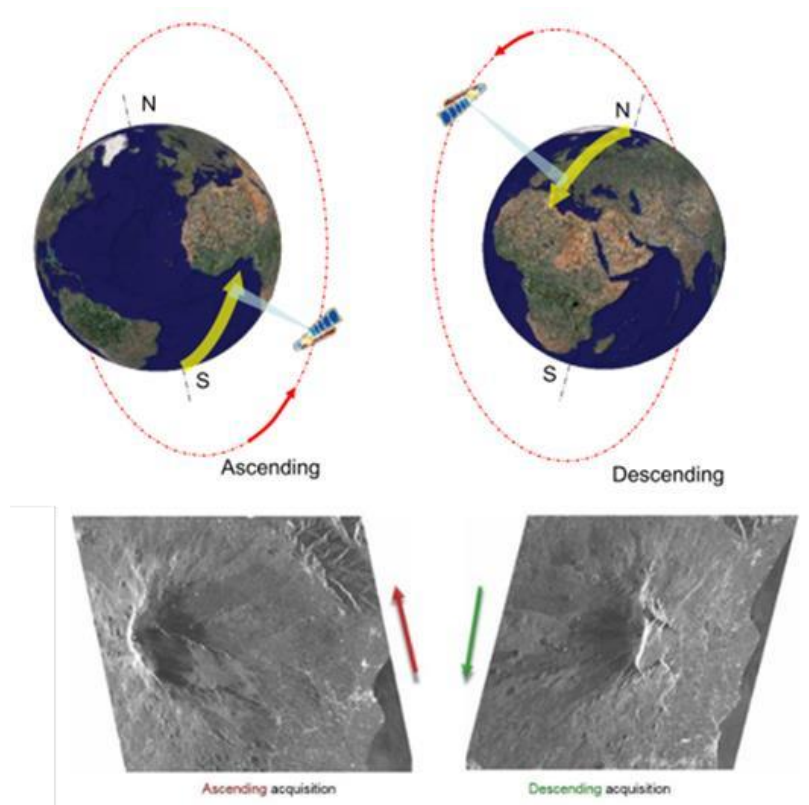
Figure 1.3.   Example of synthetic aperture radar satellite orbit geometry (after TRE-ALTAMIRA, 2018).
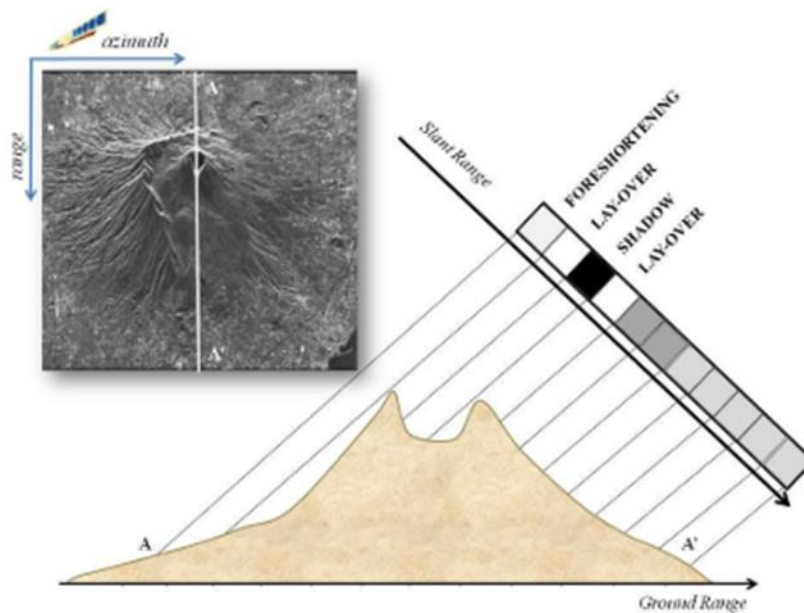
Figure 1.4.   Example of SAR geometric distortions (after TRE-ALTAMIRA, 2018).

Since the early work of Gabriel et al. (1989) which used synthetic aperture radar images to measure very small (1 cm or less) surface motions, radar imagery has been used widely in monitoring of landslide, earthquakes, and volcanoes (e.g., Bürgmann et al., 2006; Ferretti et al., 2007, 2011; Neri et al., 2009; Moro et al., 2017; Bouali et al., 2018; Huntley et al., 2020; Eker and Aydın, 2021). InSAR is now a well-established tool both in academia and industry (Wei et al., 2010; Ferretti et al., 2015; Roberti, 2018; Raspini et al., 2018) with three main techniques used for InSAR processing: 1) Differential InSAR (DInSAR; between two interferograms); 2) Persistent scatterer interferometry (PS or SqueeSAR™; stack of interferograms with a single reference; Ferretti et al., 2011; Hussain et al., 2021) and 3) small baseline subset (SBAS; stack of interferograms with Small Baseline Subset; Guo et al., 2021).

Optical Remote Sensing Imagery

The arrival of newer remote sensing systems and powerful personal computers has advanced the use of passive remote-sensing imagery (i.e., optical imagery) in the field of Earth sciences in general but particularly in studying and monitoring natural hazards such as landslides. Modern computer vision algorithms provide the ability to explore digital images at a subpixel level (Thévenaz et al., 1998; Foroosh et al., 2002; Guizar-

Sicairos et al., 2008), constructing a three-dimensional geometry of the terrain and landscape and tracking changes at sub-pixel levels both in two-dimensional space (e.g., Digital Image Correlation and Optical flow) and three-dimensional space such as Stereopair photogrammetry from two overlapped imagery and structure from motion from a sequence of images (McCormick and Lord, 2010; Pan and Li, 2011; Roberti et al., 2021b).

This thesis presents a state of the art workflow to process ground-based and satellite optical imagery based on the optical flow computer vision algorithm (Muhammad et al., 2022). It is worthwhile to mention that prior to this study, optical flow codes were rarely used in the field of Earth sciences and landslide monitoring and rather was restricted either to pilot and experimental studies or only applied to video frames for a very small-time window (Zach et al., 2007; Javier et al., 2013; Amaki et al., 2019; Kim and Gratchev, 2021; Srokosz et al., 2021). This study reduced the limitations of optical flow such as brightness consistency and successfully applied the optical flow algorithm to low-cost ground based and satellite optical imagery as well as radar backscatter imagery. The detailed workflow, methodology and applications developed here are presented in Chapters 2 and 5 and supplementary material for corresponding chapters within Appendix A and D.

1.2.3. Structural Geology

The current work includes classical structural geology techniques in the form of plotting attitude of structures on stereonets, analyzing structural trends, and spatial correlation between rock units versus structural features including fractures/veins, faults, folds, and the attitudes of basement and young volcanic units. All the data were plotted and analyzed using stereonet software by Allmendinger (2020). Various fieldwork tools are also employed such as the traditional geologic compass, Fieldmove-Clino structural geology mapping application (Hama et al., 2014; Vaughan et al., 2014) for recording bedding, joint and fracture orientations, dike trends and dips, and fault slickensides. Additionally, a Gaia GPS mobile application was used to pinpoint site and sample locations with detailed descriptions tagged for each locality. Both field technologies enabled the efficient transfer of field data to laboratory computers. The data and field observations were used to study the potential kinematic compatibility of the mapped structures: 1) relative to spatial and cross-cutting relationships of structures such as

faults, folds, and attitude of rock units, and 2) relative to the modern regional tectonic trend within the Garibaldi Volcanic Belt.

Although, conventional structural geology techniques help to identify the post-depositional deformation events particularly for sedimentary rocks; in volcanic rocks where accurate bedding measurements are difficult to achieve, conventional structural geology solely is not sufficient. Volcanic rocks can preserve the magnetic direction during emplacement and hence, record the magnetic polarity for that time. Coupling the knowledge of fossilized magnetic polarity with radiometric dating assists in identifying the post depositional deformation events (Edel et al., 2014; Williams-Jones et al., 2020; Muhammad et al., 2021, 2024).

At least eight cores should be collected at each site over an area of 5-10 m to reduce the potential errors from lightning or minor local movements along joints, etc. A portable gasoline-powered rockdrill with water swivel attachment was used to drill 2.5 cm diameter cylindrical cores. Additionally, all samples were oriented using a solar and magnetic compass to preclude orientation error due to compass deflection by strongly magnetized rocks at the outcrop. Paleomagnetic directional sampling analysis was conducted by Dr. Rene Barendregt at the Paleomagnetic laboratory at the University of Lethbridge, Alberta. The aim is to compare paleopole results with the geomagnetic polarity of the rocks at their depositional age.

1.3. Thesis Outline

This thesis aims to develop a multi-disciplinary approach to merge remote-sensing, structural geology, and geotechnical numerical analysis to design a geohazard monitoring workflow in glacio-volcanic and alpine mountainous terrains. Additionally, I aim to address some of the geological challenges to harness geothermal resources beneath the glacio-volcanic mountains of southern British Columbia, particularly the MMVC.

This thesis consists of six chapters. Chapters 1 and 6 are the introduction and conclusion and future work opportunities. Chapters 2, 3, 4 and 5 are structured as independent journal style manuscripts that have either been published or will be submitted for publication.

- Chapter 1 presents introductions, research objectives and background and methods used in this thesis. Methodologies for each chapter are discussed in greater detail within the relevant chapters.

- Chapter 2 presents the Applications of Image-Based Computer Vision for Remote Surveillance of Slope Instability (Published in Frontiers of Earth Sciences).

- Chapter 3 presents Structural Geology of the Mount Meager Volcanic Complex, BC, Canada: Implications for geothermal energy and geohazards (Published in the Canadian Journal of Earth Sciences).

- Chapter 4 presents Integrated Assessment of Rock Slope Stability Incorporating Structural Geology, Geotechnical Kinematic Modelling, and Satellite Remote Sensing: A Case Study of Mount Currie, British Columbia, Canada. This will be submitted for publication.

- Chapter 5 presents Optical Flow: A Multifaceted Approach for Analyzing and Observing Rock Glaciers and Landslides through Optical and Radar Images. This will be submitted for publication.

- Chapter 6 presents Conclusions and Future Work.

Chapter 2.   Applications of Image-Based Computer Vision for Remote Surveillance of Slope Instability

Mahmud Muhammad[1*], Glyn Williams-Jones[1], Doug Stead[1], Riccardo Tortini[2], Giacomo Falorni[2], Davide Donati [3]

[1]Centre for Natural Hazards Research, Department of Earth Sciences, Simon Fraser University, 8888 University Dr, Burnaby, BC, V5A 1S6, Canada

[2]TRE Altamira Inc., 475 W Georgia Street, suite 410, Vancouver, BC, V6B 3A3, Canada

[3]Dipartimento di Ingegneria Civile, Chimica, Ambientale e dei Materiali, Alma Mater Studiorum – Univerità di Bologna, viale del Risorgimento 2, Bologna, Italy.

Published as: Muhammad, M., Williams-Jones, G., Stead, D., Tortini, R., Falorni, G., Donati, D. (2022) Applications of image-based computer vision for remote surveillance of slope instability, Frontiers in Earth Science, 10: 909078, doi: 10.3389/feart.2022.909078

2.1. Abstract

Landslides and slope failures represent critical hazards for both the safety of local communities and the potential damage to economically relevant infrastructure such as roads, hydroelectric plants, pipelines, etc. Numerous surveillance methods, including ground-based radar, InSAR, LiDAR, seismometers, and more recently computer vision, are available to monitor landslides and slope instability. However, the high cost, complexity, and intrinsic technical limitations of these methods frequently require the design of alternative and complementary techniques. Here, we provide an improved methodology for the application of image-based computer vision in landslide and rockfall monitoring. The newly developed open access Python-based software, Akh-Defo, uses optical flow velocity, image differencing and similarity index map techniques to calculate land deformation including landslides and rockfall. Akh-Defo is applied to two different datasets, notably ground- and satellite-based optical imagery for the Plinth Peak slope in British Columbia, Canada, and satellite optical imagery for Mud Creek landslide in

California, USA. Ground-based optical images were processed to evaluate the capability of Akh-Defo to identify rockfalls and measure land displacement in steep-slope terrains to complement LOS limitations of radar satellite images. Similarly, satellite optical images were processed to evaluate the capability of Akh-Defo to identify ground displacement in active landslide regions a few weeks to months prior to initiation of landslides. The Akh-Defo results were validated from two independent datasets including radar-imagery, processed using state of the art SqueeSAR algorithm for the Plinth Peak case study and very high-resolution temporal LiDAR and photogrammetry digital surface elevation datasets for Mud Creek case study. Our study shows that the Akh-Defo software complements InSAR by mitigating LOS limitations via processing ground-based optical imagery. Additionally, if applied to satellite optical imagery, it can be used as a first stage preliminary warning system (particularly when run on the cloud allowing near real-time processing) prior to processing more expensive but more accurate InSAR products such as SqueeSAR

2.2. Introduction

Numerous monitoring approaches, including ground-based radar (Rosenblad et al., 2015), InSAR (Ferretti et al., 2007; Ferretti, 2014), LiDAR (Lin et al., 2013; Tortini et al., 2015; Kromer et al., 2017; Williams et al., 2018, 2019; Holst et al., 2021), seismometers (Suriñach et al., 2005), and more recently computer vision (O'Donovan, 2005; Zach et al., 2007; Wedel et al., 2009; Javier et al., 2013; Kim et al., 2020; Hermle et al., 2022), have been used to study landslides and slope instability. However, the elevated cost, complexity, and intrinsic technical limitations of these methods frequently necessitates the development of alternative and complementary techniques.

At the regional scale, due to its ability to measure millimeter deformation over large areas, InSAR has become one of the most powerful remote sensing monitoring techniques. However, in areas with steep topography the geometric configuration of satellite SAR systems means that some slopes will not be visible to the satellite (Ferretti, 2014). In the case of more detailed and real-time monitoring of targeted mountain slopes, ground-based Radar, and LiDAR (Kromer et al., 2017) can provide high resolution slope deformation monitoring (e.g.,Tarchi, 2003; Vallee, 2019) , but the relatively high operational costs of such techniques often limit their implementation,

particularly in isolated areas with rugged topography. Hence, introducing a lower cost technique comparable to ground-based LiDAR and Radar is of great interest.

Geophysical tools such as seismometers and infrasound sensors can also record signals generated by rockfalls and landslides. However, the applicability of such techniques strongly depends on the quality of the recording network, magnitude of the events, and the presence of technical expertise to properly interpret the signals. An important limitation of these sensors is their inability to forecast landslides and rockfalls before their occurrence (Zimmer and Sitar, 2015; Ulivieri et al., 2020). Recently, a number of studies have been undertaken using computer vision codes and surveillance video cameras to forecast landslides (Amaki et al., 2019) and monitor and assess rockfalls (Kim et al., 2020); they have mainly focused on processing video frames with very short time lapse sequences. In remote and rugged mountainous areas, the challenge of providing both sufficient power and an effective means of transmitting continuous video limits the use of real-time video datasets. These power and telemetry challenges can be addressed by collecting and processing daily static images with longer time-intervals (from hours to daily) while still enabling continuous monitoring.

In this paper, we provide an improved methodology for the application of computer vision in landslide and rockfall monitoring. The newly developed open access Python-based software, Akh-Defo (available via GitHub repository), uses optical flow velocity, image differencing and similarity index map techniques (Kim et al., 2020) to calculate land deformation (land displacement and rock fall) from a triplet of images (ground-based and satellite). Stacking of the processed triple image sets allows us to calculate the average displacement velocity over an extended period of time. Here, Akh-Defo is applied to two different datasets in British Columbia (BC), Canada and in California, United States of America. The datasets include: 1) Ground-based camera images, with hourly to daily acquisitions, collected during the summer 2021 for the Plinth Peak slope of the Mount Meager Volcanic Complex (MMVC) in BC (Fig. 2.1); and 2) Daily orthorectified satellite images, provided by Planet Labs, for the Plinth Peak slope (July 28 to August 13, 2021) and the May 20, 2017, Mud Creek Landslide in California (April 5 to May 31, 2017) (Fig. 2.1).

2.3. Research Objectives

This work has two main objectives:

1) Test whether the Akh-Defo software can complement InSAR LOS limitations via processing of ground-based optical imagery to identify rockfalls and measure land displacement in steep-slope terrain. To achieve this, we chose to apply Akh-Defo on the Plinth Peak slope of MMVC due to the presence of steep slopes and the rugged alpine mountain setting. Independent multi-temporal radar imagery processed by TRE-Altamira scientists using SqueeSAR software (Ferretti et al., 2011) provides high precision measurements of ground displacement for validation.

2) Test whether the Akh-Defo software applied to satellite optical images can identify ground displacement in active landslide regions a few weeks to months prior to initiation of landslides. To achieve this, we investigate the May 20, 2017, Mud Creek catastrophic landslide which has been very well studied and includes very high-resolution pre-, syn- and post-landslide LiDAR and photogrammetry digital surface elevation datasets (Warrick et al., 2019).
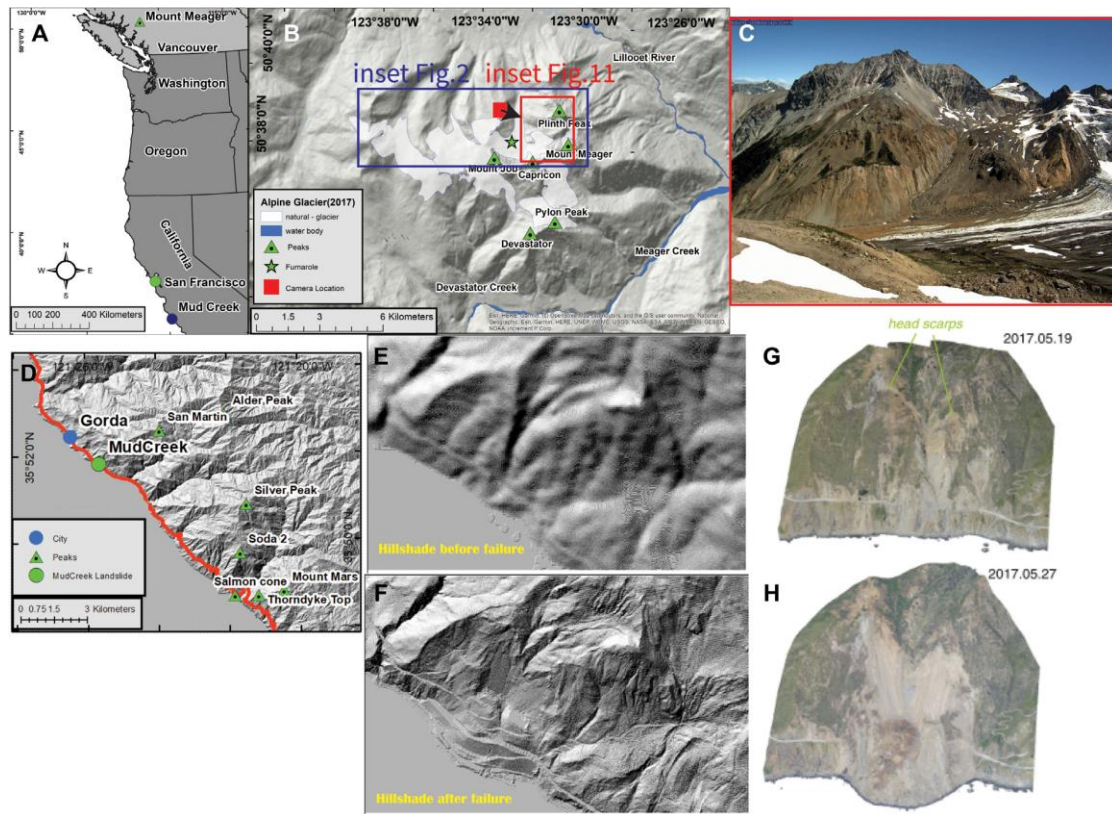
Figure 2.1. Location of the study areas. (A) Regional basemap showing the locations of Mount Meager and Mud Creek relative to western North America. (B) Hillshademap showing the location of important peaks, fumaroles, and installed camera station in the MMVC; the red inset represents the approximate area captured by the installed camera; the red square with black arrow indicates location and orientation of the camera view; the blue inset shows the area of Figure 2. (C) Example of optical image on 10 August 2021, captured at 11 a.m. by the camera station. (D) Hillshade map shows the location of Mud Creek landslide and the surrounding mountain peaks. (E) Hillshade map showing the topography of the Mud Creek area before the failure. (F) Hillshade map showing the topography of the Mud Creek area after the failure. (G) Oblique aerial view of Mud Creek 1 day before the failure derived from a photogrammetry model (after Warrick, et al., 2019). (H) Oblique aerial view of Mud Creek 7 days after the failure derived from a photogrammetry model (after Warrick, et al., 2019).

2.4. Site Overview

2.4.1. Plinth Peak Slope, Mount Meager

The slope of interest is located on the NNW flank of the MMVC in the Garibaldi Volcanic Belt of British Columbia, Canada, an area characterized by temperate rainforests, alpine glaciers, and recently observed volcanic fumaroles. The topography consists of steep, highly altered, and unstable volcanic rock slopes which are at least partially covered with snow; visibility is often limited due to fog or low-lying cloud (Fig. 2.1). The MMVC consists of overlapping volcanoes with a protracted history of basaltic to rhyodacitic volcanism generating lava flows and domes, pyroclastic deposits, and associated rock avalanche deposits from >1.9 Ma to present; these sit on Triassic to Tertiary Coastal Plutonic Complex intrusions and metasedimentary units (Read, 1990; Russell et al., 2021). The MMVC has erupted explosively at least twice in the past 25,000 years with the most recent event in 2360 B.P. (Russell et al., 2021); pyroclastic density currents from these eruptions were sourced at high elevation near the present-day Plinth Peak and since 2016, low level fumarolic degassing has been observed through glaciovolcanic caves on the west flank of Plinth Peak (Warwick et al., 2022).

The most recent and largest historic landslide in Canada occurred during the summer 2010 from the southern flank of Mount Meager; less than 3 km south of current study area (Guthrie et al., 2012; Roberti, 2018). Previous remote sensing and geomorphologic studies of the MMVC indicate that it hosts numerous historical and recent landslide deposits and numerous unstable areas have been identified, many of which are believed to be susceptible to future landslide events (Mokievsky-Zubok, 1977; Friele and Clague, 2004; Guthrie et al., 2012; Roberti et al., 2017, 2018). Hetherington, (2014) identify unstable areas on the western side of Plinth Peak and note that the eastern flank appears to have a very low factor of safety that can be presumed to be at the point of failure. The failure surface is described as being deep (Hetherington, 2014; Roberti, 2018; Roberti et al., 2021b) such that should a landslide occur in this location, a major bulk of Plinth Peak could fail. Consequently, as with the 2010 landslide, it could dam the Lillooet River and cause widespread flooding downstream.

2.4.2. Mud-Creek Landslide

The Mud Creek Landslide is located between Monterey and Morro Bay on the Big Sur coast of California, USA (Fig. 2.1). Geomorphologically, Mud Creek coincides with the rugged Big Sur coast at the western edge of the Santa Lucia Mountains. This area includes numerous peaks higher than 1000 m elevation, many of which are located less than 10 km from the coast. Geologically, the Mud Creek and surrounding mountain bedrock is composed of Mesozoic granitic and pre-Cretaceous metamorphic rocks, Miocene marine sedimentary rocks, and heterogeneous Mesozoic rocks which form the Franciscan Assemblage mélange overlying unconsolidated colluvial deposits (Warrick et al., 2019). Structurally, these rugged mountains are related to the Big Sur Bend of the San Gregorio-Hosgri fault system, a region of transpression along the region's transform plate boundary (Warrick et al., 2019). This coastal mountain landslide is in an active landslide region, with coastal retreat rates during the twentieth century averaging ~ 0.3 m/year (Warrick et al., 2019).

Knowledge of morphology and movement patterns was obtained from previously studied LiDAR and Structure from Motion (SfM) photogrammetry for the pre-May 20, 2017, landslide of Mud Creek (Warrick et al., 2019a) (Fig. 2.1). The pre-failure slope was identified as steep and planar and bisected by a large steep valley. Warrick et al., (2019) used LiDAR- and SfM-derived digital elevation surfaces from 1967 to 2017 data. Although topographic changes from 2010 to 2016 were not significant, horizontal displacement calculated from hillshade surfaces range between 2 m to 10 m for the same time period (Warrick et al., 2019). Between 2016 and 2017, these differences increased to over 10 m between March 8 and May 19, 2017, during which time large head scarps formed on the northern and southern portions of the slide (Fig. 2.1).

2.5. Data Collection

2.5.1. Ground-Based Optical Images

At Mount Meager, with support from Weir-Jones Engineering, we installed a Stardot SD500BN camera, solar power, satellite telemetry, and weather station (all donated by Nupoint Systems Inc.), on a ridge approximately 1.5 km from the slope of interest (Fig.

2.1). The camera, facing the west-side of Plinth Peak, has a maximum resolution of 5 MP, 2592 x 1944 at 30 frames per second (fps). This was remotely programmed to take one image per hour during the daytime for a total of 12 images per day and data (both weather data and images) was transmitted via satellite to the Nupoint Systems and SFU data portals.

From November 2020 to September 2021, a total 1315 images were collected (see online GitHub Repository for all the images). An automatic image-classification system (Bouti et al., 2020) was used to remove images with significant cloud, fog, and shadow (see supplementary material). As the study area receives >3-4 m of snow during the winter, we were limited to processing only summer images that include the least amount of snow coverage. Therefore, during this study, we processed approximately three weeks of images from July 27 to August 18, 2021. For consistency across the dataset, processed images were taken at four different times (11 AM, 12 PM, 1 PM, 2 PM).

2.5.2. Satellite Optical Images

For both the Plinth Peak and Mud Creek study, high resolution (3 m spatial resolution) Planet Labs optical satellite images were acquired through a research and education license (Team, 2017). The level 3B surface reflectance product of PlanetScope was chosen as it comes orthorectified and corrected for geometric, radiometric, and atmospheric noise. A total of 9 cloud-free PlanetScope orthorectified images from July 28 to August 13, 2021, were used to calculate land-displacement rates for the Plinth Peak slope. Ten cloud-free scenes of PlanetScope orthorectified images from April 5 to May 31, 2017, were used to bracket the May 20, 2017, Mud Creek event.
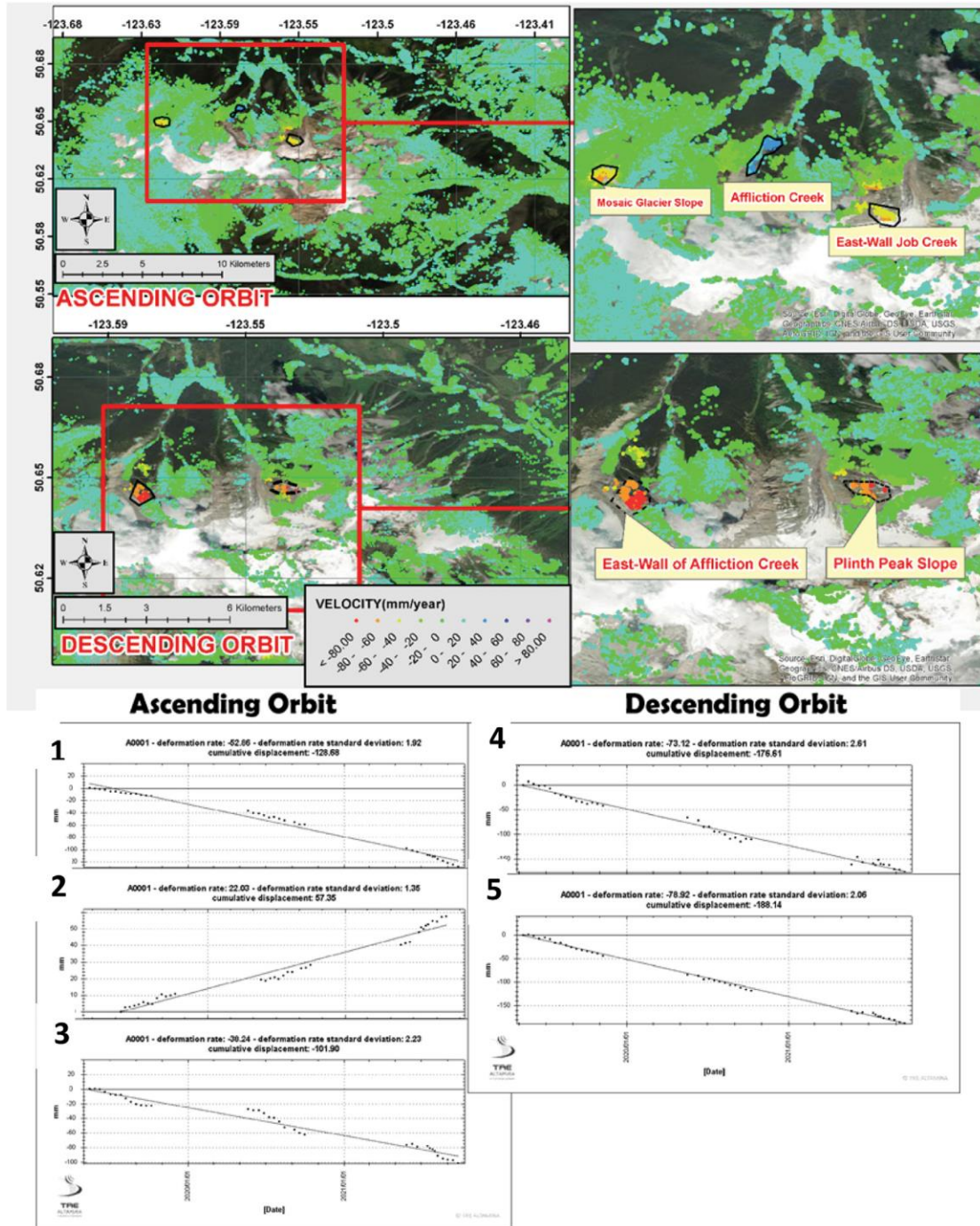
Figure 2.2. SqueeSAR results show deformation rate in mm/year north of the Mount Meager massif; see blue inset in Fig. 2.1 B for the location. Note the impact of Line of Sight (LOS) limitation to capture slope deformation for both ascending and descending satellite orbits. The graphs show the temporal deformation rate for 1. East-Wall Job Creek. 2. Affliction Creek 3. Mosaic Creek Slope in the ascending orbit, and 4. Plinth Peak slope and 5. East-Wall Affliction Creek in the descending orbit.

2.5.3. Satellite Radar Images

As part of ongoing collaborations between researchers at the Centre for Natural Hazards Research at Simon Fraser University (SFU) and TRE-Altamira, regional landslide and slope stability monitoring has been conducted since 2019 in the Garibaldi Volcanic Belt with a particular focus on the MMVC (Fig. 2.1). TRE-Altamira scientists processed temporal displacement data for the available SAR satellite (ERS, Sentinel-1, and Radarsat 1 and 2) images from 1992 to 2021 using the SqueeSAR algorithm (Ferretti et al., 2011). As the data were collected from different satellite platforms with different spatial and temporal resolution, we only present data with high temporal and spatial resolution from May 2019 to September 2021 (Fig. 2.2 and Table S2.1 in supplementary material). A total of 36 ascending and 40 descending Sentinel-1 images were processed to obtain 1D line of sight (LOS) and 2D true vertical and east-west displacements over the MMVC.

2.6. Methodology

The methodology of this paper is twofold (Fig. 2.3). The first part deals with optical image processing and the second part discusses processing Radar satellite images using TRE-Altamira's SqueeSAR algorithm. The Akh-Defo software developed in this study (Fig. 2.3) is applied to ground and satellite optical imagery. The Akh-Defo version for ground based optical imagery consists of two Jupyter Notebook files which can run on any Integrated Development and Learning Environment (IDE) with the ability to read Jupyter Notebook files (e.g., Visual Studio Code, Jupyter Lab, Jupyter Notebook). The first Jupyter Notebook file includes image-preprocessing (discussed in detail in the supplementary material) such as training the Deep-Learning Convolutional Neural Network (DLCNN) model, application of the trained model to classify and differentiate noisy from noise-free images, sorting of images based on hours of each day, and finally image-alignment analysis for quality assessment before image processing for change detection analysis (Fig. 2.3). The second Jupyter Notebook file includes a simple graphical user interface which performs the following steps: 1) image enhancement and definition of the area of interest; 2) static change detection; and 3) dynamic change detection (static and dynamic change detection described below).

The Akh-Defo version for satellite optical imagery consists of one Jupyter Notebook file and only processes orthorectified imagery (Fig. 2.3). The software also includes a simple graphical user interface that performs the following steps: 1) image enhancement and definition of the area of interest; 2) static change detection and 3) dynamic change detection. Unlike the ground-based version, the satellite version enables geocoding and orthorectification of the final products to real-world coordinates for use with any GIS platforms.
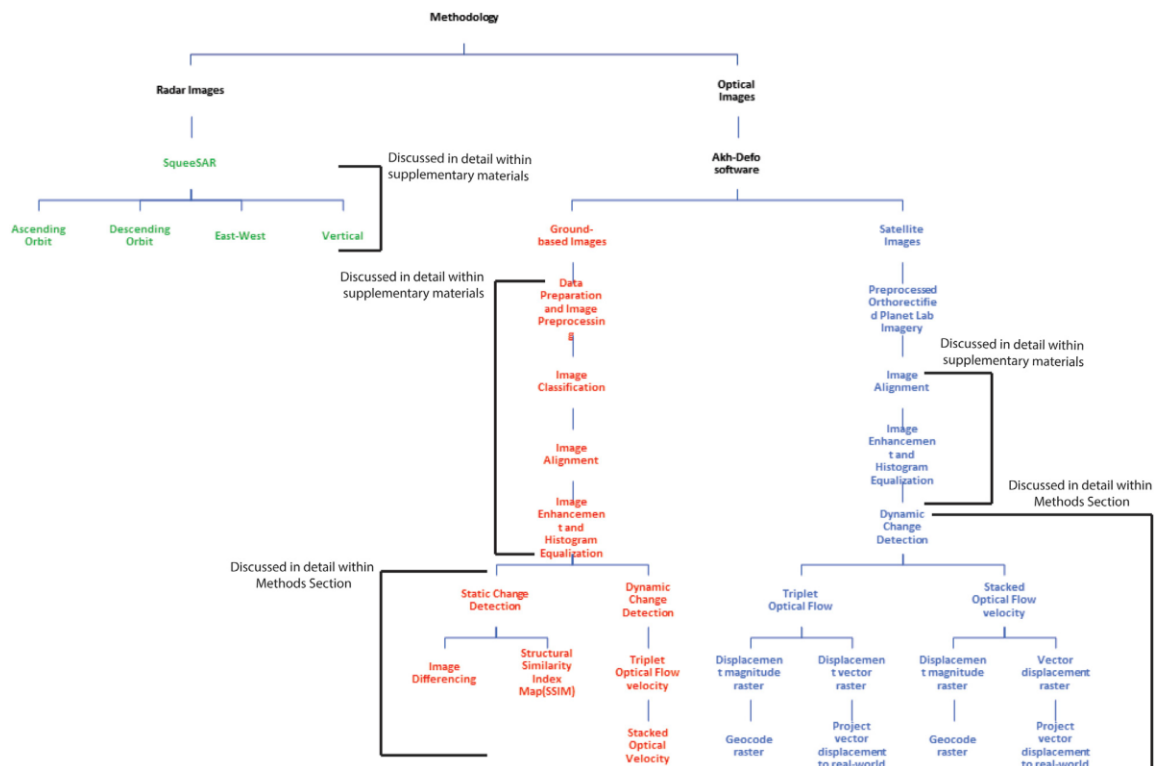
Figure 2.3. **Methodology flow chart showing the sequential data processing and analysis in this study.**

2.6.1. Optical Monitoring

Static Change Detection

Static Change detection includes image differencing such as performing subtraction between two images to identify change of the visual scene or a similarity map to differentiate areas with no change from those with change. We call this static change detection because we can only accurately identify the changes if material (objects) is removed or added within the visual scene between two separate images (Figs. 2.4, 2.5).
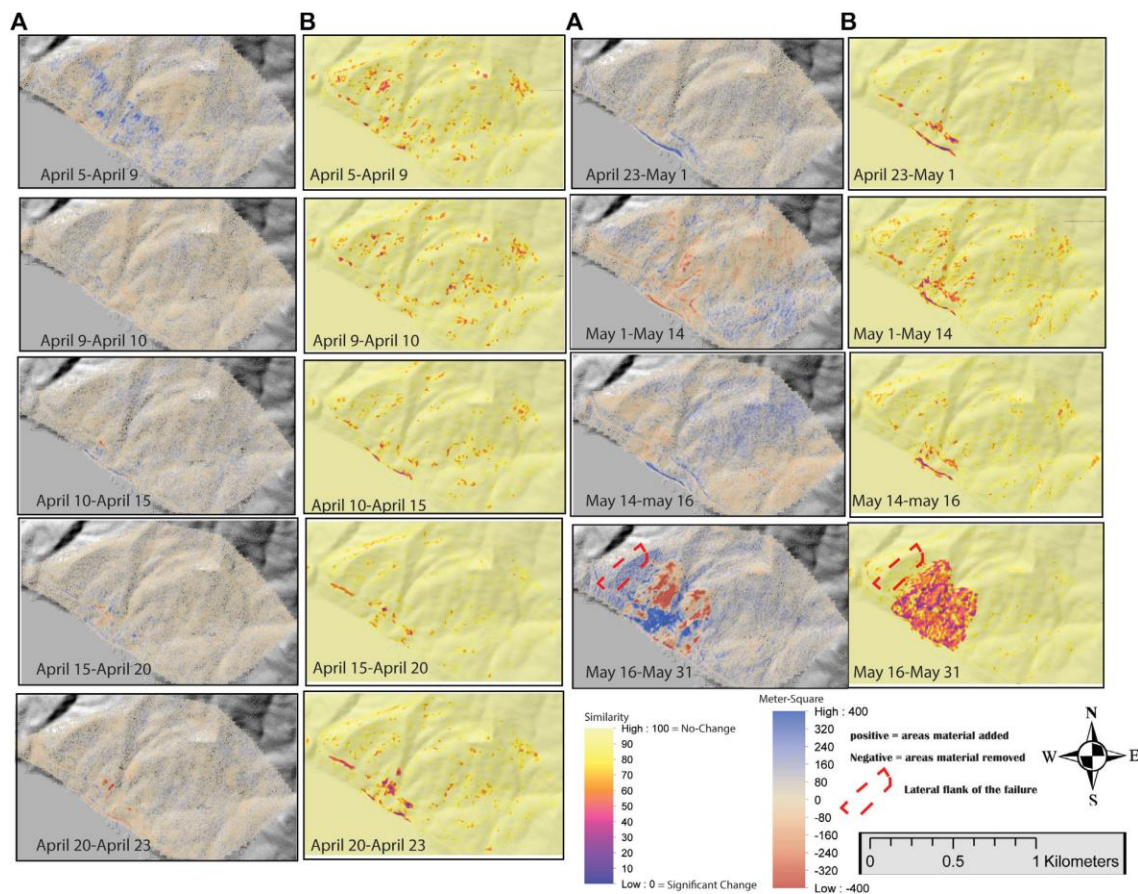
Figure 2.4.   **Static change detection timestamp results for the Mud Creek landslide. Column (A) shows the image differencing results; negative values indicate areas with material being removed, and positive values indicate areas with material being added. (B) shows the Structural Similarity Index Map, similarity map scaled between 0= no similarity and 100 = strongly similar (no change).**

Image Differencing

This technique consists of a pixel-to-pixel value subtraction of an image (Im_1) at specific time, *t*, for a given date to the same pixel in an image for a different date, Im_2, but at the same time (Figs. 2.4A and 2.5A).

$$Image\ Difference = Im_1 \text{t} - Im_2 t$$

This process is performed sequentially for the temporal images from Plinth Peak. By default, image pixel subtraction produces a significant amount of noise, and the quality of the results depends on the time interval between subsequent images as the pixel intensity changes between images. In this study, the minimum time interval between images is about 24 h, but we compensate for the relatively long-time interval by comparing images at a fixed time in subsequent days.

Similarity Indices (MSE and SSIM)

The Mean Square error (MSE) and the Structural Similarity Index Mean (SSIM) are two Similarity indices that are frequently used to measure the quality of images (e.g., Palubinskas, 2014; Kim et al., 2020). MSE is considered as a measure of signal fidelity which compares two signals (images) and provides a quantitative score that measures the degree of similarity between them. We assume $\text{x} = \{x_i \mid i = 1,2,\cdots,N\}$ and $\text{y} = \{y_i \mid i = 1,2,\cdots,N\}$ in which N denotes the number of signal samples (i.e., the number of pixels in an image) such that x_i and y_i are values of pixels at locations x and y. Therefore, MSE can be calculated as follows (Wang and Bovik, 2009):

$$\text{MSE}(x \mid y) = \frac{1}{N}\sum_{i=1}^{N}(x_i - y_i)^2.$$

The SSIM technique is based on the human visual system which is particularly powerful in extracting structural information within visual scenes. Hence, to measure similarity, the preservation of signal (image) structure is essential, and it helps to measure the structural distortion (here the distortion related to deformation of the slope). Therefore, SSIM helps to distinguish between structural and nonstructural distortions. Nonstructural distortions include those from the ambient natural environment and instrumental conditions during image acquisition such as 1) Change of luminance or brightness, 2)

Change of contrast, 3) Gamma distortion and 4) Spatial shift of pixels (Palubinskas, 2014; Kim et al., 2020). The structural distortions caused by camera lens and camera mount vibration have been corrected at the image alignment stage (Fig. 2.3); images were only left with distortions related to changes in the visual scene.

The SSIM measures similarities of images based on the combination of three independent elements i.e., the brightness values, the contrast values, and the structure of the visual image scene. Assuming that x and y are the locations of two areas within two images of the same size, the similarity of brightness value becomes l(x,y), the similarity of contrast is c(x,y), and the similarity of the area structures is s(x, y) (Palubinskas, 2014; Kim et al., 2020):

$$SSIM(\text{x,y}) = l(\text{x,y}) \cdot c(\text{x,y}) \cdot s(\text{x,y}) = \left(\frac{2\mu_x\mu_y + C_1}{\mu_x^2 + \mu_y^2 + C_1} \right)$$
$$\cdot \left(\frac{2\sigma_x\sigma_y + C_2}{\sigma_x^2 + \sigma_y^2 + C_2} \right) \cdot \left(\frac{\sigma_{xy} + C_3}{\sigma_x\sigma_y + C_3} \right)$$

where μ_x and μ_y are local sample means of x and y areas, respectively. σ_x and σ_y are local standard deviations of x and y areas; σ_{xy} allocates the sample cross-correlation of x and y after removing the means of x and y areas. To avoid numerical instability in calculating sample means, variances and correlations, small positive constants C_1, C_2, and C_3 were introduced. The SSIM map is produced by computing a sliding window moving pixel-by-pixel across the entire image (Palubinskas, 2014; Kim et al., 2020). A single SSIM score for whole image is then calculated by averaging the SSIM values across the entire image (Figs. 2.4B and 2.5B).
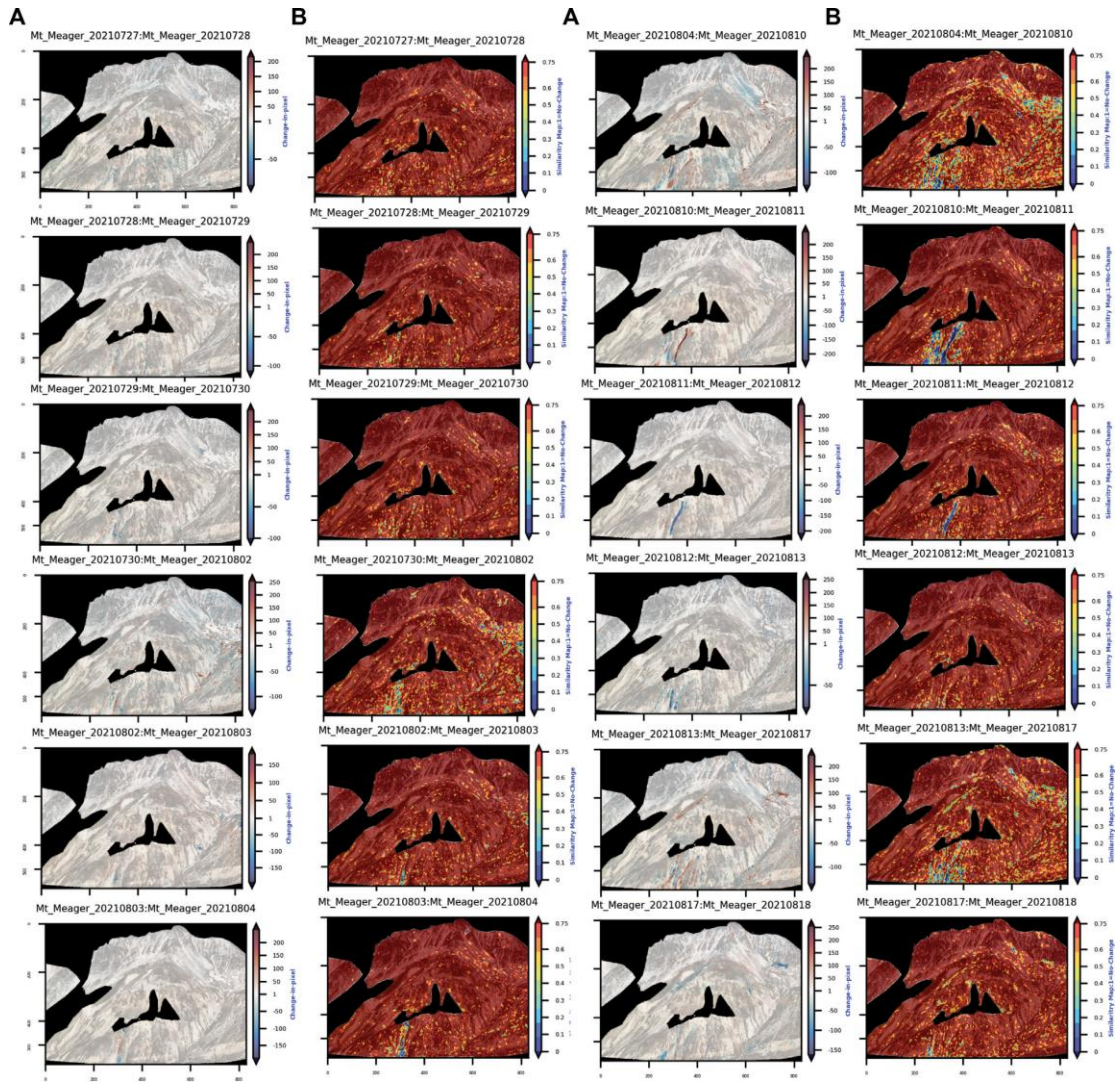
Figure 2.5.   Static change detection timestamp results for the Plinth Peak slope. Column (A) shows the image difference results, with negative values indicating areas with material being removed and positive values being added. Column (B) shows the Structural Similarity Index Map, similarity map scaled between 0 = no similarity and 1 = strongly similar (no change).
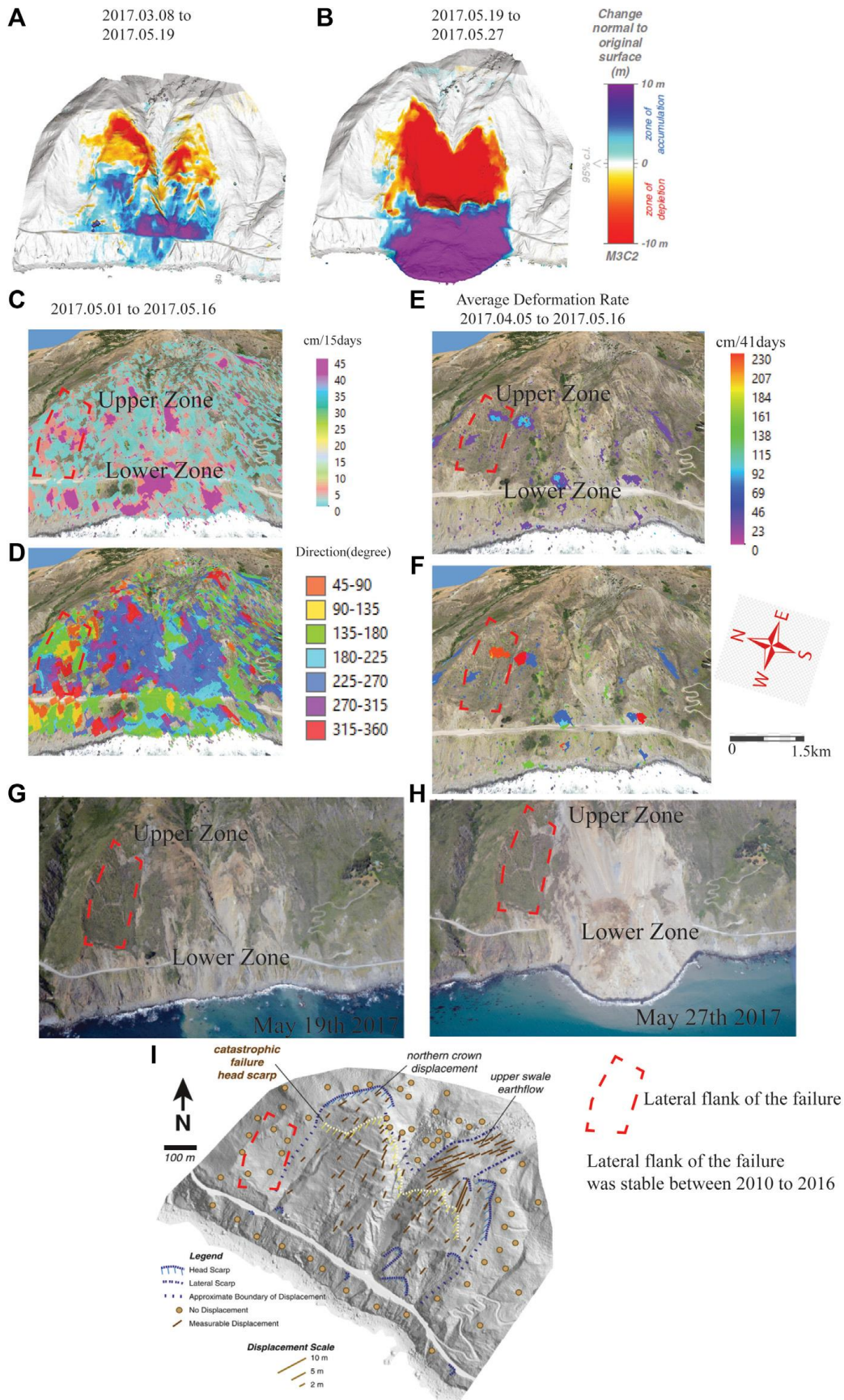
Figure 2.6. Mud Creek landslide precursor changes. (A) Elevation change calculated from SfM digital surface model between March 8 and May 19, 2017 (1 day before failure). (B) Elevation changes before and after the catastrophic failure. (C) Dynamic change detection showing horizontal displacement rates in cm per day from May 1 to May 16, 2017 (4 days before failure). (D) Displacement vector r (direction) for panel (C). (E) Average horizontal displacement rate in cm for the 41 days calculated from stacked triplets between April 5 and May 16, 2017 (4 days before the failure). (F) Displacement vector (direction) for panel (E). (G) Oblique Unmanned Aerial Vehicle (UAV) photograph taken 1 day before the May 20, 2017, failure. (H) Oblique UAV photograph taken 7 days after the May 20, 2017, failure. UAV photographs from Warrick et al. (2019). (I) Horizontal displacement map of the Mud Creek site between 2010 and 2016. Locations of observed and mapped head and lateral scarps (blue lines). The head scarp of the May 20, 2017, failure is shown for comparative purposes (yellow line). The approximate boundaries between no displacement and measurable displacement are shown with dashed lines. Shaded relief base-layer map is the May 2016 LiDAR (after Warrick et al., 2019).

Dynamic Change Detection

Dynamic Change detection involves calculating optical flow velocity between triplets of images. The temporal period between each image can be anywhere from intervals of one day to several days but the images must be taken at the same time of day in order to minimize the effects of ambient change (e.g., shadows). Subsequently, we can calculate temporal and dynamic change detection from a stack of calculated triplets. We call this dynamic change detection because we can identify the change before (precursor of rockfall and landslide), during (e.g., tracing rockfall and landslide flow path) and after (post-failure) material being removed or added within the scene between a number of subsequent images (Figs. 2.6 C to F, 2.7, 2.8).

Optical Flow Velocity

Optical flow is represented as the apparent motion of objects and surfaces between two different timeframes caused by relative motion between the observer (camera) and the scene (e.g., objects, surfaces, and edges) (Zach et al., 2007; 2005; Wedel et al., 2009; Hermle et al., 2022). The most important assumption in optical flow velocity calculations is constancy in image brightness. This assumption requires that for a short time interval, t_1 to t_2, an object may change position, while the reflectivity and illumination will remain

constant. Here we process images using an interval of 24 hours to a few days, however, it is more difficult to fulfill the assumption of brightness constancy without proper image preprocessing and appropriate image selection for processing. Longer time intervals were compensated by processing images at a fixed time as it helps to remove impact of the angular change in Sun illumination (Figs. 2.7, 2.8). For processing optical satellite images, while repeated image acquisition is not possible at the same exact time for each day, the images acquired are near vertical (i.e., similar Sun illumination) and we used orthorectified images that have been pre-processed and corrected for atmospheric and geometric noise.
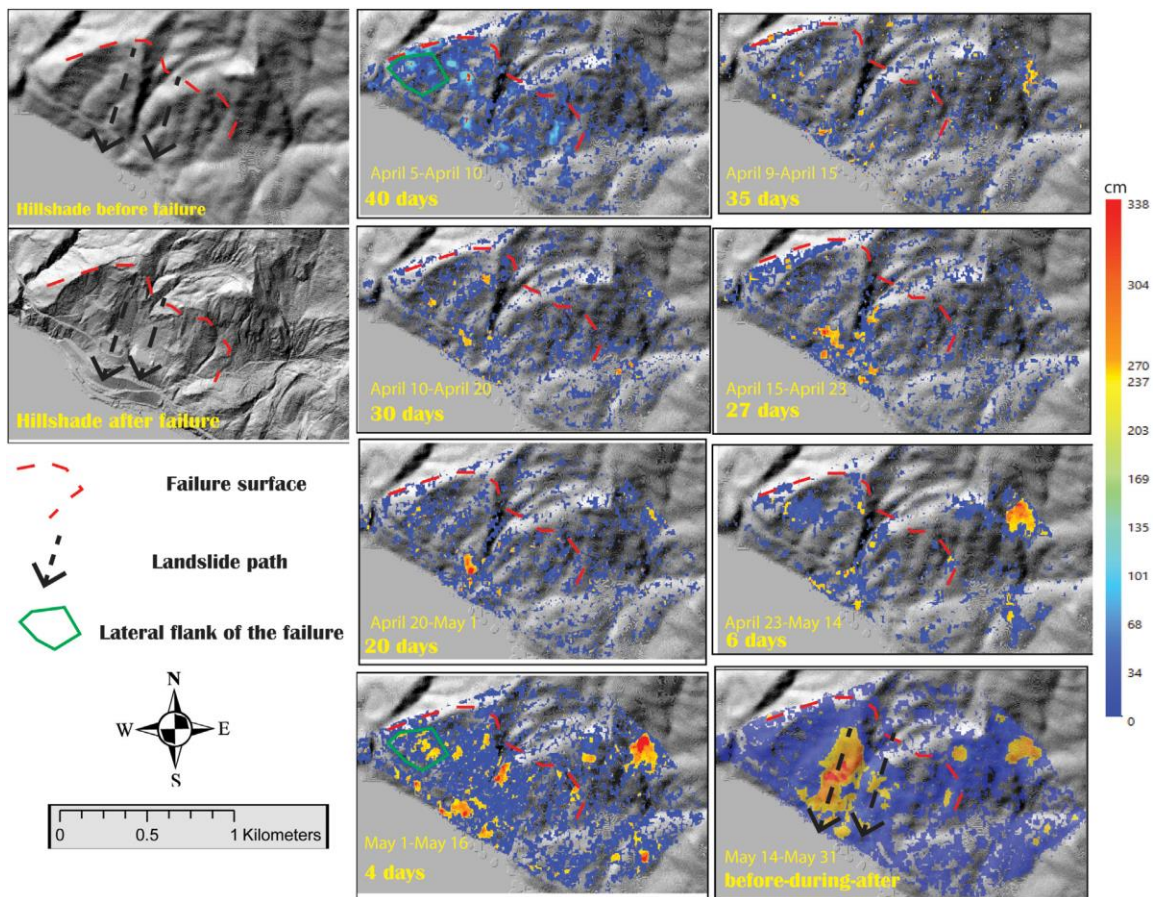
Figure 2.7. **Timestamp (number of days before the failure) horizontal displacement rate (cm per days) before the May 20, 2017, landslide. Note the location of the failure surface before and after the landslide.**

The optical flow equation includes:

$$I(x + \Delta x, y + \Delta y, t + \Delta t) = I(x, y, t)$$

where I(x, y, t) is the intensity of the image at position (x, y) for time t and the change in position is indicated by $\Delta x \ and \ \Delta y$ at change of time Δt. After applying a Taylor series expansion to the left-hand side of the equation, it can be rewritten as follows (O'donovan, 2005; Zach et al., 2007; Wedel et al., 2009; Hermle et al., 2022).

$$I(x + \Delta x, y + \Delta y, t + \Delta t) = I(x, y, t) + \frac{\partial I}{\partial x}\Delta x + \frac{\partial I}{\partial x}\Delta y + \frac{\partial I}{\partial t}\Delta t$$

By solving the above equation, we obtain the optical flow constraint equation:

$$\nabla I \cdot \text{v} + I_t = 0$$

where ∇I is the spatial intensity gradient (I_x, I_y), v = (u, v) is the flow vector for Δx and Δy and I_t is gradient through time.

Additionally, to better compensate for the image time interval, we calculate the optical flow for triplets of images (frames) instead of pairs of images. The sequence of image triplets is chosen in order to provide overlap among subsequent processed triplet datasets (Fig. 2.7). For instance, (image$_n$, image$_{n+1}$ and image$_n$, image$_{n+2}$) forms the first triplet set; the second triplet set is equal to (image$_{n+1}$, image$_{n+2}$ and image$_{n+1}$, image$_{n+3}$) and so on for the rest of the image sequences. The calculated optical flow movements are then stacked for the horizontal $\frac{\Delta x}{\Delta t}$, and vertical $\frac{\Delta y}{\Delta t}$, obtained from each set of processed triplets. The stacking process allows us to calculate more accurate optical flow motion because it uses a larger number of images and averages the results of the calculated triplet optical velocities. Additionally, it provides measurements over a longer time interval of months to even multiple years depending on the number of available processed triplets and the time-window of the triplet datasets (Figs.2.6 C to F, 2.7, 2.8).

Radar Monitoring

Synthetic Aperture Radar (SAR)

Synthetic Aperture Radar (SAR) satellites acquire images of the Earth's surface by emitting electromagnetic waves and analyzing the reflected signal. As SAR satellites are continuously orbiting the globe, a stack of SAR images can be collected for the same area over time to extract information about changes of the Earth's surface. Each SAR acquisition contains two fundamental properties: amplitude and phase. The amplitude is related to the energy of the backscattered signal and is used in Speckle/Pixel Tracking applications and change detection mapping. Phase is related to the sensor-to-target distance, and it is this which is used in interferometric applications.

InSAR

Interferometric Synthetic Aperture Radar (InSAR), also referred to as Interferometric SAR, is the measurement of signal phase change or interference over time. When a point on the ground moves, the distance between the sensor and the ground target changes affecting the phase value recorded by the SAR sensor. Figure 2.2 shows the relationship between ground movement and the corresponding shift in signal phase between two SAR signals acquired over the same area. This relationship is expressed as:

$$\Delta\varphi = \frac{4\pi}{\lambda}\Delta R$$

where $\Delta\varphi$ is the change in signal phase, λ is the wavelength and ΔR is the displacement. Consequently, any displacement of a radar target along the satellite line of sight (LOS) creates a phase shift in the radar signal that can be detected by comparing the phase values of two SAR images acquired at different times. Due to the acquisition geometry, any phase variation is detected along the satellite LOS. In general, due to the known parameters of SAR satellite orbits and acquisition geometry (approximate North-South orbital direction and side and tilted view), InSAR can detect motion components predominantly in E-W and vertical directions. In contrast, the sensitivity to N-S motion is minimal, even in the presence of strong movement. The comparison of the phase of two SAR images can only be used when the normal baseline (i.e., distance between the

satellite tracks during the first and second acquisitions) is no more than the so-called "critical baseline", a parameter depending on the SAR sensor in use.
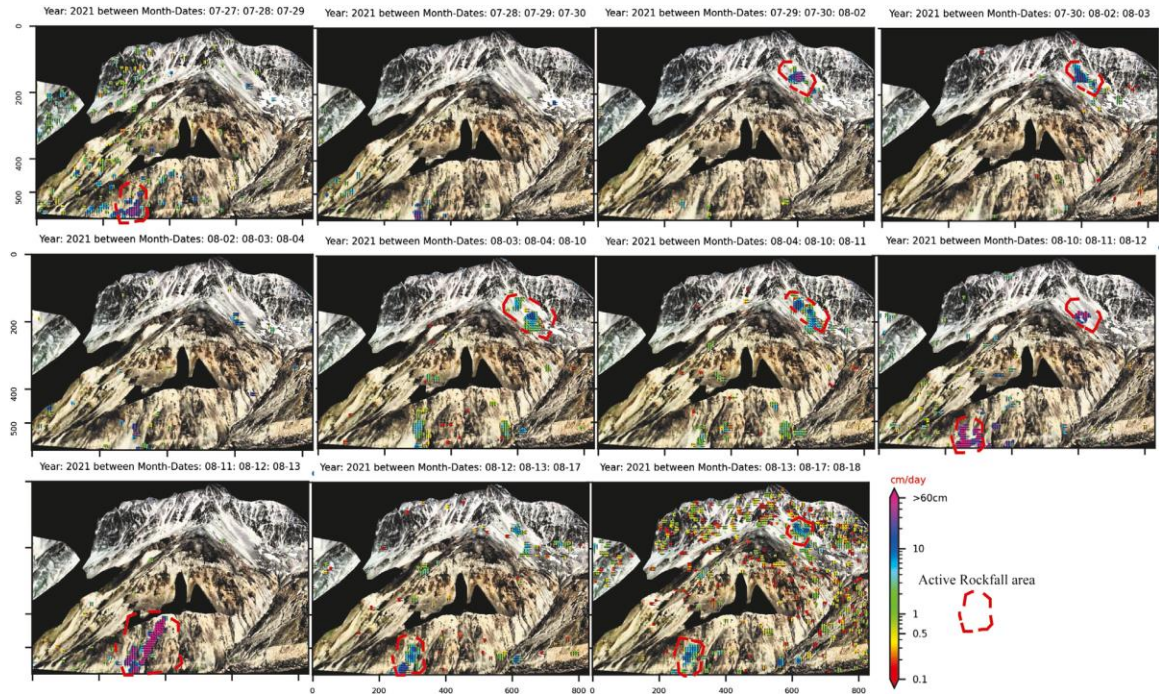
Figure 2.8. **Example of dynamic change detection at 2 p.m. daily for the Plinth Peak slope. Refer to the GitHub repository for temporal dynamic change detection results at 11 a.m., 12 p.m., and 1 p.m.**

SqueeSAR

SqueeSAR™ is the proprietary multi-interferogram technique developed by TRE Altamira which provides high precision measurements of ground displacement by processing multi-temporal SAR images acquired over the same area. SqueeSAR™ typically needs a dataset of at least 15-20 SAR images to be applied, acquired over the same area with the same acquisition mode and geometry. By statistically exploiting the image stack, SqueeSAR™ singles out measurement points (MP) on the ground that display stable amplitude and coherent phase throughout every image of the dataset (Ferretti et al., 2011). The MPs belong to two different families: (i) Permanent Scatterers (PS) point-wise radar targets characterized by high stable radar signal return (e.g., buildings, rocky outcrops, linear structures, etc.), and (ii) Distributed Scatterers (DS) such as areas of ground exhibiting a lower but homogenous radar signal return (e.g., uncultivated land, debris, deserted areas, etc.). The density and distribution of the MP is

related to the resolution of the SAR images used and the local surface characteristics and topography.

In general, the MP density increases with the satellite resolution and the presence of man-made structures and decreases with the presence of vegetation. The highest density is reached over urban and bare areas, while it is lower over heavily vegetated areas, areas affected by strong reflectivity changes with time (Fig. S2.5 in supplementary material) or where the satellite visibility is limited. No measurement points are identifiable over water. For each MP identified, SqueeSAR™ provides the following basic information: 1) The ground target's position and elevation; 2) Annual average displacement rate measured along the LOS, expressed in mm/year; calculated over the observation period and related to the reference point; 3) Displacement time series (TS) representing the evolution of the MP's displacement for each acquisition date, expressed in millimeters, and measured in the LOS direction.

When considering the Distributed Scatterer family of MPs, the information provided by SqueeSAR™ does not refer to a single target, but rather to the effective area associated to each DS. SqueeSAR™ does not provide the exact shape of the DS area only its dimension. As for any other InSAR analysis, all displacement measurements are carried out along the sensor's LOS to target direction. SqueeSAR™ measures the projection of real movement along the LOS and provides 1D measurements. Displacement measurements provided by SqueeSAR™ are differential in space and time. They are spatially related to a reference point and temporally to the date of the first available satellite acquisition. The reference point is assumed to be motionless and selected for its radar properties and motion behavior. This corresponds to a radar target with low phase noise in all the scenes of the imagery, not affected by displacement rate variations (non-linear movement or cyclical deformations) in the covered period. As such, the reference point can still be affected by a linear movement related to regional deformation phenomena. Any regional component can be identified via an independent check with other surface monitoring techniques, such as a GPS network. The selection of the reference point is imagery dependent: if the imagery changes (e.g., number of scenes in the stack or time span), the MP selected as the reference point can consequently change.

2.7. Results

2.7.1. Plinth Peak, Mount Meager, Canada

Results from the high temporal and spatial resolution InSAR data (summer 2019 to 2021), processed with SqueeSAR, identified at least five highly unstable regions on the north flank of the Mount Meager massif. These regions were observed with the ascending SAR satellite geometry and show annual average deformation rates of 5.2 cm, 2.2 cm and 3.8 cm for Mosaic Glacier slope, Affliction Creek, and East-Wall Job Creek, respectively (Fig. 2.2). The unstable regions observed via descending SAR satellite geometry show annual average deformation rates of 7.8 cm and 7.3 cm for East-Wall Affliction Creek and Plinth Peak slopes, respectively (Fig. 2.2).

We processed both ground-based optical images and orthorectified satellite images for Plinth Peak within the same time-window. Ground-based imagery processed with the Akh-Defo dynamic change detection technique measured monthly deformation rates on Plinth Peak from July 27 to August 18, 2021, of between 7 mm and 27 mm (Table 2.1 and Fig. 2.9). Low velocity rockfall (less than 600 mm/day) (Fig. 2.9) but frequent (Fig. 2.10) were observed during the four different daily time periods between July 27 and August 18, 2021. The total detected rockfalls at each time window are as follows: 15 events at 11 am, 15 events at 12 pm, 7 events at 1 pm, and 10 events at 2 pm (Fig. 2.9). A small landslide was identified on August 11, 2021, with an area of more than 3500 m^2 (Fig. 2.9). By contrast, PlanetLab orthorectified imagery processed with the Akh-Defo dynamic change detection was unable to quantify the rockfall activity on Plinth Peak. This is particularly related to the geometry of the camera viewing angle.

The land displacement results are validated from the calculated displacement rates from SqueeSAR for the equivalent period (Table 2.1) and at a location where we have active displacement data available from both techniques. The validation includes normalization of SqueeSAR annual displacement rates to match displacement rates for the same period of Akh-Defo dataset of 22 days (Table 2.1). At the location shown in Figure 2.9E, for the 22 days between July 27 and August 18, 2021, Akh-Defo stacked processing obtained a total displacement of 20 mm (equivalent 27 mm per month) (downward relative to the camera view; see Fig. 2.1 for the camera orientation and location).

Comparatively, at the same site and time window (Fig. 2.9G), the SqueeSAR deformation results obtained a ground displacement of 16.9 mm (22.5 mm per month), along SAR satellite LOS (Descending Orbit).

Our ground-based imagery results show that the Plinth Peak slope is subject to active and frequent rockfalls albeit with slow slope displacement and that the rockfalls are mainly concentrated along very-steep channels within the slope (see Fig. 2.10 rockfall frequency and Fig. 2.11 for sources of rockfalls). Rockfall trajectories were validated from the animated image time-lapse (see the online GitHub in the gif_dir folder dataset

Table 2.1.   Semi-quantitative comparison of measured land displacement obtained from Akh-Defo software for Plinth Peak with three independent sources: radar images, ground-based optical images, and orthorectified optical satellite images.

Case study	Dataset Type	Method	Displacement between July 27 and August 18, 2021	Monthly Displacement rate	Annual Displacement Rate	Location	Geometry
Plinth Peak	InSAR	SqueeSAR	16.9 mm	23 mm	280 mm	Fig.11G, Fig. 2	Descending LOS
	Ground-Based Optical Image	Akh-Defo	20 mm	27 mm	331 mm	Fig.11E	Downward Relative to Installed Camera view
	Planet Lab Satellite Optical Image	Akh-Defo	11mm	15 mm	182.5 mm	Fig.11C	Nearly overlooking (top view)
Percentage Difference (ground-based image vs InSAR)	= ((Akh-Defo – SqueeSAR)/ SqueeSAR) x 100						
Annual difference= 17%	((33.1– 28)/ 28) x 100						
Monthly difference=17.3%	((27– 23)/ 23) x 100						
Measured 22-Day Time Window difference=18.3%	((20– 16.9)/ 16.9) x 100						
Percentage Difference (satellite-based image vs InSAR)	= ((Akh-Defo – SqueeSAR)/ SqueeSAR) x 100						
Annual difference= 34.8%	((182.5– 280)/ 280) x 100						
Monthly difference=34.7%	((15– 23)/ 23) x 100						
Measured 22-Day Time Window difference=34.9%	((11– 16.9)/ 16.9) x 100						

The Akh-Defo static change detection (using Image Differencing and Structural Similarity Index Map) was effective in identifying one small landslide (rockslide) on the Plinth Peak slope, approximately 30-m-wide and 120-m-long (at least 3600 m^2) between August 10 and 11, 2021, although with different sensitivities (Fig. 2.12). For the same landslide, the SSIM visually produced clearer results compared with those using Image Differencing (Fig. 2.12). In fact, we also captured a precursor of this event using dynamic change detection 7 days before failure where the total displacement ranged from 1 to 10 cm from August 3 to 10, 2021 (Fig. 2.12G). Additionally, we reconstructed the rockslide trajectory and velocity of the rockslide at >60 cm/day between August 10 and 12, 2021 (Fig. 2.12H).
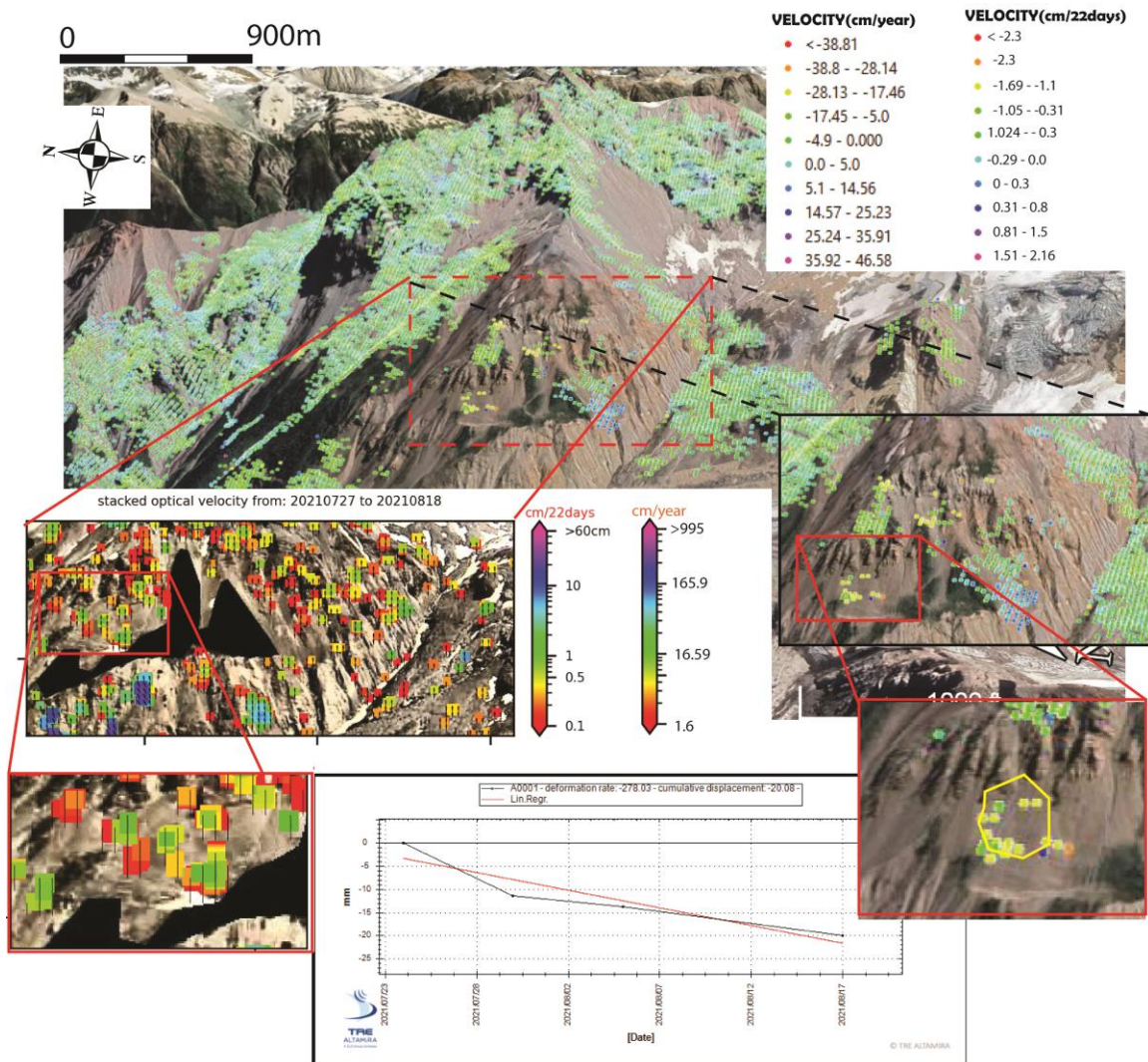
Figure 2.9. Comparison between Plinth Peak slope displacement from InSAR and average displacement rate calculated from stacked optical velocity triplets for the period from July 27 to 18 August 2021. (A) Sliced-time window of SqueeSAR results between July 24 and 17 August 2021; red dashed rectangle is zoom in location for panels (B, D, F). (B, C) are close ins of stacked optical flow velocity calculated from orthorectified optical satellite images. (D, E) are close ins of stacked optical flow velocity calculated from ground-based optical images. (F, G) are close ins of processed time-series radar images using SqueeSAR. (H) InSAR displacement timeseries for the yellow polygon in (G) See Figure 1 to locate the extent of Figure 9. The colour bar for panels (D, E) represented as logarithmic scale.

The mechanism of the rockfalls and the rockslide can be further quantified based on the morphology of the Plinth Peak slope. The slope is composed of a large talus cone (Rapp and Fairbridge, 1997) formed due to the accumulation of rock-debris at its base (Fig. 2.11). The bedrock of the slope is composed of rhyodacite lavas which may have facilitated relatively uniform weathering across the west part of the Plinth Peak resulting in a single talus slope rather than a series of cones. According to (Rapp and Fairbridge, 1997), rates of creep movement in active talus cones can be ~ 10 cm/year on the upper part of the cone decreasing to zero towards the base. These rates are similar to the SqueeSAR displacement rates for Plinth Peak of 7.3 cm/year (Fig. 2.2).

Figure 2.10. **(A) Number of observed rockfalls during four daily time periods (11 a.m., 12 p.m., 1 p.m., and 2 p.m.) between July 27 and 18 August 2021. (B) Total number of rockfalls during these time periods. (C) Hourly rainfall data between July 27 and 18 August 2021. (D) Hourly temperature data between July 27 and 18 August 2021.**

The rockfalls detected by Akh-Defo on the Plinth Peak slope can be categorized into two types of talus deposits, rockfall talus and talus creep (Rapp and Fairbridge, 1997). Rockfall talus related to individual block failing, such as the August 11 rockslide, are characterized by shattering, rolling, and bouncing caused by freeze-thaw, and heavy rain (Figs. 2.10C, D, 2.11, 2.12). One week before the August 11, 2021, rockslide, the camera weather station recorded a sharp drop in temperature as well as heavy rainfall (Fig. 2.10).

Although, at this time there is no published information regarding the structural and kinematic behavior of the Plinth Peak slope, we performed a preliminary assessment in order to map linear features from the LiDAR-based hillshade map. The Plinth Peak slope encompasses at least three sets of lineaments, striking NW-SE, ESE-WNW, and NNE-SSW. Our results show that most of the rockfalls and slope deformation occur within and along the trends of mapped lineaments (Fig. 2.13) with rockfalls particularly concentrated along the NNE-SSW striking lineaments.
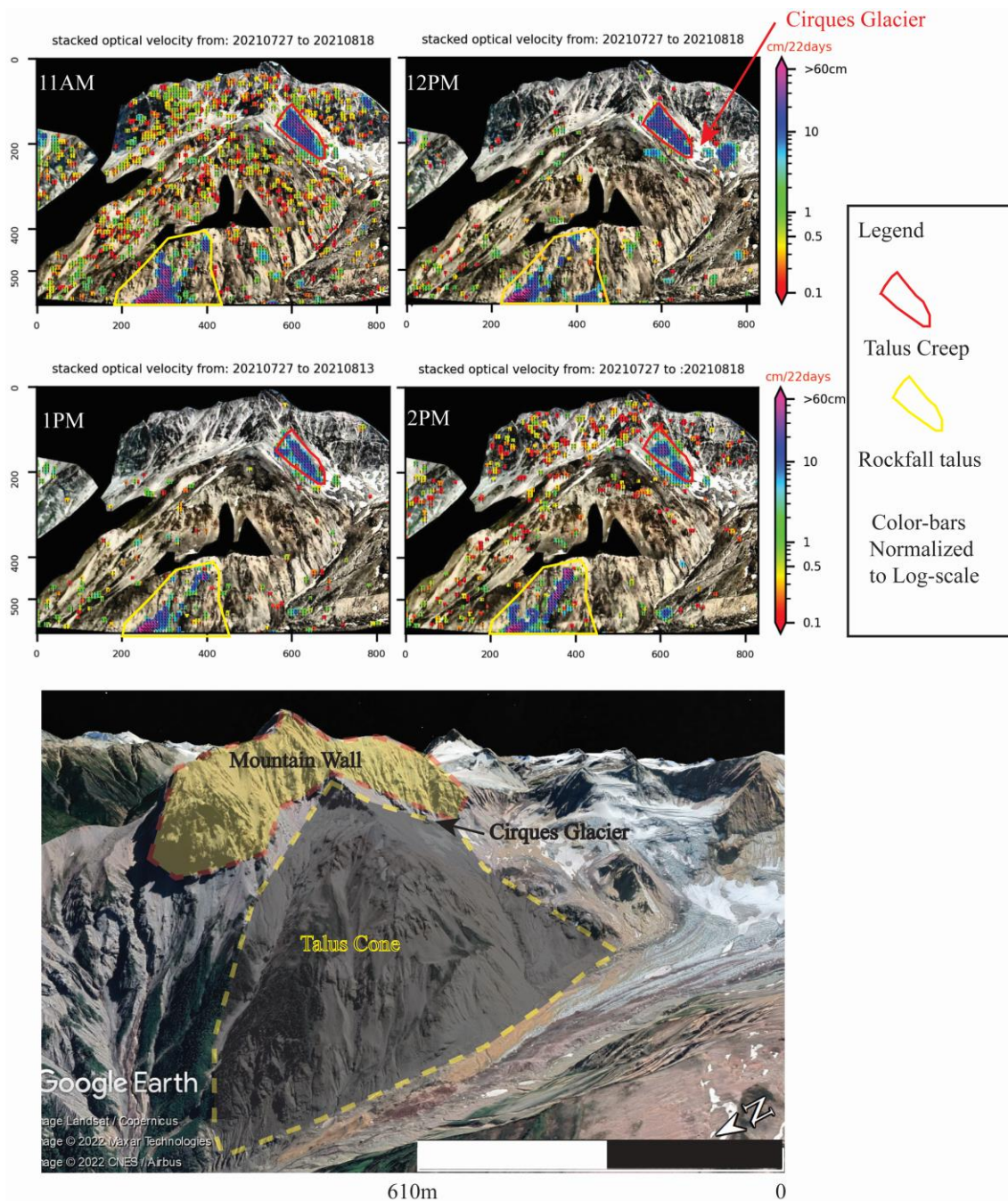
Figure 2.11. Average displacement rate and average magnitude velocity of rockfalls were calculated from a stack of processed image triplets for four different times of the day for the Plinth Peak slope. Note that the rockfall region areas show average magnitude velocity of rockfalls ranging between 20 and 60 cm.
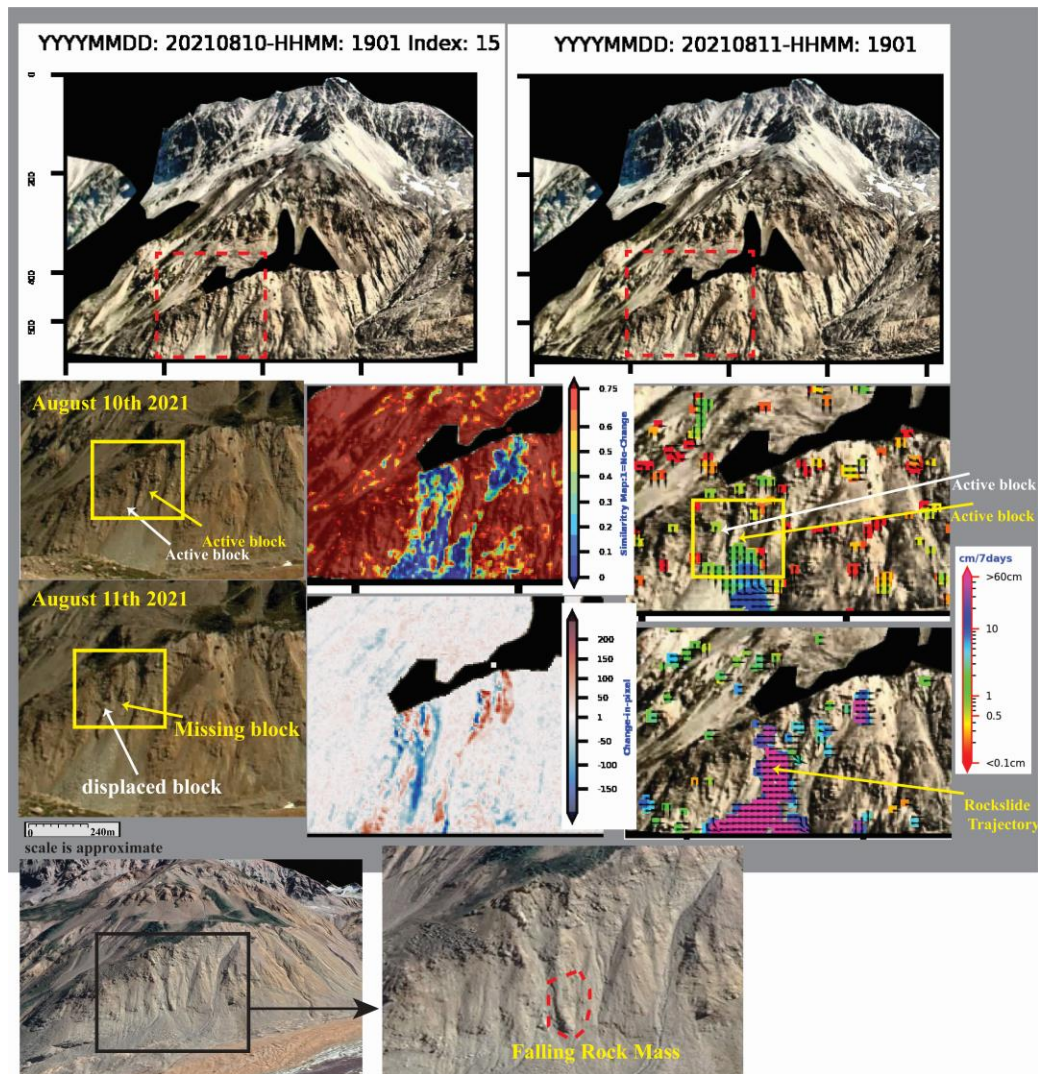
Figure 2.12. **Small landslide identification with Akh-Defo using combined static and dynamic change detection methods for the Plinth Peak slope. (A) Image taken on 10 August 2021, at 11 a.m. (B) Image taken on 11 August 2021, at 11 a.m. (C) Zoomed window of panel (A) focused on the unstable region before the rockslide failure occurred on 10 August 2021. (D) Zoomed window of panel (B) focused on the unstable region after the rockslide failure occurred on 11 August 2021. (E) Results of the structural similarity index map. Note the rockslide and change identification obtained from structural similarity map compared to image differencing. (F) Results of image differencing showing areas of change and rockslide events. (G) Displacement rate for the Plinth Peak slope calculated from triplets of images 7 days before the 11 August 2021, rockslide event. (H) Reconstructed trajectory path of the rockslide. The colour bar for panels (G, H) is log scale. (I) High resolution Google Earth imagery showing the least stable part of Plinth Peak slope. (J) Zoomed window of panel (I) show approximate size and location of the failing rock mass on 11 August 2021.**
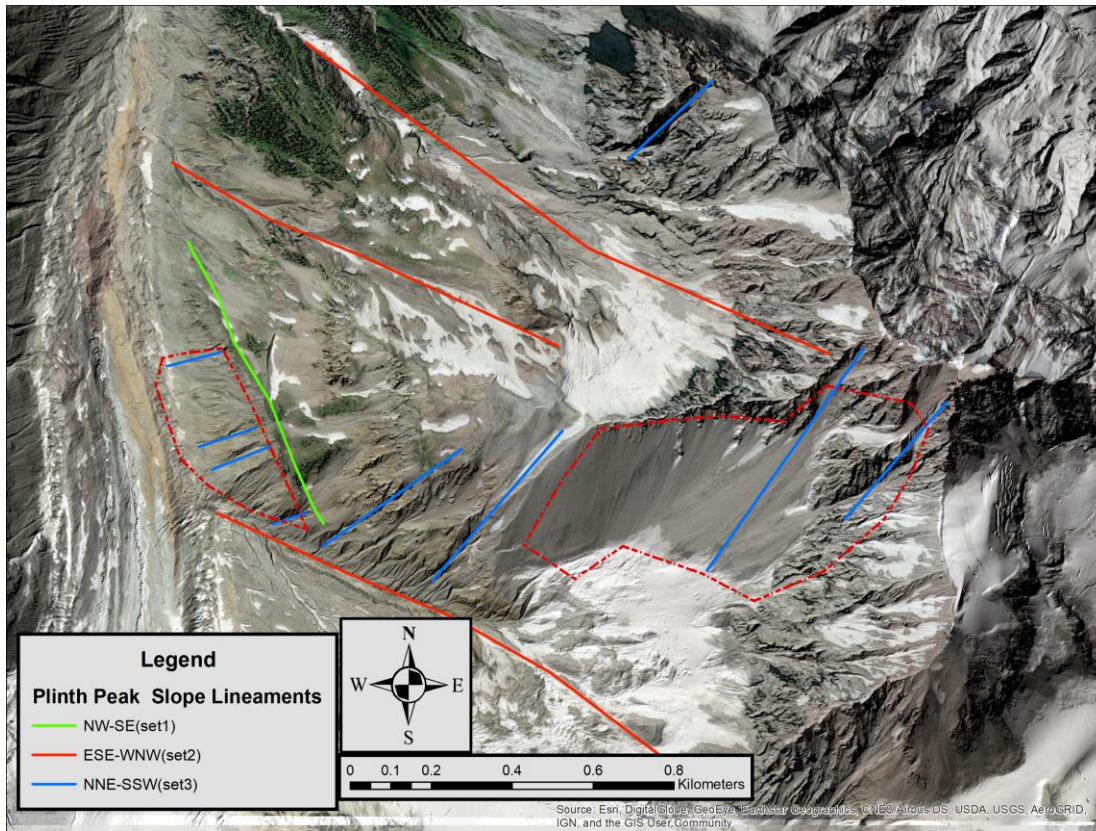
Figure 2.13. High resolution ESRI satellite image overlayed on top of the LiDAR-based hillshade map; shown are three sets of lineaments that most likely structurally control the Plinth Peak slope deformation. The dashed red polygon represents areas of frequent rockfall.

2.7.2. Mud Creek Landslide, California

Akh-Defo processing of orthorectified PlanetScope satellite imagery identified displacement between 50 to 300 cm (Figs. 2.6 and 2.7), 41 days prior to the May 20, 2017, Mud Creek landslide. The timestamp-sequential displacement (Fig. 2.7) and average displacement (Fig. 2.6) show two main unstable zones. The upper zone (referred to as the depletion zone by (Warrick et al., 2019) showed a maximum of 100 cm displacement on April 10, 2017, 40 days before the catastrophic landslide failure. In comparison, the lower zone (referred to as the accumulation zone by Warrick et al., 2019) showed displacement rates of as little as 60 to 80 cm for the same time period 40 days before the failure (Fig. 2.6).

This failure event was followed by accelerating displacement in the lower zone from 80 cm to more than 300 cm at 35 days and 6 days, respectively, before the catastrophic failure (Fig. 2.7). Four days before the event, both the upper and lower zones became extremely unstable and showed displacement of more than 300 cm. The above pattern of accelerating displacement in the lower zone at days 35 to 6, preceding the upper zone, might have facilitated the occurrence of the catastrophic failure. This would kinematically validate the loss of slope piedmont support for material from the upper slope zone. Warrick et al., (2019) show that although the lateral flank of the failure moved significantly during the failure, it did not fail completely (Fig. 2.6G, H). We were able to measure average displacement 80 cm for the lateral flank 41 days before the catastrophic failure (Fig. 2.6E, F; Table 2.2) which increased to a few meters between May 1 and 16, 2017, just 4 days before the catastrophic failure (Fig. 2.7). Although there is limited data and information available regarding the cause of the Mud Creek 2017 landslide, according to Handwerger et al. (2019), the region underwent a 5-year drought before 2017 and the failure occurred following a period of persistent rainfall lasting several days. Simple 1D hydrological modelling suggests that significant increases in pore-fluid pressure led to rapid destabilization of the slope resulting in the catastrophic Mud Creek landslide.

Table 2.2. **Average displacement from two independent datasets prior to the May 20, 2017, Mud Creek landslide.**

Case study	Dataset Type	Method	Location	Geometry/Source	Time	Average Displacement
Mud Creek	LiDAR and Photogrammetry Digital Elevation Models	Hillshade map comparison	Fig. 2.6I	Topography Change/elevation difference from DEM	2010 to 2016	600 cm
	Satellite Optical Image	Akh-Defo (this study)	Figs. 2.6E, F	Oblique to Nadir view	April 5 to May 16, 2017	92 cm

2.8. Discussion

Aside from data preprocessing, the main task of Akh-Defo is to perform static and dynamic change detection. Dynamic change detection is a powerful method for slope deformation monitoring as it provides pre-failure warning signals - for example, 7 days before the August 11, 2021, rockslide on Plinth Peak, the software measured >2 cm of slope movement at the rockslide source area (Fig. 2.12G and H); additionally, 41 days before the May 20, 2017, Mud Creek landslide, the Akh-Defo software measured more than 50 cm of slope movement (Figs. 2.6 and 2.7).

Static change detection consists of image difference maps through subtraction of subsequent images and similarity maps through measuring image similarities based on the combination of three independent elements: (i) brightness values, (ii) contrast values, and (iii) structure of the visual image scene. Unlike similarity maps, image differencing solely relies on pixel intensity change between subsequent images; hence, it is sensitive to light conditions and produces relatively more noise (Fig. 2.4). For instance, changes in solar elevation angle produce different Sun illumination patterns and different shade patterns on ground surfaces at different hours of the day. We minimized light condition variability related to daily change of Sun elevation angle and Sun azimuth at different hours of the day by processing images acquired at the same time of the day (Fig. 2.14).

The Dynamic Change-Detection approach can detect slow (sub-cm) and fast (more than a few metres) slope movement. The user needs to apply other complementary techniques to differentiate the source of calculated displacement such as rockfall, rockslide or slow slope deformation. In this study we used a number of methods to distinguish and interpret the source of slow and fast displacement rates including SqueeSAR, Static Change-Detection and visual observation of the time-lapse images. SqueeSAR (InSAR) is a valuable independent method to validate slow slope displacement (see Table 2.1 and Fig. 2.9). Static change detection and visual observation of the image time-lapse both are important to quantify fast slope movement such as rockfalls and rockslides (see Figs. 2.10 and 2.12).

Through installation of a low-cost fixed camera and telemetry system, we were able to collect more frequent images (daily to hourly) of the Plinth Peak slope compared to

exclusively relying on InSAR (Fig. 2.9 G, E). Statistical comparison between SqueeSAR results and Akh-Defo shows less than 20 % difference in displacement rate from Akh-Defo relative to InSAR (Table 2.1). SqueeSAR processes radar images and relies on the change of distance between the SAR satellite and the target on the ground. SqueeSAR can processes data collected at all times and under various weather conditions such as cloud, fog, and rain. However, SqueeSAR cannot calculate sufficient measurement points in very steep slopes or if the target is invisible to the LOS.
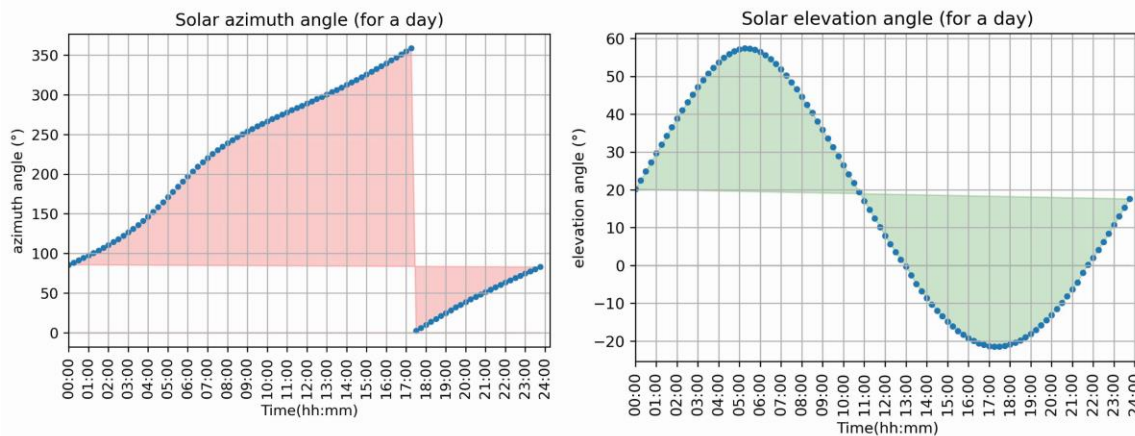
Figure 2.14. **Solar elevation and azimuth change for the Mount Meager area during August 2021. Note the change of solar elevation angle relative to change of solar azimuth angle during the day. Data from (https://keisan.casio.com/exec/system/1224682277).**

Alternatively, Akh-Defo processes optical images and relies on the change of the intensity pattern within the optical image but is restricted to only data collected during the daytime and under clear weather conditions. In this study, the Akh-Defo software was applied to the Planet Labs pre-processed orthorectified optical images to measure the Plinth Peak slope as well as the pre–Mud Creek landslide movements. The calculated land movement from orthorectified satellite optical images are more accurate and easier to project to the real-world trajectories relative to the ground-based optical images, mainly due to the geometric characteristics of the satellite images relative to the ground images. For instance, in the case of orthorectified satellite images, the pre-processed optical images have already been corrected (using digital elevation models) for external image distortion caused by the difference in depth of objects within the image scene (i.e., any distortions caused by topography have been corrected).

Akh-Defo uses optical flow algorithms to calculate slope movement. The measurement accuracy depends on the data-collection system such as resolution of the raw image, weather conditions during capturing the image, stability of the camera system (in case of ground-based images) and even time of the day the subsequent images were taken. In our methodology, we were careful to select images for processing to obtain acceptable results for validation with other independent systems such as SqueeSAR (Plinth Peak case study) and LiDAR DEM change detection (Mud Creek case study). For instance, we only processed images taken during clear weather conditions (no fog, snow, or rain), we performed image alignment to compensate for the stability of the ground camera system (see supplementary material for image alignment process) and we only processed images taken at fixed hour of subsequent days. In addition to careful selection of images and image pre-processing steps such as image alignment and image enhancement, we also integrated similarity thresholds (comparable to InSAR coherence thresholds). The advantage of using this parameter is that it enables calculation of displacement velocity only for pixels with known stable texture and light condition (Fig. 2.15B, D). Current limitations of the Akh-Defo software include the inability to accurately identify the displacement vector field for the calculated displacement from the ground-based images processed for the Plinth Peak slope. This limitation is inherent to all computer vision optical flow codes and its known as the Aperture problem (Xue et al., 2015). The significance of the aperture problem depends on the size of the object of interest; for instance, if the object of interest is larger than what can be seen through the camera scene view (such as the Plinth Peak slope), we can only estimate an approximate vector field for objects within the slope. In other words, while we cannot identify the movement of the entire slope relative to Mount Meager itself, we can calculate the displacement rate and vector of smaller landslides and rockfalls withing the field of view of our installed camera.
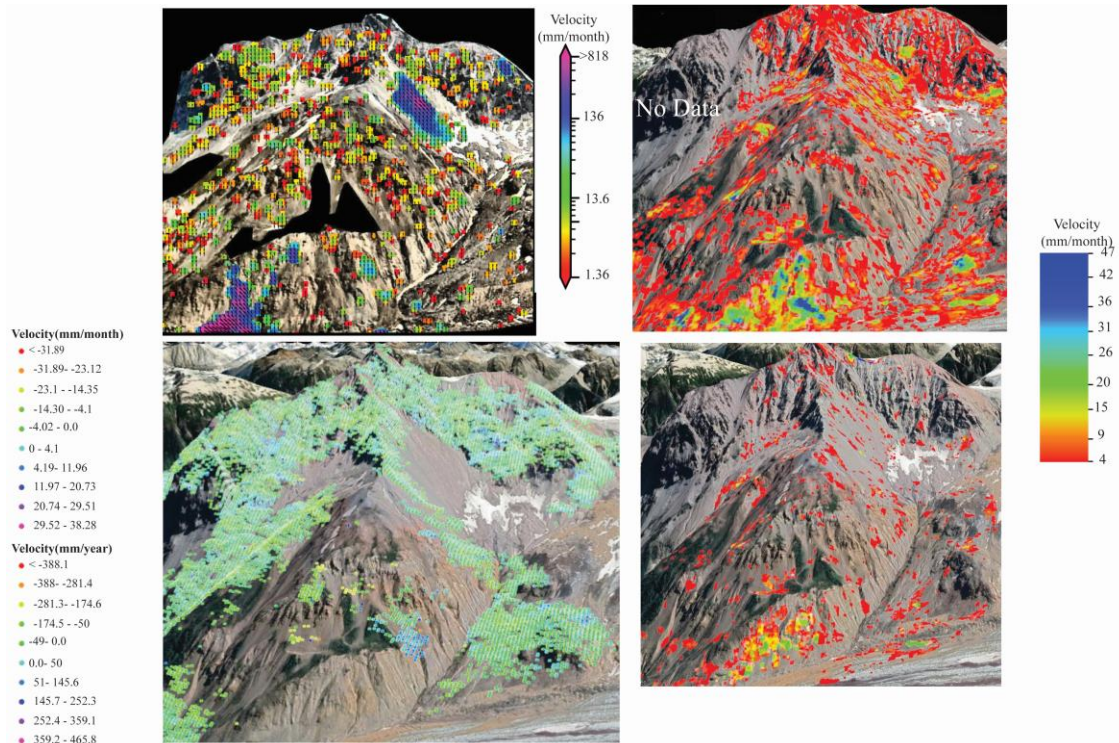
Figure 2.15. Deformation rates in millimeter per month for Plinth Peak slope. (A) Deformation rate calculated from ground-based optical images from July 27 to 18 August 2021; note, the colour-bar is shown as a logarithmic scale, deforepresenttes larger than 20 mm represents traces of slow but continuous rockfalls within the processed time window period. (B) Deformation rate calculated from orthorectified optical satellite images from July 28 to 13 August 2021, deformation map processed with similarity threshold equal to 0.75. (C) Deformation rate calculated from radar images for summer 2019, 2020, and 2021 using TRE-ALTAMIRA SqueeSAR Software. SqueeSAR by default calculate annual deformation rate, we rescaled to a monthly deformation rate. (D) Deformation rate calculated from orthorectified optical satellite images from July 28 to 13 August 2021, deformation map processed with similarity threshold equal to 0.2.

Another limitation is that the optical flow algorithm can only measure horizontal displacement in a 2-dimensional image space such as (left, right, top, and bottom). This becomes more challenging in the case of ground-based optical image processing to translate the calculated displacement magnitude vector into a real-world vector motion. In contrast, for optical satellite images the solution becomes relatively more practical by processing orthorectified optical images (Fig. 2.3); we can then reproject the calculated

velocity magnitude and vector back to the real-world projection using available digital elevation models (Fig. 2.5 C and D).

Our results show that ground-based optical images are more suitable to monitor rockfalls compared to orthorectified satellite optical images. This is mainly related to the different angles of view as the orthorectified satellite images are acquired at nearly nadir while ground-based optical images have a nearly horizontal view (Fig. 2.15).

2.9. Conclusions

In this study, we developed software to process ground-based optical images and orthorectified Planet Lab satellite optical images. The ground-based optical images were used to test the capability of the developed software to complement InSAR LOS limitations for the steep slopes of Plinth Peak. Our ground-based camera analysis, using stacks of optical images from July 27 to August 18, 2021, gives comparable and complementary results (less than 20 % difference; see Table 2.1) for the same time-period with SqueeSAR. In addition to defining deformation rates, we were able to characterize velocity of rockfall trajectories spatially within the slope itself. Additionally, we used two techniques, Image Differencing and Structural Similarity Index (SSIM), to identify areas of significant slope change such as landslide areas. Results from ground-based camera monitoring detected movements of the slope and defined areas of highest rockfall on the western flank of Plinth Peak. Our results show that ground-based optical images are more suitable to monitor rockfalls compared to orthorectified satellite optical images.

We also tested the Akh-Defo program to calculate the pre-failure movement 41 days before the catastrophic May 20, 2017, Mud Creek Landslide from the orthorectified Planet Lab satellite imagery and validated our results with those from (Warrick et al., 2019). We calculated timestamp (Fig. 2.7) and average (Fig. 2.6 C to G) displacement for the period 40 days before the catastrophic landslide occurred.

In this paper, the following conclusions are presented to enhance cost-effective and near real-time early warning landslide and rockfall monitoring:

1) Radar satellite datasets are a highly effective source to identify unstable areas as a baseline knowledge if followed by less-expensive but continuous ground-based and optical satellite monitoring.

2) Computer vision codes such as optical-flow velocity are highly effective for calculating land deformation semi-quantitively if used with a proper methodological workflow which includes choosing the appropriate type of image dataset and reasonable image pre-processing preparation.

3) Structural similarity maps appear to be more effective in identifying rockfall events and areas of change compared to classic image differencing.

4) The pre-failure Mud Creek displacement results calculated by Akh-Defo software indicate that Akh-Defo program (based on optical flow velocity code) can be used as a first stage preliminary warning system (particularly if run on the Cloud) prior to processing more expensive but more accurate InSAR products such as SqueeSAR.

2.10. Data Availability Statement

The datasets presented in this study can be found on the below Online GitHub Repository https://github.com/mahmudsfu/AkhDefo. This repository includes the following materials: A copy of the developed Akh-Defo Python-based software for Ground-based Image processing. A copy of the modified Akh-Defo program to process Planet Labs orthorectified images Ground-based Plinth Peak image dataset evaluated with the Akh-Defo software Mud-Creek Planet Lab orthorectified satellite images evaluated with the modified Akh-Defo software. Plinth Peak Planet Lab orthorectified satellite images evaluated with the modified Akh-Defo software. A step-by-step instruction manual on how to run Akh-Defo software on Jupyter notebook program.

2.11. Acknowledgements

We wish to thank two reviewers for providing constructive reviews that enhanced the quality of the manuscript. Many thanks to Nupoint Systems Inc. for donating the ground-based camera and weather system and to Weir-Jones Engineering for its installation and repeated maintenance. Thanks also to Energex Renewable Energy and the Meager

Creak Development Corporation for technical and logistical support. The Planet Lab company provided access to the satellite imagery via an educational license to SFU. This work was supported by the Canadian Space Agency (CSA), and Mitacs Accelerate and NSERC Discovery grants to GW-J.

Chapter 3. Structural Geology of the Mount Meager Volcanic Complex, BC, Canada: Implications for geothermal energy and geohazards

Mahmud Muhammad[1], Glyn Williams-Jones[1], and René W. Barendregt [2]

[1]Centre for Natural Hazards Research, Department of Earth Sciences, Simon Fraser University, Burnaby, BC, Canada.

[2]Department of Geography and Environment, University of Lethbridge, Lethbridge, AB, Canada.

Published as: Muhammad, M., Williams-Jones, G., Barendregt, R.W. (2024) Structural Geology of the Mount Meager Volcanic Complex, BC, Canada: Implications for geothermal energy and geohazards. Canadian Journal of Earth Science, 61, 158-186, doi: 10.1139/cjes-2023-0077

3.1. Abstract

The Mount Meager Volcanic Complex (Qẃelqẃelústen or Mt. Meager) coincides tectonically with the intra-arc to back-arc transition zone and exhibits the loci of strain partitioning in response to a rapid change in orientation of the Pemberton and Garibaldi Arc segments which are coeval with a shift in Pacific plate motion after 5 Ma. This strain partition is manifested through development of a transpressional deformation from 5 Ma to 1.9 Ma at the latitude of Mt. Meager. Mt. Meager is an active volcanic system with at least two explosive eruptions in the last 25,000 years, the most recent occurring around 2360 BP. Additionally, it is the site of the largest landslide in Canadian history, which occurred during the summer of 2010, originating from the southeastern side the massif. During early exploration at Mt. Meager, geothermal boreholes drilled to 3 km reached 270°C but did not find sufficient permeability to sustain self-flowing conditions. To understand the geological challenges in Mt. Meager's geothermal exploration, we analyzed outcrop-scale faults and folds, incorporating structural mapping, volcanic rock paleomagnetism, and radiometric dating to establish kinematic history and kinematic

compatibility of structural geology features including faults and folds. Our findings suggest that stress partitioning during the last 5 Ma resulted in formation of a transpressional structure exhibited as an elongate and rhomboidal structure at Mt. Meager with anomalously high topographic elevations which led to ENE-WSW crustal shortening and exhumation of crystalline basement. This new structural geology model improves our understanding of geothermal reservoirs and potentially significant geohazards.

Keywords:

Mt. Meager, Qw̓elqw̓elústen, geothermal energy, transpressional restraining bend strike-slip deformation, Garibaldi Volcanic Belt, geohazards, volcano.

3.2. Introduction

Qẃelqẃelústen, also known as the Mount Meager Volcanic Complex (MMVC, Mt. Meager), is located at the northern end of the Garibaldi Volcanic Belt (GVB) and has been identified as a promising area for geothermal resources since the 1970s (Fig. 3.1). Numerous geothermal exploration campaigns have been conducted in the area involving geophysical surveys, geochemical studies, and bedrock mapping (Fairbank et al., 1980, 1981; Ghomshei et al., 1986, 1992, 2004, 2009; Arianpoo et al., 2009; Harris et al., 2020, 2022; Grasby et al., 2021; Muhammad et al., 2021; Hormozzade Ghalati et al., 2022).

This study aims to enhance the existing ground-based geologic mapping through a comprehensive field-based structural geology examination of Mt. Meager. Subsequently, these datasets are integrated and synthesized to gain a deeper understanding of crucial geological parameters, such as the tectonic style and framework of Mt. Meager, its deformation history, and implications for mitigation of natural hazards and for geothermal exploration.

Geothermal energy is becoming more widely recognized in Canada as a viable source of low-carbon base-load energy with minimal environmental impact. However, it faces challenges such as high development costs and uncertainties related to identifying suitable subsurface reservoirs with sufficient heat storage capacity and extensive fluid pathways. Failed boreholes can negatively impact economic plans. To mitigate these uncertainties, reservoir capacity, permeability zones, fracture and fault patterns must be evaluated to reduce exploration risk. Several studies highlight the crucial role of structural geology in maximizing the success of geothermal projects, particularly in reservoirs that require permeability enhancement, such as Enhanced Geothermal Reservoir Projects (Philipp et al., 2007; Moeck, 2014; Filipovich et al., 2020; Liotta et al., 2021).

Philipp et al. (2007) conducted a study on the influence of structural geology, specifically the role of constraining the stress field, in simulating an enhanced geothermal system in Buntsandstein, northern Germany. They observed that the stress field has a significant impact on fault slip and fluid transport. The orientation of the maximum horizontal compressive stress in relation to the fractures determines whether fractures propagate

or close. When the maximum horizontal compressive stress aligns with the strike of the fractures, fractures tend to open, resulting in enhanced fluid transport. Conversely, if the maximum horizontal compressive stress is perpendicular to the strike of the fractures, fractures may close, reducing fluid transport.

Figure 3.1. **Location and simplified geology map of the Mount Meager Volcanic Complex (MMVC). Refer to the detailed description of bedrock units in Plate 1 at Appendix B1. limits of resistivity anomaly taken from (NSBG, 1975, 1982). The inset map modified from Morison and Hickson (2023); trends of Garibaldi Volcanic Belt (GVB) and Pemberton Volcanic Belt (PVB) obtained from Green et al. (1988). Map projection: WGS_1984_UTM_Zone_10N.**

Hence, understanding the major geologic structures and the timing of tectonic activity that shaped the subsurface geothermal reservoir is crucial, as it not only helps assess reservoir quality but also defines the pathways for geothermal fluids.

Since the late 1970s, extensive investigations have been conducted in the South Meager area to assess its geothermal resource potential (Ghomshei et al., 1986, 1992, 2004, 2009). Various exploration techniques, such as geology, geochemistry, geophysics, and drilling of different types of wells, including temperature gradient wells, deep slim wells, and full-diameter wells, have been utilized. In 2001 and 2002, a magneto-telluric survey was conducted, followed by the drilling of three slim holes, which yielded compelling evidence indicating the existence of a sizable geothermal reservoir with high temperatures at relatively shallow depths (GeothermEx, 2009).

Mt. Meager is also an active volcanic system which has erupted explosively at least twice in the past 25,000 years with the most recent event in 2360 BP (calibrated years BP; Russell et al., 2021). Pyroclastic density currents from these eruptions were sourced at high elevation near the present-day Plinth Peak and since 2016, low level fumarolic degassing has been observed through glaciovolcanic caves on the west flank of Plinth Peak (Unnsteinsson et al., 2024; Muhammad et al., 2022; Warwick et al., 2022) . Furthermore, the most recent and largest historic landslide in Canada occurred during the summer 2010 from the southern flank of Mt. Meager (Guthrie et al., 2012; Hetherington, 2014; Roberti et al., 2017, 2018; Roberti, 2018). The geology of Mt. Meager consists of both the basement complex and young volcanic rocks (Fig. 3.1). The basement complex is composed of high-grade metamorphic rocks of unknown age, as well as late Triassic Cadwallader group, late Jurassic to late Cretaceous intrusive rocks, late Cretaceous sedimentary rocks of the Gambier group, and Paleogene to Miocene intrusives. The young volcanic rocks were emplaced during three distinct stages, as identified by Read (1990): 1) Pliocene to Pleistocene rhyodacite (1.9-1 million years ago); 2) early Pleistocene to late Pleistocene dacite to basaltic-andesite (1-0.3 million years ago); and 3) Late Pleistocene to Recent rhyodacite to dacite (0.3-0 million years ago). Over the past 1.9 million years, volcanic eruptive centres on the Mt. Meager massif show a trend progressively younging from south to north (Figs. 3.1 and Plate 1 in Appendix B1).

A relatively young east-west trending fault was identified along Meager Creek (Figs. 3.1 and 3.2C) and is well-constrained through various methods including bedrock exposure mapping, fracture data, drill core samples, and refraction seismic data (Fairbank et al. 1980, 1981; Harris et al. 2020). Although the Meager Creek fault zone is classified as an extensional fault based on mapping (Figs. 3.2, 3.3), the presence of mylonite in drill holes indicates a possible compressional component and suggests that the fault zone may have experienced multiple episodes of deformation. From the 1970s until 2021, geothermal exploration studies at Mt. Meager categorized the timing of faulting into three broad categories. These include faults associated with 1) tectonic stress during the initial stages of mountain building, 2) faults linked to volcanic activity, and 3) faults associated with surficial mass creep and gravitational failure (Fairbank et al., 1980, 1981; Harris et al., 2020).

To summarize, geothermal energy exploration in Mt. Meager faces two geological challenges including identifying permeable zones for fluid circulation (Fig. 3.3) and mitigating geohazard risks such as the 2010 landslide and hazards related to volcanic eruptions. In this study we conducted structural geology field mapping, paleomagnetic measurements and radiometric dating of volcanic rocks to define the kinematic history and kinematic compatibility of outcrop scale structural geology features such as faults and folds (Fig. 3.2). The kinematic history can help with understanding the history of motion and onset timing of subsequent deformation stages. In contrast, kinematic compatibility can aid in understanding the geometrical and geospatial relationships between subsequent deformation stages. Consequently, a well-understood structural geology setting can help characterize the fracture pattern and define the depth to a productive geothermal reservoir with sufficient capacity to allow fluid circulation. Additionally, a better understanding of fracture patterns can help define more promising areas for the development of reservoir permeability at depth and may also allow assumptions on depth of the productive reservoir, although this is also influenced by other elements such as stratigraphy and hydrothermal alteration.
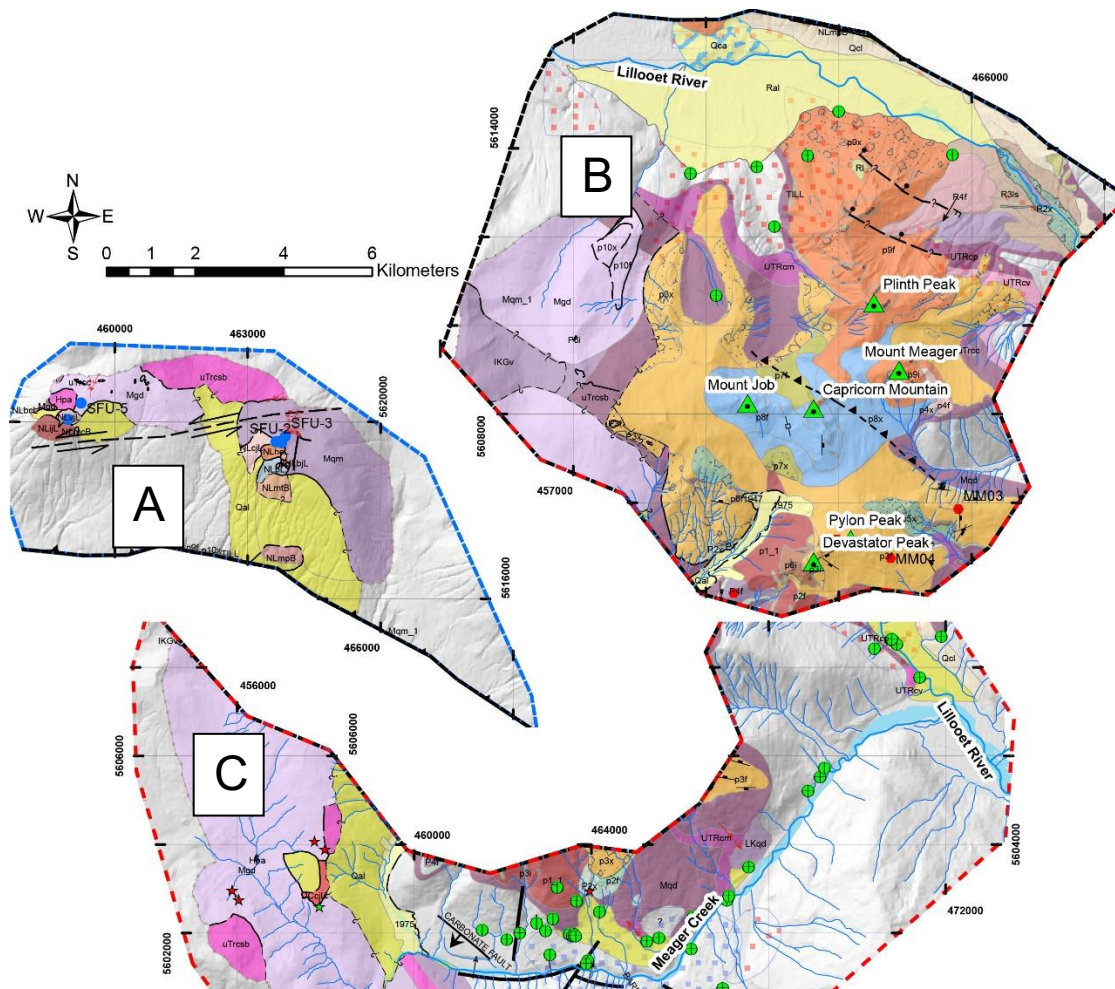
Figure 3.2.   Simplified geology map with distinctive structural Domains based on the complexity and location of the structures. A) Lillooet Ridge Domain. B) Meager Massif Domain. C) Meager Creek Domain. See Figure 1 for location of each domain relative to the MMVC and Plate 1 for detailed geologic and structural symbol descriptions. Map projection: WGS_1984_UTM_Zone_10N.

Figure 3.3. Structural geology map showing fault distribution within MMVC. The Inset map shows the location and well traces of drilled wells (taken from GeothermEx, Inc., 2009). See Figure 3.1 and Plate 1 in Appendix B1 for detailed description of structural geology symbols. Map projection: WGS_1984_UTM_Zone_10N.
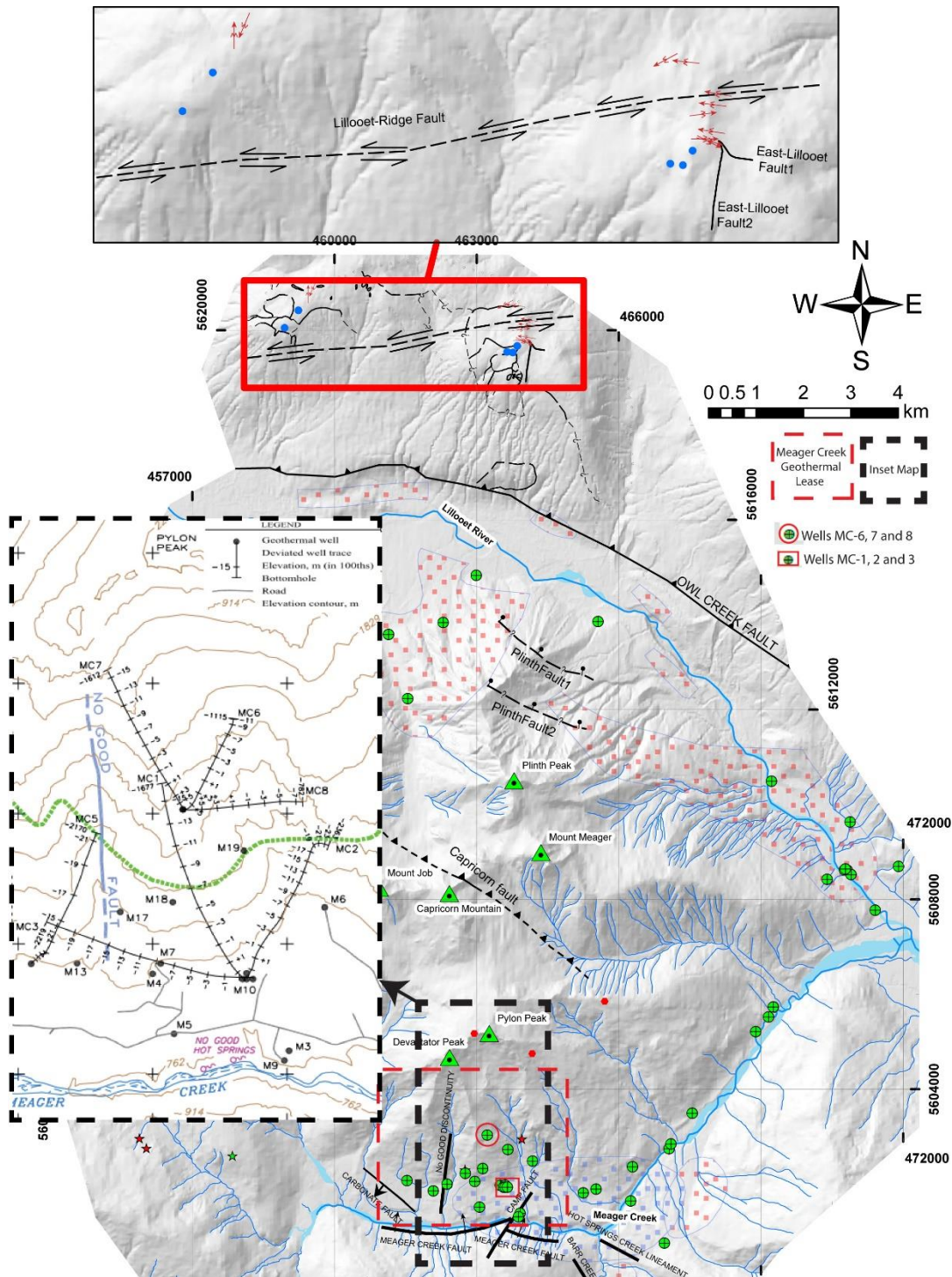
3.3. Materials and Methods

3.3.1. Structural Geology Mapping

Extensive geological field work was carried out during three separate campaigns (summers 2019, 2020, and 2022) (Fig. 3.1 and Appendix B1) at more than 846 locations around the massif to better understand the nature of the subsurface geology (Harris et al., 2020), better characterize the peripheral volcanic centres, and map the structural geology. Fieldwork involved ground-based traverses to locate outcrops, record lithological field descriptions, collect samples and structural measurements (e.g., foliations and fault orientations), and follow discernable unit contacts. Due to the rugged topography and thick vegetation at lower elevations, extensive helicopter support was necessary to access remote locations.

We employed various field tools such as the FieldMove Clino mapping application to record bedding, joint and fracture orientations, dike trends and dips, and fault slickensides. A Gaia GPS was used to pinpoint sites and sample locations with detailed tagged descriptions for each locality. Additionally, we collected aerial photographs to create a 3D photogrammetric model in Agisoft Metashape (Fig. 3.4), which was then imported into the CloudCompare software to facilitate structural geology measurements such as the strike and dip of fault surfaces in difficult to access locations. Classical structural geology techniques were used including plotting attitude of structures on stereonet, analyzing structural trends, and assessing spatial correlation between rock units versus structural features including fractures/veins, faults, folds, and the attitudes of basement and young volcanic units. We also considered syn- (i.e., intrusion and extrusion) and post- (i.e., faulting, mass movement, and glaciation) depositional processes.

3.3.2. Paleomagnetic and Radiometric Dating

Rock samples were gathered for paleomagnetic analysis (Appendix B2) and radiometric dating from both basement and younger volcanic rocks on the Mt. Meager massif as well as two ridges north of the massif (the east Lillooet ridge and west Lillooet ridge) (Fig. 3.1). A total of 9 sites were studied with eight cores collected at each site over an area of

5-10 m^2 to minimize potential errors caused by local movement along joints or lightning strikes. To ensure accuracy, all samples were oriented using both solar and magnetic compasses to eliminate any orientation errors caused by the presence of strongly magnetized rocks in the outcrop. Paleomagnetic samples were analyzed at the paleomagnetic laboratory at the University of Lethbridge, Alberta. Magnetic susceptibility was measured with a Sapphire Instruments (SI-2B) susceptibility meter. The magnetization of each sample was measured with an AGICO JR-6A spinner magnetometer prior to demagnetization and again after each level of stepwise demagnetization. Samples were kept in magnetic shields following field collection and between laboratory measurements. Most samples were subjected to alternating field demagnetization with one-third of the collection subjected to thermal demagnetization. Alternating field demagnetization was performed using an ASC Scientific D-2000 demagnetizer with a three-axis manual tumbler and carried out at 10 millitesla (mT) steps (up to 200 mT).

Thermal demagnetization was carried out at 100, 200, 300, 400, 500, 550, 580°C, and in a few cases at 600°C, and 650°C, using an ASC Model TD48 dual-chamber thermal demagnetizer to determine whether alternating field (AF) demagnetization was sufficient to resolve the primary remanence. AF Demagnetization was sufficient to resolve the primary remanence for most samples but for basement rocks (granodiorites), thermal demagnetization was required. Directions of characteristic remnant magnetization were determined for each sample by principal component analysis (Kirschvink, 1980) using Remasoft version 3.0 (Chadima and Hrouda, 2006). Mean characteristic remanent magnetization directions were calculated for each site and an overall mean was also calculated.

Four of the Paleomagnetic samples were also dated by [40]Ar/[39]Ar geochronology at the Oregon State University (OSU) Argon Geochronology Laboratory. Preparation, analysis, and data reduction followed the methods described in supplementary material (Appendix B3 and supplementary material).
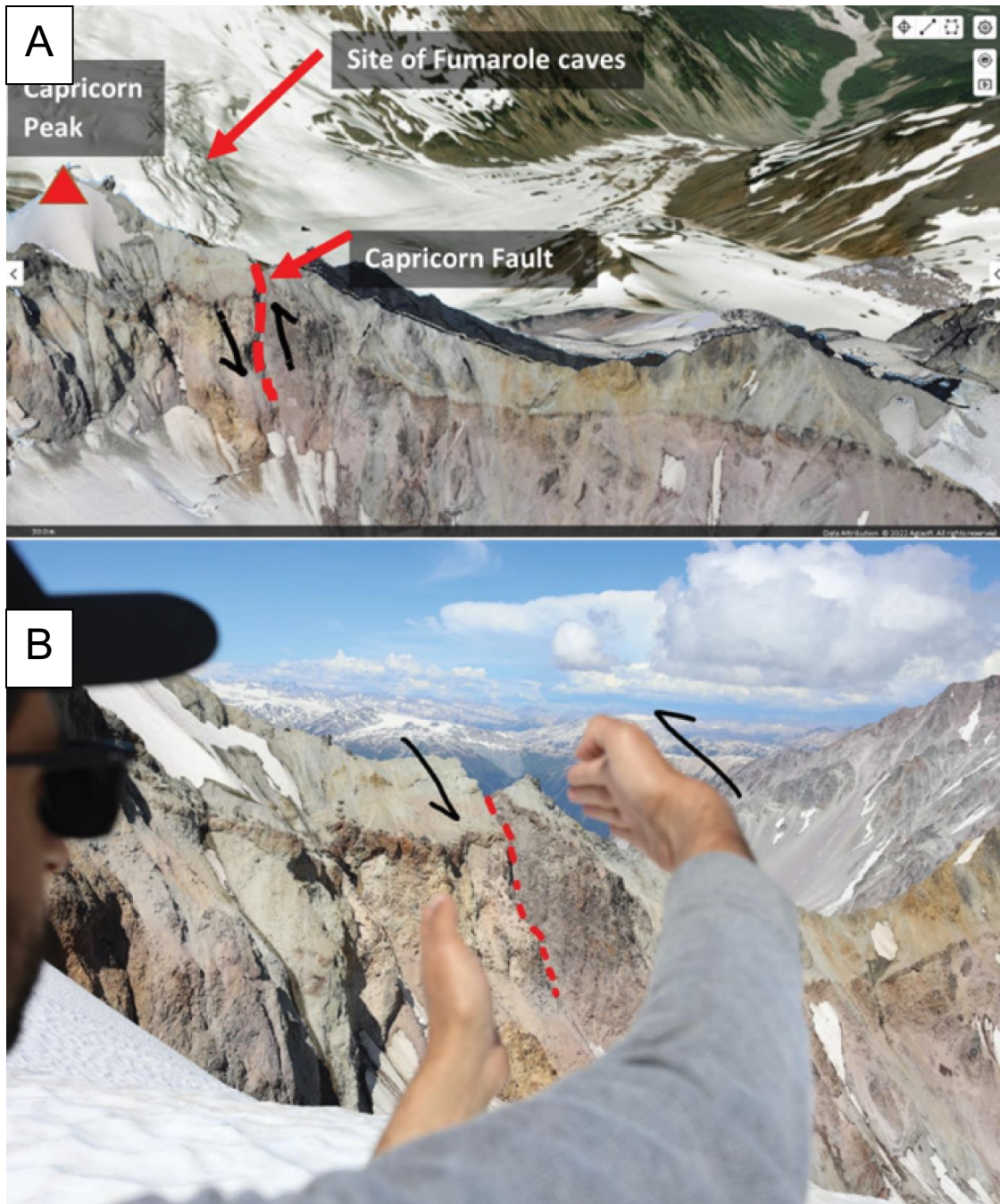
Figure 3.4. **A) 3D photogrammetry model of Capricorn fault with location of Capricorn relative to the MMVC glaciovolcanic caves. B) Field photo of the newly identified Capricorn fault. Note the cross-cutting of the fault with the Pleistocene and younger volcanic rocks in the background may indicate MMVC was tectonically active sometime after the emplacement of the volcanic deposits around 100 ka.**

3.4. Description of Main Structural Domains

For ease of description and consistency, we divide the Mt. Meager massif into three distinct domains based on spatial location and well-defined fault structures such as the Owl Creek and Meager Creek faults (Fig. 3.2). The Owl Creek fault coincides with the Lillooet River and the separate domains Lillooet Ridge and Meager Massif while the Meager Creek fault coincides with the Meager Massif and Meager Creek domains. Therefore, Owl Creek fault defines the boundary between Lillooet Ridge and Meager Massif domains, while the boundary between Meager Massif and Meager Creek domains is approximate and defined based on changes in topography.

3.4.1. Lillooet Ridge Domain

This domain is separated from the Meager Massif domain by the Owl Creek fault, a regional fault sub-parallel to the Lillooet River that extends ~95 km southeast to Lillooet Lake (Bustin et al. 2013). Within this domain, two volcanic-capped ridges, referred to as east and west Lillooet Ridge, are separated by the Lillooet Ridge fault interpreted here as a left-lateral strike slip fault (see Figs. 3.2, 3.3, and 3.5). The eastern ridge terminates at Salal Creek, while the western ridge ends at or crosses Mosaic Creek. The bedrock geology includes Triassic to Tertiary basement quartz diorite and Pleistocene volcanics consisting of dacite with an $^{40}Ar/^{39}Ar$ plateau age of 1.12 to 1.14 Ma ± 0.02 Ma, andesites with an $^{40}Ar/^{39}Ar$ plateau age of 850 to 864.8 ± 15.9 Ka, and basaltic dykes dated at 200 ka (Harris et al. ,2022).

On the eastern ridge, two faults were mapped – the first, called East-Lillooet-Fault1, is an ~ 33-m-long left-lateral strike-slip fault striking E-W with a few metres of offset. The second fault, East-Lillooet-Fault2, is cut by the first and is ~300-m-long striking NS, with signs of multiple deformation events including normal, reverse and strike-slip. Additionally, nine minor folds were mapped, mostly trending in the ENE-WSW direction except for one minor fold trending NE-SW (Fig. 3.5). Three sets of joints/fractures were mapped striking NW-SE, E-W, and NNE-SSW. The overall strike of beddings of the basement rocks are E-W and ENE-WSW (Fig. 3.5). Spatially, the East-Lillooet-Fault2 appears to cut through the young volcanic rocks. However, the fault surface predominantly crops out at the centre of the ridge and ends on the north side between

the beginning of intact young andesitic volcanic rocks and most likely displaced andesitic volcanic rocks. While the fault surface outcrops further south in an area covered with the 2360 BP eruption air-fall pumice (Fig. 3.5E, photograph 2), we found no field evidence of the fault cutting the pumice deposits.

On the western ridge, four minor faults (two fault sets) were mapped from the far west to the centre close to the eastern ridge, striking NNE-SSW (reverse), NE-SW (normal), NE-SW (reverse), and NE-SW (reverse), respectively (Fig. 3.5). Additionally, two minor folds were mapped trending N-S and NNE-SSW. Three sets of joints and veins were identified in the field striking NNW-SSE, NE-SW, and ENE-WSW (Fig. 3.5). In general, three striking trends were identified for the bedding of basement rocks on the west ridge which include NNW-SSE, NE-SW, and ENE-WSW (Fig.3.5). The ridge mostly consists of older Mesozoic granodiorite basement rocks (Fig. 3.1) except the W and SSW face of the ridge where at least three different volcanic units crop out including rhyodacite at the top of cliff, basaltic-andesitic at the slope below the cliff, and dacite on the western most part of the ridge which underlays Quaternary alluvium deposits (Figs. 3.5; photograph outcrop site 4 and Plate 1 Appendix B1). The most important lithologic feature is the presence of at least two brecciated units within the basaltic-andesitic unit. The first breccia unit, which lies topographically above the second brecciated unit, includes mixed clasts of young volcanic units and older basement rocks.
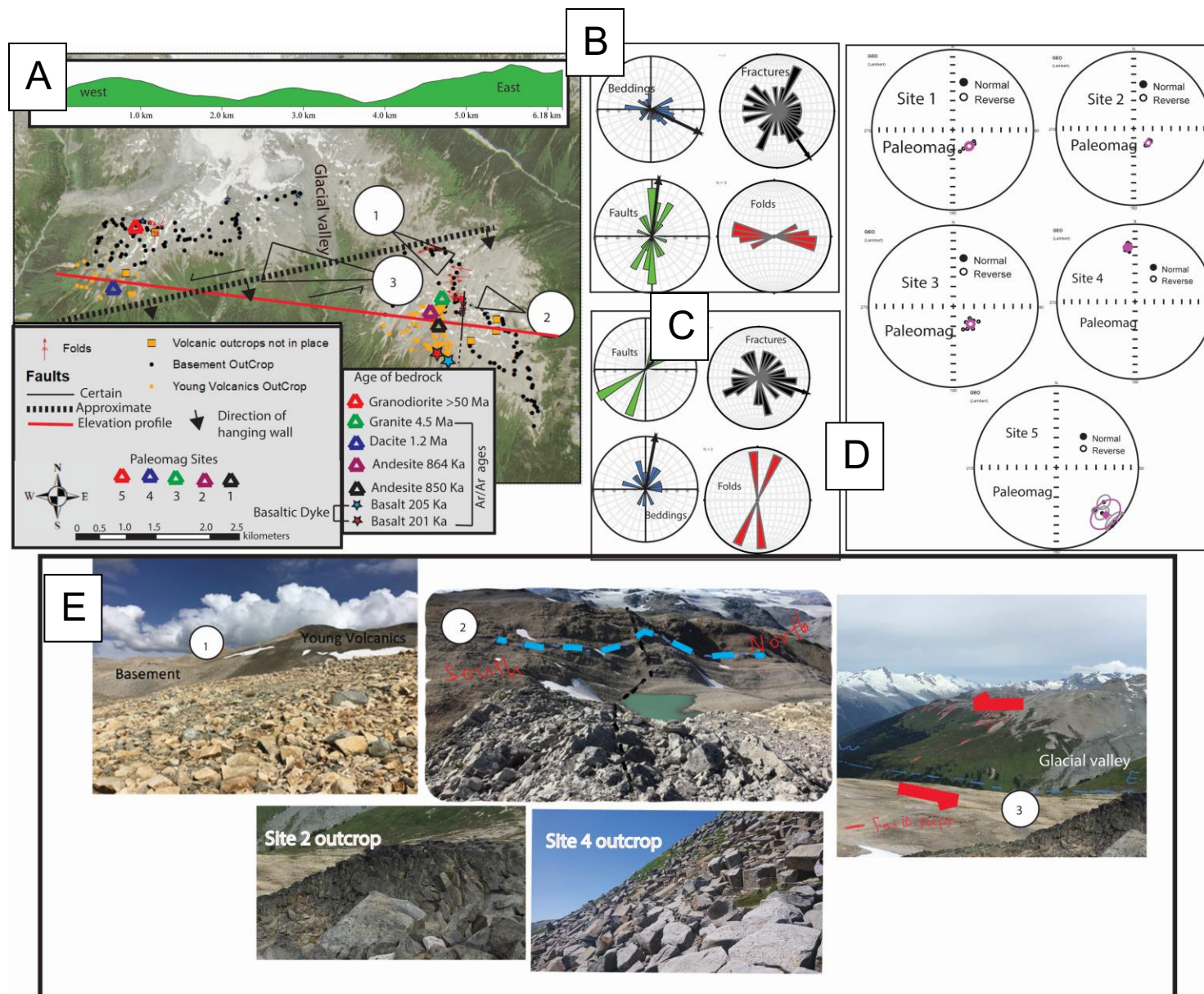
Figure 3.5. Map of important structures of Lillooet Ridge Domain. A) 3 m resolution PlanetScope satellite image draped over 1.5 m Digital Elevation Model (from historical aerial photos); orange dots represent outcrops of coherent young volcanic rocks; orange squares represent outcrops of young volcanic rocks which most likely are not in place; black dots represents sites of basement outcrops where fracture and bedding measurements were collected; red arrows represent trends of minor folds; solid lines represent certain faults; dashed lines represent concealed-approximate fault trace; Colored triangles represent sites of collected Paleomagnetic samples. Red and blue stars are sites of youngest structures dated 200 Ka based on radiometric dating (Harris et al., 2022). The red line shows elevation path profile (green section) between east and west part of the Lillooet Ridge Domain. Note, higher elevation of the eastern part and its correspondence to tilting and rotation of rocks based on paleomagnetic directions (stereo-plots) and orientation of structures (rose-diagrams). B) Rose diagrams with orientations of faults (green) fractures (black), bedding (blue) and minor folds (red) on the eastern part of Lillooet Ridge Domain. C) Rose diagrams with orientations of faults (green) fractures (black), bedding (blue) and minor folds (red) on the western part of Lillooet Ridge Domain. D) Mean paleomagnetic directions and $\alpha 95$ (P=0.05) circle of error (red dot and circle) on the eastern ridge (Sites 1 to 3) and western ridge (sites 4 and 5) of the Lillooet Ridge Domain; see panel A, coloured triangles to locate Paleomag sites on the map. E. Outcrop Field photographs: Field Photograph 1 shows sharp contact between basement and volcanic rocks, Field photograph 2 show traces of NS striking fault (blue dashed line) and EW striking fault (black dashed lines) on the east Lillooet Ridge. Field photograph 3 shows the patterns and geometry of fault steps, Site 2 and site 4 outcrop field photographs indicate columnar joints at eastern part and western ridges (ages of 860 Ka and 1.2 Ma, respectively) within Lillooet Ridge Domain.

3.4.2. Meager Massif Domain

This domain consists mainly of structures coinciding with the Mt. Meager massif. The northern side of this domain has a defined boundary and is in contact with Owl-Creek fault (Fig. 3.2). By contrast, the southern contact is gradational and approaches the southern slopes of the Pylon and Devastator peaks. The upper- and middle-part of the bedrock geology of this domain includes volcanic deposits that originated from Capricorn Assemblage (p8x and p8f) and Plinth Assemblage (p9x and 9f) (Fig. 3.1) (Woodsworth, 1977; Read ,1979, 1990). The lower part of this domain comprises volcanic deposits belonging to older Pliocene dacitic and andesitic volcanics (P2x and P4f; older than 1.8 Ma), the older rhyodacite Devastator assemblage (p1_1), porphyritic andesite flows of Pylon assemblage (p2f and p3f) and younger rhyodacite of Devastation Glacier assemblage (p7x and p7f) (Fig. 3.1 and Plate 1 Appendix B1).

Additionally, three faults were identified within this domain. The first two faults, named Plinth-Fault 1 and 2, were mapped through geological cross-section interpretation (i.e., geologic contact relationships) and are consistent with modelled 3D magnetotelluric resistivity anomalies (Hanneson and Unsworth, 2023). The third, the Capricorn fault, was determined based on visible displacement of volcanic units, field outcrop exposure, and 3D photogrammetry. Notably, this fault runs through the centre of the Mt. Meager massif and aligns with the glaciovolcanic fumaroles (Figs. 3.1 and 3.4).

3.4.3. Meager Creek Domain

The bedrock geology within this domain is relatively poorly mapped due to widespread cover from alluvial and fluvial deposits. Nevertheless, in some places, particularly on the western end of this domain, one can clearly observe outcrops of Triassic and older basement units (Figs. 3.1, 3.2, 3.3). The Meager Creek domain coincides with steep flanks on the southeast and south, and relatively gentler slope and lower elevation plateaus southwest of the Meager Massif domain. The south and southeast areas were mapped mainly using drilling data and geophysical surveys between 1970s to 2009 and four major faults were identified, including the Meager Creek fault, Camp fault, No-Good Discontinuity fault, and Carbonate fault. The Meager Creek fault is defined as a normal fault and strikes roughly east-west and dips 50 degrees north. It was mapped based on

drilling data as two concave shapes along Meager Creek, a complex juncture near drillhole M3 at 75 m depth and drillhole M9 at 80 m depth (Figs. 3.1, 3.3). Additionally, its presence is supported by an audio-magnetotelluric (AMT) survey (Hormozzade Ghalati et al., 2022) and subsurface temperature distributions which suggested the fault may act as a possible conduit for geothermal fluids (Fairbank et al.,1980, 1981). The Camp fault has been mapped as left-lateral and interpreted to be the response to differential movement of the 2 concave sections of the Meager Creek fault zone, with approximately 100 m of offset; the age of this fault is believed to be contemporaneous with or younger than Meager Creek fault zone (Fairbank et al., 1980, 1981). The No-Good Discontinuity fault strikes north-south, dips 90 degrees, and was mapped and interpreted based on resistivity surveys (Fairbank et al. 1980, 1981). Drilling data suggests an intersection of this fault with well MC-3 at a depth of approximately 3 km (Fig. 3.3). This fault bisects the volcanic complex along the approximately linear zone of volcanic vents. The Carbonate fault is located west of the No-Good Discontinuity and is oriented along a 130° strike, dipping 50 – 60° SW (Fairbank et al., 1980). The fault is interpreted to intersect drillhole M8 at 79 m to 125.7 m depth – the hanging wall is characterized by intense shearing, fault gouge and fault breccia with competent quartz diorite, whereas the footwall is characterized by incompetent amphibolite and gneiss (Fairbank et al., 1980, 1981).

The southwestern flank in the vicinity of the Meager Creek geothermal lease (Meager Creek Development Corp.) was mapped on foot during summers 2019 to 2022 (Fig. 3.3). The structural data recorded in the field includes bedding of basement units, joints, fractures, veins and fault and fold data. Relative crosscutting relations were interpreted in the field where feasible. We cannot assign timing of deformation for the rock units due to lack of age constraints of the different basement units. Instead, a relative timing of deformation based on the kinematic compatibility of the crosscutting relationship was assigned to different structural features. Two major sets of joints/veins, striking NE-SW and ENE-WSW, and a few NW-SE striking veins have been identified in the field (Fig. 3.7). The NW-SE striking veins, where found, cut the major sets striking NE-SW and ENE-WSW (Fig. 3.8). Different types of faulting were mapped including reverse, oblique-slip normal and strike-slip. The faults strike NS, NE-SW, and NW-SE, respectively (Fig. 3.8).

3.5. Structural Geology Synthesis

Tectonically, the Garibaldi Volcanic Belt coincides with the older Coast Plutonic Belt and was produced by episodic accretion of multiple plates. The most recent tectonic phase includes the late Cenozoic subduction of the Juan de Fuca plate beneath the continental margins of SW British Columbia and northwestern Washington. This was later accompanied by Neogene-Quaternary volcanism which formed the NW-SE trending Garibaldi Volcanic Belt (Fig. 3.1).

The current regional maximum horizontal principal stress within the Coast Plutonic Belt and the GVB is approximately ENE-WSW (Leonard et al., 2010; Balfour et al., 2011), perpendicular to the Juan de Fuca and SW British Columbia subduction front (Fig. 3.1). Thus, we can expect that trends of regional compressional structures such as the folds and reverse faults within the MMVC should be compatible with the regional horizontal maximum stress; possibly NNW-SSE trending structures (Figs. 3.1, 3.2, 3.3 and Plate 1 Appendix B1). Below we consider the kinematic indicators of the geologic structures within individual structural domains of Mt. Meager. The kinematic relationships within each domain and between the subdomains will then be used to determine the most likely cause and sequence of deformation in the region during the last 2 Ma.

3.5.1. Lillooet Ridge Domain

The geologic structures (e.g., faults, folds, fractures, and orientations of granitic basement units) in the Lillooet Ridge domain show very different trends over a distance of less than 5 km along two distinctive volcanic capped ridges. The Lillooet Ridge fault is interpreted as a left-lateral strike-slip fault structure between the western and eastern Lillooet ridges, mapped based on the existence of geometrically sharp contact relationships between granitoid basement and volcanic rocks (Fig. 3.3), differences in orientations of granitic basement units, and the presence of fault-step structures exhibited as a series of drainage systems on the western Lillooet Ridge face (Fig. 3.5A, B, C and E, photograph 3).

Paleomagnetic measurements and radiometric dating on samples from both ridges support the interpretation that they were separated by a left-lateral strike-slip fault. Sites

1, 2, 3, and 4 show stable magnetization (Table 1, Fig. 3.5D). Specifically, sites 1-3 exhibit reversed magnetic polarity, show rotation of approximately 15° to 20° anticlockwise (southeastward) and have $^{40}Ar/^{39}Ar$ ages of 864.8 ± 6.2 ka, 850.7 ± 15.9 ka, and 889.1 ± 28.6 ka, respectively. The inverse isochron for site 3 also suggests a similar age of 897.8 ± 34.1 ka. However, it is important to note that this sample (site 3) contains excess argon, indicating a total fusion age of at least 4.5 Ma. Previously, this area was identified as part of the Salal pluton, dated at about 8 Ma (Harris et al., 2020). The 4.5 Ma K-feldspar radiometric age constraint for site 3 could represent the exhumation age of the pluton or that the K-feldspar clock may have been reset due to its close proximity to younger andesitic lavas (sites 2, note sharp contact) (Fig. 3.5E, photograph 1). Site 4 shows normal magnetic polarity and yields an $^{40}Ar/^{39}Ar$ plateau age of 1.12 ± 0.01 Ma. Unlike other sites, there is no indication of any rotation but there is significant tilting (shallowing of the paleomagnetic inclination by approximately 30° southward). Site 5, in contrast, shows reversed magnetic polarity. While it lacks a radiometric age, bedrock geology mapping by Harris et al. (2022) suggests a relative geologic age of 40 Ma or older. Additionally, this site shows significant tilting (shallowing of the paleomagnetic inclination by approximately 40° northward).

The kinematic relationship between mapped geologic structures and the interpreted left-lateral strike slip fault separating the east and west Lillooet ridge is as follows: 1) the East-Lillooet Fault2, striking N-S is kinematically compatible with the modern regional maximum horizontal stress direction (Journeay and van Ulden, 1998; Bustin et al., 2013) and the presence of the Lillooet Ridge strike-slip fault between west and east ridges; 2) the East-Lillooet Fault1 E-W striking strike-slip fault is also compatible kinematically with other structures and may be considered as a strand of the Lillooet Ridge fault between the east and west Lillooet Ridge; 3) the NNE-SSW trending minor fold, being oblique to strike of the interpreted strike-slip fault, is also kinematically compatible with the strike-slip model. The two minor folds on the western ridge (Fig. 3.5B, C) should have a fold axis orientation (trend) NW-SE, however, these may have been affected by possible fault blocks rotation (Paleomagnetic site 5) (Table 1, Fig. 3.6) and subsequent deformation stages; 4) the other 8 minor folds trending E-W are not kinematically compatible with the other structures, nor with the modern regional horizontal stress direction (Fig. 3.5B, C). This inconsistency is likely due to the movement of individual

basement blocks in the region such as rotation of Paleomagnetic sites 1, 2 and 3 (Table 1, Fig. 3.6).
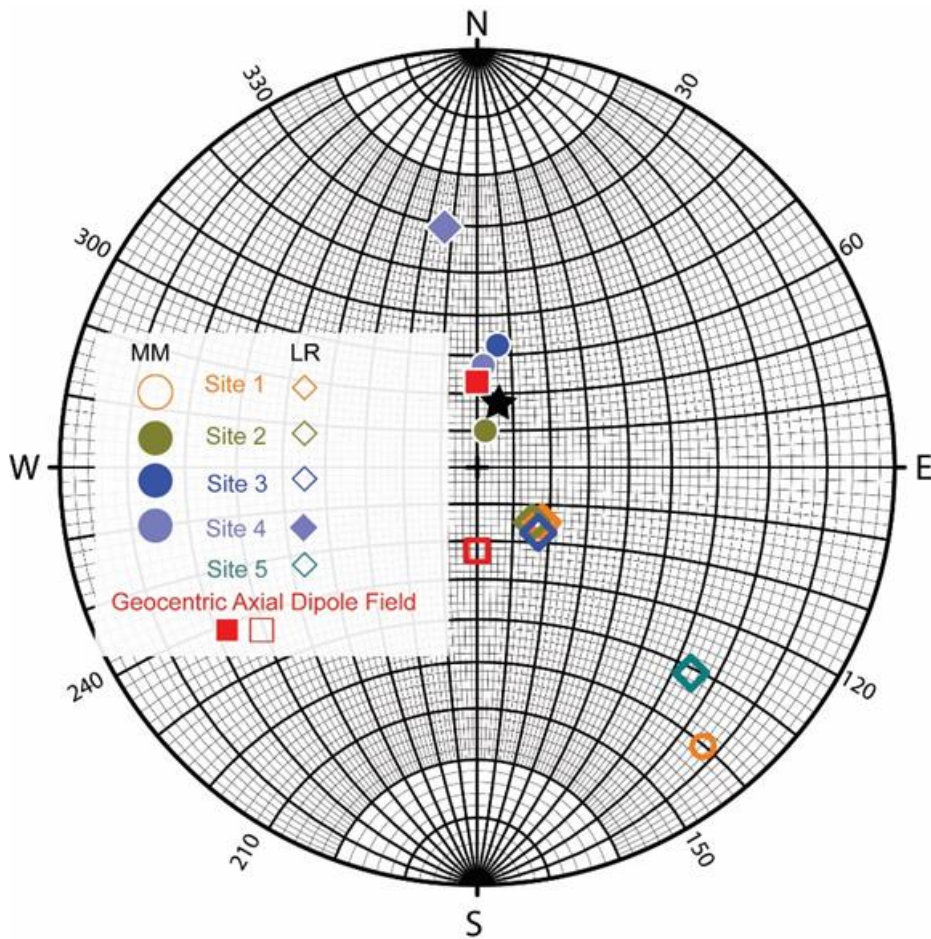
Figure 3.6. **Stereographic plot of paleomagnetic remanence mean directions for sites 1-4 at Meager Massif domain (MM; open circles) and sites 1-5 on Lillooet Ridge (LR; open diamonds). See Table 1 for detailed statistical analysis and suggested Paleomagnetic ages accompanying radiometric dating for each site. Geocentric Axial Dipole (GAD) field inclination for sampling latitude (square) and Present Earth's Field direction (PEF) shown by black star.**

The attitude of basement beddings between the western and eastern ridge (the ridges are less than 5 km apart) show more than 50° change in strike and is compatible with the tilting and rotation of the paleomagnetic signatures (Figs. 3.5 and 3.6). This suggests tilting and rotation of both the granitic basement and younger volcanics and constrains timing of latest deformation, i.e., that the Lillooet Ridge was tectonically active most likely around 800 ka. Together, the paleomagnetic data, radiometric dating, and structural geology (e.g., cross-cutting relationship of faults with the basement and younger lava flows), indicate that the dacitic and andesitic lava flows on the Lillooet Ridge were emplaced either before or during strike-slip faulting.

3.5.2. Meager Massif Domain

This domain is structurally complicated and consists of 50 Ma and older basement granitoid plutons and volcanic deposits spanning ages between 1.9 Ma to 2360 BP. Brittle structures in the Mt. Meager massif, including the underlying plutonic and metamorphic basement rocks of the Western Coast Belt, show a deformation pattern similar to what has been observed in older Miocene rocks of the Pemberton Volcanic Belt (Journeay and van Ulden,1998). A wide spectrum of orientations (striking E-W, NW-SE, and NNE-SSW) of mafic dykes within Mt. Meager suggest a pattern of plane strain likely associated with vertical uplift centred beneath the volcanic complex (Journeay and van Ulden, 1998). Deformation in the Meager Massif domain is associated with at least four fault structures mapped based on outcrop geology and contact relationships, reflection seismology, regional magnetic and gravity surveys, and magnetotelluric resistivity models (Journeay and van Ulden, 1998; Bustin et al., 2013; Hanneson and Unsworth, 2023).

The Owl Creek fault separates this domain from Lillooet Ridge domain (Figs. 3.2, 3.3) and is interpreted as a reactivated Neogene compressional oblique-dextral strike slip fault (Journeay and van Ulden, 1998; Bustin et al., 2013; Muhammad et al., 2021). The Capricorn fault, situated in the centre of the Mt. Meager massif with its northern side acting as the hanging wall, shows very limited volcanic strata aged between 1.9 and 0.1 Ma. (Figs. 3.1, 3.9 and Plate 1 Appendix B1). In contrast, the southern side of Capricorn fault, acting as the footwall, exhibits a continuous preservation of extrusive and effusive lava flows from 1.9 to 0.1 Ma (Figs. 3.9 and Plate 1 Appendix B1).

On the southern side of the massif, paleomagnetic data at sites MM1, MM2 and MM3 (Table 3.1, Fig. 3.6) show significant tilting and rotation of lava flows with ages between 1.9 to 1 Ma, while very little to no sign of deformation for lavas younger than 1 Ma is evident at site MM4 (Table 3.1, Fig.3.6). This deformation - age relationship is compatible with the northward younging of volcanic centres in Mt. Meager massif.

The contrasting volcanic stratigraphy between the hanging wall and foot wall of Capricorn fault suggests that the Capricorn fault may have accommodated ~ 1 km of uplift and erosion of volcanic units (Figs. 3.4 and 3.9). This interpretation is compatible with magnetotelluric resistivity models (Fig. 3.9) (Hanneson and Unsworth, 2023) and previous regional structural geology studies of the Garibaldi Volcanic Belt (Parrish, 1982; Journeay and van Ulden,1998).

This structure may also represent a pathway for the ascent of magmatic gases and hydrothermal fluids to the surface as seen by the extensive alteration of Plinth Peak and presently degassing glaciovolcanic fumarole field within Job glacier (Fig. 3.1). Plinth Faults 1 and 2 are most likely related to gravitational collapse of the unstable volcanic edifice and thus not controlled by tectonic stress. These two faults spatially align with the vent of the 2360 BP explosive eruption, an earlier explosive eruption (24.3 ± 2.3 ka) likely sourced from Plinth Peak (Russell et al., 2021), and cut lava flows younger than 100 ka. Indeed, Roberti et al. (2021) suggest that there may in fact be a relationship between large landslides at Mt. Meager and eruptive activity. While the 2360 BP eruption was likely triggered by magma mixing (Stasiuk et al., 1996; Hickson et al., 1999; Roberti, 2018; Russell et al., 2021), this mixing is posited to be caused by disruption of the local stress field following a large (>10^9 m^3) geologically contemporaneous landslide (Roberti, 2018; Roberti et al., 2021). Although our structural geology interpretation does not directly support the hypothesis that gravitational collapse along Plinth Faults 1 and 2 triggered the 2360 BP eruption, these faults may have nevertheless been zones of weakness or pathways for the movement of magmatic fluids, which could increase the likelihood of failure.
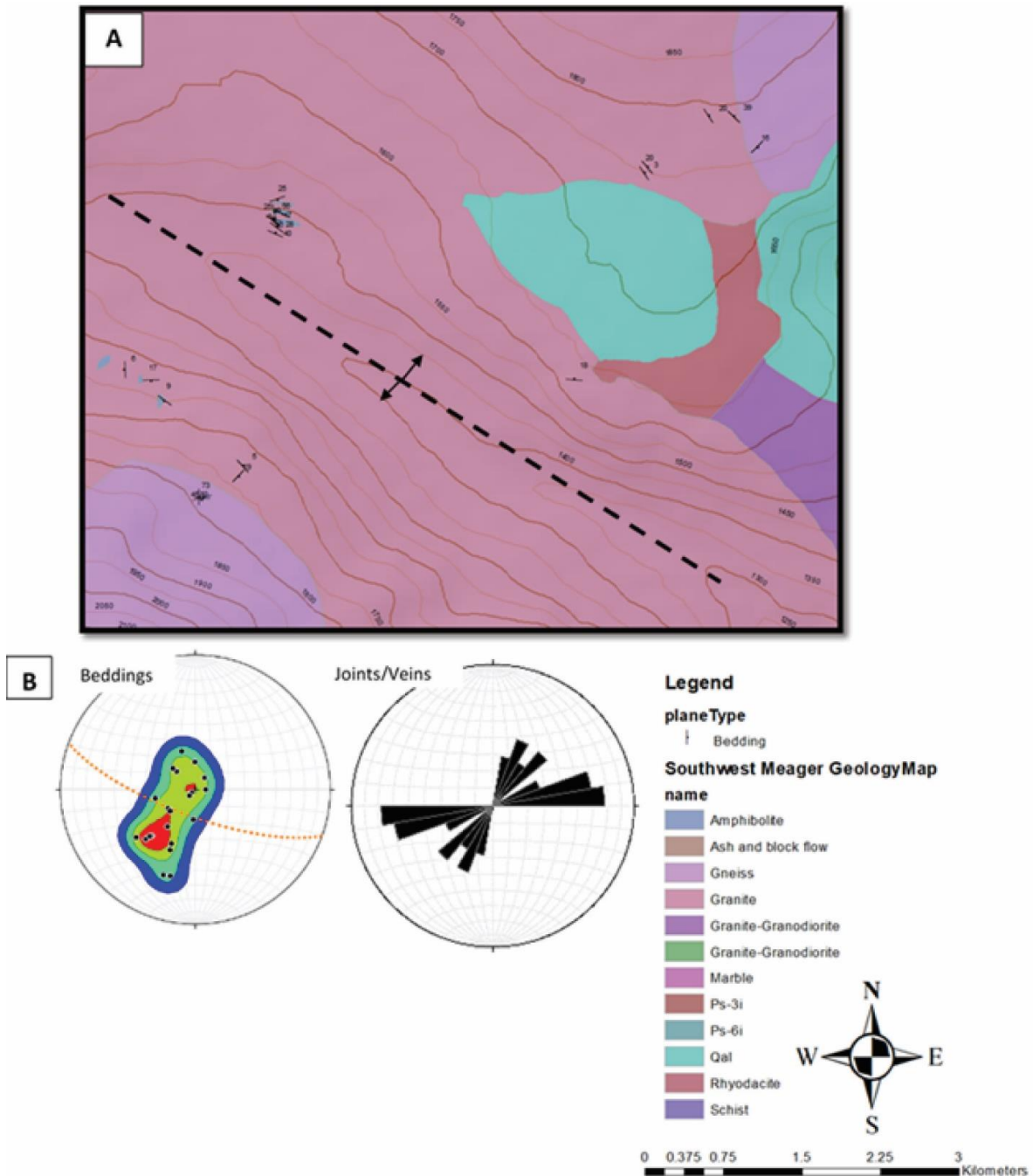
Figure 3.7. **A) Geology map of southwestern contact of Mt. Meager. B) Stereograph of basement beddings of southwestern contact of Mt. Meager: Orange dotted trace represents axial plane (striking NW-SE) of calculated fold structure; contours were drawn for poles of bedding planes for the major fold limbs.**
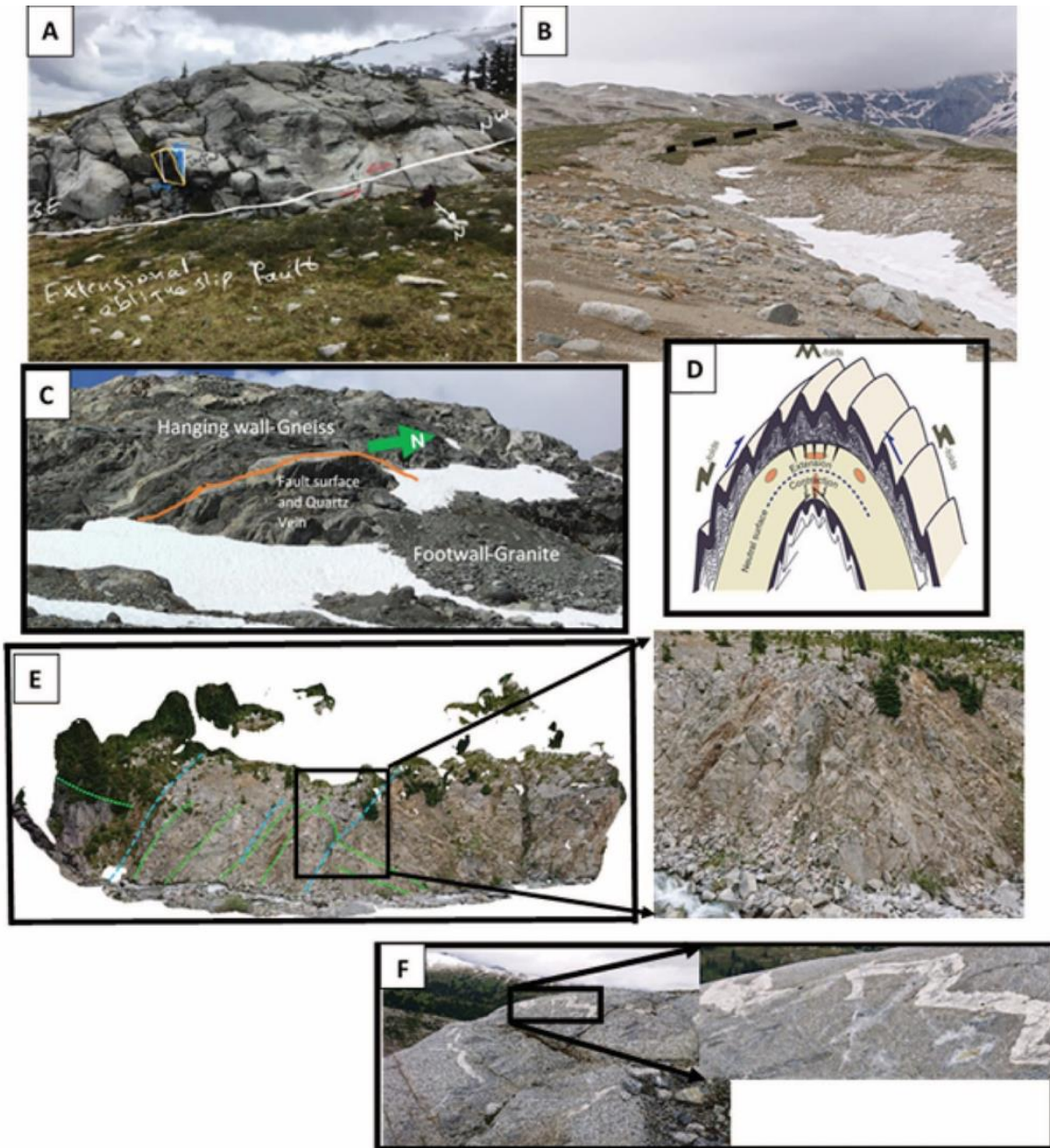
Figure 3.8. A) NW-SE striking strike-slip fault (approximately 1 m offset). B) NE-SW striking fault scarp (potentially normal fault). C) N-S striking compressional fault and S-shape minor fold. D) A cartoon model explains geometry of buckling fold on limbs of major folds. E) N-S striking compressional fault and Z-shape minor fold. F) NE-SW striking quartz vein folded (M-shape minor fold) within the hinge area of a major fold structure. Note that the folded quartz vein is cut by a NW-SE striking xenolith vein.

3.5.3. Meager Creek Domain

Very little outcrop geology was documented for the eastern structures in this domain due to poor exposure of bedrock or younger volcanic deposits. Most of the faults were thus mapped using a combination of drill-hole lithologic interpretation, geophysical surveys, and surface topographic expression. For the eastern part of the Meager Creek domain, a tentative age versus deformation relationship can be established using classic structural geology kinematic analysis based on location, geometry, orientation and collating nearby structures (Fig. 3.10). The NE-SW trending Camp fault is thought to be contemporaneous or younger than the Meager Creek fault as it appears geometrically to either cross or terminate at the Meager Creek fault. Earlier drilling and geological studies (Fairbank et al., 1980, 1981) found mylonite along the Meager Creek fault zone suggest that the area experienced significant folding and ductile deformation in the past.

This supports the hypothesis that the Meager Creek fault zone predates the Camp fault and was subsequently cut by it. As such, the Camp fault could be as old as 2 Ma. The N-S trending No-Good Discontinuity fault kinematically appears as an extensional antithetic shear fracture which accommodated NE-SW Neogene horizontal compressional stress (Fig. 3.11A) (Parrish,1982; Journeay and van Ulden,1998; Bustin et al., 2013) that defined the physiography of mountain complex prior to the deposition of the GVB volcanics.

The geometry, orientation, and proximity of the reactivated Miocene Meager Creek fault to the southern Meager volcanic vents such as Devastator and Pylon suggest the onset of fault reactivation occurred at least 2 Ma or greater, which may have facilitated the ascent of magmatic fluids and hence volcanism. This is supported by magnetotelluric resistivity data (Hormozzade Ghalati et al., 2022; Hanneson and Unsworth, 2023) which show a large conductor less than 2 km beneath Meager Creek area in the vicinity of Devastator and Pylon peaks (Fig. 3.9). The western structures within this domain are better constrained in terms of surficial bedrock geology and structural geology mapping due to readily accessible and ubiquitous bedrock exposure and gentler topography.

The kinematics of the measured structural geology features in the Meager Creek Domain are explained below. A geometrical relationship between bedding of the units and minor folds indicates the presence of a major fold (trending NNW-SSE) (Fig. 3.8)

within the SW contact of the Mt. Meager massif. Although we lack the full stratigraphic age evidence, we consider this fold to be an anticline based on the patterns and geometry of the minor folds (S-shape, M-shape, and Z-shape minor folds) at the limbs of major fold (Fig. 3.8). Geometrically, buckling within compressional systems can define deformation history and thus aid in identifying the hinge zone and limbs. For example, in the case of an anticline, Z-folds represent the left limb, S-folds represent the right limb, and M-folds indicate the hinge zone (Fig. 3.8). The coincidence of the fold hinge with a paleo-glacial valley and the cross-cutting relationship between veins within the major fold hinge zone may indicate that the fold crest has undergone possible erosion by glaciation and outer arc extension (collapse) possibly due to glacial unloading (Fig. 3.8). Within the major fold hinge zone, an ESE-WNW striking vein cuts the NE-SW and ENE-WSW striking veins (Fig. 3.8). Thus, the ESE-WNW striking set must postdate the formation of folding. In general, three sets of faults were identified within southwest contact of Mt. Meager: 1) a reverse fault, which roughly strikes NS (Fig. 3.8); 2) a NE-SW striking normal fault (Fig. 3.8B) and 3) an approximately NW-SE striking fault with major strike-slip component (Fig. 3.8A). Adjacent to the NW-SE striking strike-slip fault with a few metres of lateral offset, a ubiquitous (possibly Quaternary age) NE-SW striking fault scarp (possibly normal) is mapped (Fig. 3.8B).
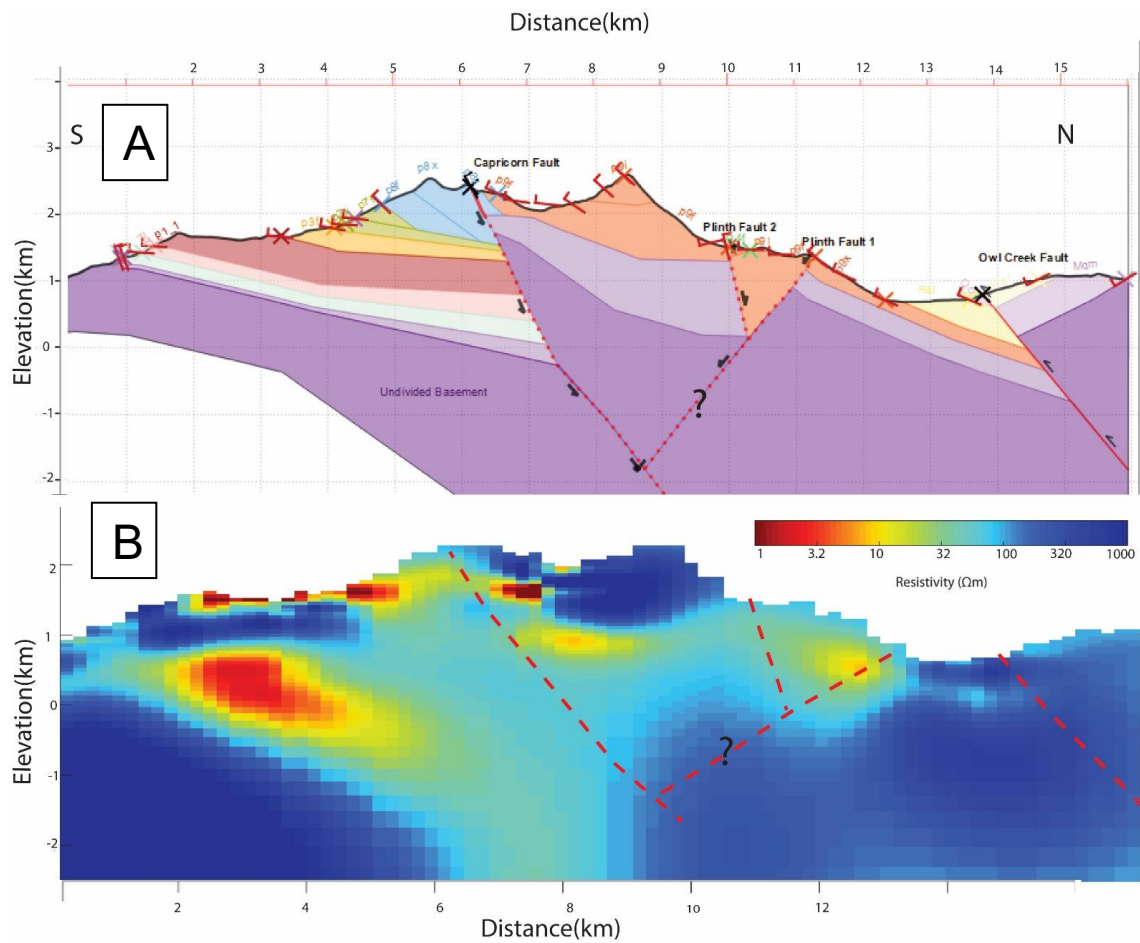
Figure 3.9. **A) Geologic cross-section from North to South see location of section profile on Figure 1. B) Magnetotelluric resistivity section (Hanneson and Unsworth, 2023) along profile path N-S on Figure 1 and with overlayed fault structures from geologic cross-section.**
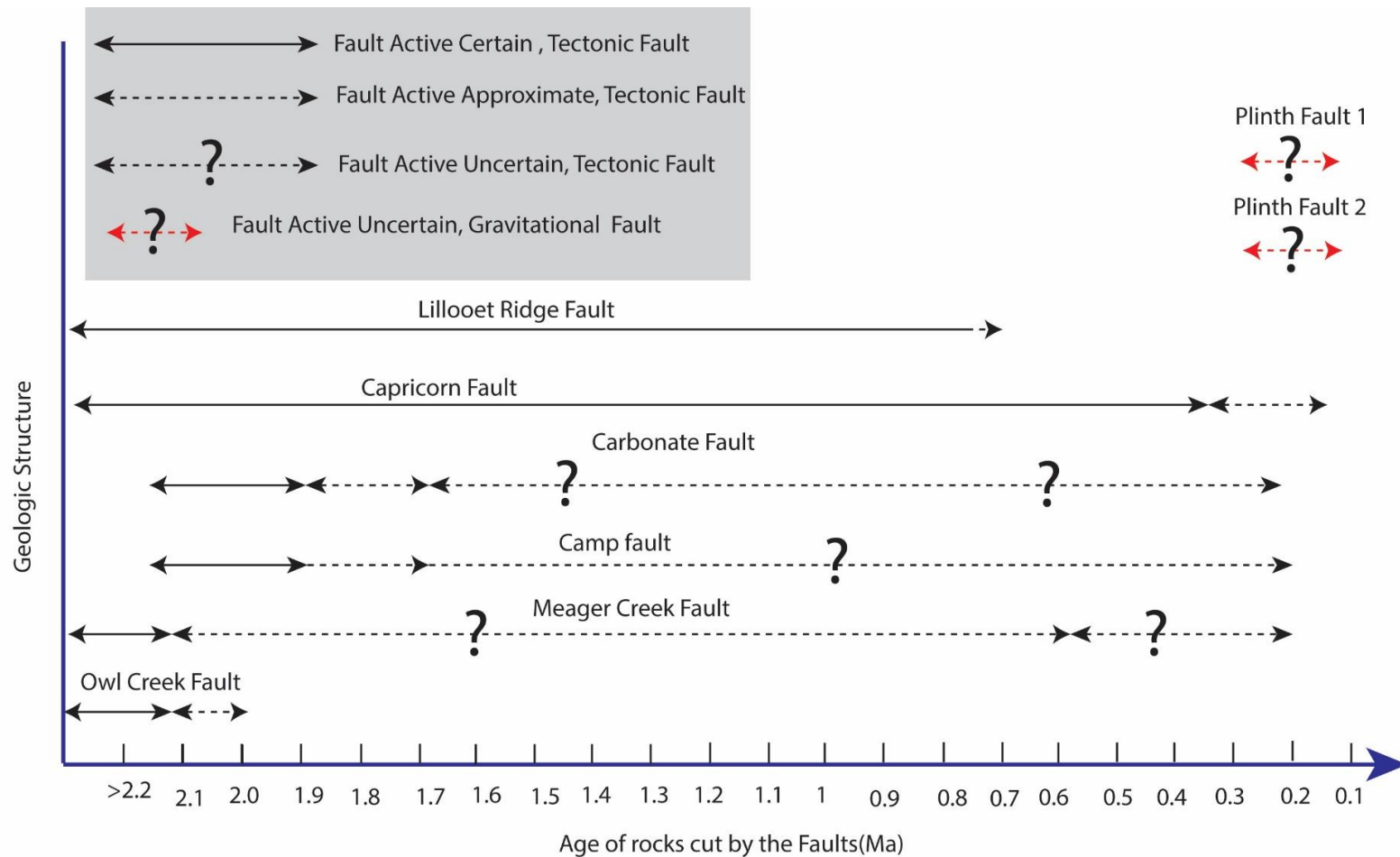
Figure 3.10. Relative ages of fault structures based on geologic map and cross-cutting relationships with bedrock units. For Lillooet Ridge fault, the age of bedrock units is derived from radiometric and paleomagnetic dating (this study); other fault ages are derived from previous studies (Woodsworth, 1977; Read 1990). Arrow and direction indicate estimated age range of active faults. The age range is well defined where the line is solid and uncertain where the line is dashed, black arrows indicate tectonic faults, red arrows indicate gravitational faults.
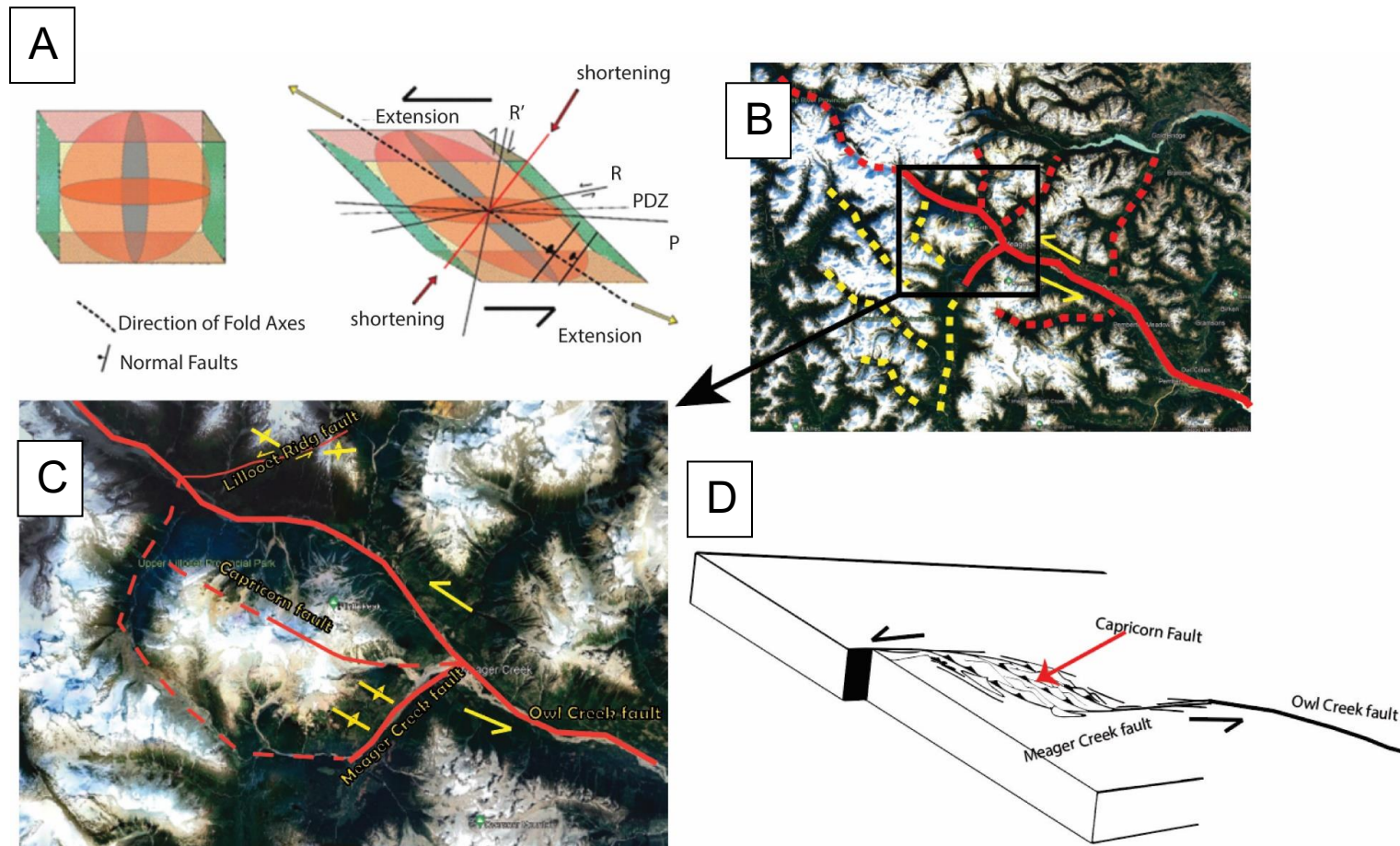
Figure 3.11.   A) Strain ellipsoid of strike-slip deformation (Muhammad, 2016) shows simple shear deformation and its associated structures. R and R' are synthetic and antithetic shears, respectively; P is a secondary fracture that may have synthetic shear; PDZ = principal displacement zone. B) The regional continuation of Owl Creek fault relative to geomorphology of the area; notice changes of valley orientation drawn in red and yellow dashed lines of the trace of OWL Creek fault taken from Bustin et al. (2013). C) Schematic illustration of the major faults and fold structure orientation at MMVC shows rhomboidal shape of Meager Massif, similar to the typical geometry of restraining bend structures. D) Schematic model with geometry of transpressional restraining bend within compressional oblique strike slip deformation setting.

Table 3.1. Paleomagnetic directional data and radiometric ages for Meager Massif samples. NC/NU = number of cores collected at each site and used in analysis; D = mean paleomagnetic declination; I = mean paleomagnetic inclination; α_{95} = 95% confidence interval (P = 0.05); k = estimated precision (Fisher statistics; Fisher, 1955).

Location	Site	NC	NU	D(°)	I(°)	α_{95}	K	P	Estimated Tilting	Estimated Rotation	Rock Type	Paleomag Age	$^{40}Ar/^{39}Ar$ Age
Lillooet Ridge	LR1	8	8	134.9	-66.5	4.3	164.7	R	NA	>20° SE	Andesite	0.78-0.9 Ma	Plateau Age of 864.8 +/- 6.2 ka
	LR2	8	6	134.9	-68.3	2.7	610.1	R	NA	>20° SE	Andesite	0.78-0.9 Ma	Plateau Age of 850.7 +/- 15.9 ka
	LR3	8	8	136.7	-65.6	3.9	179.3	R	NA	>20° SE	Granite	4.29-4.48 Ma	Total Fusion Age 4.5 Ma Plateau Age of 897.8 +/- 34.1 ka
	LR4	8	8	352.5	29.8	4	274.6	N	>25° southward	NA	Dacite	2-1.2Ma	Plateau Age of 1.24 +/- 0.02 Ma
	LR5	8	8	134	17	14	30.5	N?	>40° northward	>20° SE	Granodiorite	55-47 Ma	NA
Meager Massif	MM1	9	7	141	-8.5	6.4	89	R	>50 southward	>30° SE	Dacite	1.9 Ma	1.91 +/- 0.07 Ma
	MM2	9	8	14.3	79.7	4.9	125.9	N	10° northward	5-10° NE	Andesite	1.0 Ma	65 +/- 70.6 Ka
	MM3	12	9	9.2	57.9	4.3	142.5	N	>5° southward	5-10° NE	Andesite breccia	1.0 Ma	535.4 +/- 168.1 Ka
	MM4	11	10	359.7	57.9	4.5	114.3	N	5° southward	NA	Andesite	780-990 Ka or 1.2-1.07 Ma	245.4 +/- 35.5 Ka

3.6. Sequences of Deformation

The Mount Meager Volcanic Complex experienced multiple stages of deformation and the oldest deformation is well-preserved within Owl Creek, Capricorn, and Meager Creek fault systems. The Owl Creek fault which bounds the northern end of Meager Massif cuts plutons older than 55 Ma (Bustin et al., 2013). The Meager Creek fault is likely the second oldest and may connect to the Owl Creek fault at depth. It also bounds the southern end of the Meager Massif domain and shows evidence of older compressional activity and formed prior to deposition of GVB volcanics as shown by the presence of mylonite identified in drilling (Figs. 3.10, 3.11) (Fairbank et al., 1980, 1981).

The Lillooet Ridge fault to the north of the Meager Massif domain is most likely contemporaneous with Owl Creek or may be a strand of the Owl Creek fault which deformed rocks around 55 Ma and was active until 850 ka based on paleomagnetic and radiometric dating of andesitic lavas (Figs. 3.1, 3.2, 3.3, 3.10). Orientation measurements and paleomagnetic signatures of the plutons, which are 50 Ma and/or older to 4.5 Ma, show significant tilting of >40° northward (site LR5; Table 3.1) west of the Lillooet Ridge and more than 20° rotation southeastward (site LR5; Table 3.1). The magnitude and direction of tilting and rotation has changed over the last 2 Ma, with tilting ~ 25° southward (site LR4; Table 3.1) west of the Lillooet Ridge for 1.2 Ma dacitic lavas (Table 3.1) and rotation of more than 20° southeastward within 850 ka andesitic lavas at the eastern part of the Lillooet Ridge (sites LR1 and LR2; Table 3.1). These changes of orientation and magnitude of tilting and rotation within rocks of different ages are likely an indication of changes of regional stress since the last 2 Ma and reactivation of the older faults such as Meager Creek, Owl Creek, and Lillooet Ridge faults. By contrast, the northwest trending and north-east vergent Capricorn fault deforms basement rocks older than 55 Ma and younger lavas as old as 0.1 Ma, including the Capricorn assemblage lavas.

The geometry, age, and spatial location of the Capricorn fault with respect to other nearby fault systems (e.g., Owl Creek and Lillooet Ridge to the north, and Meager Creek and associated faults to the south), suggests that local stresses played a larger role in controlling the Capricorn fault than regional stresses at some point during the last 850 ka. Therefore, our proposed explanation is that the high topographic relief of the Mt.

Meager massif may correspond to a transpressional restraining bend strike-slip deformation that shaped the current Mt. Meager complex over the past 2 million years.

Restraining bends are frequently associated with strike-slip deformation within obliquely convergent subduction settings where interplate strain is partitioned into arc-parallel strike-slip zones within the fore-arc, arc, or back-arc regions. In addition, restraining bends can produce elongate, individual massifs with anomalously high topographic elevations which leads to crustal shortening and exhumation of crystalline basement (Cunningham and Mann, 2007; Mathieu and van Wyk de Vries, 2011; Mathieu et al., 2011; Kehoe and Kiser, 2020). The GVB and MMVC tectonically coincide with the intra-arc to back-arc transition zone, hence, exhibits the loci of strain partitioning as response to rapid change in orientation of the Pemberton and Garibaldi Arc segments which are coeval with a shift in Pacific plate motion after 5 Ma (Venugopal et al., 2020). They also correspond to changes to both the Juan de Fuca Ridge system (10-15° clockwise rotation) and the northern Cascadia subduction zone margin (Journeay and van Ulden, 1998).

The bounding faults of restraining bends such as the Meager Creek and Owl Creek faults develop first and may merge deep below the surface (Cunningham and Mann, 2007; Muhammad, 2016). The fundamental characteristics of a fault bend, such as its shape, topography, and internal structure, are influenced by several factors. These factors include the regional stress, the original width of the stepover, and whether the bend is a termination of a strike-slip fault, a double bend along a single linked strike-slip fault, or a stepover where parallel strike-slip fault segments are offset and may or may not overlap. For instance, stepovers that are wide may have fewer faults connecting the main strike-slip faults. In our case the width of the Mt. Meager massif from north to south between the two bounding faults is more than 10 km and thus comprises fewer faults connecting the main strike-slip faults such as Capricorn fault.

3.7. Geothermal Implications

In 1980 and 1982, three exploration boreholes (MC-1, MC-2, and MC-3) exceeding 3 km in depth were drilled at Mt. Meager and revealed fluid temperatures up to 270°C; three additional boreholes (MC-6, 7 and 8) were drilled in 2004 and 2005 at the base of Pylon

peak (Ghomshei et al., 2004, 2005; GeothermEx, 2009). Despite this, these drill holes did not appear to reach highly permeable zones. MC-6 and MC-8, two of the drilled wells, demonstrated notable permeability as evidenced by the circulation losses encountered during drilling and subsequent airlift-assisted flow tests, injection tests, and temperature-pressure surveys conducted in the summers of 2005 and 2006. However, despite indications of permeability, neither of these wells exhibited sustained self-flow even after multiple attempts at airlifting in 2005. The high elevation of the drilling site over the hydraulic level of the geothermal reservoir may also contribute to the occurrence of significant drilling fluid losses, and to the reduced well productivity and difficulties in sustaining a self-flow. By contrast, borehole MC-7 did not exhibit fluid circulation losses and hence failed to reach suitable permeable zones (Ghomshei et al., 2004; GeothermEx, 2009).

While potential reservoir and fluid pathways in such volcanic settings largely rely on fracture density, orientation, and geometry, the presence of fractures does not ensure successful geothermal energy production. The stress field, specifically the alignment of maximum horizontal compressive stress with fractures, can significantly impact fault activity and fluid flow. If maximum horizontal compressive stress aligns with fractures, it can widen the fracture and facilitate fluid flow. Conversely, if maximum horizontal compressive stress is perpendicular, fractures may close, inhibiting fluid flow. This interplay of geological structures, tectonic history, and stress conditions in relation to fracture orientation and behavior significantly influences geothermal reservoir quality and fluid pathways, critical for successful geothermal energy production (Philipp et al., 2007; Khodayar et al., 2018).

For instance, in contrast to wells MC-6 and MC-8 which displayed significant fluid circulation loss, indicating the presence of permeable zones, well MC-7, despite its proximity to the No-Good Discontinuity fault, did not encounter a permeable zone (Fig. 3.3). This may in fact be related to the kinematics and geometry of the tectonic fault systems within Mt. Meager. If our tectonic model of transpressional strike-slip model is accurate, then both the No-Good Discontinuity fault and Camp fault could act as an antithetic Riedel shear fracture (Fig. 3.11A) which caused lateral displacement of basement rocks. This structural interpretation is supported by available geophysical data from the early 1980s (Fairbank et al., 1980, 1981) as well as more recent 3D MT resistivity models (Hanneson and Unsworth, 2023) which show the No-Good

Discontinuity as a contact that separates rocks with distinct physical properties. Furthermore, the paleomagnetic data collected at site MM1, located to the west of the No-Good Discontinuity fault, indicates a rotation of over 30° towards the southeast. On the other hand, at site MM2, situated east of the No-Good Discontinuity fault, the paleomagnetic data reveals a rotation of more than 10° towards the northeast. This could indicate that the No-Good Discontinuity fault caused north-south displacement of subsurface stratigraphy as it's reflected on recent 3D MT resistivity models (Hanneson and Unsworth, 2023). The geometry of faults and the spatial relationship between the reservoir and fault damage zone can either increase or decrease reservoir permeability (Wallis et al., 2017). For instance, longitudinal faults such as Meager Creek fault (those running parallel to the reservoir) can enhance permeability along the fault strike. Conversely, faults that intersect perpendicular to the reservoir such as the No-Good Discontinuity fault may create a low permeability zone due to plastic deformation, which reduces the overall porosity.

3.8. Geohazard Implications

The MMVC physiography formed as a result of transpressional restraining bend strike-slip deformation. Geologically, these structures can have important societal and economic implications restraining bend structures can mitigate or accelerate natural hazards (Cunningham and Mann, 2007; Micklethwaite et al., 2015; Kehoe and Kiser, 2020). For instance, restraining bends associated to strike slip fault termination can behave as barrier to slip transfer along the faults. By contrast, slip transfer can accelerate if a restraining bend forms within a double bend along a single linked strike-slip fault, or a stepover where parallel strike-slip fault segments are offset. For example, the Komandorsky Islands earthquake that occurred in 2017, with a magnitude of 7.7, attained speeds that exceeded the speed of sound over a fault system that had a complex geometry similar to restraining bend structures (Kehoe and Kiser, 2020).

Strain transfer between interconnected fault segments can also lead to the amplification of seismic events. This process has the potential to trigger severe natural hazards like deep-seated landslides, involving significant rock-volume collapse, and even the potential for a volcanic eruption. These risks are especially relevant when considering the magmatic plumbing system beneath MMVC, situated at depths ranging from 5 to 15

km (Hanneson and Unsworth, 2023). Additionally, the complex structural geology and the prolonged volcanic history of Mt. Meager contribute to an increased risk of surface displacements, such as landslides and rockfalls. This heightened risk is primarily attributed to the enhanced alteration caused by the upward movement of hydrothermal fluids through the weakened crystalline basement and volcanic rocks in the area.

3.9. Conclusions

Qẃelqẃelústen or Mt. Meager coincides tectonically with the intra-arc to back-arc transition zone and exhibits the loci of strain partitioning as response to rapid change in orientation of the Pemberton and Garibaldi Arc segments which are coeval with a shift in Pacific plate motion after 5 Ma (Journeay and van Ulden, 1998; Venugopal et al., 2017, 2020). Such strain partitioning is manifested through the onset and development of transpressional restraining bend strike-slip deformation from 5 Ma to 1.9 Ma. This transpressional structure produced an elongate and rhomboidal massif at Mt. Meager with anomalously high topographic elevations which may have led to ENE-WSW crustal shortening and exhumation of crystalline basement along the Mt. Meager edifice.

The bounding Meager Creek and Owl Creek faults first developed after 5 Ma, and subsequently initiated internal deformation such as the NW-SE trending Capricorn fault and caused extensive uplift and exhumation at the centre of the massif after 1 Ma. The early stage of deformation, 5 Ma to 1 Ma, likely facilitated the ascent of subsurface magmas and formation of early-stage volcanism within the Mt. Meager massif. As the deformation progressed and evolved, internal faults such as Capricorn fault developed and supported further exhumation of the crystalline basement; at this stage deformation was largely controlled by local stress. Additionally, this stage is manifested over the last 1 Ma and is aligned with the volcanism due to mountain edifice instability related to uplift and exhumation of crystalline basement. In addition, secondary NNE-SSW striking faults such as the No-Good Discontinuity and Camp faults, trend oblique to the principal deformation zone (PDZ, Fig. 3.11A) and may represent antithetic Riedel shear fractures responsible for north-south displacement of basement rocks.

This complex structural geology and long-lived volcanic history of Mt. Meager also enhances the risk of surface displacements (e.g., landslides and rockfalls) due to

enhanced alteration by ascending hydrothermal fluids through the weakened crystalline basement and volcanic rocks. Strain transfer between interconnected fault segments can also lead to the amplification of seismic events which have the potential to trigger severe natural hazards like deep-seated landslides, involving significant rock-volume collapse, and even the potential for a volcanic eruption. These risks are especially relevant when considering the extensive magmatic plumbing system beneath MMVC (~5 to 15 km depth).

 The structural complexity has likely also significantly impacted geothermal exploration at Mt. Meager by making identification of permeable zones particularly challenging. As such, a more detailed fracture characterization study using imaging techniques in existing boreholes could better constrain the potential of certain fractures at depth to act as possible geothermal flow paths. When integrated with independent geophysical surveys (e.g., magnetotellurics, gravity, seismic imaging), this would likely further enhance our understanding of the extent and viability of the geothermal reservoirs within the Mt. Meager massif.

3.10. Recommendations

Further work is needed to investigate the geometry, shape, and linkage of the MMVC restraining bend structure to nearby structures in order to understand if the bend represents the termination of a strike-slip fault, a double bend along a single linked strike-slip fault, or a stepover where parallel strike-slip fault segments are offset and may or may not overlap. Restraining bend structures are also considered as important regions for resource exploration as it facilitates the exhumation of deeper basement structures that might hold significant mineral and energy resources.

Previous studies such as Lüschen et al. (2015) and Donoso et al. (2022) used 3D seismic surveys to explore a petrothermal reservoir in a late-Variscan granitic pluton within the Erzgebirge (Ore Mountains) in Saxony, Germany, and imaging of volcanogenic massive sulfides at Neves-Corvo, Portugal. A similar 3D reflection seismic survey at MMVC would be extremely beneficial in constraining the subsurface fault linkages, and extent of the geothermal and magmatic reservoirs. This would aid not only in geothermal and mineral exploration, but also in better understanding the complex

physical relationships between geohazards such as earthquakes, landslides, and volcanic eruptions.

3.11. Acknowledgement

We express our gratitude to the Lílwat Nation, Innergex Renewable Energy, Meager Creek Development Corporation, and the pilots of No Limits Helicopter Adventures for their invaluable technical and logistical support. Our heartfelt thanks go to the graduate students who contributed to the fieldwork: A. Borch, B. Coughlan, J. Connelly, M. Harris, and S. Leiter. This research took place on the ancestral lands of the Lílwat Nation, within the framework of the Garibaldi Geothermal Energy Project under BC Parks permit 109950 and BC Ministry of Forests permit S26564. Lastly, we extend our sincere appreciation to the anonymous reviewers whose constructive feedback greatly enhanced the quality of our manuscript.

3.12. Funding statement

This research was supported by a Geological Society of America Richard B and Cynthia Waitt Research Award to MM, a Natural Sciences and Engineering Research Council of Canada Discovery Grant (RGPIN-2016-03953) and Mitacs Accelerate programs (IT14053 & IT25514) granted to GWJ, and Natural Resources Canada / Geoscience BC Garibaldi Geothermal Energy Project grant to S. Grasby.

3.13. Competing Interests statement

The authors declare there are no competing interests.

3.14. Data Availability statement

Data generated or analyzed during this study are provided in full within the published article and its supplementary materials.

Chapter 4.   Integrated Assessment of Rock Slope Stability Incorporating Structural Geology, Kinematic Analysis, and Satellite Remote Sensing: A Case Study of Mount Currie, British Columbia, Canada.

Mahmud Muhammad[1], Glyn Williams-Jones[1], and Doug Stead [1]

[1]Centre for Natural Hazards Research, Department of Earth Sciences, Simon Fraser University, Burnaby, BC, Canada.

4.1. Abstract

Mount Currie, situated around 100 km north of Vancouver within the Pemberton district, is a gravitational escarpment influenced by both climate and tectonics. This study examines the impact of ongoing tectonic activity on the formation of the Mount Currie scarp and the occurrence of rockfall on its north face. We have identified specific sites that require continuous monitoring using time-series radar imagery and block theory/limit equilibrium analysis to determine the likelihood and volume of potential failures.

Our findings suggest that the main Mount Currie scarp, running ENE-WSW, likely resulted from extensional faulting related to compression along the mountain crest. This fault is not directly caused by seismic stress vectors but is instead influenced by local stress patterns within the mountain complex itself. These local stress patterns are primarily governed by the Owl Creek fault to the east, the Miller Creek fault to the west, both bounding thrust faults of the Mount Currie complex, and the impact of crustal rebound from glacial melting.

At the NE-3 peak in the centre of the Mount Currie ridge front, InSAR data shows that the NE-3 peak moves annually about 6 mm per year downward (subsidence) towards the north-northwest with a total displacement of 1.5 cm between summer 2018 and the end of summer 2020. Moreover, we identified a key block that may control instability of

the NE-3 peak at the centre of the Mount Currie ridgeline as having a higher likelihood of slope deformation compared to surrounding peaks.

 In the event of slope collapse, it is estimated that a minimum of 14.4 x 10^6 m^3 of bedrock could be involved. The 3D kinematic analyses and estimated limit equilibrium safety factor presented here are preliminary, as there is insufficient information on the subsurface geology and groundwater conditions. Therefore, our analyses may underestimate the hazard, as water pressure can greatly reduce shear strength, and consequently, reduce the safety factor and increase the likelihood of slope deformation.

4.2. Introduction

Mount Currie is located within the Coast Plutonic Belt (CPB) mountains near the Pacific Ocean. This proximity results in the piedmont of ice-covered mountains being covered with dense rainforest, obscuring many of the rock outcrops. The presence of multiple phases of glaciation and ice retreat such as the Fraser glaciation (Clague, 1991, 1997; Clague and James, 2002; Huybers and Langmuir, 2009) in conjunction with zones of active tectonics are a major limitation in determining the origin of slope failures and scarp development. It is challenging to distinguish primary rock structures and kinematic indicators. For example, it is difficult in the field without additional knowledge to distinguish the origin of slip vectors whether formed by earthquake events, glacial isostatic rebound or deep-seated gravitational collapse. Therefore, studying scarps, gravitational failure features and neotectonics of southwestern British Columbia is problematic and needs careful attention.

An example of this challenge is seen at the Mount Currie scarp, where there has been uncertainty in distinguishing between neotectonic faults and gravitational failure features. Different studies have applied various methods to analyze the geotechnical, geomorphological, and structural aspects of this scarp, leading to two primary interpretations: one suggesting a gravitational cause (Bovis and Evans, 1995), and the other suggesting a neotectonics origin (Eisbacher,1983; Blais-Stevens et al., 2011). Hence, the previous studies provide limited insight into the origins and triggering mechanisms of slope movement.

The studies by Evans (1987) and Bovis and Evans (1995) of movements of rock mass blocks and geotechnical kinematic tests for Mount Currie suggested the mechanism of failure as being related to toppling and planar failure. However, two other studies by Eisbacher (1983) and Blais-Stevens et al. (2011) suggest the mechanism of failure is most likely related to the presence of Holocene faults in the region (e.g., Green Lake fault) (Fig. 4.1). In another study, Blais-Stevenson et al. (2011) used landslide deposit samples and ^{36}Cl cosmogenic dating for the Mystery Creek Landslide near the Mount Currie scarp (Fig. 4.1). They provided an age range between 2400 and 4800 years. Additionally, they showed that the climate was similar to present day conditions and concluded that the slope failure most likely had not occurred, at least, directly, related to

glacial debuttressing. Additionally, they believe that other scarps such as Mount Currie could have been activated under similar conditions to the Mystery Creek landslide.

A 2018 study by BGC Engineering Inc. (BGC, 2018) for the Squamish Lillooet Regional District (SLRD) concentrated on a multi-geohazard assessment, including estimating the probability of rock avalanches, modeling debris flow runouts, and conducting flood and debris flow magnitude-frequency analysis. However, it did not consider the significance of structural geological features, such as faults and folds, in shaping slope geometry, the persistence and continuity of structures like faults and lineaments, as well as the potential triggers for failure at Mount Currie.

This study aims to: (1) Determine the most likely trigger mechanisms of failure at Mount Currie; (2) Identify sites requiring long term monitoring based on time-series radar imagery; and (3) Assess the role of neotectonic activity that shaped the Mount Currie ridge scarp and the current rockfall in the north face of the mountain (4) Produce a structural geology-based factor of safety map for the slopes of interest.

4.3. Geology Setting

The Coast Mountains of British Columbia experienced three Cenozoic stages of uplift from north to south (Parrish, 1982). First, intense post-orogenic uplift of the eastern and central Coast Plutonic Complex. Second, Middle Cenozoic uplift of the Coast Mountains starts from Mount Waddington to southeast Alaska. Finally, Pliocene to Recent > 3 km of uplift (<5 Ma) at the southern Coast Mountains encompassing the current Garibaldi Volcanic Belt which includes, Mount Currie (non-volcanic mountain) and the Mount Meager Volcanic Complex.

There are two critical geologic events that might have contributed to the rapid Pliocene to present uplift of the southern Coast Mountains of British Columbia: 1) The interruption of calc-alkaline volcanic activity of the Pemberton Volcanic Belt > 7 Ma and in the Garibaldi Volcanic Belt < 2 Ma; 2) Plate boundary reorganization and change in relative velocity between the Explorer and North America Plate at about 5 Ma which was subsequently followed by westward migration of the volcanic arc centres into a NW trending Garibaldi Volcanic Belt (Parrish, 1982).

In the current study, farther west of the area mapped by Riddell (1990a, 1990b, 1992) , we undertook structural geology and engineering geological mapping in the central part of the Mount Currie structure (Currie NE3 peak: Fig. 4.2) and western part of the Mount Currie ridge structure (Currie NW1 peak and Currie W1 peak: Fig. 4.3). The NE-3 peak exhibits both reverse and strike slip fault structures (Figs. 4.4, 4.5); of note, the main
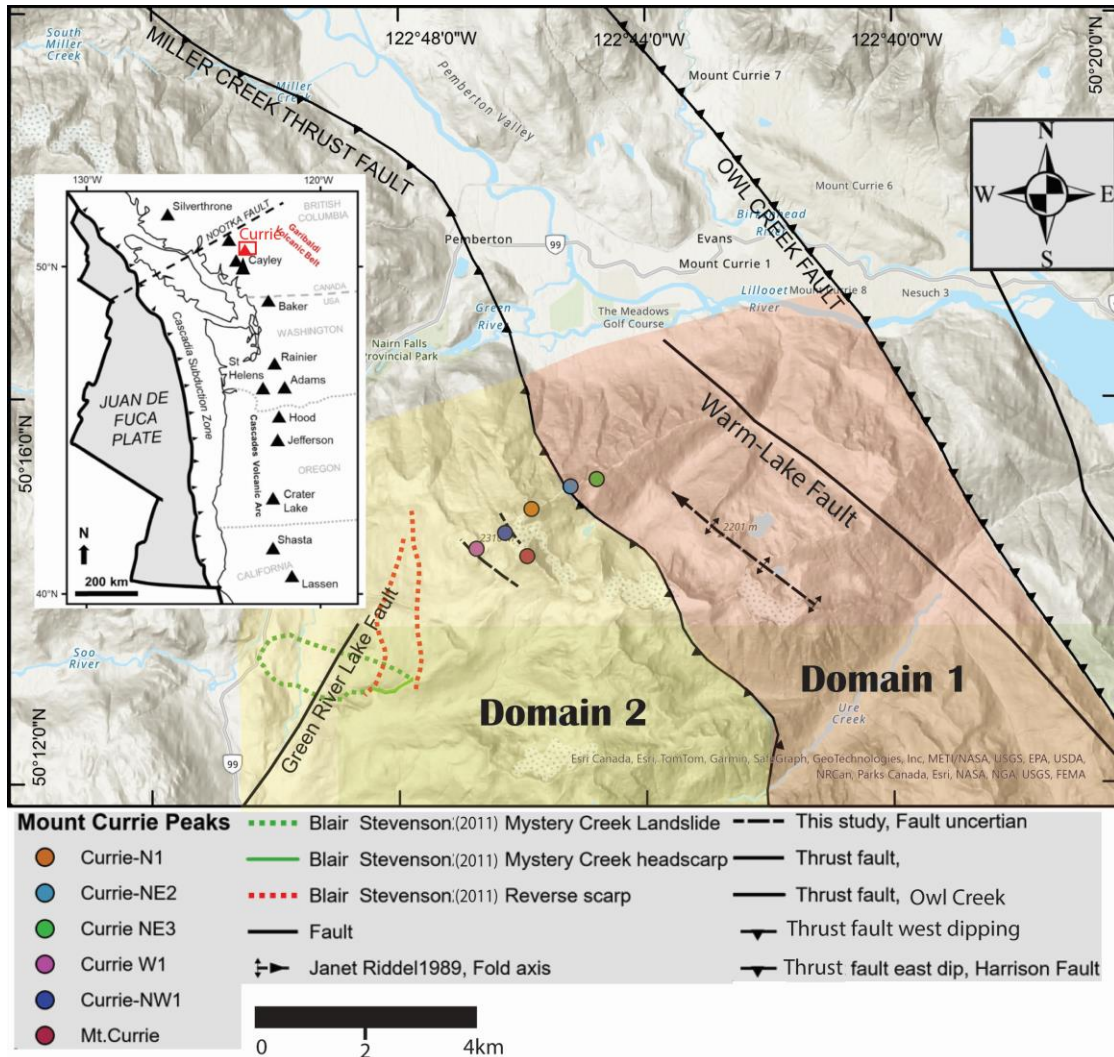
Figure 4.1. **Structural map showing location of study area and major tectonic structures. The inset map shows the relative location of Mount Currie to the Garibaldi Volcanic Belt and western North America.**

Mount Currie scarp coincides with NE3 peak and strikes ENE-WSW exhibits lateral offset of basement units (Fig.4.4). The other two peaks show intense tilting (folding) of the quartz diorite rock and foliations (Fig. 4.6). Additionally, a new N-S fault was mapped based on ubiquitous fault breccia zones (Fig. 4.7) east of Currie NW1 ridge and west of Miller Creek Thrust fault (Fig.4.1).
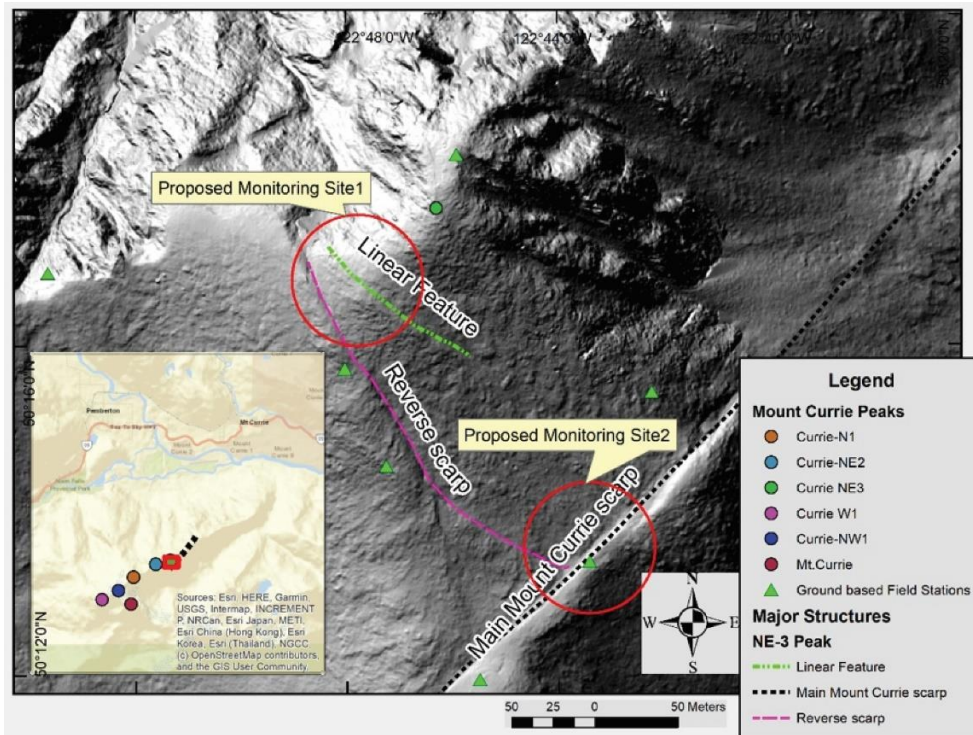
Figure 4.2. **Detailed map of structures and linear features at Currie NE3 peak. Overlain on shaded relief map constructed from 50 cm LiDAR DEM. Notice location of the reverse scarp relative to the main Mt. Currie normal scarp.**
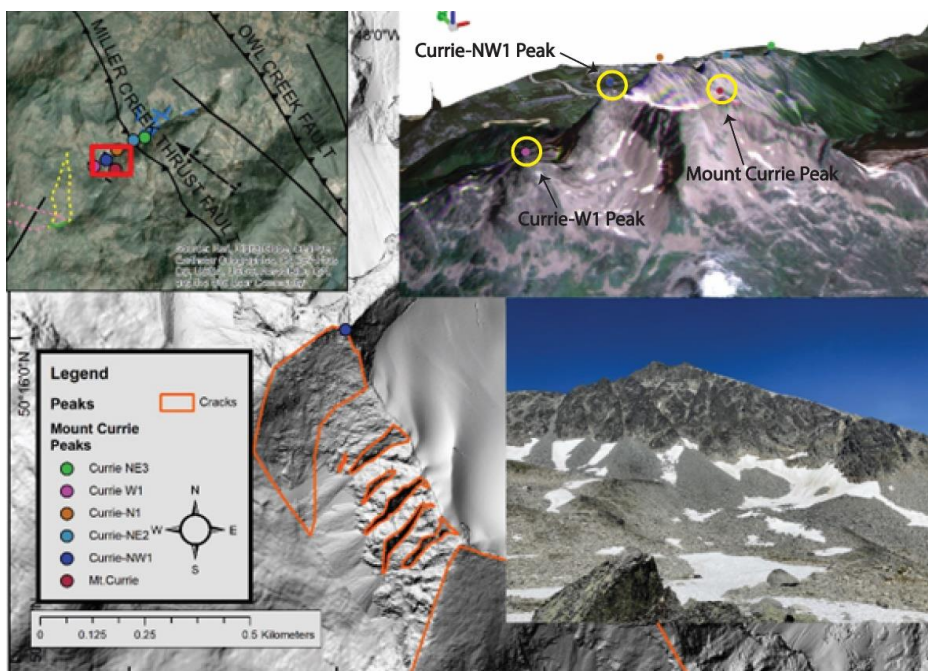
Figure 4.3. Location of Currie NW1 ridge field survey stations overlain on a 3D topographic view constructed from 50 cm LiDAR DEM. Note the arrangement of south facing ENE-WSW trending cracks along the WSW side of the Currie NW 1 ridge. Orange lines indicate a series of parallel fractures formed perpendicular to the Miller Creek thrust fault.
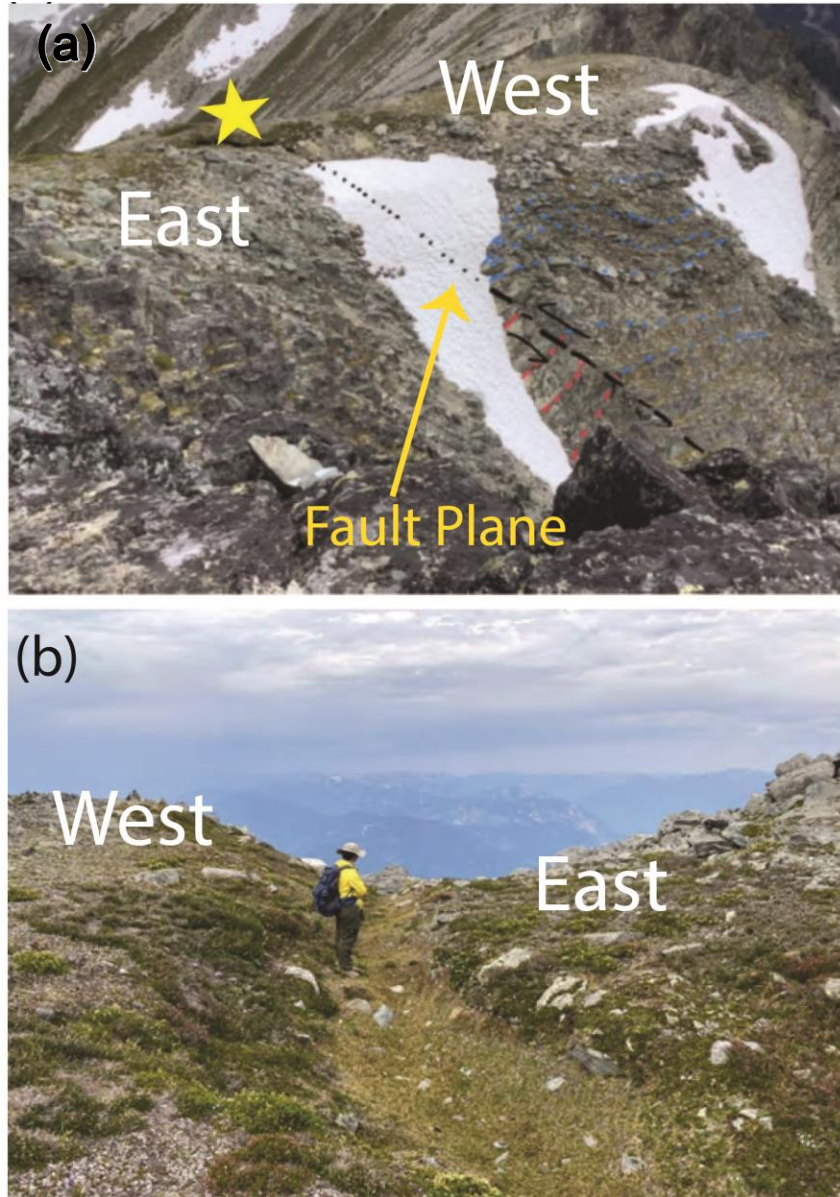
Figure 4.4. (a).Offset of the reverse NW-SE trending scarp - the yellow star indicates the location of the person in B. (b). Top view of the NW-SE trending reverse scarp in Domain 1.

Figure 4.5. Offset of reverse NW-SE trending scarp. Note highly weathered basement rock (dark) offset by metamorphosed basement rock (white).
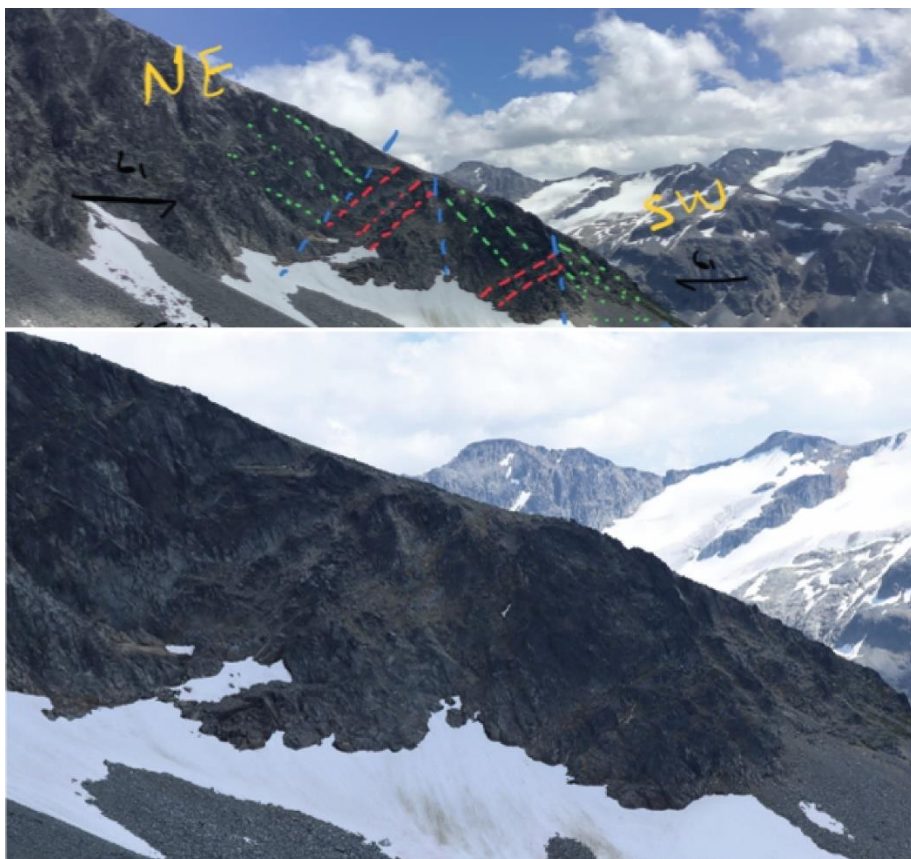
Figure 4.6. An outcrop west of Currie NW1 ridge with broad upright open minor folds with near-horizontal fold axes parallel to the trend of the Currie W1 ridge and Currie NW1 ridge. Dashed lines show tilting of bedrock due to folding and compression. Note, this outcrop is located on the footwall of the Miller Creek thrust fault.

Figure 4.6. An outcrop east of Currie NW1 ridge showing possible fault breccia and/or granite intrusion breccia.

4.4. Methodology

In this study we took a multi-disciplinary approach to study the rock slope stability for Mount Currie (Fig. 4.8). We used structural geology techniques to interpret the exist geological maps including regional faults and took field work approach to validate the existing mapped faults. Additionally, extracted linear features and zones of weakness from Lidar Digital Elevation Model. The extracted linear features were validated on the ground during the field work and from high resolution ortho-photogrammetry generated using historical aerial photographs and high-resolution satellite imagery to ensure that the extracted linear features aligned with the bedrock rather than loose sediments.

Subsequently, we wrote a python code to convert regional faults and Lidar based lineaments into 3D planes. Afterwards, the 3D planes including the extracted linear features and regional faults were imported into RocSlope3 software to perform regional scale 3D Geotechnical kinematic analysis then computed factor of safety and wedge stability analysis using Limit Equilibrium Analysis (LEA). When selecting a suitable tool to model the factor of safety for slopes, it is crucial to consider the slope's geology, especially its lithology and structure. This helps in understanding the potential failure mechanisms. RocSlope3 is a 3D limit equilibrium slope stability software designed to evaluate the safety factor for block failures in rock slopes influenced by structural features. These blocks are formed by the intersection of planar joint surfaces, which are defined by their orientation, location, size, and assigned shear strength. A crucial step in any limit equilibrium analysis is determining or estimating the shear strength parameters such as cohesion and friction angle for the surface expected to experience sliding. At Mount Currie no drilling data or laboratory tests were available therefore, in this study two different sensitivity analysis were performed to obtain the reasonable shear strength parameters including cohesion and friction angle. Additionally, we collected discontinuity measurements in the field and then imported into Dips software for outcrop scale 3D Geotechnical kinematic analysis.

In collaboration with TRE ALTAMIRA, we processed time-series Sentinel 1 Radar imagery for both ascending and descending from 2018 to 2020 along satellite Line of Sight using persistent scatter technology via SqueeSAR software (TRE ALTAMIRA, 2018). Subsequently, 2D horizontal east and vertical displacement computed from

combined ascending and descending orbits (Ferretti et al., 2007, 2015; TRE ALTAMIRA, 2018).

Finally, the results of the LEA were compared with the three years InSAR deformation monitoring to constrain the geotechnical and structural geology assessment.
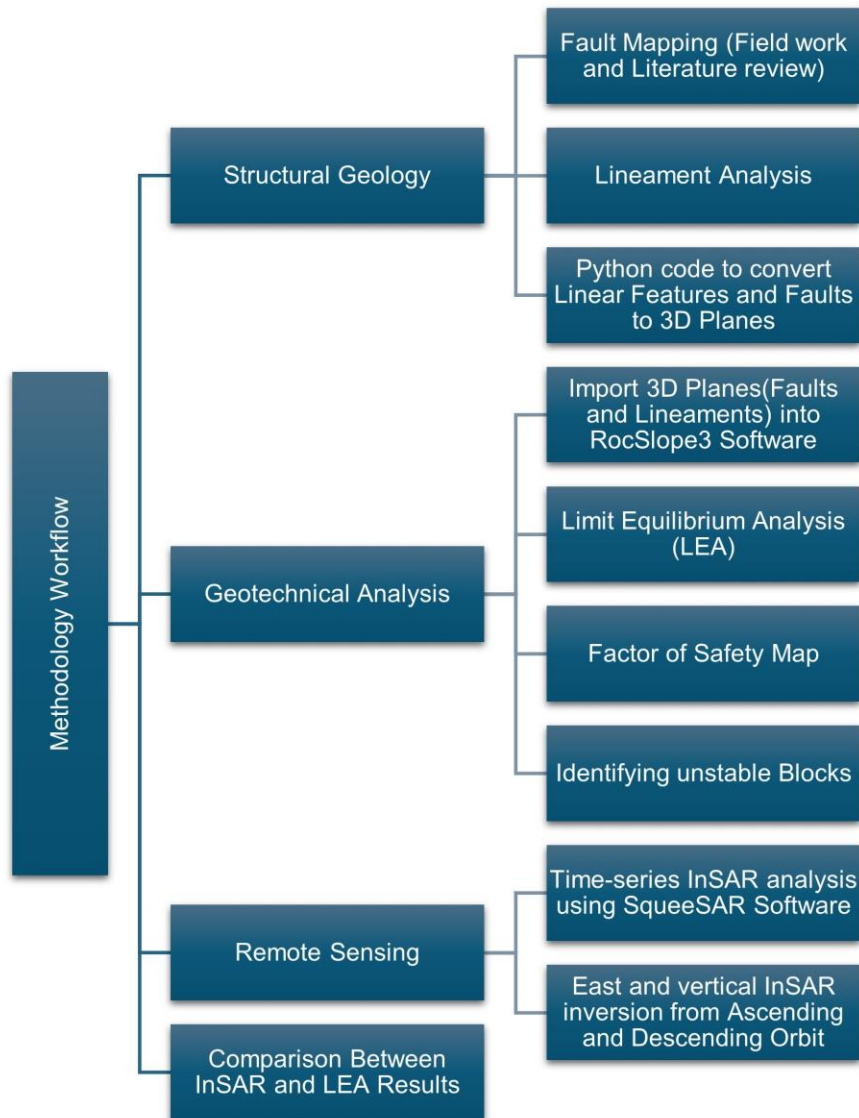
Figure 4.7.   Flow chart explain the working methodology materials and steps.

4.5. Data Description

4.5.1. Structural Geology Description

In this research, we examined regional structural geology kinematics through a traditional field study conducted over two phases during the summer of 2020. The initial phase started in mid-July 2020 employing both aerial and terrestrial photogrammetry to survey the Mount Currie ridge from the east to the west. The subsequent, more extensive phase of the survey took place from July 31 to August 9, 2020, focusing on terrestrial mapping of structural geology. This mapping effort involved documenting significant geological structures like potential faults and folds, verifying previously identified faults in the field, and examining joint sets to gain insights into the overarching regional tectonics and notable structural features. These field observations were integrated with existing regional geological maps (Parrish, 1982; Riddell, 1990a, 1990b, 1992; Monger and Journeay, 1994; Bustin et al., 2013) to delineate distinct structural domains crucial for a deeper understanding of the structural geology and tectonics of the area. Data was collected mainly at sites Currie NE-3, Currie NW-1, and Currie W-1 (Fig. 4.1). The dominant structures on the Currie NE3 ridge include a main ENE-WSW Mount Currie normal scarp and two NW-SE trending linear features (Figs. 4.2 ,4.4 and 4.5). Of the two NW-SE trending structures, one exhibits a ubiquitous reverse scarp with more than 1-meter offset at the northernmost edge of the Mount Currie ridge (Fig. 4.4). The NW-SE striking fault is spatially perpendicular to the ENE-WSW main Mount Currie scarp (Figs. 4.2 and 4.3). Additionally, the ENE-WSW main Mount Currie scarp offsets highly weathered quartz diorite rocks and metamorphosed basement rocks (Fig. 4.3). Currie W1 and NW1 ridges together consist of an approximately 700-meter-long NW-SE structure which is approximately 1 km wide. It starts north of Mount Currie peak and ends at the northern face of the E-W Mount Currie structure (Fig. 4.3).

Older structures such as the east-dipping Miller Creek Thrust located west of the Currie NW1 ridge were identified (Fig. 4.1). Also, a fault breccia and/or granite intrusion breccia zone trending NNW-SSE parallel to the trend of the ridge was found at the eastern edge of the Currie NW1 ridge (Fig. 4.7). Additionally, this ridge consists of broad upright open minor folds with near-horizontal fold axes approximately parallel to the trend of the fault breccia and the trend of the Currie W1 ridge and Currie NW1 ridge (Fig. 4.6). The west-

southwest side of the ridge includes east-northeast trending cracks perpendicular to the ridge which also serves as drainage system (Fig. 4.2). Outcrops of well-aligned primary structures such as mantle xenolith were found in between Currie W1 ridge and Currie NW1 ridge. The xenolith was all oriented NW-SE and cut by ENE-WSW trending joints (Fig. 4.9). For simplicity and using regional fault structures such as Miller Creek, Warm Lake, and Owl Creek faults, we divide the study area into two distinct domains; Domain 1 is the NE-3 peak, and Domain 2 includes W-1 and NW1 peaks (Fig. 4.1).
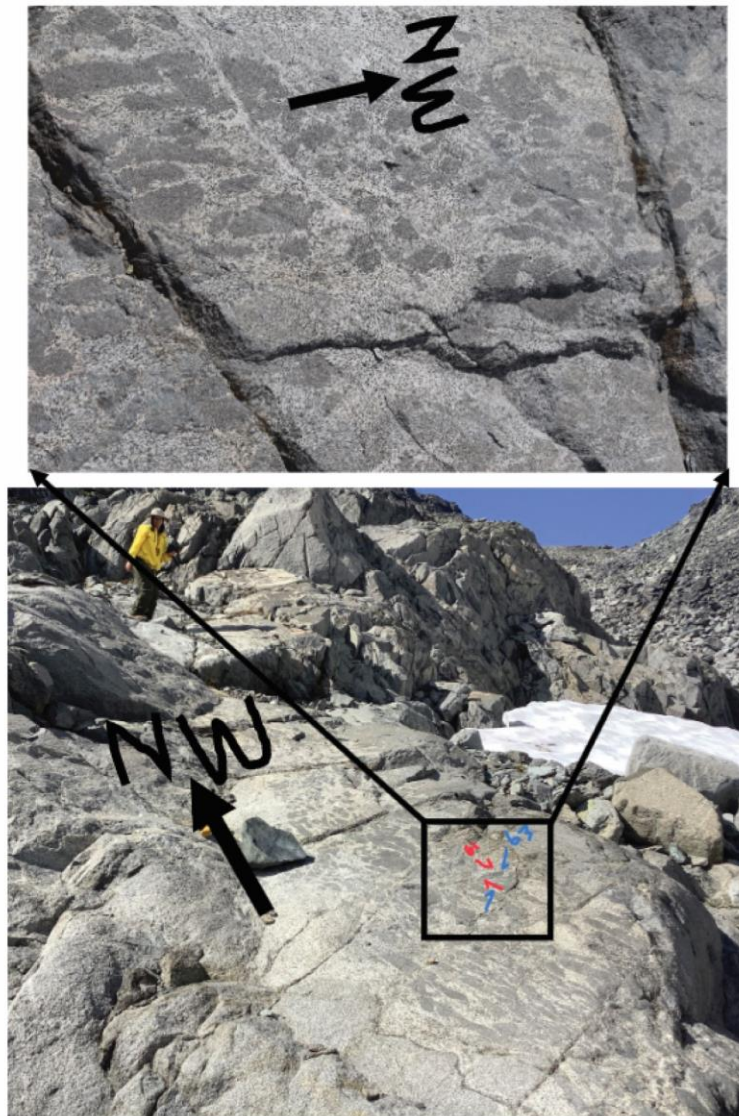
Figure 4.8. **Outcrops of xenolith within Granitic Basement rocks at sites on Currie W1 ridge and Currie NW1 ridge. Note the alignment of xenoliths as primary structure-oriented NNW-SSE and cut by secondary structures such as ENE-WSW trending joints. The blue and red arrows indicate kinematic stress indicators for both mantle xenolith and discontinuity structures.**

4.5.2. Engineering Geological Study

Discontinuity data was collected in the field aimed at kinematic slope analysis. Domain 1 was surveyed at 8 field stations (Appendix C2, Tables S4.1 and S4.2); more than 70 discontinuity measurements were collected at each site. Domain 2 was surveyed at 12 field stations (Appendix C2, Tables S4.3 and S4.4) and at each station, at least 9 discontinuity measurements were taken (Fig. 4.3). Rock description, and structural measurements such as folds and faults recorded were possible. A detailed description for the discontinuities collected in the field including rock strength, dip, dip direction, persistence, aperture, termination, nature of filling, joint roughness, and joint spacing. The outcrops in this domain show wide to moderate discontinuity spacing ranging between 20 cm to 2 m. The persistence of discontinuities is dominated by very high persistence more than 20 meters in length. The discontinuity aperture ranges between 1 cm to 10 cm with either lack of filling material or filled with clay material matrix.

The DIPS software (Rocscience Inc., 2024) was used to investigate 3D kinematic feasibility slope analysis along selected slope profiles (Fig. 4.10) for various discontinuity failure mechanisms such as toppling, planar and wedge sliding (Plates 1 to 6; Tables 1 and 2). It is worth mentioning that considering the limited number of measured field-based outcrop discontinuity data, results of 3D kinematic feasibility slope analysis from the field-based data are considered preliminary.

To complement the field data, we used an existing LiDAR digital elevation model along with both aerial and ground photographs to generate a 3D point cloud model (Agisoft LLC, 2022). This approach allowed for a more effective detection of discontinuities, acting as a supplementary data set for the collected field-based discontinuity dataset. The insights obtained from this method will be crucial for the creation of a structurally controlled 3D limit equilibrium analysis aimed at evaluating the stability of potential slopes located on the northern face of Mount Currie. For this purpose, the RocSlope3 software by Rocscience (Rocscience Inc., 2024) was employed to carry out a more sophisticated 3D kinematic analysis to estimate the volume of potentially unstable blocks. The input data for Rocslope software includes 3D discontinuity planes. For this study, we extracted 2D regional linear features from the LiDAR digital elevation model which were then converted to 3D dimensional planes using AkhDefo software fitPlane

function. AkhDefo software is an open source geospatial and remote sensing python package freely available on GitHub (Muhammad et al., 2022) (Fig. 4.3).
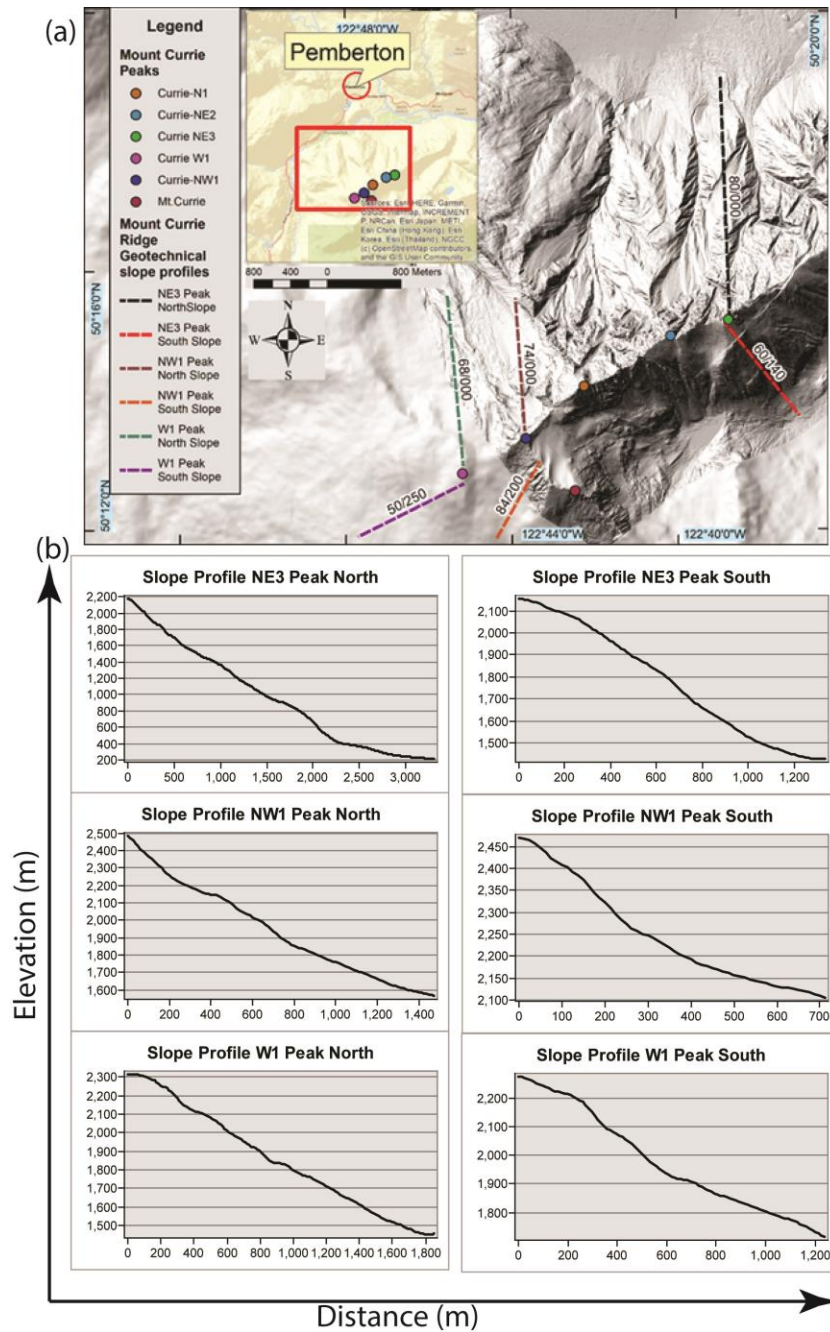
Figure 4.9. **(a) A shaded relief map showing location of slope profiles at each studied peak within Mount Currie used for kinematic analysis. (b) Slope profiles for selected peaks. Note, for kinematic analysis the steepest slope angle value along each profile segment selected for the analysis that being said the slope angle chosen does not represent the overall slope angle for the above elevation profiles.**

3D limit equilibrium analysis (LEA) was performed from the LiDAR extracted linear features using the RocSlope3 software. Limit equilibrium analysis is routinely used in combination with kinematic slope analysis as a preliminary investigation of slope instability potential. Its application is particularly useful when considering simple failure mechanisms such as rotational, transitional, and toppling instability with little or no complex internal deformation (i.e., rigid block assumption). In this study we evaluate and integrate the kinematic analysis of discontinuities derived from lineaments at different scales such as regional faults based on existing geologic maps, lineaments extracted from high resolution LiDAR DEMs. Using a Python application developed in this study and high-resolution elevation LiDAR data allowed us to reconstruct the 3D plane geometry (Fig. 4.11). These datasets were imported into the RocSlope3 software (Rocscience Inc., 2024) to produce rigid block geometry based on the intersection of the 3D planes and allow estimation of the factor of safety for the generated blocks (Figs. 4.12 a, b and 4.13).

4.5.3. Satellite Radar Remote sensing

The radar data collected over the specified area includes images with a resolution of 20 m by 5 m. These images are captured by the Sentinel-1 satellite, which operates in both ascending and descending orbits. The Interferometric Synthetic Aperture Radar (InSAR) technology utilized here measures the displacement of the surface along the satellite line-of-sight (LOS). Vertical and east-west displacement and velocity were derived using the 2D SqueeSAR technique by integrating data from both ascending and descending orbits. This analysis utilized the temporally overlapping period from May 2018 to September 2020 and the spatially overlapping areas of the LOS measurements, which were arranged on a 30 x 30 m grid. This approach enhances the accuracy of the analysis, allowing for the precise measurement of true vertical and east-west horizontal slope movements down to millimeter precision. Details of SqueeSAR can be found in Ferretti et al. (2011, 2015).
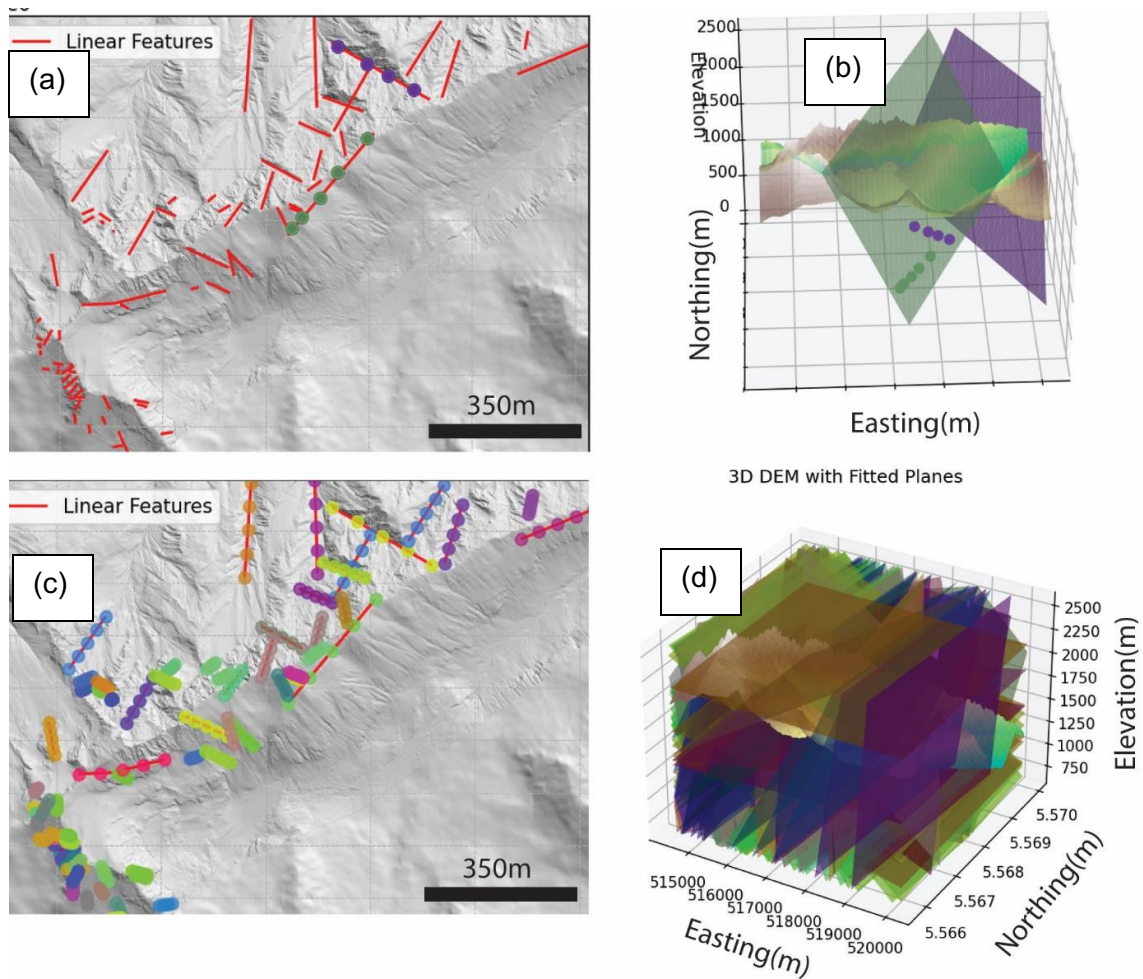
Figure 4.10. 3D planes generated from slope lineaments using the AkhDefo fit plane function (a) Manually digitized visually extracted lineament overlayed on LiDAR DEM to construct 3D plane. (b) Manually fitted 3D plane along the extracted LiDAR based lineament. (c) Automatically digitized visually extracted lineament overlayed on LiDAR DEM to construct 3D plane. (d) Automatically fitted 3D plane along the extracted LiDAR based lineament.

Table 4.1. Discontinuity sets showing of measurements taken in the field for each Discontinuity set. Note low angle dipping discontinuities present in mountain peaks likely representing exfoliating joints.

Discontinuity Sets	Studied Mount Currie Peaks Based on Field Measurements								
	NE-3 Peak			NW-1 Peak			W-1 Peak		
	Azimuth degrees	Dip degrees	Quantity	Azimuth degrees	Dip degrees	Quantity	Azimuth degrees	Dip degrees	Quantity
D1	287	18	10	261	89	15	239	85	13
D2	99	26	22	183	83	6	92	30	5
D3	22	83	6	181	48	13	25	52	12
D4	292	70	12	32	8	6	287	76	7
D5	327	83	10	274	59	5	320	19	4
D6	91	75	3	323	82	12	205	73	6
D7	207	38	7	232	80	3	161	63	2
Total			70	Total		60	Total		49

Low dipping	Moderate dipping	Steeply dipping
Dip angle < 20 degree	20 degree <Dip angle <60 degree	Dip angle >45 degree

Table 4.2. Potential failure mechanism based on interpreted discontinuity sets at each studied peak on Mount Currie relative to the steepness and orientation of the selected slopes on north and south face.

Structural Domain	Studied Mount Currie Peaks	Slop Direction degrees	Slope Angle degrees	Failure Mechanism			
				Planar Sliding	Wedge Sliding	Direct Toppling	Flexural Toppling
Domain 1	NE-3 Peak	000	80	D2, D3	D4, D6	D2, D3	D2, D3, D6
	NE-3 Peak	140	60	D4	D2, D5, D7	D4	D2, D5, D6
Domain 2	NW-1 Peak	000	74	No significant failure	D4	No significant failure	D4, D3
	NW-1 Peak	200	84	D2, D3, D4	D6 (very significant)	D2, D3, D4	No Significant failure
	W-1 Peak	000	68	D3, D6	D4 (Significant)	D3, D6	D2, D3
	W-1 Peak		50/250	No Significant failure	No Significant failure	No significant failure	D1
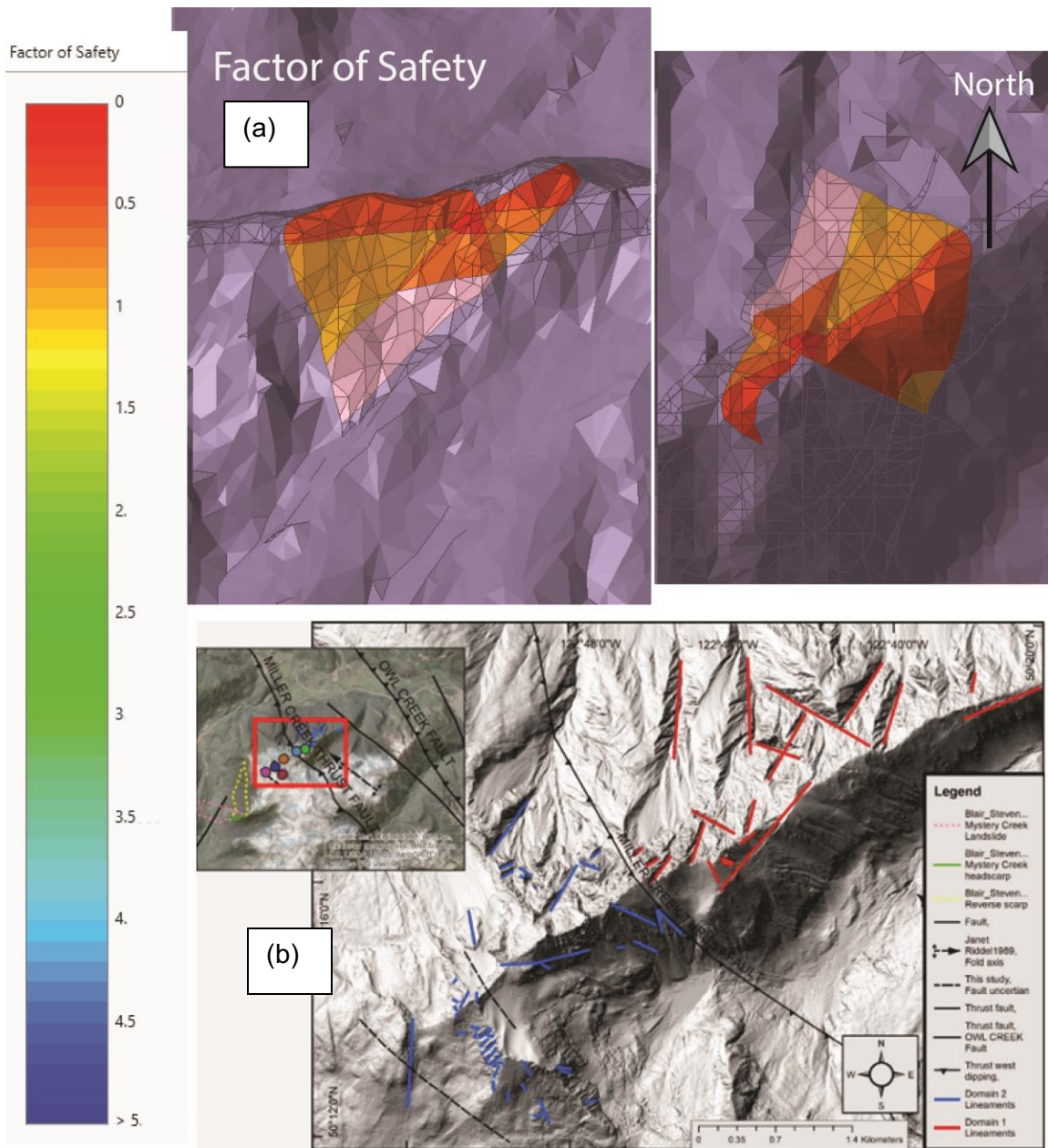
Figure 4.11. **(a) Limit Equilibrium Factor of safety slope analysis generated based on the kinematics of regional faults and LiDAR based lineaments (b) Shaded relief map showing manually mapped Lineaments within Domain 1 and Domain 2 from LiDAR digital elevation model.**
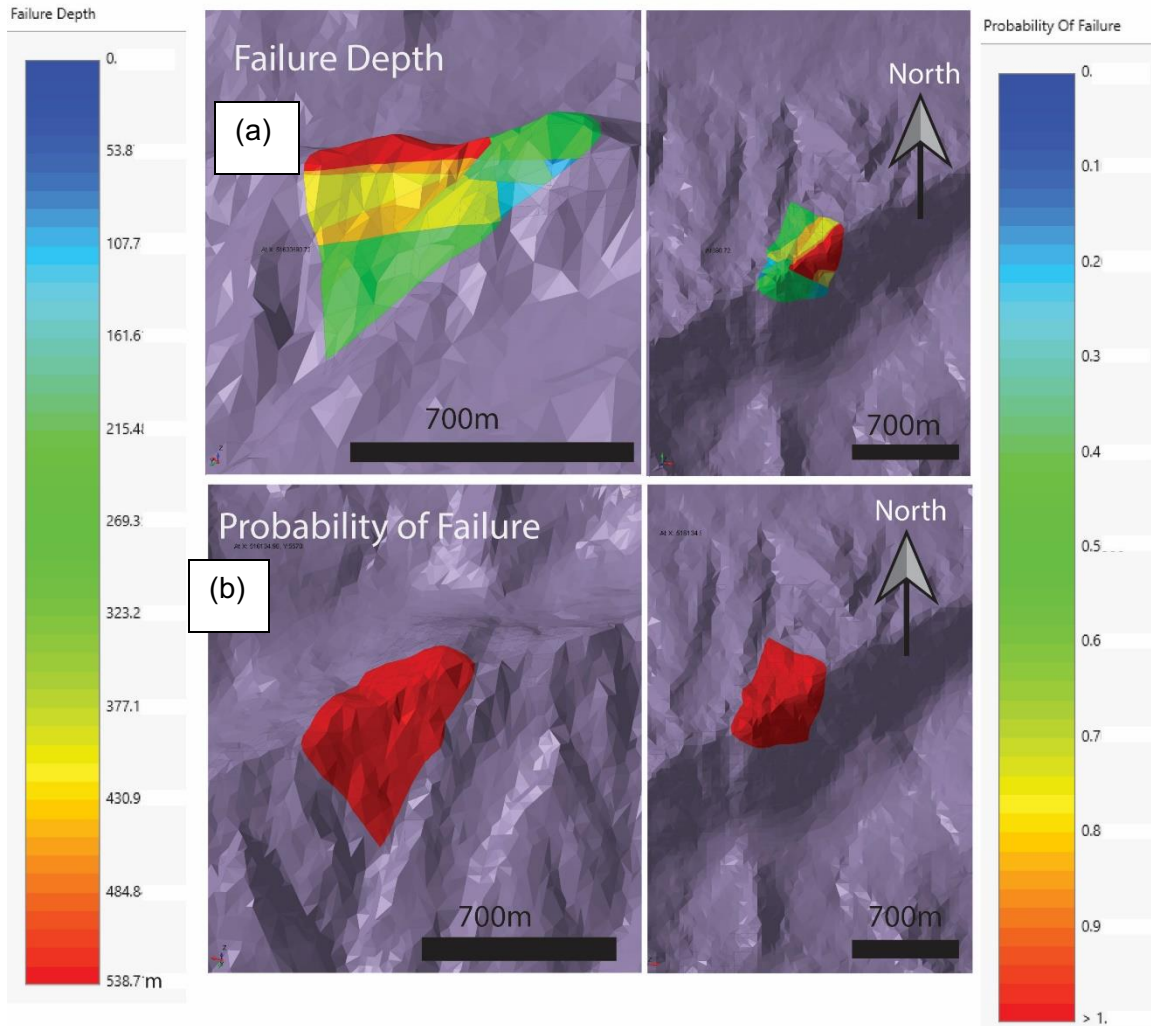
Figure 4.12. Kinematic-Limit equilibrium slope analysis of regional faults and LiDAR bases lineaments s (a) maximum depth of failure for unstable blocks based on Factor of Safety (b) Probability of failure for unstable blocks based on Factor of Safety.

4.6. Results

Our findings suggest that the Mount Currie scarp, which extends from east-northeast to west-southwest, likely originated from extensional faulting driven by compression at the mountain's crest. This faulting is influenced more by localized stress patterns within the mountain itself rather than direct seismic activity. These local stresses are mainly controlled by the nearby Owl Creek and Miller Creek faults, both of which are significant thrust faults surrounding the Mount Currie complex, as well as the effects of crustal rebound due to glacial melting. The aforementioned constraints have important

implications on mountain slope stability, particularly as it dictates the orientation and intensity of the fracture pattern on the bedrock and mountain slope geometry.

The stability of slopes consisting of bedrock such as Mount Currie is often influenced by the geological structures within the bedrock (BGC, 2018). In these instances, the stability of a slope kinematically depends on how the geological structures are oriented in relation to the slope's surface. Kinematic slope analysis focuses on the modes of potential failure, identifying which mechanisms are possible and which are not. When considering the stability of slopes, kinematic analysis is typically used to determine if rock blocks or masses can move along geological structures, potentially leading to their dislodgement from the slope's face. The aim of conducting kinematic slope analysis is to predict whether a block can move and identify possible failure mechanism at certain slope orientation and slope steepness. In this study we performed preliminary kinematic slope analysis for field-based discontinuity measurements at selected field sites (Fig. 4.1). The collected discontinuity field data was plotted in the software Dips (Rocscience Inc., 2024). Seven discontinuity sets identified based on the orientation of collected discontinuities (Table 4.1). Additionally, the friction angle for the kinematic slope analysis was derived from the BGC (2018) report. This previous study determined that the friction angles along all discontinuities were 30°, based on the planar/undulating and rough conditions of the discontinuity surfaces observed in the field. We selected two slope profiles on the northern and southern face at each studied mountain peak (Fig. 4.11). 3D geotechnical kinematic tests were performed along the steepest slope angle value for each selected profile segment. Hence, the slope angle chosen does not represent the overall slope angle for the above elevation profiles. Consequently, estimated the potential mechanisms of failure with the identified discontinuity sets.

The results of the outcrop scale 3D Geotechnical kinematic analysis at NE3 peak, on the northern slope face indicate the likelihood of failing bedrock, under toppling and possibly wedge sliding, whereas on the southern face it is mainly under flexural toppling (Table 4.2; Appendix C1 plates 1 and 2). At NW-1 peak, on the northern face, fails under flexural toppling while at southern face dominant failure mechanism includes mainly wedge sliding, direct toppling, and planar sliding (Table 4.2; Appendix C1 plates 3 and 4). At W-1 peak, on the northern slope face, possible failure mechanism includes toppling, planar sliding and wedge sliding, whereas, on the southern slope face flexural toppling seems to be the only failure mechanism (Table 4.2; Appendix C1 plates 5 and

6). The aforementioned 3D kinematic analysis results for discontinuities measured in the field align with previous results of 3D geotechnical kinematic analysis performed by BGC Engineering for Squamish Lillooet Regional District (SLRD) during 2018 (BGC, 2018).

The regional scale 3D Geotechnical Kinematic Analysis using Rocslope3 software identified over 60 valid blocks (wedges) at the NE3 peak, including one critical active key block (Fig. 4.17). A key block is of particular importance as its collapse could lead to the failure of neighboring blocks. The time-series InSAR monitoring from 2018 to 2020 shows 1.5 cm displacement downward (subsidence) to the west at NE3 peak and aligns with identified active key block based on the LEA.

4.7. Discussion

4.7.1. Structural Geology Synthesis and Regional Tectonic Setting

Riddle (1992) undertook a comprehensive structural geology and stratigraphic investigation of the Tenquille/Lillooet Lake area including the eastern most part of E-W Mount Currie ridge structure. He divided the area into four zones in which zone 1 coincides with the eastern part of the Mount Currie ridge structure. The structural fabric in Mount Currie is controlled by four main structures: 1) At the eastern end by the east-dipping Owl Creek Fault and east-dipping Warm Lake fault (Riddle, 1990a, 1990b); 2) At the centre by the west-dipping Miller Creek Thrust fault; 3) At the western side by intrusive rocks of the Pemberton Diorite Complex (Riddell, 1990a, 1990b) and the NE trending Holocene Green River Lake normal fault (Blais-Stevens, 2011); and finally 4) The ENE-WSW trending Mount Currie normal scarp (Eisbacher, 1983; Bovis and Evans, 1996; Bustin et al., 2013). Riddle (1990a) observed folded structures in the vicinity of the Warm-Lake fault, although he acknowledged this part of the fault had not been mapped in detail (Fig. 4.1).

 In the current study, farther west of the area mapped by Riddell (1990a, 1990b, 1992), we undertook structural geology and engineering geological mapping in the central part of Mount Currie structure Currie NE3 peak and western part of the Mount Currie ridge structure, Currie NW1 peak and Currie W1 peak.

Domain 1

This domain coincides with the footwall of the west dipping Miller Creek thrust fault. It includes NW-SE trending reverse scarps that show more than 1 m of vertical displacement (Fig. 4.2) and the ENE-WSW main Mount Currie normal fault scarp. The main Currie fault scarp in this domain shows a vertical displacement of a few meters increasing in magnitude further to the eastern side of the structure. Slickenlines were observed in the field for the main Currie scarp, but due to the complexity of the structure, it was difficult to define their origin. The complexities include heavy vegetation cover in the region, remnants and impact of multiple glacial-deglaciation periods, and very high rates of uplift in the region during the last 5 Ma (Parrish, 1982). Thus, it is difficult to constrain whether the scarp correlates to deep-seated gravitational collapse or to crustal fault activity. However, the geometry, structural kinematic compatibility and spatial location of the Mount Currie scarp is in accordance with mountain crest extension because of thickening on both sides of the mountain and thinning at the crest. Below we suggest a geologic model that agrees with the existing well-documented regional faults, glaciation/deglaciation effects and modern regional stress vectors.

Our data and field observations favour a structural model that kinematically supports both gravitational collapse and the modern regional horizontal compressive stress (Fig. 4.15). The basis of the structural model for the origin of the Mount Currie scarp stems from the fact that it is a very wide structure (> 15 km wide), trending NW-SE and bounded by major thrust faults (e.g., east-dipping Owl Creek and Warm Lake thrust faults to the east and west-dipping Miller Creek thrust fault to the west) (Fig. 4.1). These compressive structures may have facilitated thickening of the crustal rocks on both sides of the mountain and thinning and uplifting of the crustal rocks at the centre between the eastern and western thrust fault systems. It is well documented that the Coast Mountains, including Mount Currie, experienced more than 3 km of uplift during the last 5 Ma (Parrish, 1982). This uplift is most likely accommodated by the regional NW-SE trending thrust faults and possibly by crustal rebound from periods of glaciation and deglaciation. The forces are sufficient to cause mountain crest extension in Mount Currie and formation of normal dip-slip fault scarps such as the Mount Currie main scarp. Thus, the ENE-WSW main Mount Currie scarp is most likely formed by compression related mountain crest extensional faulting. This fault is not directly formed due to the seismic principal stress vectors (Thompson et al., 1997) but rather is controlled by the local

stress vectors within the mountain complex itself. The local stress vectors are mainly controlled by the bounding thrust faults on both sides of the Mount Currie complex and the crustal rebound impact due to glacial melting on the mountain.

Domain 2

This domain lies at the hanging wall of the Miller Creek thrust fault. It includes both Currie W-1 and Currie NW-1 peaks. The main ENE-WSW Mount Currie scarp appears to either terminate or continue with a change in strike into a more NE-SW direction along the Green River Lake Holocene normal fault (Fig. 4.1). Field observations and structural geology/kinematic slope analysis including the orientations of discontinuities, fractures, and well mapped faults (discussed in more detail below) suggest the ENE-WSW Mount Currie scarp terminates at the western edge of the Mount Currie (i.e., the scarp appears within Domain 1 only) and deformed independent of the Holocene Green River Lake normal fault. The ENE-WSW trending cracks (Fig. 4.3) on the west side of the NW-1 peak, possibly indicate the presence of exfoliation joint structures that resulted from stress relief due to glacial unloading. The current glacier is still present adjacent to the ENE-WSW cracks (Fig. 4.3).

Unlike Domain 1 where compressional structures are overprinted by ubiquitous normal scarp displacement, Domain 2 lacks evidence of normal (extensional) displacement of the Mount Currie scarp; hence, it may indicate termination of the scarp at Domain 2. Additionally, the presence of upright open minor folds suggests Domain 2 is located at the hanging wall of the Miller Creek Thrust fault. The fault breccia zone within the basement rocks, trending NNW-SSE (Fig. 4.7) is kinematically compatible with the hanging wall collapse and/or growth of the west-dipping Miller Creek Thrust fault as the fault propagates eastward.

4.7.2. Lineament Characterization

Lineaments are considered an important feature that may reflect deeper structures and zones of weakness such as faults and discontinuities (Abdullah et al., 2010; Muhammad et al., 2012; Alhirmizy, 2015; Akram et al., 2019; Shebl and Csámer, 2021; Hajaj et al., 2022). There are various methods to identify lineaments including field mapping, and aerial imagery, satellite images, and high-resolution digital elevation models based on

photogrammetry and ground and aerial Light Detection and Ranging (LiDAR) mapping (Stead et al., 2019).

We sorted the outcrop discontinuities based on the dip angle for both Domains 1 and 2. In Domain 1 (Fig. 4.14b), low to moderate dipping joints (dip <50 deg.) show two major trends NNW-SSE and NNE-SSW which in Domain 1 is approximately parallel to sub-parallel to the slope of the Mount Currie ridge. The high angle dipping joints dominantly trend N-S, NE-SW, and ESE-WNW. The field cross-cutting relationships show that NNW-SSE low to moderate dipping joints are cut by ESE-WNW high angle dipping joints (Table 4.1). Additionally, the major trends of shallow to moderately dipping joints within Domain 1 are parallel to sub-parallel to trends of major thrust faults (Figs. 4.1 and 4.14). In Domain 2, low to moderate dipping joints (dip <50 deg) show variable trends although no major dominant trend was observed. By contrast, steeply dipping joints, dominantly trend sub-parallel, oblique, and orthogonal to trends of major thrust faults in the region.

A 50 cm spatial resolution LiDAR DEM and aerial photographs were used to visually extract more than 60 distinctive linear features across the East-West Mount Currie structure. We took care not to include linear features that coincided with loose deposits at the piedmonts on both sides of the E-W Mount Currie ridge. Drainage patterns in alluvial deposits at the base of the mountain can also produce linear features which are less likely to resemble deeper structures; nevertheless, we also analyzed the trend of the drainage patterns (Fig. 4.15). More specifically, we quantified the significance of stream order and its relation to the well-mapped lineaments within the bedrock (Fig. 4.15). The directional analysis of trends of the drainage pattern indicates that only streams with magnitude greater than 5 correlate well with the geometry of the outcrop joints and visually extracted lineaments; as such they more likely correspond to zones of major structural weakness (Fig. 4.15).

Streams of orders 1 to 5 appear to have similar trends with shallow to moderate dipping outcrop-scale discontinuities and are associated with sheet joint structures commonly formed in granitic rocks that may pre-date or post-date tectonic events (Nichols, 1980; Hencher et al., 2011). Sheeting joints geometrically defined as extensive fractures usually form parallel or sub-parallel to natural slopes (Hencher et al., 2011). Additionally,

most sheeting joints are geologically young, and some have been observed to develop rapidly as tensile fractures in response to unloading (Nichols, 1980).
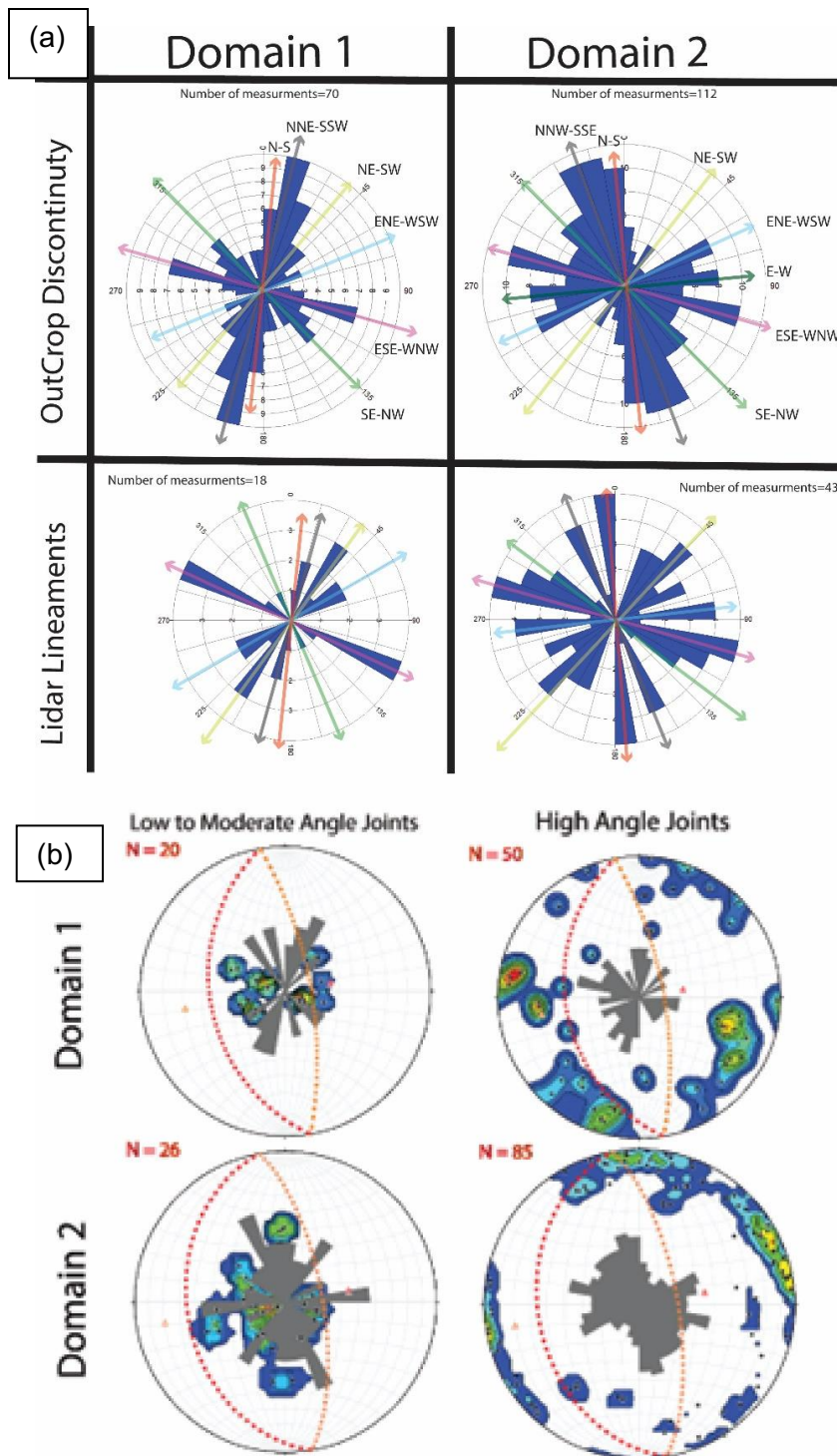
Figure 4.13. **(a) Rose diagrams showing mean orientation of outcrop scale discontinuities and visually mapped LiDAR lineaments. (b) Stereograph contour of poles of shallow dip angle joints and rose diagram showing trends of shallow dip angle joints.**
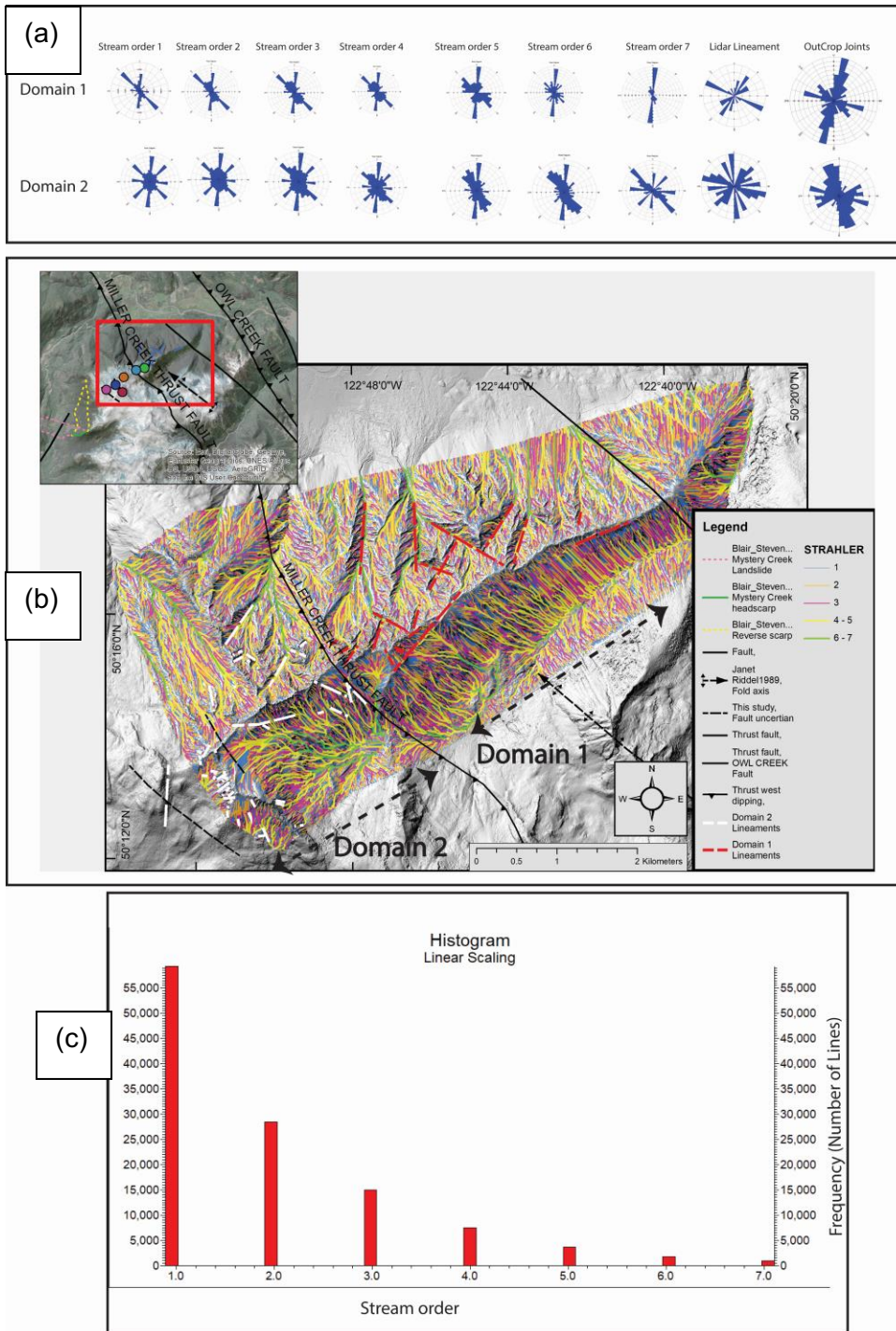
Figure 4.14. **(a) Trends of individual stream order relative to visually extracted LiDAR lineaments and outcrop measured joints. (b) Spatial distribution of extracted drainage stream magnitude relative to spatial distribution of mapped lineaments. Note, stream orders 6 and 7 correspond to the visually extracted LiDAR lineaments. (c) Histogram showing number of extracted drainages per stream order magnitude.**
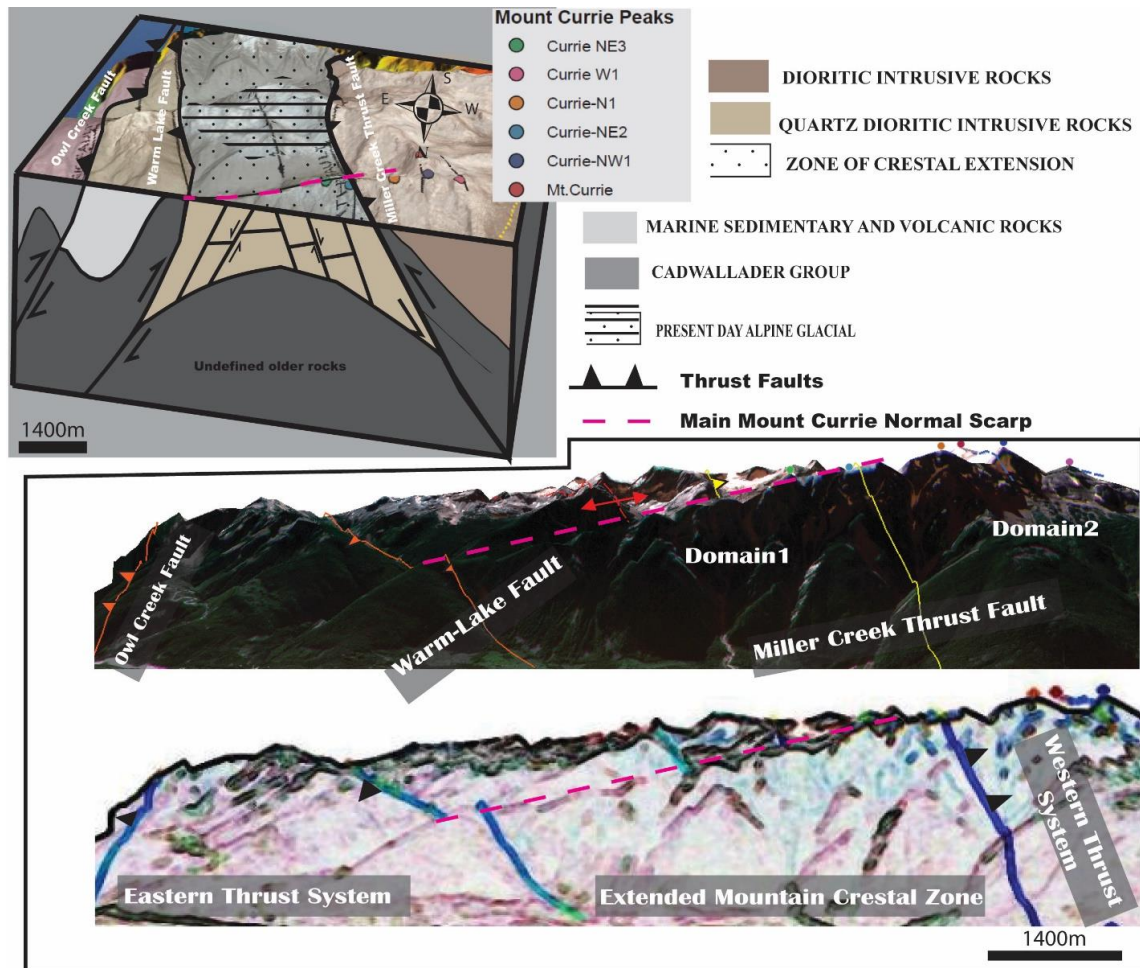
Figure 4.15. **(a) Conceptual geology model of potential trigger forces showing structures and factors controlling Mount Currie scarp. Note: the presence of today's Alpine glacier coincided with the suggested zone of mountain crest extension. Information about regional thrust faults taken from from Parish (1982), Monger and Journeay (1994) and Bustin et al. (2013); (b) Front view (Northern face) of Mt Currie structure shows distinct structural domains.**

The study area is controlled by two major thrust systems which define the boundary between Domains 1 and 2. As such, east-dipping thrust faults to the east and west-dipping thrust system to the west (Figs. 4.1, 4.18). Trends of drainage pattern geometry (Fig. 4.16), visually extracted lineaments (Figs. 4.12b), and outcrop measurements of discontinuities (Figs. 15b) agree with the above defined structural domains. They show two distinct structural domains that control the eastern and western part of the east-west trending Mount Currie structure (Fig. 4.1). In Domain 1, five major lineaments and discontinuity trends observed include NNE-SSW, NE-SW, ENE-WSW, ESE-WNW, and

SE-NW. In domain 2, five major lineament and discontinuity trends were observed including NNW-SSE, NE-SW, ENE-WSW, ESE-WNW, and SE-NW (Fig. 4.15).

4.7.3. Sequences of Deformation

The current physiography of Mount Currie was shaped during the last 5 Ma, however the oldest rocks that make up the mountain are more than 140 Ma. We quantified different episodes of deformation based on cross-cutting of well mapped geologic structures, kinematic analysis of outcrop measured fractures relative to regional faults and the age of the last deglaciation period. The kinematic compatibility of structures on Mount Currie corresponds to the regional structural faults and modern regional horizontal compressive stress.

In Domain 1, the geology model corresponds to the measured outcrop data in which discontinuities, and lineaments are controlled by stress partitioning between the eastern and western thrust fault systems and unloading because of deglaciation (Figs. 4.1 and 4.16). By contrast, discontinuities, and lineaments in Domain 2 located in the hanging wall of the west dipping Miller Creek thrust fault are mainly controlled by horizontal compressive stress of the western thrust fault system and glacial unloading (Figs. 4.1 and 4.16). Therefore, Domain 2 is more likely to preserve and show structures that belong to different timing of deformation including syn-deposition fractures related to cooling of granitic basement rocks (140 Ma to 5 Ma), fault related fractures and discontinuities due to thrusting and bending of the basement rocks (less than 5 Ma), and glacial unloading fractures (less than 10,000 years) (Figs. 4.12b and 4.14b).

High dip angle joints, trending NNW-SSE and lineaments formed parallel and sub-parallel to the Miller Creek Thrust fault and close to the fault zone region may correlate to syn-tectonic (fault related) structures. The geometry of such fractures can be defined as tension joints that accommodate bending of the basement rocks due to thrusting (Figs. 4.12b and 4.14b). ENE-WSW and ESE-WNW high angle dipping joints and lineaments (Figs. 12b and 14b) that formed further west of the Miller Creek thrust fault may correspond to shear joints as the rocks stretch upwards due to thrust propagation eastward. Shallow dipping joints and lineaments that do not show any dominant structural trends may predate thrust faulting and formed because of contraction due to

cooling of granitic rocks; or postdate thrust faulting and formed as exfoliation joints (sheet joints) as the rocks expanded due to glacial unloading (Fig. 4.14b).

4.7.4. 3D Kinematic Slope Analysis

The 3D Geotechnical Kinematic Analysis conducted in this study from the outcrop discontinuity measurements, as well as in previous studies like BGC (2018), provides an approximate assessment and should not be considered fully representative of the entire slope. This limitation arises because the analysis relies on a relatively small number of discontinuity measurements taken from localized outcrop areas. As a result, there is a lack of comprehensive data on the persistence and continuity of geological structures across the slope.

To address these limitations and provide a more comprehensive assessment, a complementary and more robust Limit Equilibrium Analysis (LEA) was performed. This analysis is based on structural kinematic principles and considers regional-scale faults and lineaments, thereby incorporating the persistence of these structures. By doing so, the LEA can estimate the factor of safety for 3D blocks that are formed by the intersections of major geological structures, such as faults and lineaments.

In summary, while the 3D Kinematic Analysis provides valuable insights, it is not sufficient on its own to fully characterize the slope stability. The inclusion of LEA, which considers broader structural factors, offers a more reliable estimation of the slope's stability by accounting for the persistence and continuity of key geological features.

4.7.5. Limit Equilibrium Analysis

Two different sensitivity analyses were performed to obtain the reasonable shear strength parameters including cohesion and friction angle. The first analysis involves the relationship between factor of safety and friction angle for different cohesion and water pressure conditions (Fig.4.17a) through fixing the cohesion value and then incrementally increasing the friction angle. This approach helps to monitor the transition of block stability and determine a critical range of cohesion and friction angle values that could lead to block failure. The results indicate that for Mount Currie under dry conditions, the critical friction angle ranges between 10 to 16 degrees with cohesion less than 0.2 MPa.

This range is crucial as it highlights the conditions under which the slope may become unstable. Additionally, in a jointed rock mass, water pressure distribution is not uniform and depends on joint connectivity and permeability. Water can accumulate in certain areas, creating localized high-pressure zones that significantly impact cohesion and friction angle.

The second analysis involves the relationship between cohesion, factor of safety, and shear strength vs friction angle (Fig. 4.17b) by increasing both cohesion and friction angle in equal intervals. By performing this analysis, a clear linear relationship between cohesion and friction angle is established, providing insights into how these parameters interact to influence slope stability. An increase in cohesion directly increases the shear strength, regardless of the friction angle (Fig. 4.17b). As the friction angle increases, the shear strength also increases (Fig. 4.17b) due to the increased resistance to sliding. However, the relationship between friction angle and shear strength is not linear because shear strength depends on both cohesion and the product of normal stress and the tangent of the friction angle. As the friction angle (ϕ) increases, the $\tan(\phi)$ term increases non-linearly. The tangent function is non-linear, especially as ϕ approaches higher values, which means that small changes in the friction angle at higher values result in larger changes in $\tan(\phi)$.

Accurate models for slope stability must incorporate the non-linear relationship between shear strength and friction angle to predict failures accurately. Simplified linear models might underestimate the true shear strength at higher friction angles, leading to conservative or unsafe designs. We repeated multiple modeling iterations and established a minimum volume threshold of 100 m^3 to avoid generating invalid blocks. This method successfully identified over 60 valid blocks at the NE3 peak, including one critical active key block (Fig. 4.18). A key block is of particular importance as its collapse could lead to the failure of neighboring blocks. It is therefore important to closely examine the geometry and characteristics of this key block to pinpoint the discontinuities and joints that could precipitate its failure. The key block at NE3 Peak is kinematically governed by a wedge formation, aligning with field-based outcrop discontinuity which occurs along two discontinuity sets, D1 and D7 (Table 4.1). The block has substantial size, with a depth of 225 m and a volume of approximately 14.4 x 10^6 m^3 (Figs. 4.12a, 4.13 and 4.18).

A key-block is a block that is removable; it also has a sliding mode and is unstable without support (Goodman and Shi, 1985; Yeung et al., 2003). The aforementioned key block formed through the intersection of five joints in which the block slides along joints 1 (D1) and 2 (D7) (Fig. 4.18). The stability of the key block depends on factors such as the condition of the joints (whether they are open or closed), and the mechanical weathering (freezing and thawing can open tightly closed joints) and chemical weathering can exacerbate weaknesses and increase the accessibility of joint surfaces, as well as joint non-planarity. RocSlope3 assumes that all joints are perfectly planar, which is often adequate, but this can lead to errors when curved joints are misrepresented. For example, sheet joints and joints in severely folded rocks are typically curved (Figs. 4.4 and 4.6).

The 3D kinematic tests and estimated factor of safety used here are considered preliminary, since we did not consider water pressures along the joint planes. The Mount Currie region, like other areas in southern British Columbia, experiences issues related to permafrost thawing. Additionally, the climate is predominantly influenced by temperate rainforest conditions. These environmental factors suggest that our model may underestimate the actual hazard, as high pore water pressures can significantly reduce cohesion and hence reduce the factor of safety and increase the probability of failure. Consequently, further analysis considering these climatic impacts is recommended to provide a more accurate assessment of stability risks.

4.7.6. Rock Slope Movement Rates

A previous study by Bovis and Evans (1995) established baseline measurements of rock slope movements from 1987 to 1991, using a Geodimeter 122 laser EDM device attached to a Wild T-2 theodolite. They observed average vertical displacements along the Mount Currie scarp that varied from 60 mm in the east to 15 mm in the west (Fig. 4.17). In the current study, we employed SqueeSAR, to capture more consistent spatial and temporal movements of the Mount Currie scarp from 2018 to 2020. At the NE-3 peak at the centre of the Mount Currie ridge front, the InSAR data shows that the NE-3 peak moves annually about 6 mm per year downward (subsidence) towards north northwest with a total displacement of 1.5 cm between summer 2018 to end of summer

2020 (Figs. 4.19 and 4.20). It is important to note that the displacement rates might have been underestimated because the Mount Currie slope is oriented north-south. Satellite InSAR has difficulty accurately detecting north-south movement due to line-of-sight limitations (SAR satellite configuration). However, the spatial location of the displaced area is kinematically compatible with our limit equilibrium analysis (Fig. 4.18) and in agreement with 3D Kinematic analysis from the field discontinuity measurements (Table 4.1).
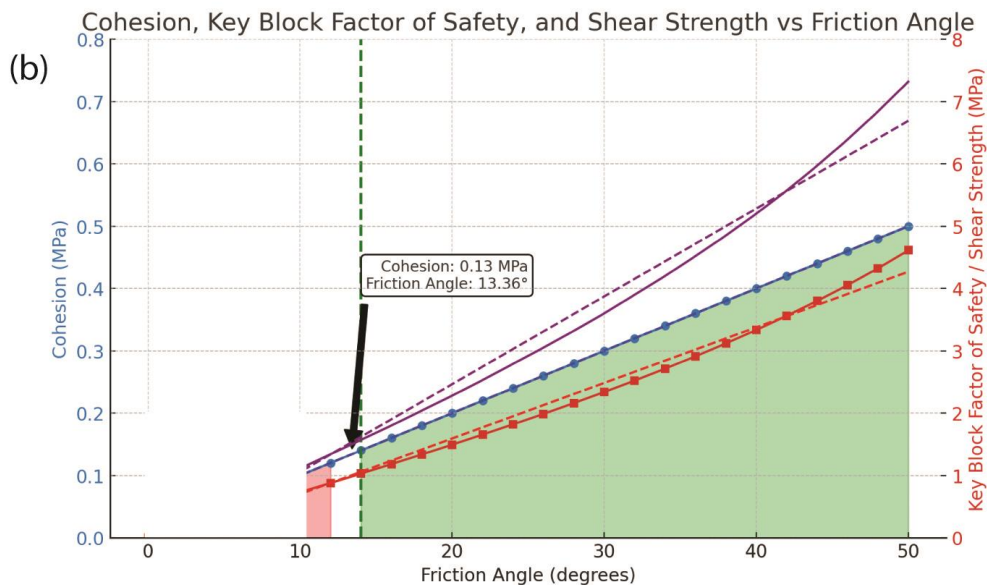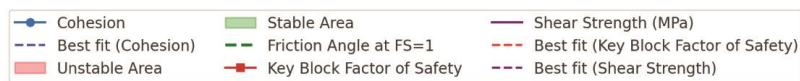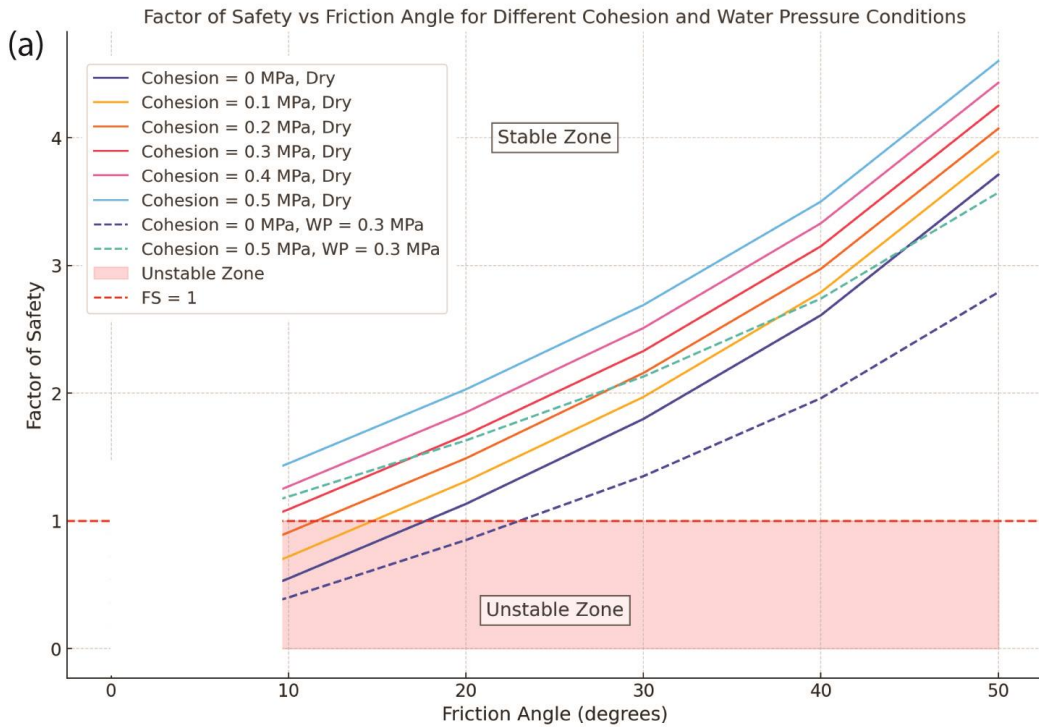
Figure 4.16. The sensitivity analysis shows the relationship between shear strength parameters vs factor of safety. (a) Factor of Safety vs Friction Angle for Different Cohesion and Water Pressure Conditions. (b) Cohesion, Key Block Factor of Safety, and Shear Strength vs Friction Angle.
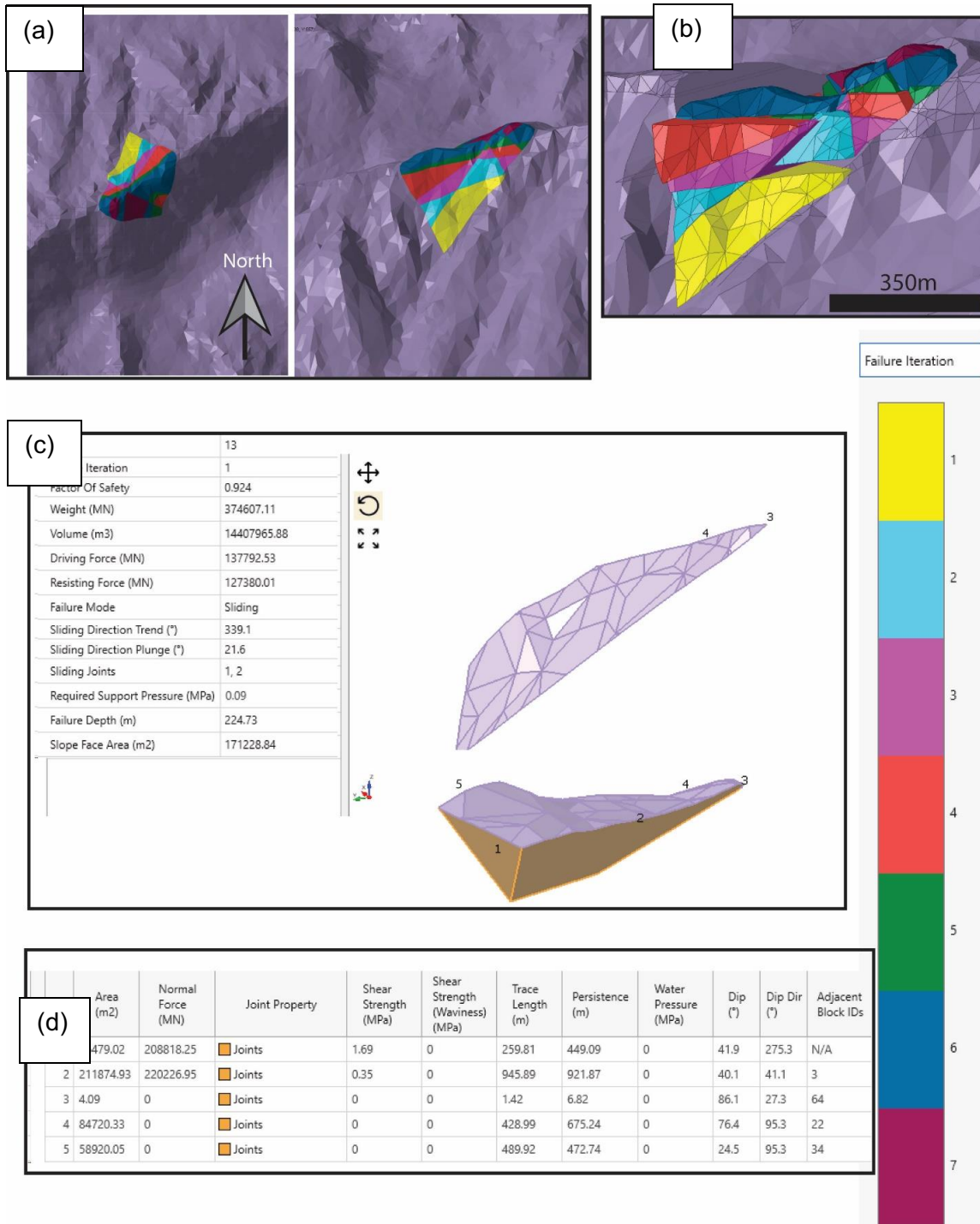
Figure 4.17. **(a) Top and front view of valid removable blocks. (b) Front view shows wedge sliding that initiated by displacing the key block (yellow block). (c) detailed key block kinematic information. (d) Table detailing the geometry of the discontinuities responsible for generation of the key block.**
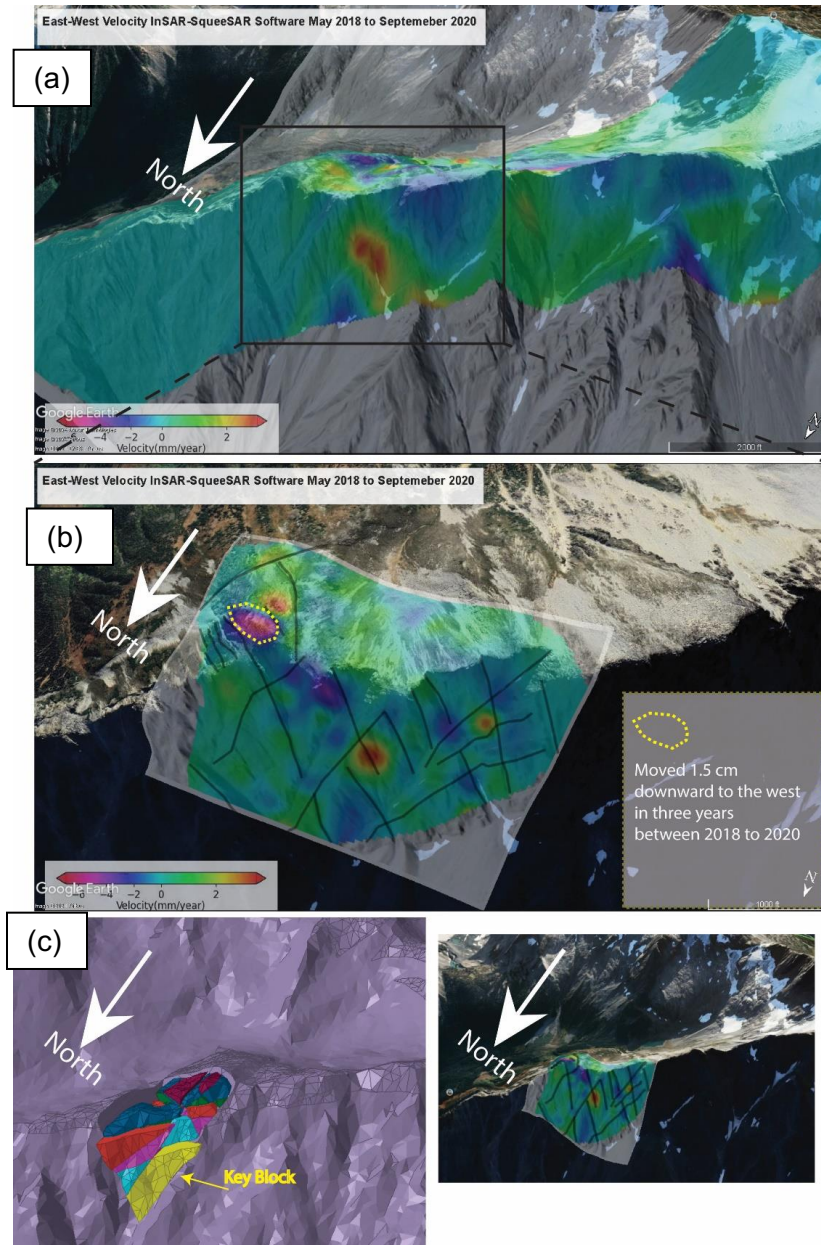
Figure 4.18. **(a) Mean velocity interpolated from three years 2018 to 2020 Sentinel 1 (Ascending and Descending) east-west component from SqueeSAR for the entire Mount Currie ridge. (b) Mean velocity interpolated from three years 2018 to 2020 Sentinel 1 (Ascending and Descending) east-west component from SqueeSAR for the NE3-Peak only on Mount Currie ridge. (c) Comparison between Limit Equilibrium model on the left and east-west displacement velocity on the right. The grey lines overlayed on the displacement velocity represents linear features. Note, the spatial relation between displacement velocity and linear features.**
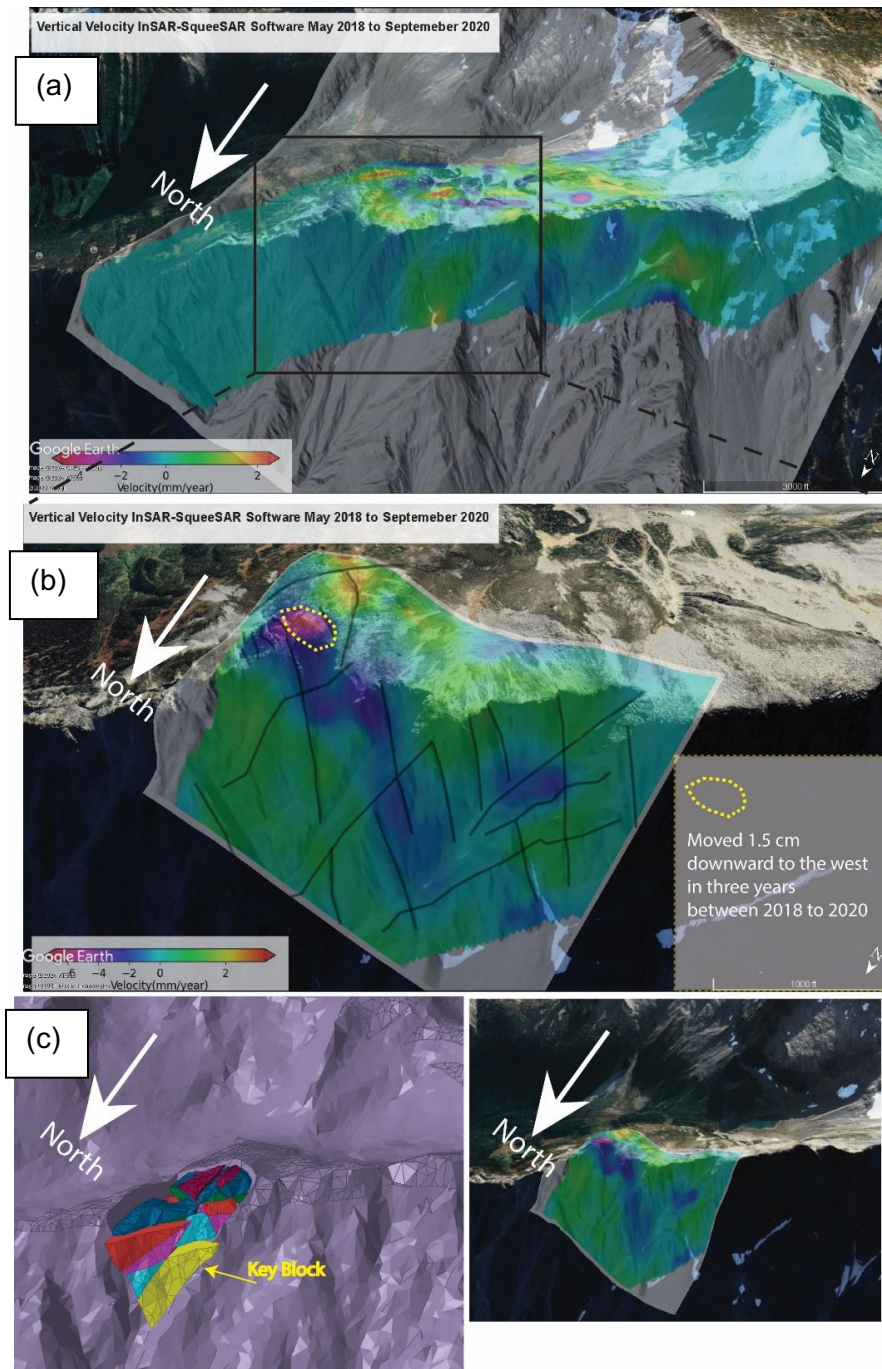
Figure 4.19. (a) Mean Velocity interpolated from three years 2018 to 2020 Sentinel 1 (Ascending and Descending) vertical component from SqueeSAR for the entire mount Currie ridge. (b) Mean Velocity interpolated from three years 2018 to 2020 Sentinel 1 (Ascending and Descending) vertical component from SqueeSAR for the NE3-Peak only on mount Currie ridge. (c) Comparison between Limit Equilibrium model on the left and east-west displacement velocity on the right.

4.8. Conclusions

In this research, we developed an advanced workflow that integrates various disciplines such as structural geology, slope kinematic/limit equilibrium analysis, and satellite remote sensing. This approach aims to overcome the complexities and obstacles of investigating landslides and natural disasters in alpine regions characterized by tectonic and climatic variations and surrounded by temperate rainforests.

We specifically applied this workflow to Mount Currie in southern British Columbia, Canada, focusing on addressing key questions such as the primary triggers for failures and, identifying critical areas requiring long-term monitoring through radar time-series imagery. The aim was also to understand the influence of neotectonic activity on the formation of Mount Currie's ridge scarp and ongoing rockfalls on the mountain's north face and creating a structural factor of safety map for specific slopes.

Our findings suggest that the Mount Currie scarp, which extends from east-northeast to west-southwest, likely originated from extensional faulting driven by compression at the mountain's crest. This faulting is influenced more by localized stress patterns within the mountain itself rather than direct seismic activity. These local stresses are mainly controlled by the nearby Owl Creek and Miller Creek faults, both of which are significant thrust faults surrounding the Mount Currie complex, as well as the effects of crustal rebound due to glacial melting. Additionally, we pinpointed a critical block on the NE3 peak at the centre of the Mount Currie ridge that shows a significantly higher risk of failure compared to other areas. Should this block fail, we estimate that at least 14.4 x 10^6 m^3 of bedrock could be displaced.

The 3D kinematic slope analyses and the estimated safety factor presented are preliminary as they do not account for water pressures along the joint planes. Like other parts of southern British Columbia, the Mount Currie area is affected by permafrost thawing and, the climate is largely characterized by temperate rainforest conditions. These environmental factors indicate that our analyses might underestimate the real hazard, as high pore water pressures can greatly influence both the safety factor and the likelihood of failure by reducing the effective shear strength along discontinuities. Therefore, additional analysis that considers these climatic effects is advised for a more precise evaluation of stability hazards.

4.9. Future work

The proposed potential volume of failure on Mount Currie requires further investigation, additionally it is important to incorporate subsurface geology knowledge, permafrost assessment, and groundwater conditions. Mount Currie natural hazards, including rockfall and potential landslide is mainly controlled by gravitational collapse and climate. Some additional work would be useful to constrain the subsurface geology and the estimated volume of potential slope failures. It would be useful to attempt to constrain whether the height of the critical keyblock could be truncated at depth by unidentified structure i.e., the likelihood of one large wedge failure or smaller failures. Hence, further geotechnical analysis and modelling is advised such as incorporating photogrammetry derived discontinuity measurement to perform 3D kinematic analysis. This will aid in achieving more accurate spatial coverage for the likelihood of failed blocks at selected mountain slopes. Additionally, it is advised to perform more complex geotechnical modelling such as 3DEC (3D Distinct Element Code) to better understand the deformation mechanisms for the slopes of interest.

 It is important to note that the displacement rates estimated from the InSAR satellite data presented in this study might have been underestimated due to the north-south orientation of the Mount Currie slope. Satellite InSAR struggles to accurately detect north-south movement because of line-of-sight limitations. Therefore, high temporal resolution terrestrial LiDAR monitoring, conducted weekly to monthly, is recommended, particularly during the summer months.

BGC (2018) conducted rockfall and debris flow runout modelling for Mount Currie, however, based on our results we suggest a more in-depth scenario-based deep-seated landslide runout modelling for different bedrock volume failure mechanism, especially considering the proximity of human infrastructure at the base of the mountain, such as Pemberton Airport, Indigenous communities, and, most importantly, the presence of the Green River. A large deep-seated landslide could create a temporary dam at the Green River, and its failure could generate secondary hazards such as flooding to nearby communities in the Pemberton Valley.

Chapter 5.   Optical Flow: A Multifaceted Approach for Analyzing and Observing Mass Movements through Optical and Radar Images.

Mahmud Muhammad[1], Glyn Williams-Jones[1], Doug Stead[1], Maqsad Suriev[1]

[1] Centre for Natural Hazards Research, Department of Earth Sciences, Simon Fraser University, Burnaby, British Columbia, Canada.

5.1. Abstract

Landslides are triggered by various factors, including seismic activity, climate-related events, and gravitational forces. These events pose significant risks to life, property, and the environment, necessitating effective monitoring and quantification for mitigation and prevention. Traditional monitoring methods like in-situ sensors face limitations in cost, scalability, and real-time data processing. In the realm of landslide and hazard mitigation, time is of the essence because the quicker data is processed, the sooner policymakers and emergency responders can act to protect lives and safeguard economic infrastructure. The urgency and the critical role of rapid, real-time data processing have inspired us to expand and further develop a novel open-source package called AkhDefo.

This study introduces new features to AkhDefo, transforming it from an open-source code into a standalone geospatial python library. These enhancements include optical flow algorithms for measuring displacement using satellite radar backscatter, optical images, and real-time live stream camera data from ground-based sources. The satellite radar and optical images were processed to study rock-glacier and landslide kinematics in the Morenny rock-glacier in the Tien Shan Mountains, Kazakhstan, and the May 2017 Mud Creek landslide in California, USA, respectively. Further, the live-stream webcam data was used to investigate the September 20, 2021, rockfall event at Stawamus Chief in Squamish, British Columbia, Canada. The results of this study document the kinematic behavior of Morenny rock-glacier between 2017 to 2023. The volume of landslide failure for the 2017 Mud Creek landslide is estimated from pre-failure optical

imagery. Finally, we developed a state-of-the-art rock-fall detection system from live-stream webcam footage of Stawamus Chief in Squamish, British Columbia Canada.

5.2. Introduction

Landslides can occur due to multiple triggers, including seismic activity (Suriñach et al., 2005; Jibson, 2013; Zimmer and Sitar, 2015; Moro et al., 2017), climate-related processes (e.g., heavy rainfall, thawing permafrost), and gravitational forces. Landslides can pose significant threats to life, property, and the environment and thus monitoring and quantifying the scale of the potential landslide beforehand is important to mitigate and/or prevent the landslide-related impacts.

Traditional monitoring methods such as in-situ sensors, while effective, often have limitations in terms of cost, scalability, and real-time data processing. With advances in technology, satellite remote sensing (radar and optical) datasets have emerged as an important tool in landslide monitoring, offering new possibilities for early detection, risk assessment, and mitigation strategies (Bürgmann et al., 2006; Wei et al., 2010). Such tools are crucial for establishing a reliable and effective monitoring system that can support timely decision-making and improve overall disaster preparedness and response.

Radar images include two components - phase and amplitude. The phase represents the position of the radar wave in its cycle at a given time, while amplitude indicates the intensity or strength of the radar backscatter from the ground surface (Ferretti et al., 2007; Ferretti, 2014; TRE ALTAMIRA, 2018). Radar imagery is typically processed via various Interferometric Synthetic Aperture (InSAR) techniques which rely on the phase differences between successive radar pulses between multiple radar images and include Differential Interferometric Synthetic Aperture Radar (DInSAR) that processes pairs of radar images. Additionally, processing stacks of radar images using Permanent Scatterer (PS) and the Small Baseline Subset (SBAS) approaches enhances the capability of detecting sub-millimeter ground movement (Wei et al., 2010; Ferretti, 2014; Sun et al., 2015; Ferretti et al., 2015; Barnhart, 2017; Moro et al., 2017; Zhang et al., 2020; Fobert et al., 2021; Ma et al., 2021). The radar amplitude can be processed as complementary to the phase component which adds robustness to the analysis, especially in areas where the phase signal is compromised or in the presence of large

displacements. The processing of the amplitude component of the radar images involves various techniques such as Speckle tracking (Liu et al., 2008; Scheiber et al., 2014) and digital image correlation (DIC) techniques (Louis et al., 2007; McCormick and Lord, 2010; Pan and Li, 2011). This often requires significant computing power and thus limits the real-time processing applications particularly when applied to large areas of interest.

Despite its strengths, InSAR is not without limitations as it is sensitive to movements only in the line of sight of the radar sensor, which can lead to underestimation of actual ground movement. In areas with heavy vegetation or rapid change, the radar signal may lose coherence over time, making it difficult to track long-term movements. Variations in atmospheric conditions can also introduce errors in the radar signal, affecting the accuracy of displacement measurements. Additionally, radar images use active remote sensing technology (Chen, 1996) which requires a significant amount of energy to emit signals, which can be a limitation on the satellite's resources. Consequently, it can result in higher cost and lower spatial and temporal resolution. Alternatively, optical imagery uses passive remote sensing technology (Asner, 1998) which involves detecting natural energy from sunlight that is emitted or reflected by the Earth's surface. Consequently, optical imagery has potentially superior spatial and temporal resolution and has been employed to complement some of the limitations of radar imagery (Amaki et al., 2019; Kim and Gratchev, 2021; Srokosz et al., 2021; Hermle et al., 2022; Muhammad et al., 2022).

Several methods and techniques, including digital image correlation (DIC) and optical flow (Amaki et al., 2019; Hermle et al., 2022; Muhammad et al., 2022), have been applied to process and measure displacement from optical imagery. Currently, DIC stands out as the primary technique for assessing displacement via optical imagery. While DIC and related speckle tracking techniques are acknowledged for their proficiency in determining ground displacement from radar backscatter and optical images, their application in real-time is limited due to the considerable processing involved. Additionally, these techniques depend on a trial-and-error approach to select a suitable matching correlation window (Fig. 5.1 a, b, c, and d) influencing the precision of the measurements (McCormick and Lord, 2010; Pan and Li, 2011). If the window is too small, large displacements (Fig. 5.1 a) may not be fully captured leading to inaccurate or incomplete measurements. The displacement could also move objects outside of the

small window, causing the algorithm to lose track of the movement. With a large window, small displacements (Fig. 5.1d) may be diluted or lost amidst the larger area of analysis.

Commonly employed methods for monitoring rockfalls encompass light detection and ranging (LiDAR), doppler laser scanning, and video image analysis (Yan et al., 2019; Casagli et al., 2023). In terms of real-time monitoring doppler laser scanning is a reliable existing rockfall monitoring technique which depends on the use of costly and advanced radar systems based on the Doppler effect for real-time detection and alerting (Casagli et al., 2023). These radars emit microwave signals that are reflected and analyzed to identify fast-moving objects on slopes. If an object moves quickly enough, it alters the signal's frequency, triggering an alert through the observed Doppler effect (Casagli et al., 2023).

The optical flow algorithm is used extensively in a range of applied scientific disciplines, such as fluid mechanics, solar physics, navigation for autonomous vehicles, biomedical imaging, traffic management, virtual reality, face tracking and action recognition. However, its use in the fields of landslide study and Earth sciences has been relatively limited (Kim and Gratchev, 2021; Srokosz et al., 2021; Muhammad et al., 2022) when compared to techniques like DIC. In this study, we expand upon the open-source optical flow Python package developed in Chapter 2 (Muhammad et al., (2022) and show its proficiency in measuring and quantifying displacement from both satellite radar backscatter images and optical imagery (satellite and ground-based cameras). Furthermore, we demonstrate its effectiveness in measuring land deformation and analyzing landslide hazards by applying the new AkhDefo 2.0 Python package to three extensively researched case studies: 1) the May 2017 Mud Creek landslide in California USA; 2) the September 2021 Stawamus Chief rockfall in BC, Canada, and 3) the Morenny rock-glacier in Tien Shan mountains of Kazakhstan.

5.3. AkhDefo- package

The initial version of AkhDefo, developed by Muhammad et al. (2022), consisted of two Jupyter notebooks with approximately 1,000 lines of Python code. This program was designed to measure displacement using optical satellite imagery and static hourly ground-based optical imagery. In contrast, the current study builds on that previous work by transforming it into a standalone Python library. This new version is capable of

processing live video from webcams, satellite and ground-based optical imagery, as well as satellite radar backscatter imagery.

The AkhDefo package, available on PyPI (https://pypi.org/project/akhdefo-functions/), is a collection of independent Python scripts that facilitate batch processing and manipulation of geospatial datasets, including both raster and vector data. It is especially useful for applications in geology, geotechnical engineering, and natural hazard studies, enabling the production and visualization of geospatial data. The package can download Sentinel-1 radar imagery via an Earthdata API account (https://search.asf.alaska.edu/) and daily PlanetScope imagery using a Planet Labs account (https://account.planet.com).

Alternatively, it can access and process data from static ground-based camera snapshots or live ground-based camera feeds. Additionally, AkhDefo can process both radar and optical imagery to generate temporal and time-series deformation maps.

Impact of Window Size on DIC in Terms of Pixel Movements
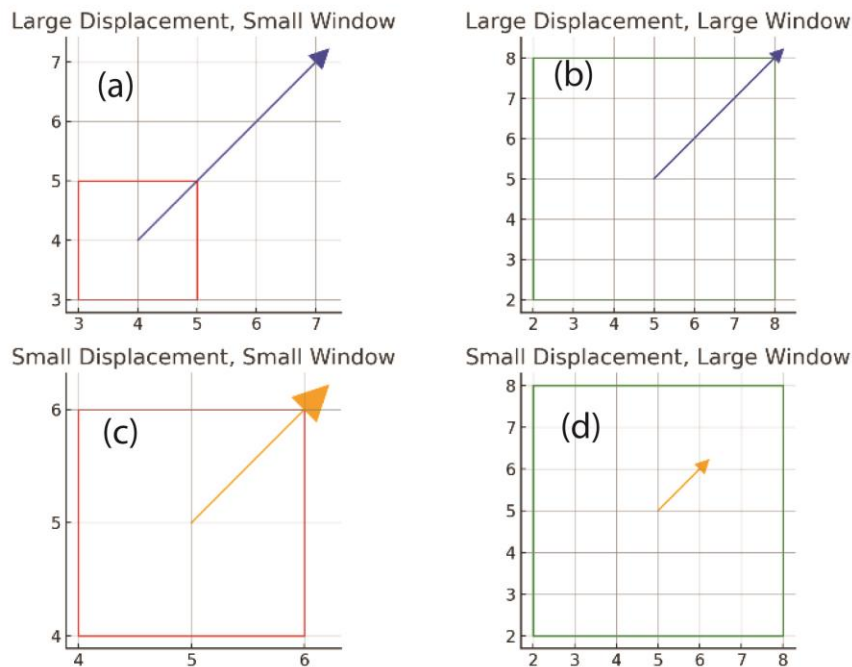
Figure 5.1. Red square depicts matching window, and the arrow depicts movement. (a) Top Left - Large Displacement, Small Window. (b) Top Right - Large Displacement, Large Window. (c) Bottom Left - Small Displacement, Small Window. (d) Bottom Right - Small Displacement, Large Window.

5.4. Methodology

Optical flow refers to the perceived movement patterns of objects within a visual scene which occur due to the movement of either the object itself, the camera, or both. When a camera captures a scene over a period of time, the sequence of images produced can be viewed as a function of the grayscale values at specific pixel locations and the specific time. Movement within the scene, whether by the camera or an object, leads to a temporal shift in these gray scale values across the sequence of images. This creates a two-dimensional field of apparent motion within the image plane, known as the Optical Flow Field (Amaki et al., 2019; Kim and Gratchev, 2021; Srokosz et al., 2021; Muhammad et al., 2022).

For ground-based imagery, one can establish a fixed camera position, however, for satellite-based imagery, it is necessary to apply corrections and orthorectification to ensure consistent ground pixel locations over time. Accurate computation of optical flow therefore represents a significant challenge in the field of computer vision (Barron et al., 1994; O'Donovan, 2005; Javier et al., 2013). Furthermore, since the primary assumption underpinning optical flow is that the patterns of light intensity in successive images exhibit temporal consistency, there has been only limited use in natural settings with highly variable environmental conditions.

In the current AkhDefo 2.0 workflow, we apply the coarse to fine dense optical flow implementation from OpenCV (Farnebäck, 2003). By filtering and re-sampling, the original image at progressively lower resolutions, a pyramid structure of down-sampled images, ranging from coarse to fine, is generated. Initially, a rough match is established at the lower resolution level, which then guides the identification of a smaller region in the next higher resolution image. This process is iteratively refined, gradually moving towards the full resolution of the original image. The adoption of the coarse to fine optical

flow algorithm has significantly enhanced performance of optical flow calculation, yet these methods have inherent limitations. The main challenge of all methods of optical flow is to maintain stability of image illumination (O'Donovan, 2005; Javier et al., 2013; Amaki et al., 2019). Another inherent limitation is that objects smaller than their displacement magnitude can become obscured at coarser levels due to the smoothing process. There is a risk of error propagation since at coarser scales, overlapping motion layers can lead to errors that are carried through to different scales (O'Donovan, 2005).

To minimize the effect of illumination persistency error propagation, we implement a number of approaches including the Structural Similarity Index Map (SSIM) (Palubinskas, 2014), Scale Invariant Feature Transform (SIFT) (Lowe, 2004) and statistical z-score outlier removal to mask invalid pixels. A detailed methodological workflow addressing these issues is shown in the supplementary material (Appendix D) along with a high-level summary of the application of AkhDefo Python package (https://pypi.org/project/akhdefo-functions/). The AkhDefo package also includes a collection of independent Python codes to perform batch processing and manipulation of geospatial datasets such as raster and vector datasets. In the current study, we added scripts to the AkhDefo software to download and process Sentinel 1 radar imagery via earth-data API account (https://search.asf.alaska.edu/) for Morenny rock-glacier in Kazakhstan, download daily PlanetScope imagery using a Planet lab account (https://account.planet.com) for Mud Creek Landslide, USA and process live-stream webcam video for the Stawamus Squamish Chief rockfall in Canada.
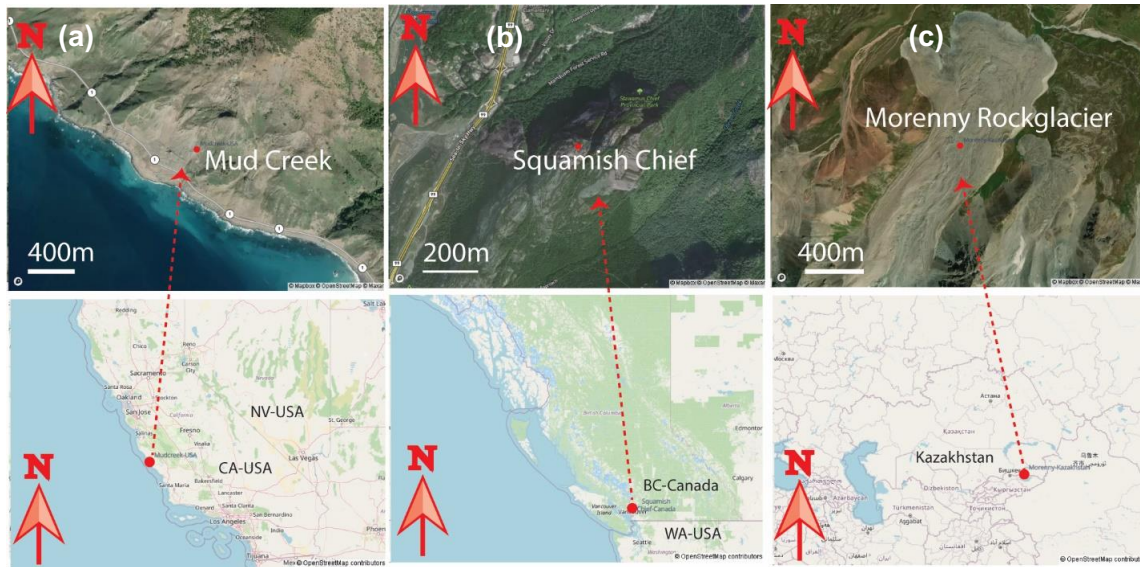
Figure 5.2. Locations of the selected case studies at (a) Mud creek, California, USA, (b) Squamish Chief, British Columbia, Canda, and (c) Morenny rock-glacier in Kazakhstan.

5.5. Case Study 1 - The 2017 Mud Creek landslide, California, USA

The 2017 Mud Creek landslide occurred in the Big Sur region along the California coast (Fig. 5.2), approximately halfway between Monterey and Morro Bay. This area is known for its rugged terrain, located on the western side of the Santa Lucia Mountains, which boasts several peaks exceeding 1000 m in elevation. These mountains are linked to the Big Sur Bend of the San Gregorio-Hosgri Fault system, a region characterized by transpression along the transform plate boundary in this area (Warrick et al., 2019). The bedrock geology of the mountains includes Mesozoic granitic and pre-Cretaceous metamorphic rocks, as well as patches of Miocene marine sedimentary rocks and a diverse mix of Mesozoic rocks collectively known as the Franciscan Assemblage. This variety of rock types leads to considerable spatial variability in the strength characteristics of the rock masses (Warrick et al., 2019), which in turn results in varying levels of susceptibility to landslides and differing spatial densities. Near Mud Creek, the primary bedrock geology consists of the Franciscan Assemblage, which is covered by loose colluvial deposits. This area is characterized by discrete planes of weakness within the mélange, which have been linked to landslides occurring approximately 10 km

around the Mud Creek area (Wills et al., 2001). The geological features that further influence stability and act as pathways for subsurface water movement include shear zones of various sizes as well as more recent faults that intersect the region (Warrick et al., 2019). The area within 5 km of the Mud Creek site has been identified as having a high potential for landslides, and Highway 1 at Mud Creek has frequently required debris removal due to rockfalls (Warrick et al., 2019). However, the likelihood of extensive, rapid changes in the landscape in the area remained unrecognized until 2017.

5.5.1. Landslide Kinematics

The highly altered and weathered bedrock geology, along with the numerous shear zones in the Mud Creek site (Warrick et al., 2019) and the proximity to areas in California often affected by earthquakes, combined with the region's high rainfall, could readily lead to a disastrous landslide like the one that occurred at Mud Creek on May 20, 2017.

The key aspect of landslide monitoring with remote sensing data is the ability to predict not only the timing of landslide failure but also recognize landslide behavior and deformation kinematics. Leveraging the capabilities of the AkhDefo Package, we collected, processed, and analyzed data to visualize and interpret both spatial and temporal displacement patterns. In Chapter 2 (Muhammad et al., 2022) we processed one month of daily cloud free PlanetScope optical satellite imagery. The current analysis focused on daily satellite imagery from PlanetScope, covering the period from October 2, 2016, to May 16, 2017, four days before the landslide failure event. Specifically, we generated seven months' worth of 2D horizontal displacement data (in east-west and north-south directions) for the Mud Creek site, utilizing imagery obtained from November 2016 through May 2017.

The following maps including aspect velocity map, plunge velocity map, height change map, bedrock volume change map (Fig. 5.3) and time-space inverse velocity map (Fig. 5.4) were constructed from both two-dimensional horizontal displacement datasets and a pre-failure digital elevation model. The maps were employed to assess the change in the slope, utilizing the magnitude and direction of displacement on the digital elevation model, and in turn, the likely volume of the displaced bedrock material. Our estimate suggests a rock volume displacement of approximately 2.976 x 10^6 m^3 which is in broad

agreement with the volume estimated by Warrick et al. (2019) from LiDAR point cloud change detection of 3.5 x 10^6 m^3.

The inverse velocity, displacement aspect, and magnitude maps (Fig. 5.3) revealed two areas of downward movement: plunging more than 50 degree south-southwest (Fig. 5.3 a, b, and Fig. 5.4b) the lower area at the base of the failure and the upper area at the top of the landslide head-scarp (Fig. 5.3 a, b, and Fig. 5.4b). These maps also suggest that the onset of landslide failure began in early May 2017, with the instability starting at the toe of the landslide, corresponding to the lower area, and then progressing to the formation of the landslide scar weeks before the catastrophic failure. The inverse velocity map and profile (Fig. 5.4 b and c) indicates that the failure initiated around May 2, 2017, at least two weeks before the catastrophic landslide failure. Additionally, the identified upper swale earthflow was detected from the LiDAR digital elevation model study (Warrick et al., 2019) (Fig. 5.4a), confirmed by the inverse velocity map (Fig. 5.4b) and deformed at least one month prior to the landslide event around April 20, 2016 (Fig. 5.4b). This pattern aligns with the daily time-lapse PlanetScope imagery and the inverse velocity profile and time-space inverse velocity map for the Mud Creek site (Figs. 5.4 and 5.5).

Our data identified creep-to-failure behavior at Mud Creek months before the major failure. We also pinpointed specific dates of increased landslide movement: November 30, 2016, March 2, 2017, April 10, 2017, and May 16, 2017 (Fig. 5.4c). and, the initial stages of the failure, starting in early May 2017, were clearly observable in the daily PlanetScope time-lapse optical imagery (Fig. 5.5). Utilizing optical imagery that provided a daily acquisition interval, especially during April 2017 (Fig. 5.6), proved highly advantageous in the period preceding the landslide failure. This frequent imaging enabled more precise and prompt tracking of the site's changing conditions, offering essential insights unattainable with less regular monitoring techniques like the 12-day data acquisition intervals of Sentinel 1 dataset. By contrast, previous work based on InSAR and LiDAR change detection (Warrick et al., 2019; Handwerger et al., 2019) were unable to identify the creep-to-failure behavior at Mud Creek due to limited temporal data acquisition and the landslide movements being much larger than the measured InSAR deformation. Additionally, the 12-day interval of the Sentinel 1 InSAR dataset was too infrequent to closely monitor the landslide deformation, and InSAR measures deformation along the line of sight, thus it is only capable of measuring deformation in

one dimension. The annual displacement data showcased in this study, prior to the catastrophic event, not only had the potential to forecast such an incident but also to conduct a pre-event analysis of the landslide's movement. However, the accuracy of this assertion hinges on whether real-time or near-real-time monitoring was operational.
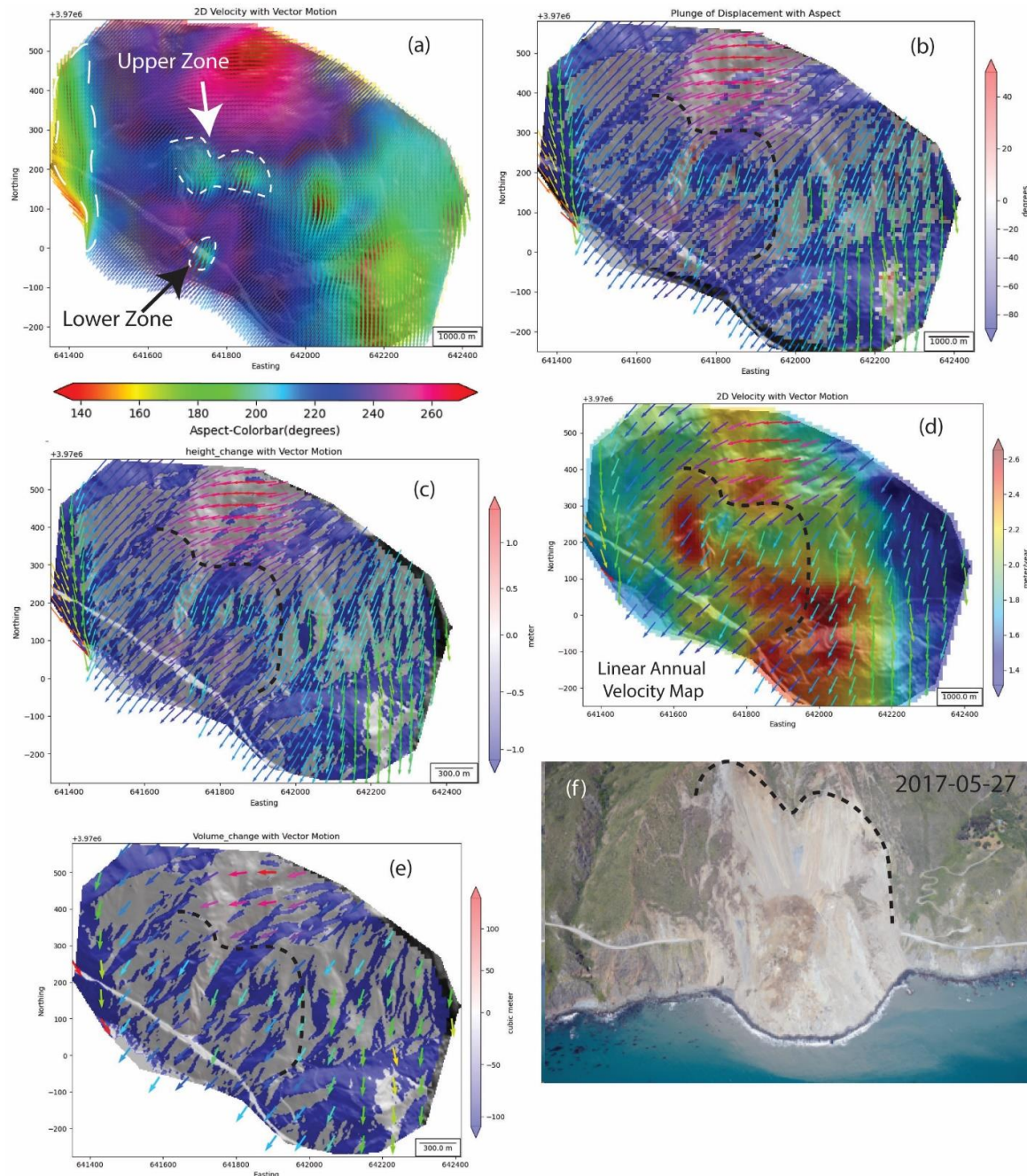
Figure 5.3. **Mud Creek deformation kinematics. (a) 2D Horizontal displacement aspect. (b) Plunge of displacement vector motion in degree; negative is downward movement, positive upward movement and zero is pure horizontal movement. (c) estimate elevation change map. (d) 2D linear annual displacement magnitude calculated between October 2, 2016, to May 16, 2017. (e) Estimated landslide volume map calculated from pre failure digital elevation model and linear annual velocity. (f) Oblique aerial photograph one week after the catastrophic failure (Warrick et al., 2019).**
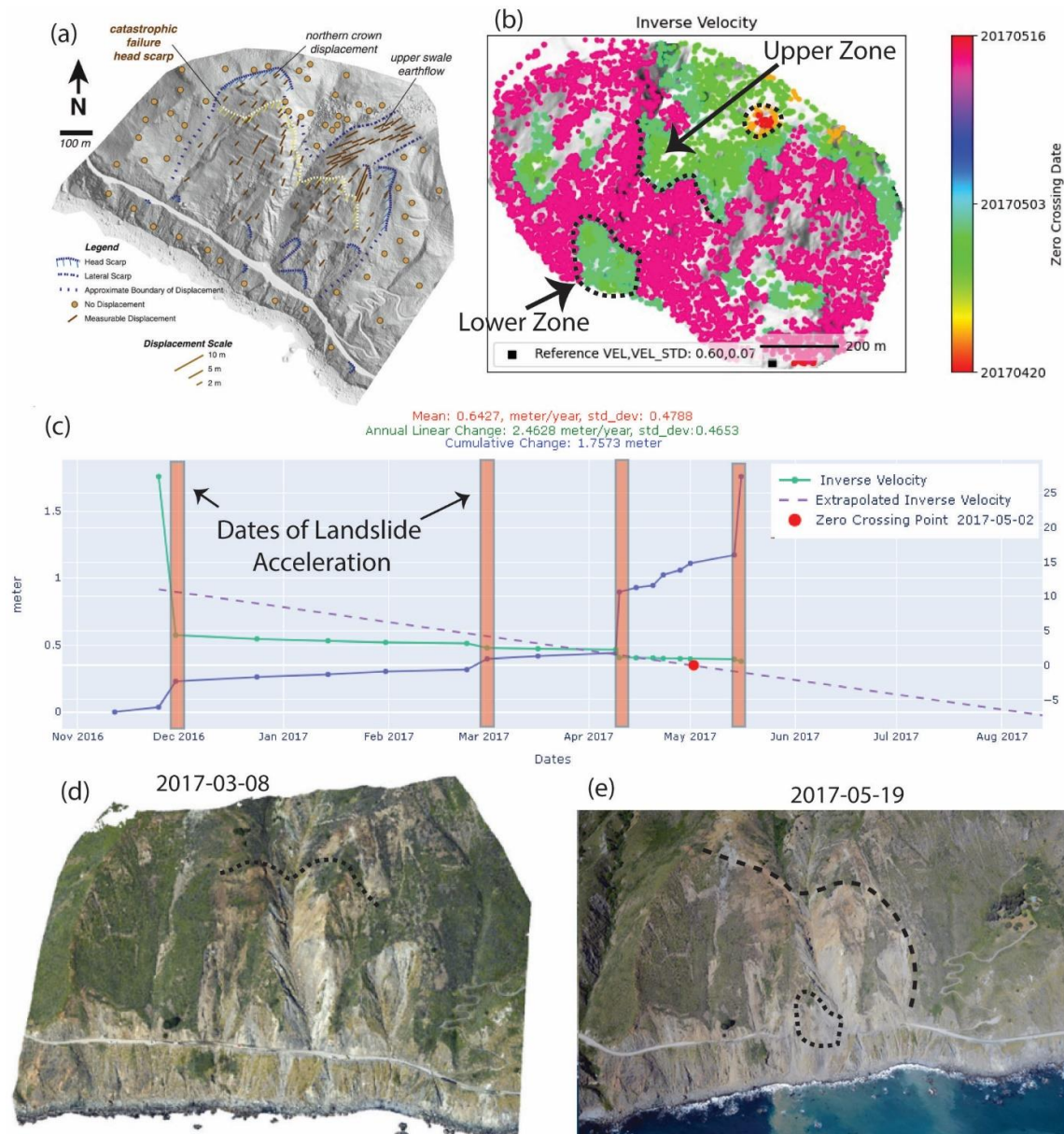
Figure 5.4.   (a) Horizontal displacement map shows active areas between 2010 and 2016 derived from LiDAR digital elevation model (after Warrick et al., 2019). (b) Inverse Velocity map shows spatial prediction date of deformation within the landslide body. (c) Time-series velocity and inverse velocity profile for the average pixels inside the lower zone denoted on plot b. (d) Oblique aerial ortho-photograph for Mud Creek slide on March 3, 2017 (after Warrick et al., 2019). (e) Oblique aerial orthophotograph for Mud Creek slide on May 19, 2017 (after Warrick et al., 2019).
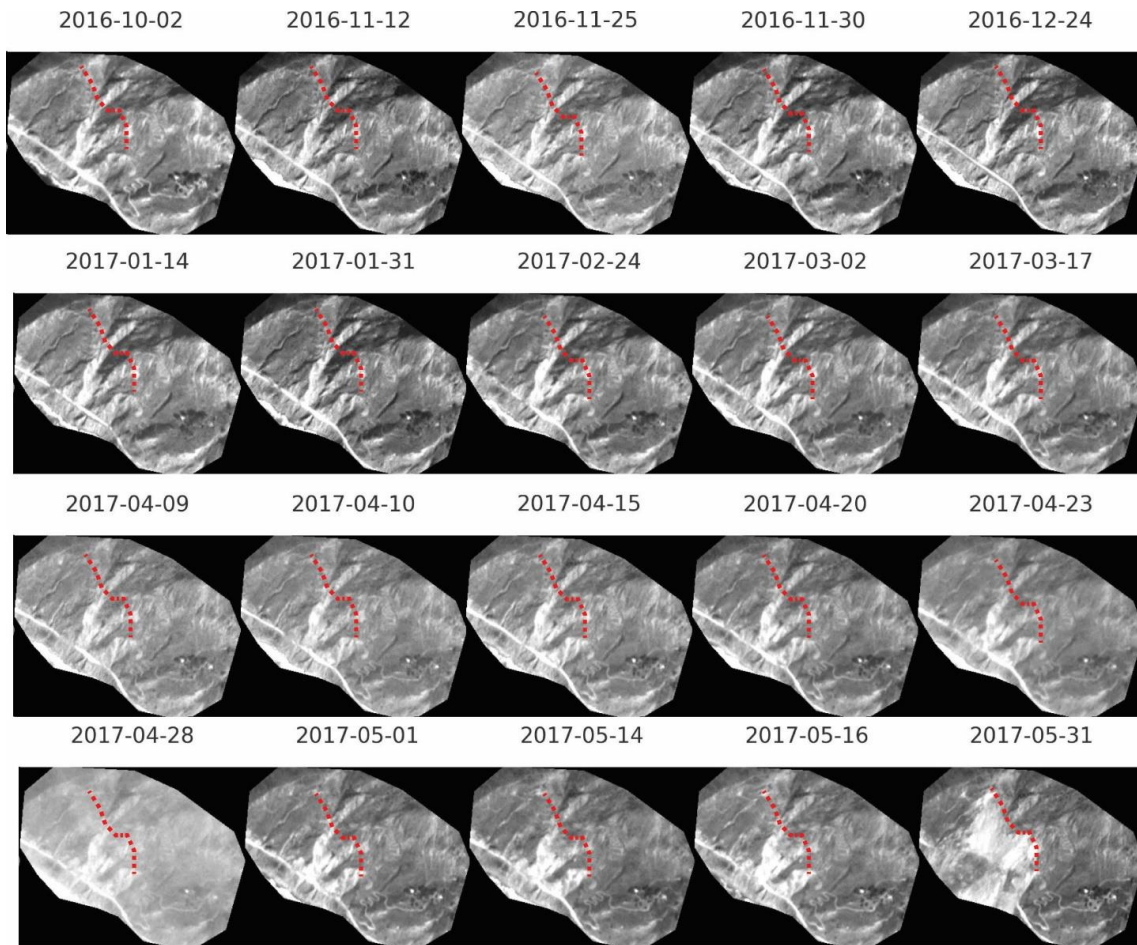
Figure 5.5. **Static Time-lapse for Mud Creek site before and after the catastrophic failure. Red dashed outline represents the location of the scar. A high resolution colour timestamp animation is available in the following link:**[https://raw.githubusercontent.com/mahmudsfu/AkhDefo/main/src_akh defo/docs/notebooks/data/mudcreek/movie.gif](https://raw.githubusercontent.com/mahmudsfu/AkhDefo/main/src_akhdefo/docs/notebooks/data/mudcreek/movie.gif)
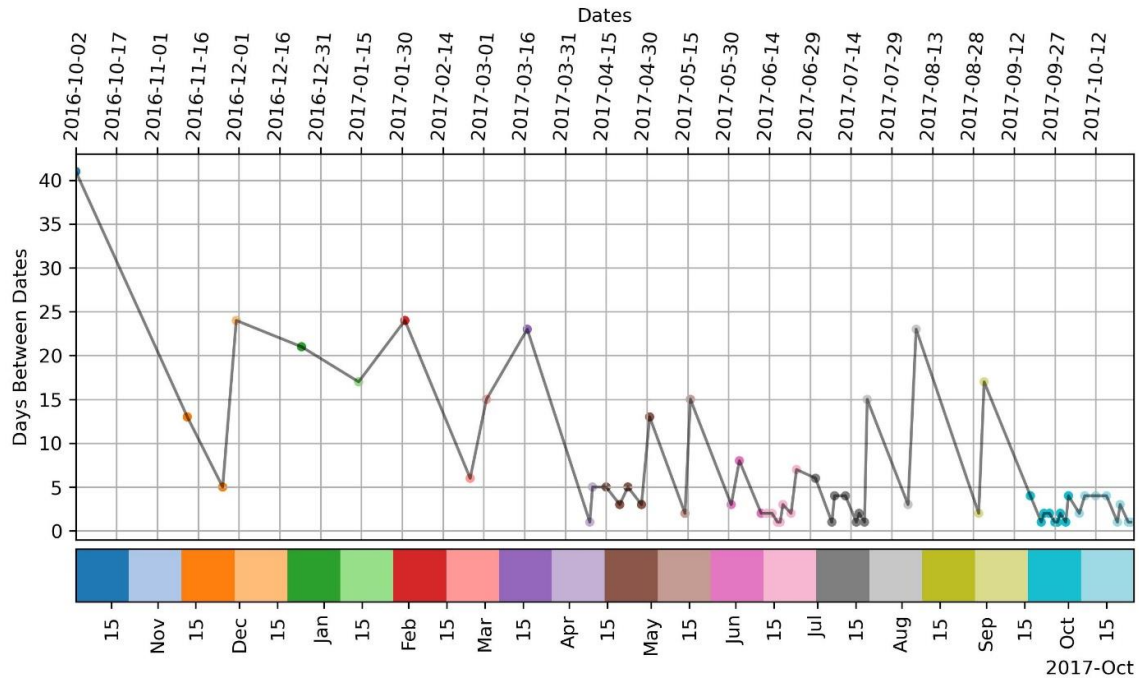
Figure 5.6.   **Data frequency interval for cloud free PlanetLab optical imagery.**

5.6. Case Study 2 - The Stawamus Chief Rockfall, British Columbia, Canada

The Stawamus Chief (also known as "The Chief"), is a significant granodiorite pluton situated next to Highway 99, near Squamish in British Columbia, Canada (Fig. 5.2). This geological formation, which originated around 100 million years ago during the early Cretaceous, became exposed through the tectonic activity that formed the Coast Mountain Range (Mathews and Monger, 2005). In the most recent ice age, the region was blanketed by ice, reaching a depth of about 1300 m. The distinctive exfoliation joints seen on The Chief and similar granitic structures are the result of both tectonic forces and glacial pressure release (Tuckey, 2012; Sampaleanu, 2017; Coughlan et al., 2023). The area is a popular region for tourism particularly as a world-class rock-climbing site (Melanson, 2015; Coughlan et al., 2023) and over the past decades has been subjected to increased rockfall activity (Sampaleanu, 2017; Coughlan et al., 2023).

Currently, the only source of continuous visual surveillance for the Chief is from a live-stream webcam with the capacity of 30 frames per second, installed and operated by a citizen scientist residing in Squamish (Birkill, 2024). The camera is affixed to a tree approximately 2.3 km away from the Chief. The Dahua IPC-HFW8232E-Z IP camera is equipped with a Sony Exmor sensor, capable of delivering clear images even during cloudy nights and with an estimated ground pixel resolution of 80 cm (Alex Birkill, 2024 pers. comm.). During September 20, 2021, the camera recorded a rockfall event at 1:34 am PST (Pacific Standard Time). The sound of tumbling rocks resonated across a large portion of Squamish, particularly in the Valleycliffe area, positioned near the base of the Chief's north side. The event led to vibrations in nearby homes (Birkill, 2024), and the seismicity was recorded on the seismograph managed by the Canadian National Seismograph Network (Alex Birkill, 2024 pers. comm) at Watts Point, BC, approximately 10 km to the southeast of the Stawamus Chief.

5.6.1. Real-time Rockfall Monitoring System

We processed the streaming webcam data with the AkhDefo real-time change detection module which uses an optical flow algorithm to measure the motion field between subsequent video frames. This module can process video frames directly from the server, facilitating instantaneous data analysis without the requirement to download video files. Optical flow, like other techniques, has inherent limitations such as difficulty to maintain the stability of light exposure between subsequent video frames as well proper installation of the webcam to avoid camera movement due to wind gusts. Those challenges were minimized using various techniques such as image frame alignment (Lowe, 2004), masking of still objects as background (Muhammad et al., 2022; Verma et al., 2023) and structural similarity index map (Kim et al., 2020; Muhammad et al., 2022) between subsequent frames.

To assess the capacity of real-time monitoring and mitigating potential discrepancies caused by instrumental installation errors, such as webcam vibrations due to wind, a sensitivity analysis was conducted. On March 26, 2024, we executed a continuous four-hour live stream analysis from 3 pm to 7 pm, during which we also performed frame alignment procedures. The latency of video frame processing reaches a few minutes per hour (Fig. 5.7a, b) with a baseline displacement error of 1 cm (Fig. 5.7c). Additionally,

our findings indicate a direct correlation between video frame shifts and wind speed. For example, in Squamish on March 26, between 3 pm and 4 pm, the wind speed increased to 21 km/h, coinciding with a 6-to-8-pixel shift in video frame alignment (Fig. 5.8c). Conversely, as the wind speed decreased to below 10 km/h between 4 pm and 5 pm, a concurrent decrease in video frame pixel shifts was observed, with shifts ranging between 2 to 6 pixels (Fig. 5.8d).
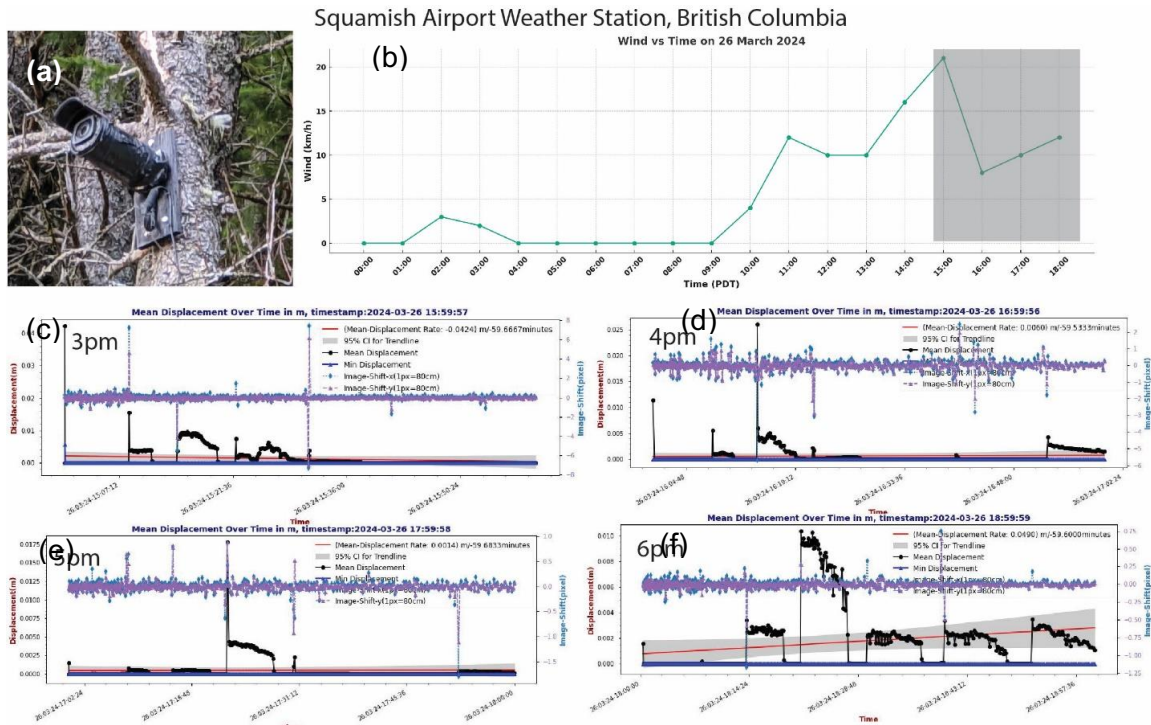
Figure 5.7.   a) Photograph showing the installation of the webcam. b) Hourly windspeed data at the Squamish airport weather station. c) Mean displacement and image shift between subsequent video frames on March 26, 2024, between 3 pm and 4 pm. d) Mean displacement and image shift between subsequent video frames, between 4pm to 5pm. e) Mean displacement and image shift between subsequent video frames from 5 pm to 6 pm. f) Mean displacement and image shift between subsequent video frames between 6 pm and 7 pm.

For more precise analysis, the September 20, 2021, video recording (approximately two minutes duration) was transferred to a local computer. As the video data was sourced from a local machine, the software examined each frame thoroughly, processing at a rate of 30 frames per second. This meticulous frame-by-frame analysis resulted in a prolonged processing period compared to live-stream webcam data ingestion, where the software selectively captures frames based on real-time occurrences. The onset timing

of rockfall occurrence was determined to be at 1:28:42 am and ended approximately around 1:28:55 am as it appears from the recorded video (https://akhdefo.readthedocs.io/en/latest/_images/frame_2024-03-26_0_image.gif). It is worth noting that although the area was covered with cloud and fog at the time of the rockfall, we were able to clearly differentiate between background noise and signal of the rockfall event (Fig. 5.9b).
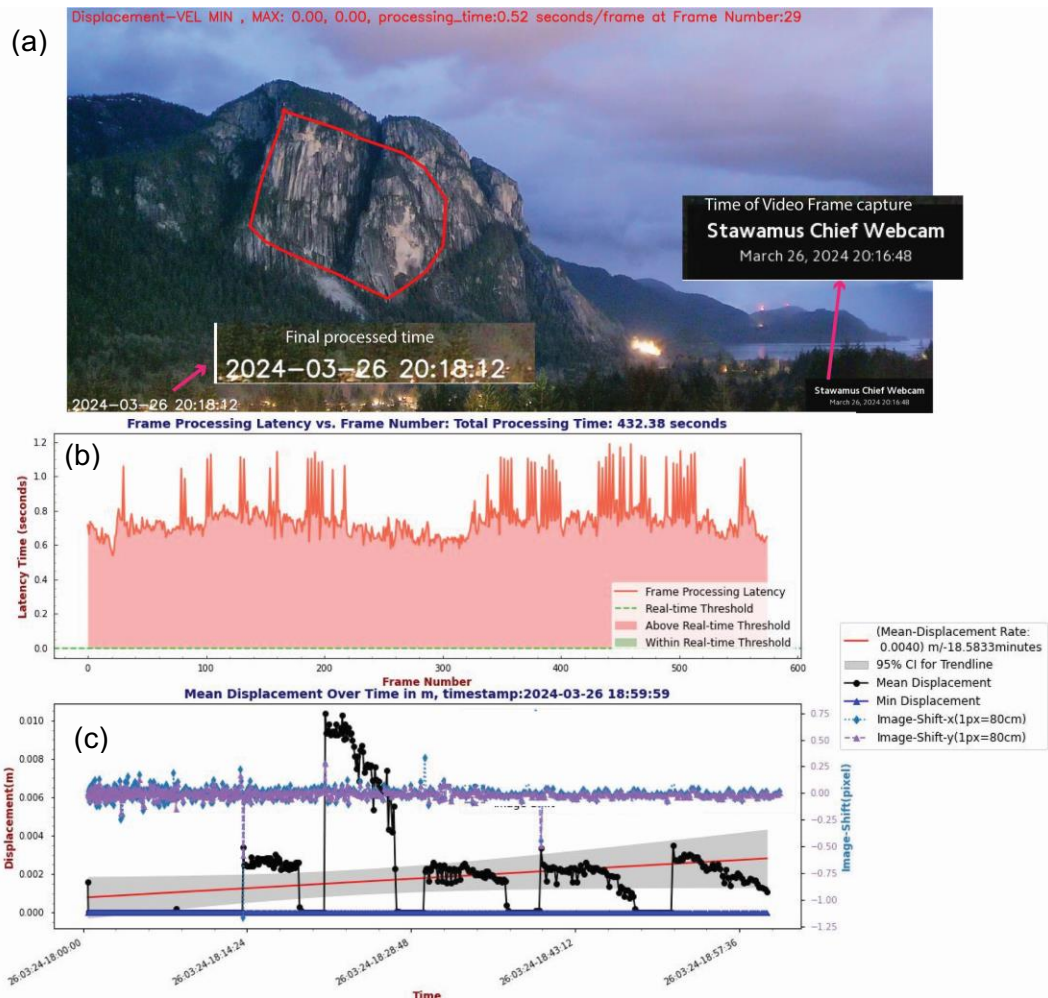
Figure 5.8. **Rockfall monitoring system latency time. a) Video frame capture showing time of captured frame and time after frame being analyzed. b) Plot of time required to process two consecutive frames and total latency time per two frames being processed over a period of one hour. c) Mean displacement for the red polygon in a and sensitivity of the system to 1 cm (i.e., movements less than 1 cm is considered as noise).**
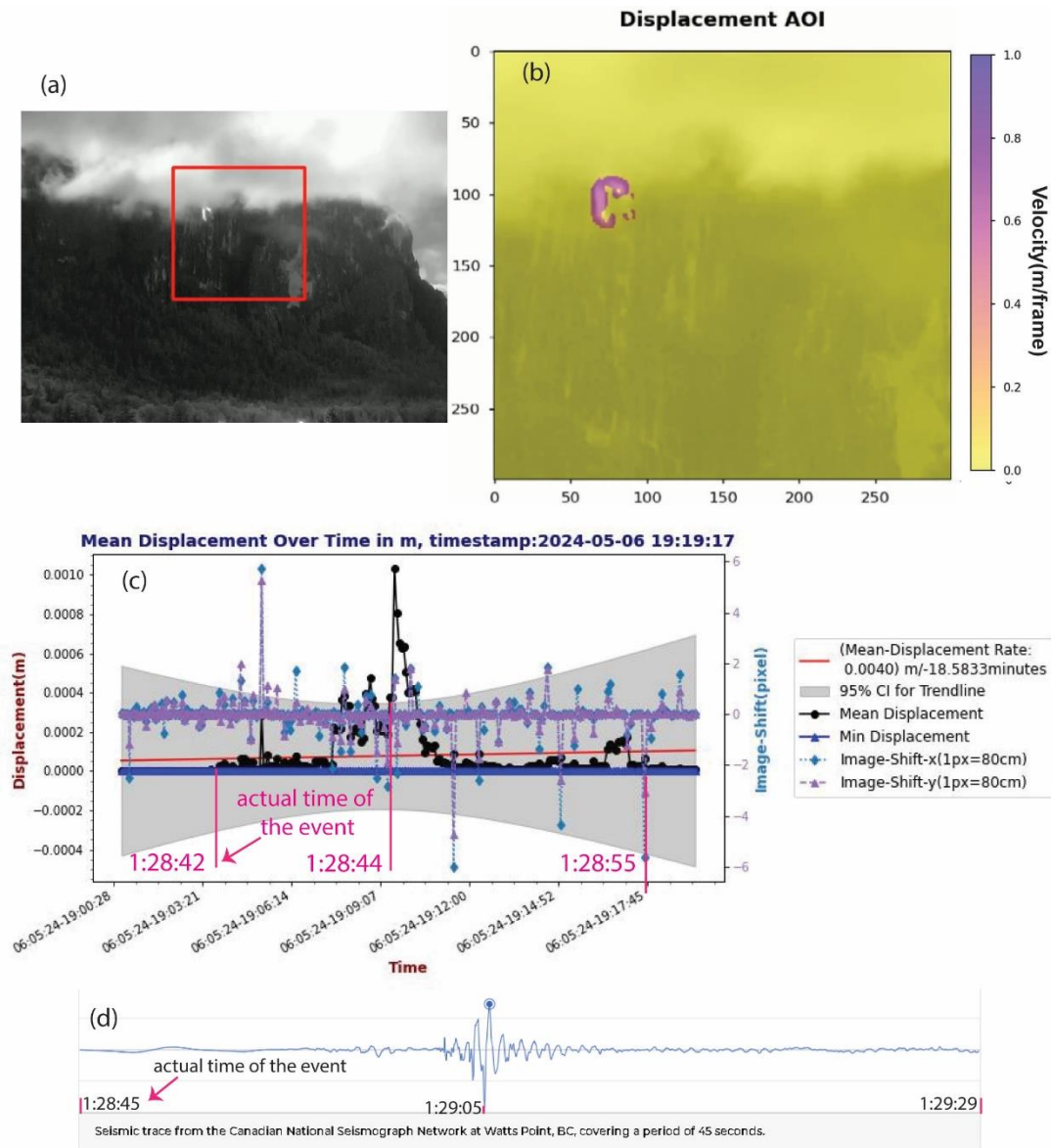
Figure 5.9. Screen shot of processed video of the 20 September 2021 Stawamus Chief rockfall. a) Screenshot of the rockfall site seen with night vision camera. b) Processed displacement velocity for the red square area in a in meter per frame during the onset timing of rockfall event; note the background cloud and clarity of measured displacement velocity. c) Time-series mean displacement in meters for the red square area in a and frame stability displacement shift in pixels. d) Seismic trace from the Canadian National Seismograph Network at Watts Point, BC, covering a period of 45 seconds.

5.7. Case Study 3 - Morenny Rock-Glacier, Tien Shan Mountains, Kazakhstan.

The Tian Shan, is a vast system of mountain ranges in Central Asia that spans several countries, mainly located in Kyrgyzstan and the northwestern territory of China. Tectonic activity in the Tien Shan is the result of northward-moving India plate colliding with Eurasia plates that also uplifted other adjacent mountain ranges: Alai, Karakoram, Pamirs and Hindu Kush (Avouac and Tapponnier, 1993; Komatsu, 2016; Blayney et al., 2019). The geological composition of the Tian Shan system varies across its expanse, with the geology of the northeastern part predominantly characterized by bedrock formations (dominant lithology is granite), that probably have a role in shaping the landscape and influencing the hydrology of the area (Brunet et al., 2017). The northern Tien Shan mountains encompass a significant area of periglacial landscapes, representing extremely cold, non-glaciated terrain that is typically adjacent to alpine glaciers in mountainous regions (Bolch and Marchenko, 2009; Bolch and Gorbunov, 2014; Liu et al., 2017; Kääb et al., 2021). Within periglacial landscapes, common mass wasting types associated with cryogenic process are creep, gelifluction, and sliding (Black, 1976) which give rise to various cryogenic landforms. As a response to warming of alpine permafrost in Tien Shan, rock glaciers have begun to creep faster, as has been observed in other alpine regions globally (Haeberli et al., 2006; Haberkorn et al., 2021). The dynamics of rock glaciers is important to understand for assessing short- and long-term environmental changes that permafrost degradation can cause in alpine regions (Harris, 2005; Streletskiy et al., 2015; Arenson and Jakob, 2015). One of the fast-moving rock glaciers in the Bolshaya Almatinka valley in northern Tien Shan is the Morenny rock glacier, with displacement rates exceeding 1 m/year and classified as "active" according to the International Permafrost Association standardized guidelines for rock glaciers inventory (RGIK, 2023).

The spatial and temporal changes in the movement of Morenny rock glacier were studied independently by analyzing image correlation techniques (Fig. 5.10a) via offset tracking of aerial, historical, and modern high-resolution optical images (Kääb et al., 2021) and differential SAR interferograms (Fig. 5.11a). The study has shown 2-4 times increased surface velocity on rock glaciers within northern Tien Shan mountains compared to 1950 and 1960. Besides the overall rapid movement of Morenny rock

glacier, exceeding displacement velocity by 1 m/year, a distinct fast-flowing branch with up to 2.5 m/year displacement diverts from the main body of the rock glacier towards the northwest (Figs. 5.10, 5.11). We processed both PlanetScope optical imagery (Figs. 5.10 and 5.11) and Sentinel 1 (Ascending and Descending orbits) (Figs. 5.12, 5.13) back scatter radar imagery using AkhDefo software to produce temporal deformation maps for the summer periods between 2017 to 2023. Additionally, the land surface temperature over the northern Tien Shan region was estimated using Google Earth Engine from Landsat 8 dataset between 2017 to 2020 (Figs. 5.13, 5.14) for summer months of July and August for each year.

5.7.1. Kinematics of the Rock Glacier Movement

The kinematic process of rock glaciers is characterized by gradual downslope movement, which results from the internal deformation of the permafrost ice within these landforms (Müller et al., 2016; Strozzi et al., 2020; Kummert et al., 2021). This movement is not just an internal phenomenon but is also apparent on the surface, showing displacement that varies across the landform exterior. This displacement is indicative of the underlying processes at work and is crucial for the study of rock glacier dynamics. In exploring the kinematics of rock glaciers, researchers (Müller et al., 2016; Strozzi et al., 2020; Kummert et al., 2021) focus on various parameters including the speed at which the surface moves, the patterns of flow observed, the displacement rates at which these movements occur, and how these movements change over time. Understanding these kinematic attributes is essential for deciphering the complex behavior and dynamics of rock glaciers, especially considering the backdrop of evolving environmental conditions. Rock glaciers are complex systems influenced by a variety of factors including the amount of sediment and ice they receive, the state of the permafrost within them, and their geomorphological setting (Kummert et al., 2021). These factors collectively shape the physical properties and morphology of rock glaciers. Understanding the rock glacier movement patterns is essential for forecasting their reactions to climatic changes, which is becoming increasingly crucial as global temperatures rise.

During summer 2018 from August 24 to September 5, a previous study (Kääb et al., 2021) identified four zones of active deformation at Morenny rock glacier based on

Sentinel 1 descending orbit interferogram (Fig. 5.11). However, due to the limitations of traditional InSAR, the study was unable to unwrap the interferogram hence, and only approximate deformation was provided. We reanalyzed the same Sentinel 1 descending orbit radar backscatter images (from August 24 to September 5) using an optical flow algorithm technique, which was incorporated into the AkhDefo software for this study. Zones 1 and 2 show displacement rates 30 to 40 cm per twelve days towards north northwest, hence, movement away from the satellite line of site. In contrast, zones 3 and 4 show slower displacement rate around 10 cm per 12 days towards north, northwest and north northeast, respectively. Our results were consistent with the aforementioned study and provided accurate deformation measurements along line of site for the four active zones with rock glacier body (Fig. 5.11 a and c).

The analysis of Sentinel 1 radar backscatter images (Ascending and Descending) and PlanetScope optical imagery over 7 summer seasons from 2017 to 2023, provided detailed deformation patterns of the Morenny rock glacier have been documented. The Morenny rock glacier exhibits a complex and varied movement pattern, with its slope oriented in a north-south direction (Fig. 5.12d). Motion velocity vectors show significant subsidence exceeding 5 to 10 cm annually on the upper slope (Fig. 5.13), and an uplift exceeding 5 to 10 cm annually on the lower slope (Fig. 5.13) and overall north-northwest direction horizontal movement (Fig. 5.12). We conducted simulations of both subsidence and uplift patterns (Fig. 5.15) and used them for validation against the actual motion vectors observed on the rock glacier. Specifically, subsidence is characterized by inward-moving vectors (Fig. 5.15), while uplift is indicated by outward-moving vectors (Fig. 5.15). These patterns were discerned from both radar (Ascending and Descending) and optical imagery datasets, with the motion vector patterns being more pronounced in optical imagery. This is attributed to the fact that optical satellites capture data from a nearly vertical perspective, whereas radar satellites acquire data at an oblique angle, a difference that was clearly evident in our analysis of the velocity vector motions.

This period also included the analysis of processed land surface temperatures over four summers, from 2017 to 2020. The analysis points to a significant increase in the movement of the rock glacier by approximately 1 meter annually since 2017, which aligns with findings from prior studies(Kääb et al., 2021). Additionally, a consistent annual increase in the summer land surface temperature of about 0.5°C from 2017 to 2020 was observed, suggesting a correlation with the accelerating movement of the rock glacier (Sorg et al., 2015; Kääb et al., 2021).
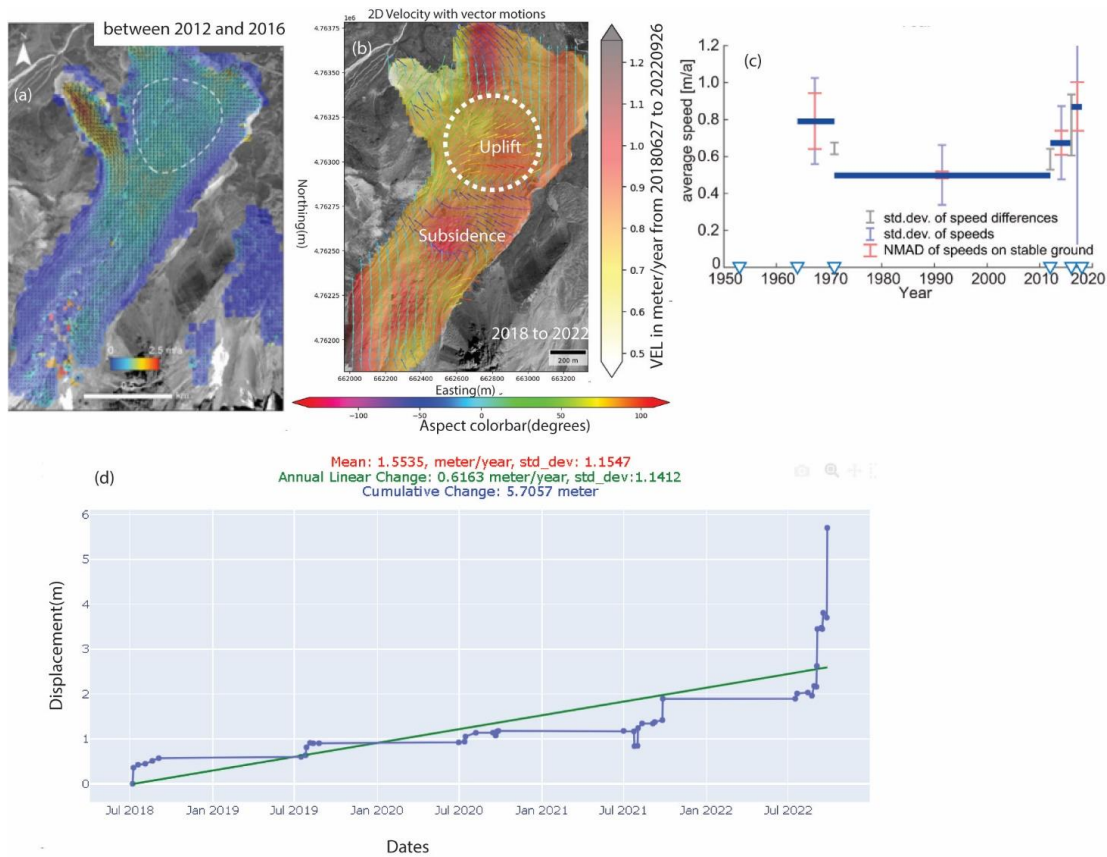
Figure 5.10. **Velocities and speed variations on the Morenny rock glaciers from optical imagery. (a) Colour-coded velocity fields with vectors superimposed from image matching between two images 2012 and 2016 high-resolution satellite images (after Kääb et al., 2021). (b) Mean annual velocity with vector motion from AkhDefo optical flow for five years during summers 2018 to 2022. (c) Average time series of speeds for clusters of points (white dashed outline in panel a). (d) Average time series profile shows cumulative deformation from 2018 to 2022 (white dashed outline in panel b).**
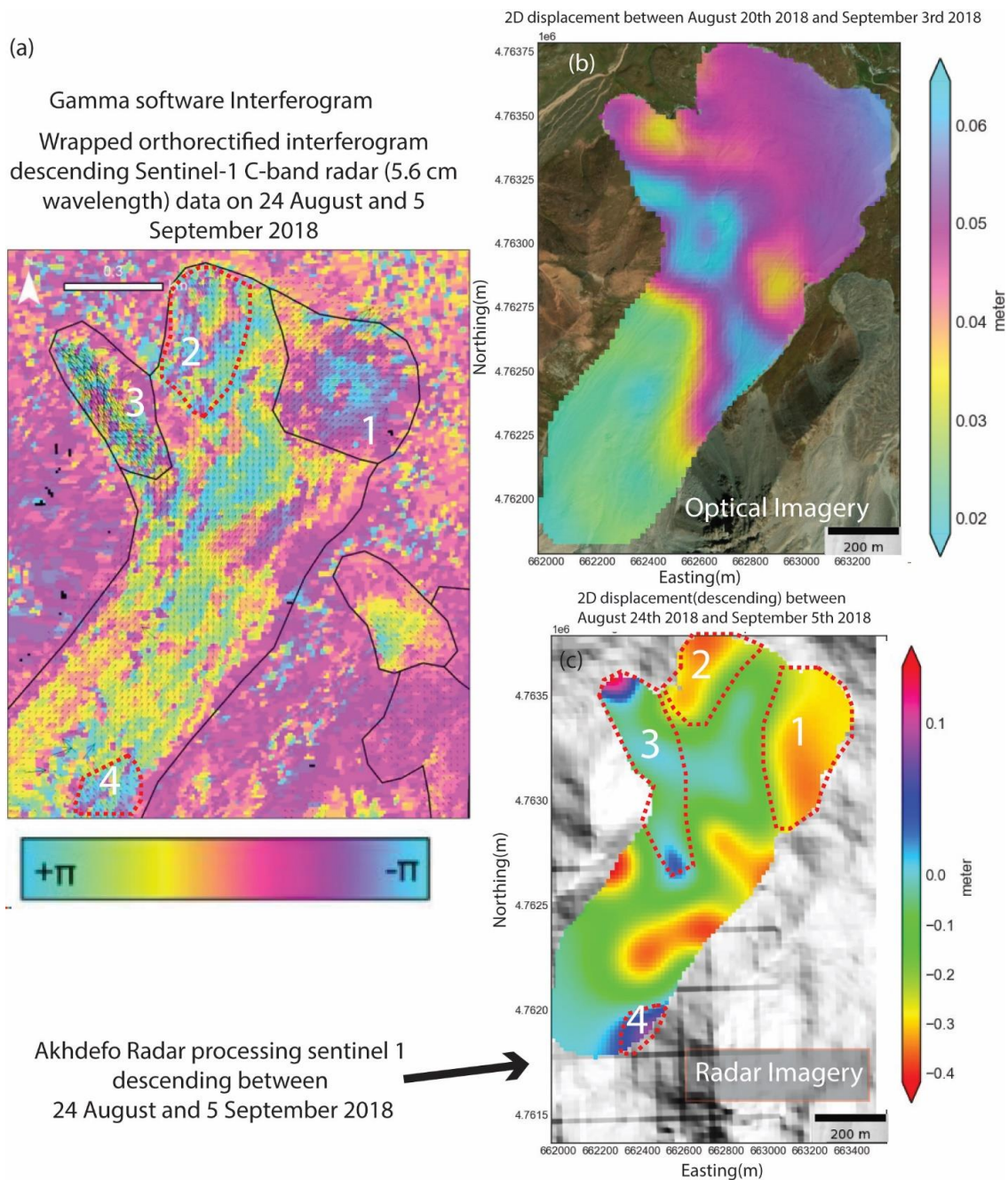
Figure 5.11. **Comparison between Gamma software interferogram with AkhDefo software processing results for both Radar and Optical imagery. (a) Wrapped orthorectified interferogram descending Sentinel-1 C-band radar (5.6 cm wavelength) data on 24 August and 5 September 2018. (b) Displacement product calculated from optical imagery between August 20 and September 3, 2018. (c) Displacement product calculated from Sentinel 1 Descending orbit radar back scatter imagery between August 24 and September 5, 2018. Note, the decorrelation due to large movement appears in the interferogram which is beyond traditional InSAR capability to unwrap.**
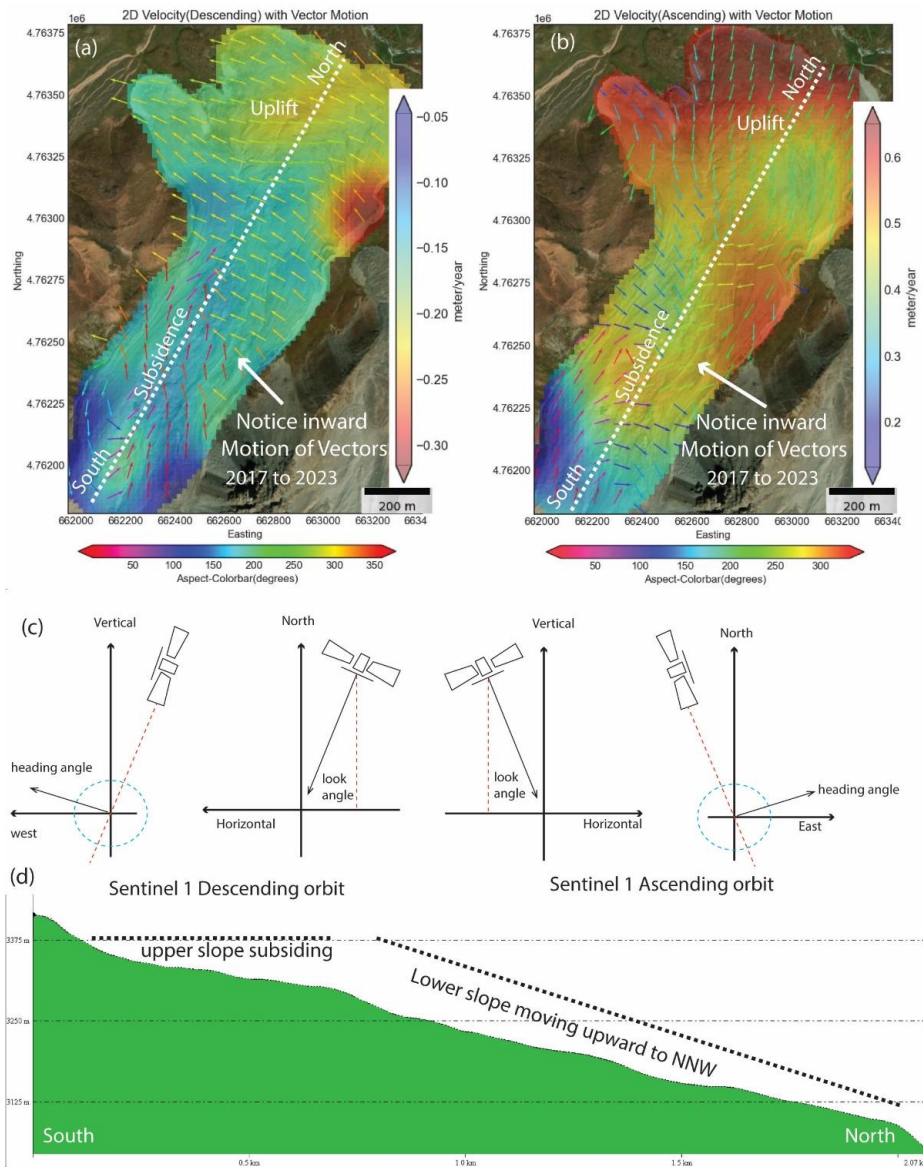
Figure 5.12. **2D linear annual displacement magnitude. (a) Mean annual velocity calculated based on Sentinel 1 Descending orbit Radar back-scatter imagery between July 2017 and August 2023. (b) Mean annual velocity calculated based on Sentinel 1 Ascending orbit Radar back-scatter imagery from July 2017 to September 2023. The arrows represent the displacement aspect; notice the displacement vectors in both Ascending and Descending indicate overall North and Northwest movement of the rock-glacier. (c) Diagram explaining the concept of radar satellite Line of Sight geometry. (d) Elevation profile from south to north show slope geometry along the white dotted line in a and b.**
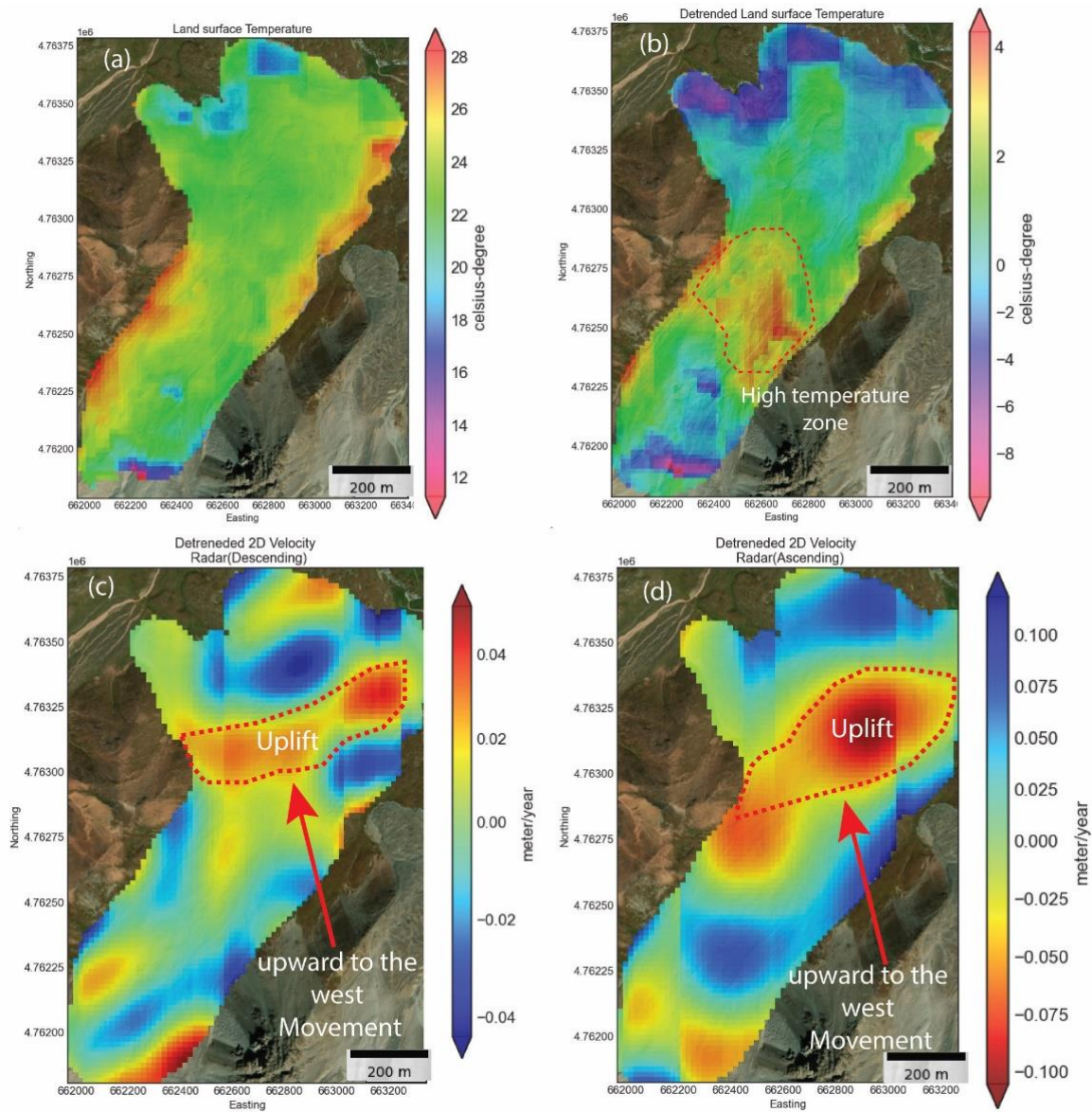
Figure 5.13. Comparison between land surface temperature and detrended displacement velocity. (a) Mean land surface temperature for July and August between 2017 and 2020. (b) Detrended mean land surface temperature for July and August between 2017 and 2020. (c) Detrended linear annual velocity calculated based on Sentinel 1 Ascending orbit Radar back-scatter imagery from July 2017 to September 2023. (d) Detrended linear annual velocity calculated based on Sentinel 1 Descending orbit Radar back-scatter imagery from July 2017 to September 2023. Note, the dashed red polygon in both ascending and descending orbit moves upward to the west direction.
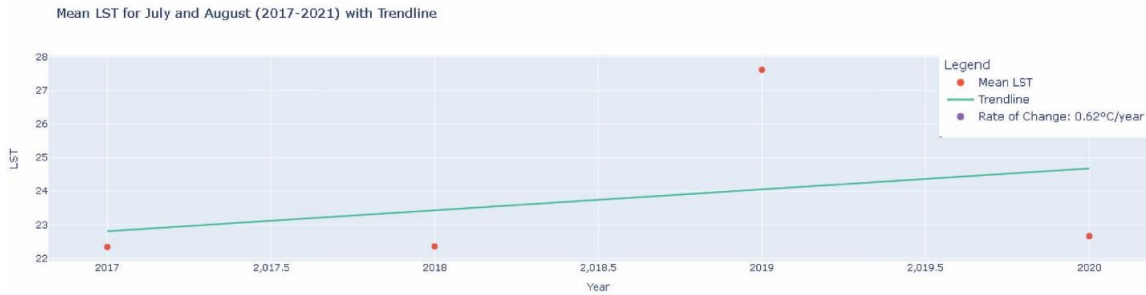
Figure 5.14. **Time-series for mean land surface temperature for combined months July and August between 2017 and 2020. Notice, increased land surface temperature rate by more than 0.5°C per year particularly during the summer of 2019.**
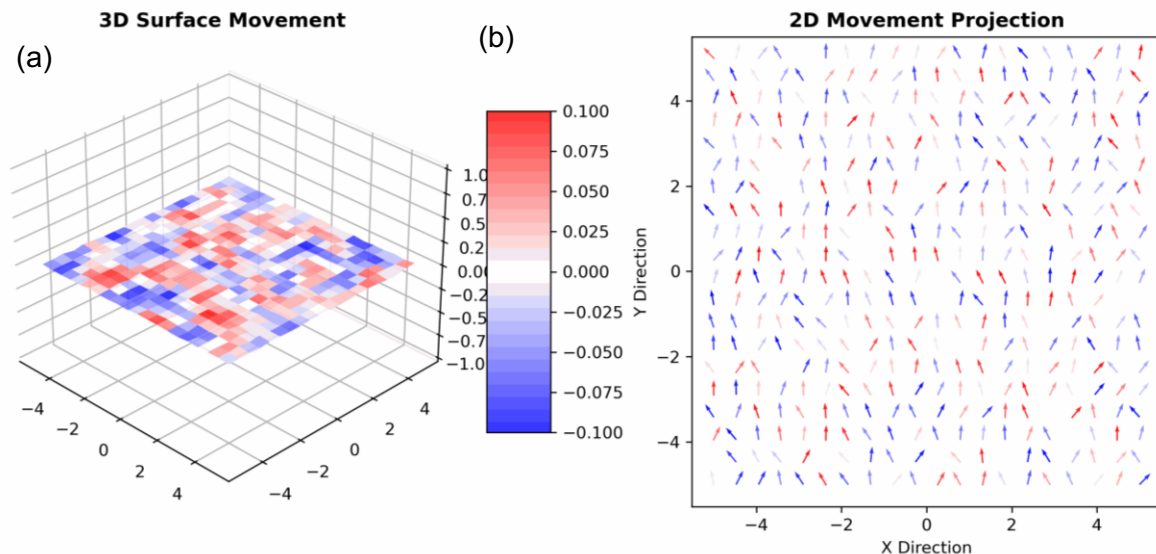
Figure 5.15. **(a) 3D synthetic simulation of motion pattern. (b) 2D projection of 3D motion pattern. Notice in case of upward motion (red arrows) the motion of arrows is outward and in case of subsidence (blue arrow) the motion of arrows is inward. See Figures 5.12 and 5.13 and notice subsidence at the upper slope (south) and uplift at the lower slope (North).**

5.8. Discussion

Remote sensing datasets, particularly those derived from satellite imagery such as radar and optical, have become invaluable tools in landslide monitoring. They offer new

avenues for early warning, risk assessment, and the formulation of mitigation strategies (Bürgmann et al., 2006; Wei et al., 2010). Furthermore, there is a wide range of both commercial and open-source software options for analyzing these remote sensing datasets. However, in the realm of landslide and hazard mitigation, time is of the essence. The quicker the data is processed; the sooner policymakers and emergency responders can act to protect lives and safeguard economic infrastructure.

The importance and the critical role of rapid, real-time data processing have inspired us to further develop a novel open-source package called AkhDefo. This study's contribution to the AkhDefo software package allows for the processing of both radar satellite imagery and optical imagery (from satellite and ground sources), using innovative techniques different from those found in existing software solutions. The core processing mechanism is anchored in the utilization of the hierarchical optical flow algorithm which operates on a principle of multi-resolution computation, initiating the process at a coarse lower resolution before progressively refining the analysis at higher resolutions. Such a multi-scale approach dramatically lessens the computational burden and accelerates the overall process. This efficiency enables quicker motion estimation compared to traditional exhaustive image correlation methods that analyze images at their full resolution.

Despite the advantages, optical flow techniques face certain challenges, including the assumption of consistent brightness across sequences of images and the handling of scenes with both minor and significant motion changes. Nevertheless, the AkhDefo implementation and workflow effectively mitigated these drawbacks. The strategies employed to overcome these challenges are described in the supplementary materials (Appendix D) and the methodology section.

In this research, we applied optical flow techniques to analyze real-time ground-based webcam footage, optical satellite images, and radar images. These datasets were applied to study different types of landslides, including the Mud Creek rockslide in California, USA, rockfall at Squamish Chief in British Columbia, Canada, and the rock glacier deformation at the Morenny rock-glacier in Kazakhstan.The well studied May 2017 Mud Creek landslide was an ideal case study to perform back analysis and test various remote sensing datasets and hypotheses. Here we processed daily satellite optical imagery and estimated the landslide volume solely based on pre-failure datasets.

Our study provided reasonable estimates of 2,976,000 m^3 which agreed with volume estimation from LiDAR point cloud change detection of 3,500,000 m^3 (Warrick et al., 2019). Additionally, we provided higher temporal resolution up to one-day interval time-series deformation for the Mud Creek Landslide, months before the landslide event which in turn if the data had been processed beforehand, we could have predicted the landslide occurrence solely based on the satellite optical imagery.

To scale the reliability of landslide and rockfall monitoring system, it is important to assess the strength and limitations of the system in terms of efficiency such as speed of data processing and measurement quality such as identifying uncertainty and reliability of the measurements. The developed system's capability to analyze 600 frames per hour (Fig. 5.7b and c) from a high-definition live video stream via an online server, which translates to roughly 0.167 frames per second, indicates its processing power. Although, in real-time processing terms, the system seems slow for video processing to initiating instant warning, its application can nevertheless be seen as an important tool for natural hazard monitoring. For instance, this system can be used to monitor the frequency of rockfalls, hence, understanding the mechanisms and patterns of rockfall occurrence. Additionally, unlike rockfalls which often occur without knowing precursor instability or warning if applied to other natural hazards such as rapid moving landslides and debris flow settings, it allows the generation of timely warning and alert to communities living close by such natural hazards within a fraction of minutes of the landslide failure.

The fast-moving Morenny rock glacier is a profound example of the recent permafrost warming problem in the high alpine regions of Central Asia. Developing countries in this region have significant areas of periglacial landscapes yet lack sufficient resources and infrastructure to study the alpine permafrost. This might be the case in many other alpine regions in the world. Thus, publicly available remote sensing data, as well as accessible computational software such as AkhDefo are often the only resources for scientists and practitioners in developing countries to conduct research on most recent environmental changes related to alpine permafrost.

Deformation data, such as displacement rates derived from Sentinel 1 radar imagery and PlanetLab satellite optical imagery, alongside land surface temperature measurements can be used as a foundation for forming preliminary assumptions about

the driving forces behind the increased movement observed in Morenny rock glaciers and for shedding light on the morphological characteristics of these movements.

5.9. Conclusions

In this research, we utilized optical flow techniques to analyze real-time ground-based webcam footage, optical satellite images, and radar images. These datasets were applied to study different types of landslides, including the Mud Creek rockslide in California, USA, rockfall at Squamish Chief in British Columbia, Canada, and the rock glacier deformation at the Morenny rock-glacier in Kazakhstan. Our findings include:

1. We achieved a higher temporal resolution, providing daily time-series deformation data for the Mud Creek Landslide, and calculated the volume of the landslide using a pre-failure dataset.
2. We created a near real-time system for detecting rockfalls using live-streamed webcam footage, with video processes latency time of a few minutes per hour. Therefore, we propose a low cost, near real-time rockfall detection workflow system as an additional toolbox to the existing rockfall monitoring methods.
3. We analyzed the temporal displacement rates of an active rock-glacier utilizing both satellite optical and radar imagery. The AkhDefo software was applied to rock glaciers as a relatively cost effective and user-friendly method in contrast to more time-consuming and heavy data processing methods, including the digital image correlation, and offset tracking techniques mentioned above.
4. We introduced cutting-edge optical flow algorithm workflows, which have been incorporated into the open-source Python package AkhDefo, enabling the processing of various datasets, including live-streamed webcam footage, satellite optical, and radar backscatter imagery.
5. Our use of the AkhDefo software's workflow has shown that optical flow techniques can outperform traditional computer vision methods like DIC, particularly in handling large datasets for long-term, real-time analysis.
6. We have made the datasets, tutorials, and the open-source Python package publicly available, facilitating the replication of our research and methodologies worldwide.

Chapter 6.   Conclusions and Future Work

6.1. Synthesis

Exploration of natural resources frequently occurs in areas with challenging climates and geological conditions. Southwestern British Columbia, with its significant potential for geothermal resources stemming from volcanic centres like the Mount Meager Volcanic Complex, is one such area. However, it has also experienced significant glaciation and deglaciation periods, leading to natural hazards including landslides. The coexistence of opportunities and challenges such as geothermal exploration and natural hazards requires thorough consideration of existing technologies and a need to develop new workflows to maximize the benefits of the resources while mitigating the associated natural hazards.

This thesis brings together structural geology, remote sensing, and geotechnical analysis to define the challenges, opportunities and proposed new solutions to complement the existing technologies to mitigate and monitor landslides and rockfalls in Southwestern British Columbia, particularly Mount Meager Volcanic Complex (MMVC) and Mount Currie scarp. Additionally, the proposed workflow and newly developed solutions were tested on other well studied landslides such as the May 20, 2017, Mud Creek landslide in California, USA, mass movement such as the Morenny Rock-Glacier, Tien Shan Mountains in Kazakhstan and rockfalls from the Stawamus Chief in Squamish, Vancouver-Canada.

6.2. Thesis chapters in a nutshell

Chapter 1 presented a literature review and existing knowledge of southwestern British Columbia and MMVC geothermal potential and associated natural hazards. It reviewed the existing solutions such as structural geology, remote sensing and geotechnical modeling, advantages, and limitations available in the literature to study natural hazards. Furthermore, it discussed the possibility of various methodologies to deploy low-cost solutions such as ground-based camera installation to complement the current remote sensing techniques such as Synthetic Aperture Radar.

Chapter 2 documents the application of low-cost static ground-based imagery for remote surveillance of slope instability. It describes a computer vision open-source code developed here to process daily and hourly static ground based optical imagery. The open-source code is capable of measuring sub-centimetre scale displacement of slopes of interest using an optical flow algorithm.

Chapter 3 documented detailed bedrock mapping and structural geology of the Mount Meager Volcanic Complex. It explained and collated the benefits of the existing known structural geology features such as faults and folds to geothermal resource exploration as well as associated natural hazards. The study employed field-based geology mapping, classic structural geology kinematic analysis, paleomagnetic dating and isotope geochronology to date the sequence of deformation in the last 5 Ma in MMVC.

Chapter 4 developed an advanced workflow that integrates various disciplines such as structural geology, geotechnical modeling, and satellite remote sensing. This approach aims to overcome the complexities and obstacles of investigating landslides and natural disasters in alpine regions characterized by tectonic and climatic variations and surrounded by rainforests. The developed approach was applied to Mount Currie in southern British Columbia, Canada. We addressed key questions such as the primary triggers for failures at Mount Currie, identified critical areas requiring further investigation and long-term monitoring through radar time-series imagery, documented the influence of neotectonic activities on the formation of Mount Currie's ridge scarp and ongoing rockfalls on the mountain's north face, and constructed a structural safety map for specific slopes.

Chapter 5 further justified the application of the newly developed in Chapter 2 remote sensing technology to other mass movements around the world such as rock glacier and rockfall. Additionally, new capabilities were added to the developed software to enable processing of not only static optical imagery bult also radar imagery and processing live video streams. This led to expansion of the developed open-source code and transformation to a stand-alone geospatial python programming software.

6.3. Added Value to Mount Meager Knowledge

Q̓welq̓welústen, also known as the Mount Meager Volcanic Complex (MMVC, Mt. Meager), is located at the northern end of the Garibaldi Volcanic Belt (GVB) and has been identified as a promising area for geothermal resources since the 1970s. Since then, numerous geothermal exploration campaigns have been conducted in the area involving geophysical surveys, geochemical studies, and bedrock mapping. This volcanic complex has a history of a catastrophic volcanic eruption dates to 2360 years before present. Additionally, it hosts the largest historical landslide in Canada that occurred in 2010 at the southeastern flank of the volcanic massif. Despite this wealth of existing data and intermittent geothermal exploration campaign at MMVC, very little known about the surface structural geology, sequence of deformation and structural kinematic relationship between faults and folds within the mountain complex.

This study conducted detailed surface structural geology field mapping, paleomagnetic measurements, and radiometric dating of volcanic rocks to define the kinematic history and kinematic compatibility of outcrop scale structural geology features such as faults and folds. This study documented geometrical and geospatial relationships between subsequent deformation stages, proposed in depth structural geology model to explain how MMVC deformed and shaped at least during the last 5 Ma. Subsequently, it presented explanations of how and where to harness geothermal exploration within the mountain complex. Furthermore, we identified the likelihood of geological structure that might pose natural hazard such as earthquake, landslide, and volcanic activity.

The explained structural geology hypothesis supports the fact that the bounding Meager Creek and Owl Creek faults first developed after 5 Ma, and subsequently initiated internal deformation such as the northwest–southeast-trending Capricorn fault and caused extensive uplift and exhumation at the centre of the massif after 1 Ma. The early stage of deformation, 5–1 Ma, likely facilitated the ascent of subsurface magmas and formation of early-stage volcanism within the Mt. Meager massif. As the deformation progressed and evolved, internal faults such as Capricorn Fault developed and supported further exhumation of the crystalline basement; at this stage deformation was largely controlled by local stress. Additionally, this stage is manifested over the last 1 Ma and is aligned with volcanism due to mountain edifice instability related to uplift and exhumation of crystalline basement. In addition, secondary north northeast–south

southwest striking faults, such as the No-Good Discontinuity and Camp faults, trend oblique to the principal deformation zone and may represent antithetic Riedel shear fractures responsible for north–south displacement of basement rocks.

This complex structural geology and long-lived volcanic history of Mt. Meager also enhances the risk of surface displacements (e.g., landslides) due to enhanced alteration by ascending hydrothermal fluids through the weakened crystalline basement and volcanic rocks. Strain transfer between interconnected fault segments can also lead to the amplification of seismic events that have the potential to trigger severe natural hazards like deep-seated landslides, involving significant rock-volume collapse, and even the potential for a volcanic eruption. These risks are especially relevant when considering the extensive magmatic plumbing system beneath MMVC (~5–15 km depth).

The contrasting volcanic stratigraphy between the hanging wall and foot wall of the Capricorn fault at the centre of the MMVC suggests that the fault may have accommodated approximately 1 km of uplift and erosion of volcanic units. The Líĺwat people of the Interior Plateau of British Columbia have an oral tradition describing how their ancestors used to climb Mount Meager (Angelbeck et al., 2024). According to the account, these climbers could see the ocean, which is not possible today due to the mountain being surrounded by many other high peaks and the Strait of Georgia being several mountain ridges to the west. However, viewshed analyses of the mountain's potential height before its eruption revealed that the ocean would have been visible if the mountain were at least 950 meters taller than it is today (Angelbeck et al., 2024). Furthermore, andesitic lavas dated using the $^{40}Ar/^{39}Ar$ at Pylon Peak (Table. 3.1 in Chapter 3 and Appendix B3) provided a radiometric age of 65 ± 70.6 ka, along with paleomagnetic signatures indicating approximately 10 degrees of rotation and tilting of the andesitic lavas. This suggests that the Mount Meager Volcanic Complex (MMVC) has been tectonically active in the last 60,000 years.

6.4. Added Value to Mount Currie Knowledge

Mount Currie, situated around 100 km north of Vancouver within the Pemberton district, is a gravitational escarpment structure influenced by both climate and tectonics. Tectonically, Mount Currie coincided with the present-day Garibaldi Volcanic Belt (GVB)

within the Coast Plutonic Belt (CPB). The proximity of CPB in the western Canadian Cordillera to the Pacific Ocean results in the ice-clad mountain piedmonts being enveloped by dense rainforests. The region has undergone multiple glaciations, including the Fraser glaciation, and is also an area of active tectonics, which complicates the identification of the causes of slope failures and scarp development, especially within the CPB. This complexity obscures the visibility of rock exposures. Moreover, the region's history of repeated ice ages has made it even more challenging to differentiate between original rock formations and kinematic indicators. Consequently, the study of scarps, features of gravitational failure, and neotectonics in southwestern British Columbia is fraught with difficulties and requires thorough assessment.

In this research, we conducted a detailed examination of how structural geology, specifically the sequence of deformation and related fracture patterns, affected geological formations. We discussed how primary features of structural geology, like faults and folds, contributed to slope instability. We then applied three-dimensional geotechnical modeling at different scales, ranging from field-based discontinuity assessments at the outcrop levels to regional-scale analyses of well-defined faults. Additionally, from 2018 to 2020, we monitored displacement through Synthetic Aperture Radar, pinpointing areas of active movement.

The current results suggest that the Mount Currie scarp, which extends from east-northeast to west-southwest, likely formed as a gravitational collapse fault. This faulting is influenced more by localized stress patterns within the mountain itself rather than direct seismic activity. These local stresses are mainly controlled by the bounding Owl Creek and Miller Creek faults, both of which are significant thrust faults surrounding the Mount Currie complex, as well as the effects of crustal rebound due to glacial melting. Additionally, we pinpointed a critical block on the NE-3 peak at the core of the Mount Currie ridge that shows a significantly higher risk of failure compared to other areas. Should this block fail, we estimate that at least 14.4×10^6 m^3 of bedrock could be displaced.

6.5. The Merit of AkhDefo Software

Remote sensing data, especially from satellite sources like radar and optical imaging, have proven essential for monitoring landslides. These tools provide early warning

possibilities, risk evaluations, and the development of strategies to mitigate disasters. Additionally, numerous commercial and open-source software are available for processing these datasets. However, in the context of landslide risk management, prompt data analysis is crucial. Faster data processing allows for quicker decision-making by policymakers and emergency services, which is vital for protecting lives and preserving economic assets.

Digital Image Correlation (DIC) is a widely used method for measuring displacement and slope instability from optical imagery and radiometrically corrected radar images. DIC is particularly noted as a leading method for detecting displacement through optical imagery. While DIC and similar speckle tracking methods are recognized for their ability to determine ground displacement from radar backscatter and optical images, their real-time application is restricted by the extensive processing they require. Moreover, these techniques rely on a trial-and-error method to choose an appropriate correlation window for matching, which affects the accuracy of the measurements. If the window is too small, particularly in cases of large displacements, it may not cover the entire movement, resulting in partial or inaccurate measurements. Conversely, a large window can cause small displacements to be overlooked or obscured within a larger analysis area.

In contrast, the recently introduced AkhDefo utilizes a coarse-to-fine dense optical flow algorithm that involves filtering and re-sampling the original image at progressively lower resolutions. This creates a pyramid of down-sampled images, from coarse to fine. The process starts with establishing an approximate match at the lowest resolution, which then directs the focus to a smaller area in the subsequent higher resolution image. This method is iteratively refined, moving step-by-step towards the full resolution of the original image. Subsequently, the algorithm can then detect the movement of both small and large objects. Additionally, the AkhDefo workflow has shown that optical flow techniques can outperform traditional computer vision methods like DIC, particularly in handling large datasets for long-term, real-time analysis.

In the field of optical flow visualization, selecting the right interpolation method is critical, particularly when handling datasets that include a variety of displacements ranging from minor to major. Small motions are generally simpler to interpolate due to less variability; however, the complexity escalates with the inclusion of larger displacements. AkhDefo software uses more sophisticated interpolation techniques like Kriging, which is favored

for its ability to incorporate spatial correlations and adapt to varying scales of motion, providing a more accurate representation of the movement in the visualized data. The AkhDefo package utilizes an auto variogram method that aligns data with various models to find the best fit based on the coefficient of determination ($R2$), thus ensuring the interpolation reflects true spatial patterns effectively and accurately. This approach is instrumental in enhancing the precision and reliability of interpolations across various applications, from environmental science to geostatistics.

6.6. Future work

In this thesis geological challenges and opportunities in Mt. Meager's geothermal exploration are presented, discussed the importance of genesis, structural geology kinematic analysis and geotechnical kinematic analysis of major structures such as folds and faults in producing slope instability in Mt. Currie and developed state of the art remote sensing software and methods to monitor land deformation and landslides.

For Mount Meager, a comprehensive structural geology model is presented that could open new opportunities for mineral exploration in addition to the existing geothermal potential. Further work is needed to investigate the geometry, shape, and linkage of the MMVC restraining bend structure to nearby structures to understand if the bend represents the termination of a strike-slip fault, a double bend along a single linked strike-slip fault, or a stepover where parallel strike-slip fault segments are offset and may or may not overlap. Restraining bend structures are also considered as important regions for resource exploration as it facilitates the exhumation of deeper basement structures that might hold significant mineral and energy resources. Additionally, 3D reflection seismic survey at MMVC would be extremely beneficial in constraining the subsurface fault linkages, and extent of the geothermal and magmatic reservoirs. This would aid not only in geothermal and mineral exploration, but also in better understanding the complex physical relationships between geohazards such as earthquakes, landslides, and volcanic eruptions.

Mount Currie natural hazards including rockfall and potential landslide is mainly controlled by gravitational collapse and climate. Additional work would be useful to better constrain the subsurface geology and the estimated volume of potential slope failures. It would be important to constrain whether the height of the critical keyblock could be

truncated at depth by unidentified structures i.e., the likelihood of one large wedge failure or smaller failures. Hence, further geotechnical analysis and modelling is advised such as incorporating photogrammetry derived discontinuity measurement to perform 3D kinematic analysis.

This will aid in achieving more accurate spatial coverage for the likelihood of failed blocks at selected mountain slopes. Additionally, it is advised to perform more complex geotechnical modelling such as 3DEC (3D Distinct Element Code) to better understand the deformation mechanisms for the slopes of interest. It is important to note that the displacement rates estimated from the InSAR satellite data presented in this study might have been underestimated due to the north-south orientation of the Mount Currie slope. Satellite InSAR struggles to accurately detect north-south movement because of line-of-sight limitations. Therefore, high temporal resolution terrestrial LiDAR monitoring, conducted weekly to monthly, is recommended, particularly during the summer months. Furthermore, a risk assessment should be conducted, including landslide runout modeling, especially considering the proximity of human infrastructure at the base of the mountain, such as Pemberton Airport, Indigenous communities, and, most importantly, the presence of the Green River. A landslide could create a temporary dam, and its failure could generate secondary hazards such as flooding to nearby communities in the Pemberton Valley.

I also aim to further develop the state-of-the-art remote sensing and geospatial software AkhDefo to monitor landslide and Rock Falls. The current capabilities of the software include measuring land deformation from satellite and ground based optical imagery, satellite Radar imagery and live-stream video for rockfall detection. I strongly recommend further investment in processing optical digital imagery due to its low cost and the availability of datasets with better spatial and temporal resolution.

References

Abdullah, A., Akhir, J., and Abdullah, I., 2010, Automatic Mapping of Lineaments Using Shaded Relief Images Derived from Digital Elevation Model (DEMs) in the Maran – Sungi Lembing Area, Malaysia: Electronic Journal of Geotechnical Engineering, 15 Bundle J, v. 15.

Agisoft LLC, 2022, AgiSoft PhotoScan Professional:, Retrieved from http://www.agisoft.com/downloads/installer/ (accessed May 2024).

Akram, M.S., Mirza, K., Zeeshan, M., and Ali, I., 2019, Correlation of Tectonics with Geologic Lineaments Interpreted from Remote Sensing Data for Kandiah Valley, Khyber Pakhtunkhwa, Pakistan: v. 93, doi:https://doi.org/10.1007/s12594-019-1224-7.

ALHIRMIZY, S., 2015, • Automatic Mapping of Lineaments Using Shaded Relief Images Derived From Digital Elevation Model (DEM) in Kirkuk northeast Iraq: International Journal of Science and Research (IJSR), v. 4, p. 2319–7064.

Amaki, K., Yamaguchi, T., and Harada, H., 2019, Landslide occurrence prediction using optical flow, in 2019 19th International Conference on Control, Automation and Systems (ICCAS), Jeju, Korea, IEEE, v. 2019-Octob, p. 1311–1315, doi:10.23919/ICCAS47443.2019.8971698.

Angelbeck, B., Springer, C., Jones, J., Williams-Jones, G., and Wilson, M.C., 2024, Líĺwat Climbers Could See the Ocean from the Peak of Qẃelqẃelústen: Evaluating Oral Traditions with Viewshed Analyses from the Mount Meager Volcanic Complex Prior to Its 2360 BP Eruption: American Antiquity, p. 1–21, doi:10.1017/aaq.2024.26.

Arenson, L.U., and Jakob, M., 2015, Periglacial Geohazard Risks and Ground Temperature Increases, in Engineering Geology for Society and Territory - Volume 1, Cham, Springer International Publishing, p. 233–237, doi:10.1007/978-3-319-09300-0_44.

Arianpoo, N., Ghomshei, M.M., and Meech, J.A., 2009, the geothermal potential of clarke lake and milo gas fields in northeast british: The University of British Columbia, 123 p., doi:https://dx.doi.org/10.14288/1.0070835.

Asner, G.P., 1998, Biophysical and Biochemical Sources of Variability in Canopy Reflectance: Remote Sensing of Environment, v. 64, p. 234–253, doi:10.1016/S0034-4257(98)00014-5.

Avouac, J., and Tapponnier, P., 1993, Kinematic model of active deformation in central Asia: Geophysical Research Letters, v. 20, p. 895–898, doi:10.1029/93GL00128.

Balfour, N.J., Cassidy, J.F., Dosso, S.E., and Mazzotti, S., 2011, Mapping crustal stress and strain in southwest British Columbia: Journal of Geophysical Research: Solid Earth, v. 116, p. 1–11, doi:10.1029/2010JB008003.

Barnhart, W.D., 2017, Fault creep rates of the Chaman fault (Afghanistan and Pakistan) inferred from InSAR: Journal of Geophysical Research: Solid Earth, v. 122, p. 372–386, doi:10.1002/2016JB013656.

Barron, J.L., Fleet, D.J., and Beauchemin, S.S., 1994, Systems and Experiment Performance of Optical Flow Techniques: International Journal of Computer Vision, v. 12, p. 43–77.

Benko, B., 1997, Numerical Modelling of Complex Slope Deformations: University of Saskatchewan, 278 p.

BGC, 2018, Mount Currie Landslide Risk Assessment – Final: Squamish-Lillooet Regional District.

Birkill, A., 2024, Stawamus Chief webcam:, https://chiefcam.com.

Black, R.F., 1976, Periglacial features indicative of permafrost: Ice and soil wedges: Quaternary Research, v. 6, p. 3–26, doi:10.1016/0033-5894(76)90037-5.

Blais-Stevens, A., Hermanns, R.L., and Jermyn, C., 2011, A 36Cl age determination for Mystery Creek rock avalanche and its implications in the context of hazard assessment, British Columbia, Canada: Landslides, v. 8, p. 407–416, doi:10.1007/s10346-011-0261-0.

Blayney, T., Dupont-Nivet, G., Najman, Y., Proust, J., Meijer, N., Roperch, P., Sobel, E.R., Millar, I., and Guo, Z., 2019, Tectonic Evolution of the Pamir Recorded in the Western Tarim Basin (China): Sedimentologic and Magnetostratigraphic Analyses of the Aertashi Section: Tectonics, v. 38, p. 492–515, doi:10.1029/2018TC005146.

Bolch, T., and Gorbunov, A.P., 2014, Characteristics and Origin of Rock Glaciers in Northern Tien Shan (Kazakhstan/Kyrgyzstan): Permafrost and Periglacial Processes, v. 25, p. 320–332, doi:10.1002/ppp.1825.

Bolch, T., and Marchenko, S., 2009, Significance of glaciers, rockglaciers and ice-rich permafrost in the Northern Tien Shan as water towers under climate change conditions:, doi:10.5167/uzh-137250.

Bouali, E.H., Oommen, T., and Escobar-Wolf, R., 2018, Mapping of slow landslides on the Palos Verdes Peninsula using the California landslide inventory and persistent scatterer interferometry: Landslides, v. 15, p. 439–452, doi:10.1007/s10346-017-0882-z.

Bovis, M.J., and Evans, S.G., 1996, Extensive deformations of rock slopes in southern Coast Mountains, southwest British Columbia, Canada: Engineering Geology, v. 44, p. 163–182, doi:10.1016/s0013-7952(96)00068-3.

Bovis, M.J., and Evans, S.G., 1995, Rock slope movements along the Mount Currie "fault scarp," southern Coast Mountains, British Columbia: Canadian Journal of Earth Sciences, v. 32, p. 2015–2020, doi:10.1139/e95-154.

Bovis, M.J., and Jakob, M., 2000, The July 29, 1998, debris flow and landslide dam at Capricorn Creek, Mount Meager Volcanic Complex, southern Coast Mountains, British Columbia: Canadian Journal of Earth Sciences, v. 37, p. 1321–1334, doi:10.1139/e00-042.

Brunet, M.-F., Sobel, E.R., and McCann, T., 2017, Geological evolution of Central Asian Basins and the western Tien Shan Range: Geological Society, London, Special Publications, v. 427, p. 1–17, doi:10.1144/SP427.17.

Bürgmann, R., Hilley, G., Ferretti, A., and Novali, F., 2006, Resolving vertical tectonics in the San Francisco Bay Area from permanent scatterer InSAR and GPS analysis: Geology, v. 34, p. 221, doi:10.1130/G22064.1.

Bustin, A.M.M., Clowes, R.M., Monger, J.W.H., and Journeay, J.M., 2013, The southern Coast Mountains, British Columbia: New interpretations from geological, seismic reflection, and gravity data (G. Spence, Ed.): Canadian Journal of Earth Sciences, v. 50, p. 1033–1050, doi:10.1139/cjes-2012-0122.

Capra, L., 2006, Abrupt climatic changes as triggering mechanisms of massive volcanic collapses: Journal of Volcanology and Geothermal Research, v. 155, p. 329–333, doi:10.1016/j.jvolgeores.2006.04.009.

Capra, L., Bernal, J.P., Carrasco-Núñez, G., and Roverato, M., 2013, Climatic fluctuations as a significant contributing factor for volcanic collapses. Evidence from Mexico during the Late Pleistocene: Global and Planetary Change, v. 100, p. 194–203, doi:10.1016/j.gloplacha.2012.10.017.

Casagli, N., Intrieri, E., Tofani, V., and Raspini, F., 2023, Landslide detection, monitoring and prediction with remote-sensing techniques:, doi:10.1038/s43017-022-00373-x.

Cecchi, E., van Wyk de Vries, B., and Lavest, J.-M., 2004, Flank spreading and collapse of weak-cored volcanoes: Bulletin of Volcanology, v. 67, p. 72–91, doi:10.1007/s00445-004-0369-3.

Chadima, M., and Hrouda, F., 2006, Remasoft 3.0 a user-friendly paleomagnetic data browser and analyzer: Travaux Géophysiques, v. 27, p. 20–21.

Chen, J.M., 1996, Evaluation of Vegetation Indices and a Modified Simple Ratio for Boreal Applications: Canadian Journal of Remote Sensing, v. 22, p. 229–242, doi:10.1080/07038992.1996.10855178.

Clague, J.J., 1997, Evidence for large earthquakes at the Cascadia Subduction Zone: Reviews of Geophysics, v. 35, p. 439–460, doi:10.1029/97RG00222.

Clague, J.J., 1991, Quaternary Glaciation and Sedimentation, *in* Geology of the Cordilleran Orogen in Canada, Geological Society of America, v. 434, doi:10.1130/DNAG-GNA-G2.419.

Clague, J.J., and James, T.S., 2002, History and isostatic effects of the last ice sheet in southern British Columbia: Quaternary Science Reviews, v. 21, p. 71–87, doi:10.1016/S0277-3791(01)00070-1.

Coughlan, B., Sampaleanu, C., Williams-Jones, G., and Stead, D., 2023, Rockfall Instability on High Granitic Domes: Stawamus Chief, B.C., Canada, *in* 15th ISRM Congress 2023 & 72nd Geomechanics Colloquium. Schubert & Kluckner, OnePetro, https://dx.doi.org/ (accessed January 2024).

Cruden, D.M., and Varnes, D., 1996, Landslide Types and Processes:, https://trid.trb.org/view/462501 (accessed February 2021).

Cunningham, W.D., and Mann, P., 2007, Tectonics of strike-slip restraining and releasing bends: Geological Society, London, Special Publications, v. 290, p. 1–12, doi:10.1144/SP290.1.

Delcamp, A., Roberti, G., and van Wyk de Vries, B., 2016, Water in volcanoes: evolution, storage and rapid release during landslides.: Bulletin of Volcanology, v. 78, p. 87, doi:10.1007/s00445-016-1082-8.

Donoso, G.A., Malehmir, A., Carvalho, J., and Araujo, V., 2022, 3D reflection seismic imaging of volcanogenic massive sulphides at Neves-Corvo, Portugal: Geophysical Prospecting, doi:10.1111/1365-2478.13269.

Eberhardt, E., 2008, Twenty-ninth Canadian Geotechnical Colloquium: The role of advanced numerical methods and geotechnical field measurements in understanding complex deep-seated rock slope failure mechanisms: Canadian Geotechnical Journal, v. 45, p. 484–510, doi:10.1139/T07-116.

Edel, J.B., Schulmann, K., Hanžl, P., and Lexa, O., 2014, Palaeomagnetic and structural constraints on 90° anticlockwise rotation in SW Mongolia during the Permo–Triassic: Implications for Altaid oroclinal bending. Preliminary palaeomagnetic results: Journal of Asian Earth Sciences, v. 94, p. 157–171, doi:10.1016/j.jseaes.2014.07.039.

Eisbacher, G.H., 1983, Slope stability and mountain torrents, Fraser Lowland and Southern Coast Mountains, field trip guidebook: Victoria, Geological Association of Canada, v. 15.

Eker, R., and Aydın, A., 2021, Long-term retrospective investigation of a large, deep-seated, and slow-moving landslide using InSAR time series, historical aerial photographs, and UAV data: The case of Devrek landslide (NW Turkey): CATENA, v. 196, p. 104895, doi:10.1016/j.catena.2020.104895.

Evans, S.G., 1987, Surface displacement and massive toppling on the northeast ridge of Mount Currie, British Columbia: Current Research Part A, Geological survey of Canada, Paper, v. 87–1A, p. 181–189, doi:10.4095/122508.

Fairbank, B., Reader, J., and Nevin Sadlier-Brown, T., 1980, NSBG Ltd 1980 Mar - 1979 Drilling & Exploration Program, Meager Creek Geothermal Area, Upper Lillooet River: B.C. Hydro and power Authority.

Fairbank, B., Reader, J., Openshaw, R.E., and Nevin Sadlier-Brown, T., 1981, 1981 Jun. 1980 Drilling and Exploration Program - Meager Creek Geothermal Area, Upper Lillooet River: B.C Hydro and Power Authority.

Farnebäck, G., 2003, Two-frame motion estimation based on polynomial expansion: Lecture Notes in Computer Science (including subseries Lecture Notes in Artificial Intelligence and Lecture Notes in Bioinformatics), v. 2749, p. 363–370, doi:10.1007/3-540-45103-X_50/COVER.

Ferretti, A., 2014, Satellite InSAR Data: Reservoir Monitoring from Space (EET 9): HOUTEN, The Netherlands, EAGE, https://bookshop.eage.org/product/satellite-insar-data-reservoir-monitoring-from-space-eet-9/.

Ferretti, A., Colombo, D., Fumagalli, A., Novali, F., and Rucci, A., 2015, InSAR data for monitoring land subsidence: Time to think big, *in* Proceedings of the International Association of Hydrological Sciences, Copernicus GmbH, v. 372, p. 331–334, doi:10.5194/piahs-372-331-2015.

Ferretti, A., Fumagalli, A., Novali, F., Prati, C., Rocca, F., and Rucci, A., 2011, A new algorithm for processing interferometric data-stacks: SqueeSAR: IEEE Transactions on Geoscience and Remote Sensing, v. 49, p. 3460–3470, doi:10.1109/TGRS.2011.2124465.

Ferretti, A., Monti-guarnieri, A., Prati, C., Rocca, F., and Massonnet, D., 2007, InSAR Principles: Guidelines for SAR Interferometry Processing and Interpretation: ESA Publications, TM-19. ISBN 92-9092-233-8.:, 1–48 p.

Filipovich, R. et al., 2020, Geological Map of the Tocomar Basin (Puna Plateau, NW Argentina). Implication for the Geothermal System Investigation: Energies, v. 13, p. 5492, doi:10.3390/en13205492.

Fobert, M.-A., Singhroy, V., and Spray, J.G., 2021, remote sensing InSAR Monitoring of Landslide Activity in Dominica:, doi:10.3390/rs13040815.

Foroosh, H., Zerubia, J.B., and Berthod, M., 2002, Extension of phase correlation to subpixel registration: IEEE Transactions on Image Processing, v. 11, p. 188–199, doi:10.1109/83.988953.

Friele, P.A., and Clague, J.J., 2004, Large Holocene landslides from Pylon Peak, southwestern British Columbia: Canadian Journal of Earth Sciences, v. 41, p. 165–182, doi:10.1139/e03-089.

Friele, P., Jakob, M., and Clague, J., 2008, Hazard and risk from large landslides from Mount Meager volcano, British Columbia, Canada: Georisk: Assessment and Management of Risk for Engineered Systems and Geohazards, v. 2, p. 48–64, doi:10.1080/17499510801958711.

Gehrels, G.E. et al., 2009, U-Th-Pb geochronology of the Coast Mountains batholith in north-coastal British Columbia: Constraints on age and tectonic evolution: Bulletin of the Geological Society of America, v. 121, p. 1341–1361, doi:10.1130/B26404.1.

GeothermEx, Inc., 2009, Summary of The Status of The South Meager Geothermal Project British Columbia, Canada for Western Geopower Corporation: WESTERN GEOPOWER CORPORATION, 1–20 p.

Ghomshei, M.M., Brown, T.L.S., and MacRae, J.M., 1992, Geothermal prospects in British Columbia: resource, market and regulatory aspects, *in* Transactions - Geothermal Resources Council, v. 16, p. 57–63.

Ghomshei, M.M., Croft, S.A.S., and Stauder, J.J., 1986, Geochemical evidence of chemical equilibria in the South Meager Creek geothermal system, British Columbia, Canada: Geothermics, v. 15, p. 49–61, doi:10.1016/0375-6505(86)90028-3.

Ghomshei, M.M., Kimball, S.J., and Porkial, S., 2009, Geochemical evidence of a geothermal power resource the Canadian Rockies: Canoe hot springs, British Columbia, *in* Transactions - Geothermal Resources Council, v. 33, p. 419–423.

Ghomshei, M., Sanyal, S.& M., K., MacLeod, K., Henneberger, R., Ryder, A.& M., J., Meech, J., and Fainbank, B., 2004, Status of the South Meager geothermal project British Columbia, Canada: Resource evaluation and plans for development, *in* Transactions - Geothermal Resources Council, v. 28, p. 339–344.

Glicken, H., 1996, Rockslide-debris avalanche of May 18, 1980, Mount St. Helens volcano, Washington: U.S. Geological Survey Open-File Report 96-677, p. 90P, 5 plates.

Goodman, R. e., 1995, Block theory and its application: Géotechnique, v. 45, p. 383–423, doi:10.1680/geot.1995.45.3.383.

Goodman, R.E., and Shi, G., 1985, Block theory and its application to rock engineering:, https://www.osti.gov/biblio/5649281 (accessed May 2024).

Grämiger, L.M., Moore, J.R., Gischig, V.S., Ivy-Ochs, S., and Loew, S., 2017, Beyond debuttressing: Mechanics of paraglacial rock slope damage during repeat glacial cycles: Journal of Geophysical Research: Earth Surface, v. 122, p. 1004–1036, doi:10.1002/2016JF003967.

Grasby, S.E., Ansari, S.M., and Calahorrano-Di Patre, A; Chen, Z; Craven, J A; Dettmer, J; Gilbert, H; Hanneson, C; Harris, M; Liu, J; Muhammad, M; Russell, K; Salvage, R O; Savard, G; Tschirhart, V; Unsworth, M J; Vigouroux-Caillibot, N; Williams-Jones, G., 2021, Garibaldi Geothermal Energy Project - Phase 1 Final Report:, 7–34 p.

Grasby, S.E., and Hutcheon, I., 2001, Controls on the distribution of thermal springs in the southern Canadian Cordillera: Canadian Journal of Earth Sciences, v. 38, p. 427–440, doi:10.1139/cjes-38-3-427.

Guizar-Sicairos, M., Thurman, S.T., and Fienup, J.R., 2008, Efficient subpixel image registration algorithms: Optics Letters, v. 33, p. 156, doi:10.1364/ol.33.000156.

Guo, R., LI, S., Chen, Y., Li, X., and Yuan, L., 2021, Identification and monitoring landslides in Longitudinal Range-Gorge Region with InSAR fusion integrated visibility analysis: Landslides, v. 18, p. 551–568, doi:10.1007/s10346-020-01475-7.

Gupte, S.S., 2006, Modern techniques in rock slope stability analysis - Applications and limitations: Journal of Mines, Metals and Fuels, v. 54, p. 384–389.

Guthrie, R.H., Friele, P., Allstadt, K., Roberts, N., Evans, S.G., Delaney, K.B., Roche, D., Clague, J.J., and Jakob, M., 2012, The 6 August 2010 Mount Meager rock slide-debris flow, Coast Mountains, British Columbia: Characteristics, dynamics, and implications for hazard and risk assessment: Natural Hazards and Earth System Science, v. 12, p. 1277–1294, doi:10.5194/nhess-12-1277-2012.

Haberkorn, A., Kenner, R., Noetzli, J., and Phillips, M., 2021, Changes in Ground Temperature and Dynamics in Mountain Permafrost in the Swiss Alps: Frontiers in Earth Science, v. 9, doi:10.3389/feart.2021.626686.

Haeberli, W. et al., 2006, Permafrost creep and rock glacier dynamics: Permafrost and Periglacial Processes, v. 17, p. 189–214, doi:10.1002/ppp.561.

Hajaj, S., El Harti, A., and Jellouli, A., 2022, Assessment of Hyperspectral, Multispectral, Radar, and Digital Elevation Model data in structural lineaments mapping: A case study from Ameln valley shear zone, Western Anti-Atlas Morocco: Remote Sensing Applications: Society and Environment, v. 27, p. 100819, doi:10.1016/j.rsase.2022.100819.

Hama, L., Ruddle, R.A., and Paton, D., 2014, Geological orientation measurements using an iPad: Method comparison, *in* TPCG 2014 - Theory and Practice of Computer Graphics, Proceedings, p. 45–50, doi:10.2312/cgvc.20141207.

Handwerger, A.L., Huang, M.-H., Fielding, E.J., Booth, A.M., and Bürgmann, R., 2019, A shift from drought to extreme rainfall drives a stable landslide to catastrophic failure: Scientific Reports, v. 9, p. 1569, doi:10.1038/s41598-018-38300-0.

Hanneson, C., and Unsworth, M.J., 2023, Magnetotelluric imaging of the magmatic and geothermal systems beneath Mount Meager, southwestern Canada: Canadian Journal of Earth Sciences, doi:10.1139/cjes-2022-0136.

Harris, C., 2005, Climate Change, Mountain Permafrost Degradation and Geotechnical Hazard, *in* p. 215–224, doi:10.1007/1-4020-3508-X_22.

Harris, M., Muhammad, M., Williams-Jones, G., and Russell, J., 2020, Bedrock Mapping for Mount Meager Geothermal Research Initiative: In the Garibaldi Volcanic Belt Geothermal Energy Project – Mount Meager 2019 Field Program.:

Harris, M., Russell, J.K., Muhammad, M., and Williams-Jones, G., 2022, Mount Meager Volcanic Complex, Garibaldi Volcanic Belt, British Columbia: expanded bedrock map including Cracked Mountain, north Lillooet Ridge, and west Mount Meager: Geological Survey of Canada, Open File 8881, 1 sheet p., doi:10.4095/329886.

Heap, M.J., Farquharson, J.I., Baud, P., Lavallée, Y., and Reuschlé, T., 2015, Fracture and compaction of andesite in a volcanic edifice: Bulletin of Volcanology, v. 77, p. 55, doi:10.1007/s00445-015-0938-7.

Hencher, S.R., Lee, S.G., Carter, T.G., and Richards, L.R., 2011, Sheeting joints: Characterisation, shear strength and engineering: Rock Mechanics and Rock Engineering, v. 44, p. 1–22, doi:10.1007/s00603-010-0100-y.

Hermle, D., Gaeta, M., Krautblatter, M., Mazzanti, P., and Keuschnig, M., 2022, Performance Testing of Optical Flow Time Series Analyses Based on a Fast, High-Alpine Landslide: Remote Sensing, v. 14, p. 455, doi:10.3390/rs14030455.

Hetherington, R., 2014, Slope Stability Analysis of Mount Meager, South-Western British Columbia: Master's Thesis, Michigan Technological University, 68 p., http://digitalcommons.mtu.edu/etds/764.

Hickson, C.J., Russell, J.K., Stasiuk, M.V., and Swanson, D.A., 1999, Volcanology of the 2350 B.P. Eruption of Mount Meager Volcanic Complex, British Columbia, Canada: implications for Hazards from Eruptions in Topographically Complex Terrain 1: Springer-Verlag, 489–507 p.

Highland, L., 2004, Landslide types and processes: U.S. Geological Survey Fact Sheet 2004-3072, 4 p.

Hoek, E., and Bray, J.D., 1981, Rock Slope Engineering: CRC Press, doi:10.1201/9781482267099.

Hoek, E., and Brown, E.T., 2019, The Hoek–Brown failure criterion and GSI – 2018 edition: Journal of Rock Mechanics and Geotechnical Engineering, v. 11, p. 445–463, doi:10.1016/j.jrmge.2018.08.001.

Holm, K., Bovis, M., and Jakob, M., 2004, The landslide response of alpine basins to post-Little Ice Age glacial thinning and retreat in southwestern British Columbia: Geomorphology, v. 57, p. 201–216, doi:10.1016/S0169-555X(03)00103-X.

Holst, C., Janßen, J., Schmitz, B., Blome, M., Dercks, M., Schoch-Baumann, A., Blöthe, J., Schrott, L., Kuhlmann, H., and Medic, T., 2021, Increasing spatio-temporal resolution for monitoring alpine solifluction using terrestrial laser scanners and 3d vector fields: Remote Sensing, v. 13, doi:10.3390/rs13061192.

Hormozzade Ghalati, F., Craven, J.A., Motazedian, D., Grasby, S.E., and Tschirhart, V., 2022, Modeling a fractured geothermal reservoir using 3-D AMT data inversion: Insights from Garibaldi Volcanic Belt, British Columbia, Canada: Geothermics, v. 105, p. 102528, doi:10.1016/j.geothermics.2022.102528.

Huggel, C., 2009, Recent extreme slope failures in glacial environments: effects of thermal perturbation: Quaternary Science Reviews, v. 28, p. 1119–1130, doi:10.1016/j.quascirev.2008.06.007.

Hungr, O., Leroueil, S., and Picarelli, L., 2014, The Varnes classification of landslide types, an update: Landslides, v. 11, p. 167–194, doi:10.1007/s10346-013-0436-y.

Huntley, D., Rotheram-Clarke, D., Bobrowsky, P., Lintern, G., MacLeod, R., and Brillon, C., 2020, InSAR investigation of sackung-like features and debris flows in the vicinity of Hawkesbury Island and Hartley Bay, British Columbia, Canada, *in* Proceedings of the 2020 International Symposium on Slope Stability in Open Pit Mining and Civil Engineering, Australian Centre for Geomechanics, Perth, p. 207–226, doi:10.36487/ACG_repo/2025_09.

Hussain, S., Hongxing, S., Ali, M., and Ali, M., 2021, PS-InSAR based validated landslide susceptibility modelling: a case study of Ghizer valley, Northern Pakistan: Geocarto International, v. 0, p. 1–22, doi:10.1080/10106049.2020.1870165.

Huybers, P., and Langmuir, C., 2009, Feedback between deglaciation, volcanism, and atmospheric CO2: Earth and Planetary Science Letters, v. 286, p. 479–491, doi:10.1016/j.epsl.2009.07.014.

Javier, S., Meinhardt-Llopis, E., Facciolo, G., Sánchez Pérez, J., Meinhardt-Llopis, E., and Facciolo, G., 2013, TV-L1 Optical Flow Estimation: Image Processing On Line, v. 3, p. 137–150, doi:10.5201/ipol.2013.26.

Jellinek, A.M., Manga, M., and Saar, M.O., 2004, Did melting glaciers cause volcanic eruptions in eastern California? Probing the mechanics of dike formation: Journal of Geophysical Research: Solid Earth, v. 109, p. n/a-n/a, doi:10.1029/2004JB002978.

Jibson, R.W., 2013, Models of the triggering of landslides during earthquakes: Landslides, p. 196–206, doi:10.1017/cbo9780511740367.018.

Journeay, J.M., and van Ulden, J., 1998, Neogene structural elements of northern Cascadia, British Columbia: Geological Survey of Canada, Current Research, 1998-A/B, doi:https://doi.org/10.4095/209503.

Kääb, A., Strozzi, T., Bolch, T., Caduff, R., Trefall, H., Stoffel, M., and Kokarev, A., 2021, Inventory and changes of rock glacier creep speeds in Ile Alatau and Kungöy Ala-Too, northern Tien Shan, since the 1950s: The Cryosphere, v. 15, p. 927–949, doi:10.5194/tc-15-927-2021.

Kehoe, H.L., and Kiser, E.D., 2020, Evidence of a Supershear Transition Across a Fault Stepover: Geophysical Research Letters, v. 47, doi:10.1029/2020GL087400.

Kim, D., Balasubramaniam, A.S., Gratchev, I., Kim, S.R., and Chang, S.H., 2020, Application of image quality assessment for rockfall investigation, *in* 16th Asian Regional Conference on Soil Mechanics and Geotechnical Engineering, ARC 2019, http://seags.ait.asia/16arc-proceedings/16arc-proceedings/.

Kim, D.H., and Gratchev, I., 2021, Application of optical flow technique and photogrammetry for rockfall dynamics: A case study on a field test: Remote Sensing, v. 13, p. 1–17, doi:10.3390/rs13204124.

Kirschvink, J.L., 1980, The least-squares line and plane and the analysis of palaeomagnetic data: Geophysical Journal International, v. 62, p. 699–718, doi:10.1111/j.1365-246X.1980.tb02601.x.

Komatsu, T., 2016, Cenozoic Tectonic Evolution of the Pamir: A Review: Journal of Geography (Chigaku Zasshi), v. 125, p. 661–698, doi:10.5026/jgeography.125.661.

Kromer, R.A., Abellán, A., Hutchinson, D.J., Lato, M., Chanut, M.-A., Dubois, L., and Jaboyedoff, M., 2017, Automated terrestrial laser scanning with near-real-time change detection – monitoring of the Séchilienne landslide: Earth Surface Dynamics, v. 5, p. 293–310, doi:10.5194/esurf-5-293-2017.

Kummert, M., Bodin, X., Braillard, L., and Delaloye, R., 2021, Pluri-decadal evolution of rock glaciers surface velocity and its impact on sediment export rates towards high alpine torrents: Earth Surface Processes and Landforms, v. 46, p. 3213–3227, doi:10.1002/esp.5231.

Leonard, L.J., Currie, C.A., Mazzotti, S., and Hyndman, R.D., 2010, Rupture area and displacement of past Cascadia great earthquakes from coastal coseismic subsidence: Bulletin of the Geological Society of America, v. 122, p. 2079–2096, doi:10.1130/B30108.1.

Li, Y., and Mo, P., 2019, A unified landslide classification system for loess slopes: A critical review: Geomorphology, v. 340, p. 67–83, doi:10.1016/j.geomorph.2019.04.020.

Lin, Z., Kaneda, H., Mukoyama, S., Asada, N., and Chiba, T., 2013, Detection of subtle tectonic–geomorphic features in densely forested mountains by very high-resolution airborne LiDAR survey: Geomorphology, v. 182, p. 104–115, doi:10.1016/j.geomorph.2012.11.001.

Liotta, D., Brogi, A., Ruggieri, G., and Zucchi, M., 2021, Fossil vs. Active Geothermal Systems: A Field and Laboratory Method to Disclose the Relationships between Geothermal Fluid Flow and Geological Structures at Depth: Energies, v. 14, p. 933, doi:10.3390/en14040933.

Liu, Q., Liu, Q., Liu, Y., Gao, S., Yang, T., Luo, Y., and Jin, Z., 2008, Magnetic study of mafic granulite xenoliths from the Hannuoba basalt, north China: Geochemistry, Geophysics, Geosystems, v. 9, p. n/a-n/a, doi:10.1029/2008GC001952.

Liu, G., Zhao, L., Li, R., Wu, T., Jiao, K., and Ping, C., 2017, Permafrost Warming in the Context of Step-wise Climate Change in the Tien Shan Mountains, China: Permafrost and Periglacial Processes, v. 28, p. 130–139, doi:10.1002/ppp.1885.

Louis, L., Wong, T.F., and Baud, P., 2007, Imaging strain localization by X-ray radiography and digital image correlation: Deformation bands in Rothbach

sandstone: Journal of Structural Geology, v. 29, p. 129–140, doi:10.1016/j.jsg.2006.07.015.

Lowe, D.G., 2004, Distinctive Image Features from Scale-Invariant Keypoints: International Journal of Compluter Vision, v. 60, p. 91–110, doi:10.1023/B:VISI.0000029664.99615.94.

Lüschen, E., Görne, S., von Hartmann, H., Thomas, R., and Schulz, R., 2015, 3D seismic survey for geothermal exploration in crystalline rocks in Saxony, Germany: Geophysical Prospecting, v. 63, p. 975–989, doi:10.1111/1365-2478.12249.

Ma, P., Cui, Y., Wang, W., Lin, H., and Zhang, Y., 2021, Coupling InSAR and numerical modeling for characterizing landslide movements under complex loads in urbanized hillslopes: Landslides, doi:10.1007/s10346-020-01604-2.

Mathews, W.H., and Monger, J.W.H., 2005, Roadside geology of southern British Columbia: , p. 403.

Mathieu, L., and van Wyk de Vries, B., 2011, The impact of strike-slip, transtensional and transpressional fault zones on volcanoes. Part 1: Scaled experiments: Journal of Structural Geology, v. 33, p. 907–917, doi:10.1016/j.jsg.2011.03.002.

Mathieu, L., van Wyk de Vries, B., Pilato, M., and Troll, V.R., 2011, The interaction between volcanoes and strike-slip, transtensional and transpressional fault zones: Analogue models and natural examples: Journal of Structural Geology, v. 33, p. 898–906, doi:10.1016/j.jsg.2011.03.003.

McColl, S., TRH, D., and MJ, M., 2010, Glacier retreat and rock-slope stability: debunking debuttressing, *in* Auckland, New Zealand; pp. 467-474, Delegate papers 11th Congress of the International Association for Engineering Geology and the Environment.

McCormick, N., and Lord, J., 2010, Digital Image Correlation: Materials Today, v. 13, p. 52–54, doi:10.1016/S1369-7021(10)70235-2.

Micklethwaite, S., Ford, A., Witt, W., and Sheldon, H.A., 2015, The where and how of faults, fluids and permeability - insights from fault stepovers, scaling properties and gold mineralisation: Geofluids, v. 15, p. 240–251, doi:10.1111/gfl.12102.

Moeck, I.S., 2014, Catalog of geothermal play types based on geologic controls: Renewable and Sustainable Energy Reviews, v. 37, p. 867–882, doi:10.1016/j.rser.2014.05.032.

Mokievsky-Zubok, O., 1977, Glacier-caused slide near Pylon Peak, British Columbia: Canadian Journal of Earth Sciences, v. 14, p. 2657–2662, doi:10.1139/e77-230.

Monger, J.W.H., and Journeay, J.M., 1994, Basement Geology and Tectonic Evolution of the Vancouver Region:, doi:10.4095/203245.

Moro, M. et al., 2017, New insights into earthquake precursors from InSAR: Scientific Reports, v. 7, p. 1–11, doi:10.1038/s41598-017-12058-3.

Muhammad, M., 2016, Structural Evolution of the Maynard Lake Fault Within the Left-Lateral Pahranagat Shear Zone, Nevada, USA: University of Nevada, Las Vegas, https://digitalscholarship.unlv.edu/thesesdissertations/2798 (accessed May 2021).

Muhammad, M., Awdal, A., and University-Hawler, S., 2012, Automatic Mapping of Lineaments Using Shaded Relief Images Derived from Digital Elevation Model (DEM) in Erbil-Kurdistan, northeast Iraq, https://api.semanticscholar.org/CorpusID:130039466.

Muhammad, M., Williams-Jones, G., and Barendregt, R.W., 2021, Applications of structural geology to the exploration of geothermal systems, Mt. Meager, BC in The Garibaldi Volcanic Belt Geothermal Energy Project Phase 1 Final Report. Geoscience BC Report, 8, p.276: Geoscience BC Report, 8, p.276, 177–242 p.

Muhammad, M., Williams-Jones, G., and Barendregt, R.W., 2024, Structural geology of the Mount Meager Volcanic Complex, BC, Canada: implications for geothermal energy and geohazards: Canadian Journal of Earth Sciences, v. 61, p. 158–186, doi:10.1139/cjes-2023-0077.

Muhammad, M., Williams-Jones, G., Stead, D., Tortini, R., Falorni, G., and Donati, D., 2022, Applications of Image-Based Computer Vision for Remote Surveillance of Slope Instability: Frontiers in Earth Science, v. 10, p. 1–22, doi:10.3389/feart.2022.909078.

Müller, S., Schüler, L., Zech, A., and Heße, F., 2022, GSTools v1.3: a toolbox for geostatistical modelling in Python: Geosci. Model Dev, v. 15, p. 3161–3182, doi:10.5194/gmd-15-3161-2022.

Müller, J., Vieli, A., and Gärtner-Roer, I., 2016, Rock glaciers on the run - understanding rock glacier landform evolution and recent changes from numerical flow modeling: The Cryosphere, v. 10, p. 2865–2886, doi:10.5194/tc-10-2865-2016.

Neri, M., Casu, F., Acocella, V., Solaro, G., Pepe, S., Berardino, P., Sansosti, E., Caltabiano, T., Lundgren, P., and Lanari, R., 2009, Deformation and eruptions at Mt. Etna (Italy): A lesson from 15 years of observations: Geophysical Research Letters, v. 36, p. n/a-n/a, doi:10.1029/2008GL036151.

Nichols, T.C., 1980, Rebound, its nature and effect on engineering works: Quarterly Journal of Engineering Geology, v. 13, p. 133–152, doi:10.1144/GSL.QJEG.1980.013.03.01.

O'donovan, P., 2005, Optical Flow : Techniques and Applications: International Journal of Computer Vision, p. 1–26.

Palubinskas, G., 2014, Mystery behind similarity measures mse and SSIM, *in* 2014 IEEE International Conference on Image Processing (ICIP), Wessling, Germany, IEEE, p. 575–579, doi:10.1109/ICIP.2014.7025115.

Pan, B., and Li, K., 2011, A fast digital image correlation method for deformation measurement: Optics and Lasers in Engineering, v. 49, p. 841–847, doi:10.1016/J.OPTLASENG.2011.02.023.

Parrish, R.R., 1982, Cenozoic Thermal and Tectonic History of the Coast Mountains of British Columbia as Revealed by Fission Track and geological Data and Quantitative Thermal Models: 1–10 p., doi:https://dx.doi.org/10.14288/1.0052431.

Philipp, S.L., Gudmundsson, A., and Oelrich, A.R.I., 2007, How structural geology can contribute to make geothermal projects successful: Proceedings European Geothermal Congress 2007, p. 1–10.

Pola, A., Crosta, G.B., Fusi, N., and Castellanza, R., 2014, General characterization of the mechanical behaviour of different volcanic rocks with respect to alteration: Engineering Geology, v. 169, p. 1–13, doi:10.1016/j.enggeo.2013.11.011.

Rampino, M.R., Self, S., and Fairbridge, R.W., 1979, Can Rapid Climatic Change Cause Volcanic Eruptions? Science, v. 206, p. 826–829, doi:10.1126/science.206.4420.826.

Rapp, A., and Fairbridge, R.W., 1997, Talus fan or cone; Scree and cliff debris, *in* Geomorphology, Dordrecht, Kluwer Academic Publishers, p. 1106–1109, doi:10.1007/3-540-31060-6_367.

Raspini, F., Bianchini, S., Ciampalini, A., Del Soldato, M., Solari, L., Novali, F., Del Conte, S., Rucci, A., Ferretti, A., and Casagli, N., 2018, Continuous, semi-automatic monitoring of ground deformation using Sentinel-1 satellites: Scientific Reports, v. 8, p. 7253–7253, doi:10.1038/s41598-018-25369-w.

Read, P., 1990, Mt Meager Complex, Garibaldi Belt, Southwestern BC.: Geoscience Canada, v. 17, p. 167–170.

Reid, M.E., Sisson, T.W., and Brien, D.L., 2001, Volcano collapse promoted by hydrothermal alteration and edifice shape, Mount Rainier, Washington: Geology, v. 29, p. 779, doi:10.1130/0091-7613(2001)029<0779:VCPBHA>2.0.CO;2.

RGIK, 2023, Guidelines for inventorying rock glaciers:, doi:10.51363/unifr.srr.2023.002.

Riddell, J., 1990a, Geology west of Lillooet Lake, near Pemberton, southwestern British Columbia: Geological Survey of Canada report 90-01E, p. 219–225.

Riddell, J., 1990b, Preliminary Report on The Lillooet Lake Mapping Project Southwestern British Columbia: British Columbia Ministry of Energy, Mines and Petroleum Resources report 1990–1991, p. 39–44.

Riddell, J.M., 1992, Structure stratigraphy and contact relationships in Mesozoic volcanic and sedimentary rocks east of Pemberton southwestern British Columbia, https://scholarworks.umt.edu/etd.

Roberti, G. et al., 2021a, Could Glacial Retreat-Related Landslides Trigger Volcanic Eruptions? Insights from Mount Meager, British Columbia, *in* Springer, Cham, p. 147–151, doi:10.1007/978-3-030-60319-9_15.

Roberti, G., 2018, Mount Meager, a Glaciated Volcano in a Changing Cryosphere: Hazards and Risk Challenges, PhD Thesis: 207 p.

Roberti, G., Friele, P., van Wyk de Vries, B., Ward, B., Clague, J.J., Perotti, L., and Giardino, M., 2017, Rheological evolution of the mount meager 2010 debris avalanche, southwestern british columbia: Geosphere, v. 13, p. 1–22, doi:10.1130/GES01389.1.

Roberti, G., Ward, B., van Wyk de Vries, B., Friele, P., Perotti, L., Clague, J.J., and Giardino, M., 2018, Precursory slope distress prior to the 2010 Mount Meager landslide, British Columbia: Landslides, v. 15, p. 637–647, doi:10.1007/s10346-017-0901-0.

Roberti, G., Ward, B.C., van Wyk deVries, B., Perotti, L., Giardino, M., Friele, P.A., Clague, J.J., Menounos, B., Anderson, L.S., and Freschi, S., 2021b, Structure from motion used to revive archived aerial photographs for geomorphological analysis: an example from Mount Meager volcano, British Columbia, Canada: Canadian Journal of Earth Sciences, v. 58, p. 1253–1267, doi:10.1139/cjes-2020-0140.

Rocscience Inc., 2024, RocSlope3, 3D Block Stability Risk Assessment for Rock Slopes:

Rosen, P.A., Gurrola, E., Sacco, G.F., and Zebker, H., 2012, The InSAR scientific computing environment, *in* EUSAR 2012; 9th European Conference on Synthetic Aperture Radar, p. 730–733, https://ieeexplore.ieee.org/document/6217174 (accessed May 2024).

Rosenblad, B.L., Gilliam, J., Gomez, F., and Loehr, J.E., 2015, Ground-based Interferometric Radar for Rockfall Hazard Monitoring: University of Nebraska. Mid-America Transportation Center, 35, University of Nebraska. Mid-America Transporta p., https://rosap.ntl.bts.gov/view/dot/37148.

Rosenqvist, A., and Killough, B., 2018, A Layman's Interpretation Guide to L-band and C-band Synthetic Aperture Radar data:, 0–38 p., https://ceos-dev.ceos.org/publications/a-laymans-interpretation-guide-to-l-band-and-c-band-synthetic-aperture-radar-data/ (accessed March 2021).

Roverato, M., Capra, L., Sulpizio, R., and Norini, G., 2011, Stratigraphic reconstruction of two debris avalanche deposits at Colima Volcano (Mexico): Insights into pre-failure conditions and climate influence: Journal of Volcanology and Geothermal Research, v. 207, p. 33–46, doi:10.1016/j.jvolgeores.2011.07.003.

Russell, J.K., Edwards, B.R., Williams-Jones, G., and Hickson, C.J., 2023, Pleistocene to Holocene volcanism in the Canadian Cordillera: Canadian Journal of Earth Sciences, v. 60, p. 1443–1466, doi:10.1139/cjes-2023-0065.

Russell, J.K., Stewart, M., Wilson, A., and Williams-Jones, G., 2021, Eruption of Mount Meager, British Columbia, during the early Fraser glaciation: Canadian Journal of Earth Sciences, v. 58, p. 1146–1154, doi:10.1139/cjes-2021-0023.

Sampaleanu, C.I.A., 2017, The Role of Intact Rock Fracture in Rockfall Initiation by, https://summit.sfu.ca/item/17771 (accessed March 2024).

Scheiber, R., Jager, M., Prats-Iraola, P., De Zan, F., and Geudtner, D., 2014, Speckle tracking and interferometric processing of TerraSAR-X TOPS sata for mapping nonstationary scenarios: IEEE Journal of Selected Topics in Applied Earth Observations and Remote Sensing, v. 8, p. 1709–1720, doi:10.1109/JSTARS.2014.2360237.

Shebl, A., and Csámer, Á., 2021, Reappraisal of DEMs, Radar and optical datasets in lineaments extraction with emphasis on the spatial context: Remote Sensing Applications: Society and Environment, v. 24, p. 100617, doi:10.1016/j.rsase.2021.100617.

Siebert, L.E.E., 1984, Large volcanic debris avalanches: Characteristics of source areas, deposits, and associated eruptions: J. Volcanol. Geotherm. Res, v. 22, p. 163–197.

Sorg, A., Kääb, A., Roesch, A., Bigler, C., and Stoffel, M., 2015, Contrasting responses of Central Asian rock glaciers to global warming: Scientific Reports 2015 5:1, v. 5, p. 1–6, doi:10.1038/srep08228.

Srokosz, P.E., Bujko, M., Bocheńska, M., and Ossowski, R., 2021, Optical flow method for measuring deformation of soil specimen subjected to torsional shearing: Measurement: Journal of the International Measurement Confederation, v. 174, p. 1–27, doi:10.1016/j.measurement.2021.109064.

Stead, D., and Coggan, J., 2012, Numerical modeling of rock-slope instability, *in* Stead, D. and Clague, J.J. eds., Landslides: Types, Mechanisms and Modeling, Cambridge, Cambridge University Press, p. 144–158, https://www.cambridge.org/core/books/landslides/numerical-modeling-of-rockslope-instability/59D9F8C6B0D24A8EC9A8DE159F5A3973.

Stead, D., and Coggan, J.S.S., 2006, Numerical Modelling of Rock Slopes Using A Total Slope Failure Approach (S. G. Evans, G. S. Mugnozza, A. Strom, & R. L. Hermanns, Eds.): Landslides from Massive Rock Slope Failure, v. 49, p. 129–138, doi:10.1007/978-1-4020-4037-5_7.

Stead, D., Donati, D., Wolter, A., and Sturzenegger, M., 2019, Application of remote sensing to the investigation of rock slopes: Experience gained and lessons learned: ISPRS International Journal of Geo-Information, v. 8, doi:10.3390/ijgi8070296.

Stead, D., Eberhardt, E., and Coggan, J.S., 2006, Developments in the characterization of complex rock slope deformation and failure using numerical modelling techniques: Engineering Geology, v. 83, p. 217–235, doi:10.1016/j.enggeo.2005.06.033.

Stead, D., Eberhardt E, Benko, B., and Coggan, J., 2001, Advanced Numerical Techniques in Rock Slope Stability Analysis – Applications and Limitations, *in* Landslides: Causes, Impacts and Countermeasures 17-21 June 2001 Davos, Switzerland pp. 615-624", p. 615–624.

Streletskiy, D., Anisimov, O., and Vasiliev, A., 2015, Permafrost Degradation, *in* Snow and Ice-Related Hazards, Risks, and Disasters, Elsevier, p. 303–344, doi:10.1016/B978-0-12-394849-6.00010-X.

Strozzi, T., Caduff, R., Jones, N., Barboux, C., Delaloye, R., Bodin, X., Kääb, A., Mätzler, E., and Schrott, L., 2020, Monitoring Rock Glacier Kinematics with Satellite Synthetic Aperture Radar: Remote Sensing, v. 12, p. 559, doi:10.3390/rs12030559.

Sun, Q., Zhang, L., Ding, X.L., Hu, J., Li, Z.W., and Zhu, J.J., 2015, Slope deformation prior to Zhouqu, China landslide from InSAR time series analysis: Remote Sensing of Environment, v. 156, p. 45–57, doi:10.1016/j.rse.2014.09.029.

Suriñach, E., Vilajosana, I., Khazaradze, G., Biescas, B., Furdada, G., and Vilaplana, J.M., 2005, Seismic detection and characterization of landslides and other mass movements: Natural Hazards and Earth System Science, v. 5, p. 791–798, doi:10.5194/nhess-5-791-2005.

Tarchi, D., 2003, Monitoring landslide displacements by using ground-based synthetic aperture radar interferometry: Application to the Ruinon landslide in the Italian Alps: Journal of Geophysical Research, v. 108, p. 2387, doi:10.1029/2002jb002204.

Team, P., 2017, Planet Application Program Interface: In Space for Life on Earth.: Planet Publications: Fort Mill, SC, USA,.

Terlien, M.T.J., 1998, The determination of statistical and deterministic hydrological landslide-triggering thresholds: Environmental Geology, v. 35, p. 124–130, doi:10.1007/s002540050299.

Thévenaz, P., Ruttimann, U.E., and Unser, M., 1998, A pyramid approach to subpixel registration based on intensity: IEEE Transactions on Image Processing, v. 7, p. 27–41, doi:10.1109/83.650848.

Tortini, R., Van Wyk de Vries, B., and Carn, S.A., 2015, Seeing the faults from the hummocks: Tectonic or landslide fault discrimination with LiDAR at Mt Shasta, California: Frontiers in Earth Science, v. 3, p. 1–7, doi:10.3389/feart.2015.00048.

TRE ALTAMIRA, 2018, TRE ALTAMIRA InSAR Products - Handbook: TRE-ALTAMIRA.

Tuckey, Z.S., 2012, An Integrated Field Mapping-Numerical Modelling Approach to Characterising Discontinuity Persistence and Intact Rock Bridges in Large Open Pit Slopes:, https://summit.sfu.ca/item/12708 (accessed May 2024).

Ulivieri, G., Vezzosi, S., Farina, P., and Meier, L., 2020, On the use of acoustic records for the automatic detection and early warning of rockfalls, *in* Proceedings of the

2020 International Symposium on Slope Stability in Open Pit Mining and Civil Engineering, Australian Centre for Geomechanics, Perth, p. 1193–1202, doi:10.36487/ACG_repo/2025_80.

Unnsteinsson, T., Flowers, G., and Williams-Jones, G., 2021, An analytical approach to understanding the morphologies of glaciovolcanic caves and chimneys: Earth and Space Science Open Archive, doi:10.1002/essoar.10505976.1.

Vallee, M., 2019, Falling in Place: Geoscience, Disaster, and Cultural Heritage at the Frank Slide, Canada's Deadliest Rockslide: Space and Culture, v. 22, p. 66–76, doi:10.1177/1206331218795829.

Varnes, D.J., 1978, SLOPE MOVEMENT TYPES AND PROCESSES: Transportation Research Board Special Report, https://trid.trb.org/view/86168 (accessed February 2021).

Vaughan, A., Collins, N., Krus, M., and Rourke, P., 2014, Recent Development of an Earth Science App – FieldMove Clino: Geophysical Research Abstracts, v. 16, p. 14751.

Venugopal, S., Moune, S., Williams-Jones, G., Druitt, T., Vigouroux, N., Wilson, A., and Russell, J.K., 2020, Two distinct mantle sources beneath the Garibaldi Volcanic Belt: Insight from olivine-hosted melt inclusions: Chemical Geology, v. 532, p. 119346, doi:10.1016/j.chemgeo.2019.119346.

Venugopal, S., Moune, S., Williams-Jones, G., Vigouroux, N., Wilson, A., and Russell, J.K., 2017, Gas emissions and magma source of the Mount Meager Volcanic Complex, Garibaldi Volcanic Belt, BC, *in* IAVCEI Scientific Assembly, p. 244.

Verma, P., Verma, K., Singh, A., Sundaram, A.K., and Bramhe, V.S., 2023, Real-Time Vehicle Detection and Tracking System Using Cascade Classifier and Background Subtractor: , p. 431–441, doi:10.1007/978-981-19-7892-0_34.

Voight, B. et al., 2002, The 26 December (Boxing Day) 1997 sector collapse and debris avalanche at Soufrière Hills Volcano, Montserrat: Geological Society, London, Memoirs, v. 21, p. 363–407, doi:10.1144/GSL.MEM.2002.021.01.17.

Voight, B., Glicken, H., Janda, R.J., and Douglass, M., 1981, Catastrophic rockslide avalanche of May 18 (Mount St. Helens).: U.S. Geological Survey Professional Paper, v. 1250, p. 347–377.

Wallis, I.C., Rowland, J.V., Cumming, W., and Dempsey, D., 2017, The subsurface geometry of a natural geothermal reservoir, *in* Proceedings 39th New Zealand Geothermal Workshop, p. 1–8, https://www.researchgate.net/publication/343710737.

Wang, Z., and Bovik, A.C., 2009, Error : Love It or Leave It ? IEEE Signal Processing Magazine, v. 26, p. 98–117.

Warrick, J.A., Ritchie, A.C., Schmidt, K.M., Reid, M.E., and Logan, J., 2019, Characterizing the catastrophic 2017 Mud Creek landslide, California, using

repeat structure-from-motion (SfM) photogrammetry: Landslides, v. 16, p. 1201–1219, doi:10.1007/s10346-019-01160-4.

Warwick, R., Williams-Jones, G., Kelman, M., and Witter, J., 2022, A scenario-based volcanic hazard assessment for the Mount Meager Volcanic Complex, British Columbia: Journal of Applied Volcanology, v. 11, p. 5, doi:10.1186/s13617-022-00114-1.

Wedel, A., Pock, T., Zach, C., Bischof, H., and Cremers, D., 2009, An Improved Algorithm for TV-L 1 Optical Flow, *in* p. 23–45, doi:10.1007/978-3-642-03061-1_2.

Wei, M., Sandwell, D., and Smith-Konter, B., 2010, Optimal combination of InSAR and GPS for measuring interseismic crustal deformation: Advances in Space Research, v. 46, p. 236–249, doi:10.1016/j.asr.2010.03.013.

Williams, J.G., Rosser, N.J., Hardy, R.J., and Brain, M.J., 2019, The Importance of Monitoring Interval for Rockfall Magnitude-Frequency Estimation: Journal of Geophysical Research: Earth Surface, v. 124, p. 2841–2853, doi:10.1029/2019JF005225.

Williams, J.G., Rosser, N.J., Hardy, R.J., Brain, M.J., and Afana, A.A., 2018, Optimising 4-D surface change detection: an approach for capturing rockfall magnitude–frequency: Earth Surface Dynamics, v. 6, p. 101–119, doi:10.5194/esurf-6-101-2018.

Williams-Jones, G., Barendregt, R.W., Russell, J.K., Le Moigne, Y., Enkin, R.J., and Gallo, R., 2020, The age of the Tseax volcanic eruption, British Columbia, Canada: Canadian Journal of Earth Sciences, v. 57, p. 1238–1253, doi:10.1139/cjes-2019-0240.

Wills, C., Manson, M.W., Brown, K., Davenport, C., and Domrose, C., 2001, Landslides in the highway 1 corridor: geology and slope stability along the Big Sur coastal between Point Lobos and San Carpoforo Creek, Monterey and San Luis Obispo counties, California.: California Geological Survey Special Report 185, 42 p., https://www.semanticscholar.org/paper/LANDSLIDES-IN-THE-HIGHWAY-1-CORRIDOR%3A-GEOLOGY-AND-Wills-Manson/e2e86d59abc5aaeb57653fe4bbdd226f9d291149 (accessed May 2024).

van Wyk de Vries, B., and Francis, P.W., 1997, Catastrophic collapse at stratovolcanoes induced by gradual volcano spreading: Nature, v. 387, p. 387–390, doi:10.1038/387387a0.

Yan, Y., Li, T., Liu, J., Wang, W., and Su, Q., 2019, Monitoring and early warning method for a rockfall along railways based on vibration signal characteristics: Scientific Reports, v. 9, p. 6606, doi:10.1038/s41598-019-43146-1.

Yeung, M.R., Jiang, Q.H., and Sun, N., 2003, Validation of block theory and three-dimensional discontinuous deformation analysis as wedge stability analysis methods: International Journal of Rock Mechanics and Mining Sciences, v. 40, p. 265–275, doi:10.1016/S1365-1609(02)00137-5.

Yunjun, Z., Fattahi, H., and Amelung, F., 2019, Small baseline InSAR time series analysis: Unwrapping error correction and noise reduction: Computers & Geosciences, v. 133, p. 104331, doi:10.1016/j.cageo.2019.104331.

Zach, C., Pock, T., and Bischof, H., 2007, A Duality Based Approach for Realtime TV-L 1 Optical Flow, *in* Pattern Recognition, Berlin, Heidelberg, Springer Berlin Heidelberg, v. 3665 LNCS, p. 214–223, doi:10.1007/978-3-540-74936-3_22.

Zhang, Y., Meng, X.M., Dijkstra, T.A., Jordan, C.J., Chen, G., Zeng, R.Q., and Novellino, A., 2020, Forecasting the magnitude of potential landslides based on InSAR techniques: Remote Sensing of Environment, v. 241, p. 111738, doi:10.1016/j.rse.2020.111738.

Zimmer, V.L., and Sitar, N., 2015, Detection and location of rock falls using seismic and infrasound sensors: Engineering Geology, v. 193, p. 49–60, doi:10.1016/j.enggeo.2015.04.007.

Appendix A. Supplementary Material for Chapter 2

Optical Images

Image Classification

We used an artificial intelligence technique called Deep-Learning Convolutional Neural Network (DLCNN) to perform image classification (Wang et al., 2019; Bouti et al., 2020). The classification process distinguished images with significant noise including fog, low clouds, and large amounts of shadows (Fig. S1). We then use a Python code to sort daily images based on the fixed hour of each day for further processing.

Figure S 2. 1. Example of image classification results from the Plinth Peak slope. The left image is considered as noisy and has been discarded while the right image was selected as a candidate image for further processing. See Github repository online for more image examples

A total of 1315 images were collected from November 2020 to September 2021. The images were classified by our DLCNN algorithm to produce 334 noise free images including winter and summer images. In order to measure changes of the bedrock more precisely, we only processed it in the snow free period between July 27 and August 18, 2021, resulting in 44 images in total for a period of 22 days during summer 2021.
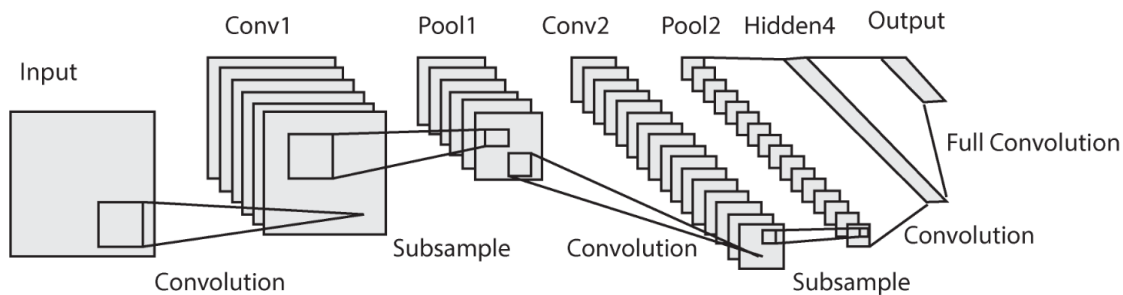
Figure S6.2. A graphical representation of a model LeNet Architecture used in our image classification code. Modified after Bouti et al., 2020.

The Convolutional Neural Networks (CNN) is currently among the most widespread techniques to classify images (Bouti et al., 2020) and in constructing landslide susceptibility maps (Wang et al., 2019). A CNN is made of a stack of multiple layers of convolution filters including pooling, correction layer and the fully connected layer (Fig. S2.2). Each input image will be convolved, reduced, and corrected several times, to finally form a vector. This vector contains the probability of belonging to given classes (Bouti et al., 2020). The convolutional layer is the cornerstone of convolutional neural networks as it is used to determine the location of a set of features in the images received as input. In between two convolution layers, a pooling layer is placed which receives feature maps as input and applies the pooling operation to each of them. An example of pooling operation used in our CNN model is maximum pooling which down-samples an image for the sake of computational capacity while retaining the important information.

Image Alignment

In the lab setting, the user can control the lighting conditions and camera stability while imaging objects. In contrast, under natural conditions, the camera and optical sensor are subject to considerable environmental challenges including strong vibration of the camera mounting pole due to wind, instability of the ground, or a combination of both (Fig. 2.2 in the main text and Fig. S2.3 A, B below). This will cause structural (geometrical) distortion of the images and shifts or misalignments in image pixels which must be removed (Szczęsny, 2015). The PyStackReg Python library was used to compensate structural distortion as it can compensate for five types of image distortion including translation, rigid body (translation + rotation), scaled rotation (translation + rotation + scaling), affine (translation + rotation + scaling + shearing), and bilinear (non-linear transformation) (Thévenaz et al., 1998b).

Subsequently, we performed sub-pixel image registration using the phase cross-correlation algorithm from the Scikit-image Python library (e.g., Foroosh et al., 2002b; Khan et al., 2021) (Fig. 3A). This technique relies on the Fourier shift property which states that a shift in the coordinate frames of two functions is transformed in the Fourier domain as linear phase differences (Foroosh et al., 2002). Therefore, from the result of the phase change, the image translation in both horizontal (x) and vertical (y) directions between sub-sequent images can be calculated.

Assuming that M x N represents original image position, the image shift amount is zero at A(i,j) where *i* and *j* are the initial pixel location; if the image at $A(i, j)$ shifts to a new position B, then B is equal to $B(i - m, j - n)$. Using equations (1) and (2), the cross-correlation of the Fast-Fourier Transform of the two images can be calculated. X_A is the FFT of the reference (fixed) image and directional shifts between A to B of x, y directions represented by m and n, respectively. Thus the magnitude of horizontal (m-pixels) and vertical (n-pixels) translation of the shifted image can be obtained from the Fourier Transform (iDFT) of equation (3) (Foroosh et al., 2002b; Khan et al., 2021):

$$A(i, j) \overset{FFT}{\rightarrow} X_A(u, v) \; \longrightarrow \; eq(1)$$

$$B(i - m, j - n) \xrightarrow{FFT} X_A(u, v)e^{-j2\pi\left(\frac{um}{M} + \frac{pn}{N}\right)} \quad \longrightarrow eq(2)$$

$$T(u, v) = \frac{X_A(u, v)\overline{X_A(u, v)}e^{-j2\pi\left(\frac{um}{M} + \frac{vn}{N}\right)}}{\left|X_A(u, v)\overline{X_A(u, v)}\right|} = \frac{|X_A(u, v)|^2 e^{j2\pi\left(\frac{um}{M} + \frac{vn}{N}\right)}}{|X_A(u, v)|^2} = e^{j2\pi\left(\frac{um}{M} + \frac{vn}{N}\right)} -$$

$$\rightarrow eq(3)$$

$$T(u, v) \xrightarrow{iDFT} \delta(i - m, j - n) = \begin{cases} 1, \text{ if } i = m \wedge j = n \\ \quad 0, \text{ elsewhere} \end{cases} \longrightarrow eq(4)$$

Equation (4) shows the sequential translation affected by horizontal and vertical image shifts. Finally, we can obtain subsequent image alignment by translating each shifted image by the negative of m-pixels in the horizontal direction and negative n-pixels in the vertical direction.

Image Enhancement and Histogram Equalization

The difference in lighting within uncontrolled and harsh natural environments such as alpine regions near a temperate rainforest climate causes unbalanced distribution of brightness and contrast among image pixels. To mitigate/eliminate errors resulting from uneven lighting, some image correction processes are required prior to extracting information from the images. The image corrections consist of three steps of image histogram equalization.

The first step is to flatten the image histogram in a process using the OpenCV Python library. The second step involves automatically calculating global brightness and contrast from equations 5 and 6. To calculate reasonable brightness and contrast values, we first convert the image to grayscale and then determine the maximum and minimum pixel intensity:

Contrast=255 / (maximum gray - minimum gray) →*Equation (5)*

*Brightness= -minimum gray * contrast*→ *Equation (6)*

Finally, a function (equation 7) is used to rescale the intensity of every pixel using the brightness and contrast values.

*New Image = Original Image * Contrast + brightness*→ *Equation (7)*

The third step, called Calibrated Limited Adaptive Histogram Equalization (CLAHE), locally corrects image pixel contrast and brightness with a user specified window. The CLAHE filter is available as a Python tool within both OpenCV and Scikit libraries (Fig. S4).
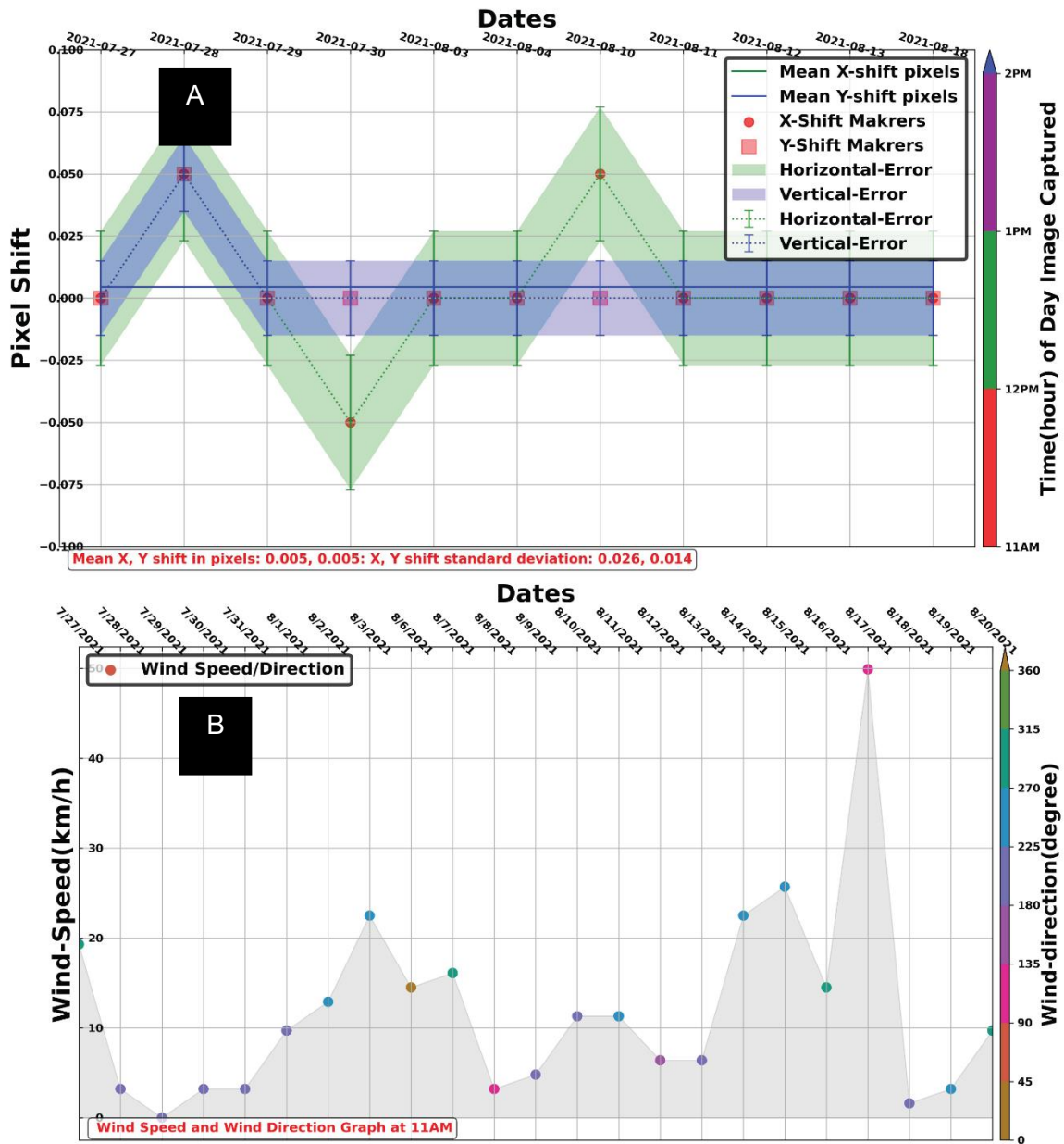
Figure S2.3. A. Image registration and alignment for images taken at 11 AM to show stability of the camera. Note, the amount of pixel shift has been corrected using image registration techniques discussed above. B. Hourly wind-speed and wind-direction at the same time of camera image acquisition collected for the Plinth Peak station.
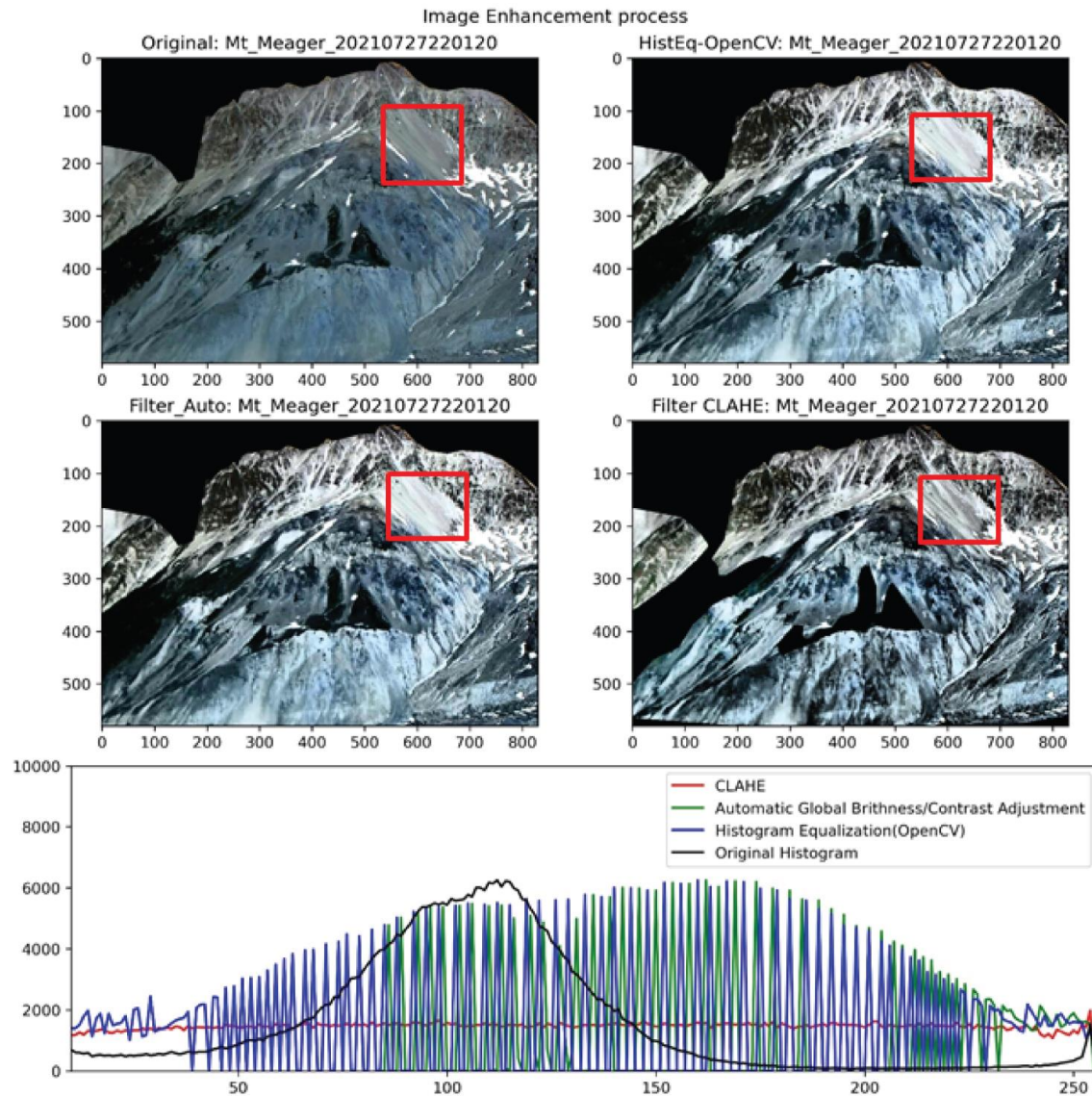
Figure S2.4. Image enhancement processes used in this study. Top left: Plinth Peak slope image with no applied filter. Top right: Plinth Peak slope image after applying automatic brightness/contrast adjustment filter. Middle left: Plinth Peak slope image after applying OpenCV histogram equalization. Middle right: Plinth Peak slope image after applying Calibrated Limited Adaptive Histogram Equalization filter (CLAHE). Bottom panel shows the image histogram for the Plinth Peak slope images after applying subsequent filters. Note: All the filters applied sequentially; notice image quality improvement exemplified in the red box from top left image to middle right image after applying the filters sequentially.

Radar Satellite Image Processing

The radar data processed over the site consists of 20 m x 5 m resolution images acquired by the Sentinel-1 satellite from both ascending and descending orbits. InSAR measures surface displacement along the satellite line of sight (LOS), which is inclined with respect to the vertical (θ angle) and the north-south (δ angle) directions (

). An ascending orbit denotes a satellite travelling from south to north and imaging to the east, while a descending orbit indicates a satellite travelling from north to south and imaging to the west (Fig. S5). Details of SqueeSAR can be found in (Ferretti et al., 2011).

Table S2. 1 Satellite viewing angles for this study.

Satellite	Wavelength	Orbit	Track	Symbol	Angle
Sentinel-1	C-band	Ascending	137	θ	**38.44º**
	5.55 cm			δ	**9.7º**
		Descending	86	θ	**37.05º**
				δ	**10.91º**
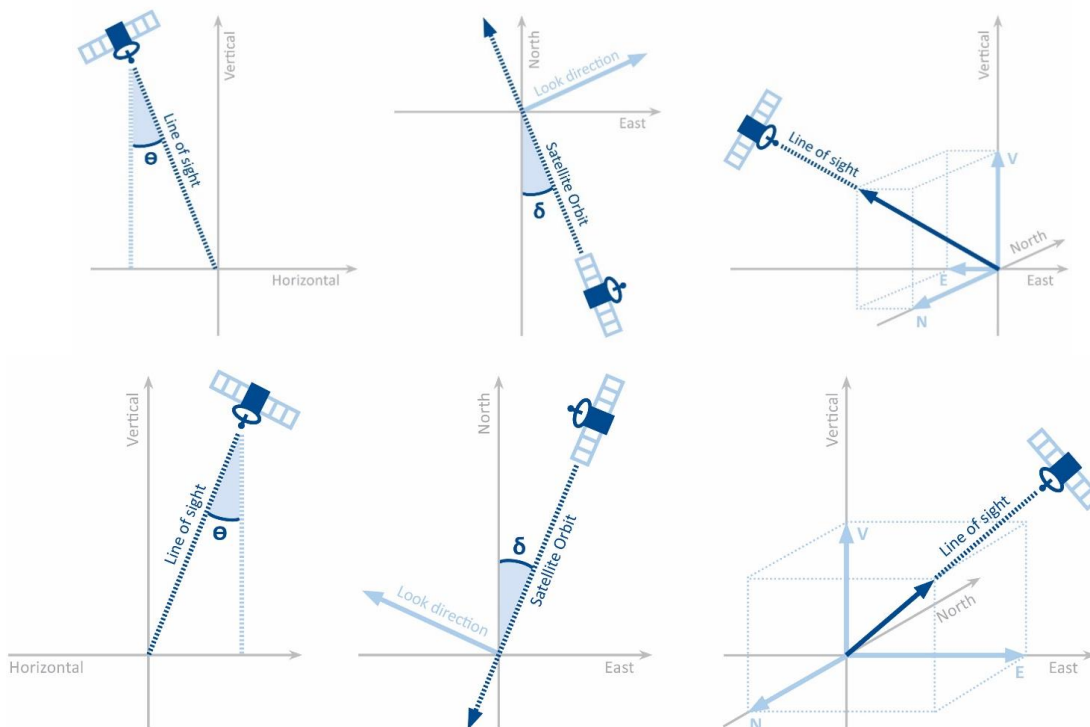
Figure S2.3. Geometry of the radar image acquisitions along the ascending (top) and descending (bottom) orbit.

SqueeSAR^{TM} Results

The SqueeSAR^{TM} analysis over the MMVC provided a density of approximately 2,000-2,500 measurement points per square kilometre (Table). The 2-D SqueeSAR analysis used the temporally overlapping portion (16 May 2019 to 22 September 2021) and spatially overlapping areas of the LOS measurement points on a 30 x 30 m spatial grid to obtain true vertical and east-west horizontal movements with millimetre precision.

Table S2.2: Statistics and data processing characteristics of the SqueeSAR analyses.

Attribute	Ascending	Descending	Vertical	East-West
Date Range	16 May 2019 – 26 Sep 2021	12 May 2019 – 22 Sep 2021	16 May 2019 – 22 Sep 2021	
N. of Images	36	40	73	
Total points (PS + DS)	2,363,131	1,880,635	255,583	
Number of PS	43,133	376,127	-	
Number of DS	1,949,998	1,504,508	-	
Average Point Density (pts/km^2)	2,425	1,929	262	
Average Displacement Rate Standard Deviation (mm/yr)	±3.0	±3.2	±1.8	±2.6
Average Time Series Error Bar (mm)	±2.3	±2.7	NA	NA
Reference Point Location	50°40'37.581"N 123°34'3.921"W	50°40'21.504"N 123°34'7.024"W	50°33'20.07"N 123°36'6.961"W	
Coordinate System	GCS WGS 1984			

GitHub Repository Link

https://github.com/mahmudsfu/AkhDefo

This repository includes the following materials:

1. A copy of the developed Akh-Defo Python-based software for Ground-based Image processing

2. A copy of the modified Akh-Defo program to process Planet Labs orthorectified images

3. Ground-based Plinth Peak image dataset evaluated with the Akh-Defo software.

4. Mud-Creek Planet Lab orthorectified satellite images evaluated with the modified Akh-Defo software.

5. Plinth Peak Planet Lab orthorectified satellite images evaluated with the modified Akh-Defo software.

6. A step-by-step instruction manual on how to run Akh-Defo software on Jupyter notebook program.

Appendix B. Supplementary Materials for Chapter 3

B.1. **Plate 1. Detailed Geology Map of Mount Meager Volcanic Complex, Garibaldi Volcanic Belt, British Columbia, Canada at a scale 1:30,000 showing bedrock and structural geology features. High resolution can be downloaded from the digital format using the below link.** **https://cdnsciencepub.com/cms/10.1139/cjes-2023-0077/asset/images/cjes-2023-0077_uf1.jpg**

Plate 1: Geology Map of Mount Meager Volcanic Complex, Garibaldi Volcanic Belt, British Columbia, Canada

Geologic Cross-Section

Map Projection:

WGS_1984_UTM_Zone_10N
WKID: 32610 Authority: EPSG

Projection: Transverse_Mercator
False_Easting: 500000.0
False_Northing: 0.0
Central_Meridian: -123.0
Scale_Factor: 0.9996
Latitude_Of_Origin: 0.0
Linear Unit: Meter (1.0)

Scale 1:30000

Recommended Citation

Muhammad, M., Williams-Jones, G., Barendregt, R.W., 2023. Structural Geology of the Mount Meager Volcanic Complex, BC, Canada: Implications for geothermal energy and geohazards. Canadian Journal of Earth Sciences.

References

Harris, M., Russell, J.K., Muhammad, M., Williams-Jones, G, 2021: Mount Meager Volcanic Complex, Garibaldi Volcanic Belt, Canada: Expanded Bedrock Map including Cracked Mountain, North Lillooet Ridge, and West Mount Meager: Geological Survey of Canada.

NSBG. 1982. Hg & As Soil Geochemistry of the Meager Creek Geothermal Area, British Columbia; Ram Meager Data, Reports. doi:https://www.geosciencebc.com/projects/2017-006/.

Read, P.,1979. Meager Creek Geothermal Area: p. 1 Sheet. doi:10.4095/129507

NSBG. 1975. Resistivity Survey in Meager Creek Selected Area, Pemberton British Columbia; Ram Meager Data, Reports. doi:https://www.geosciencebc.com/projects/2017-006/.

B.2. Stepwise alternating field and thermal demagnetization behavior (left) for typical samples chosen from each of the four sampling sites at Meager Massif domain (samples labeled MM) and four samples at Lillooet Ridge (samples labelled LR). Stereographic plots (middle) show magnetization directions after stepwise AF and thermal demagnetization, where filled circles lie on the lower hemisphere. Orthogonal plots (right) show horizontal projections as filled circles and vertical projections as open circles. Natural remanent magnetization is shown with a circle and cross. Units are in amperes per meter.
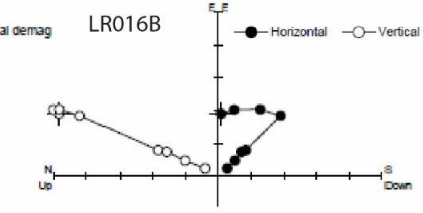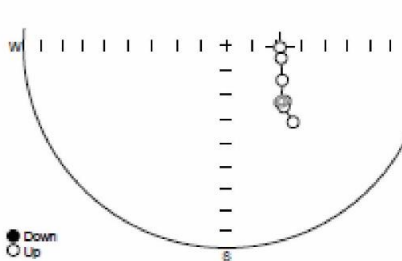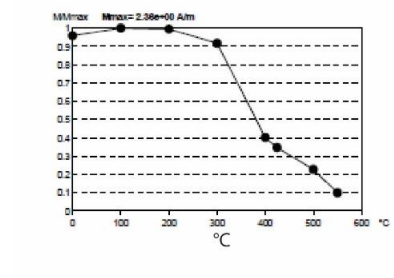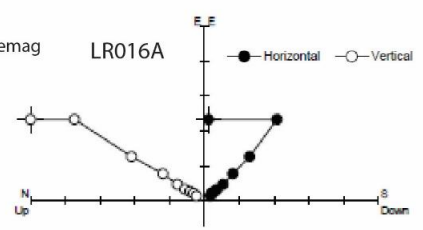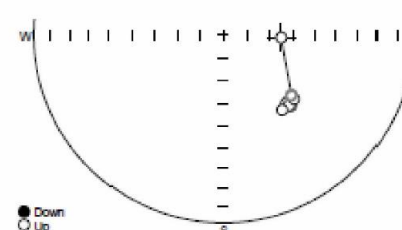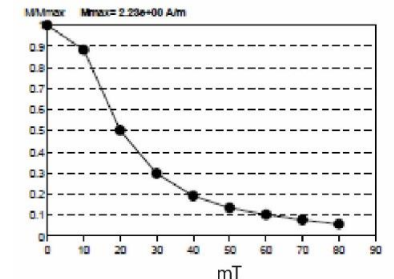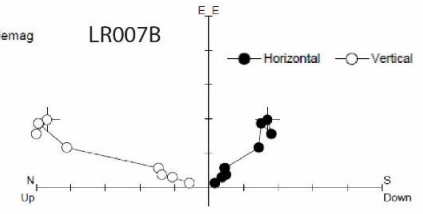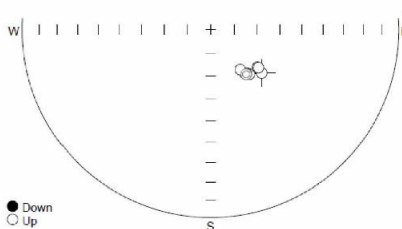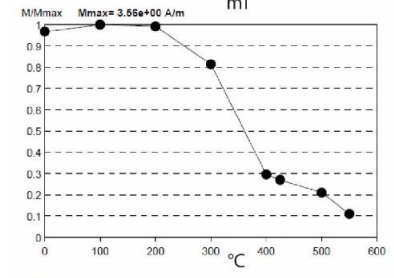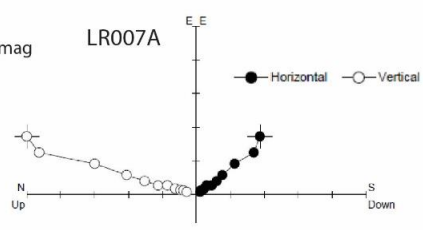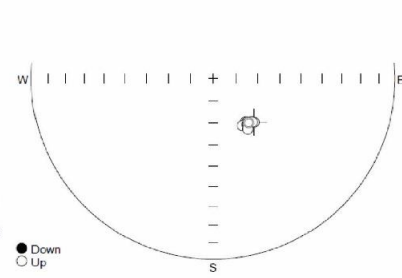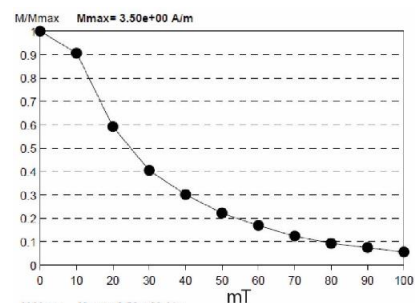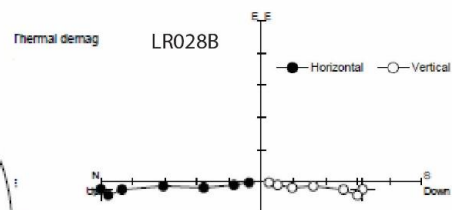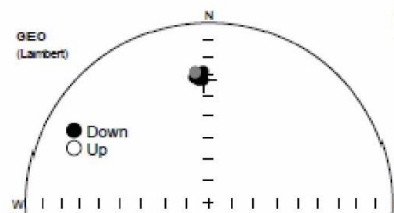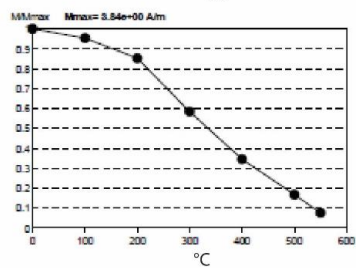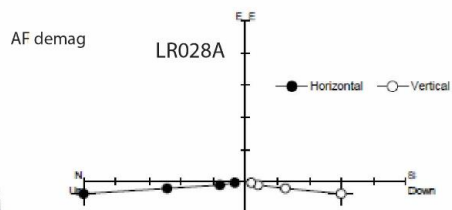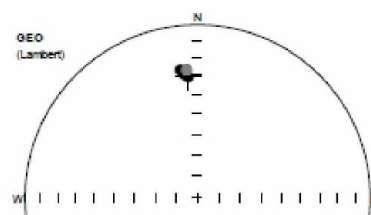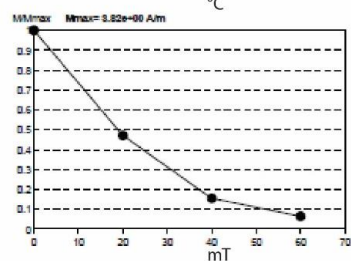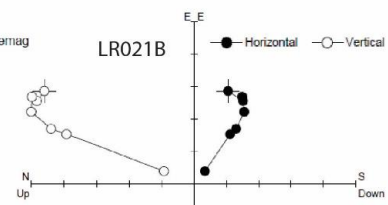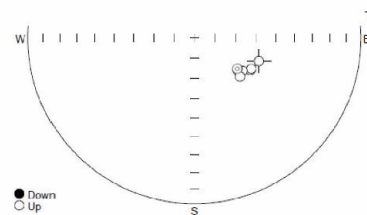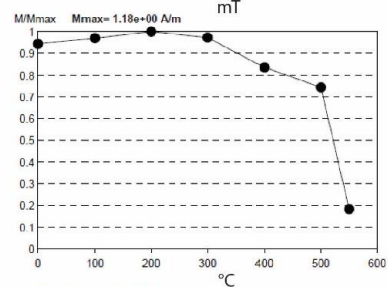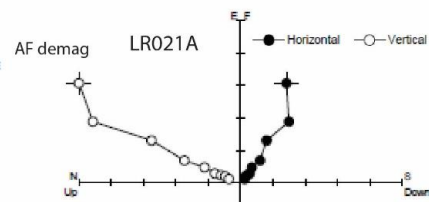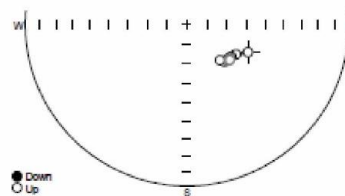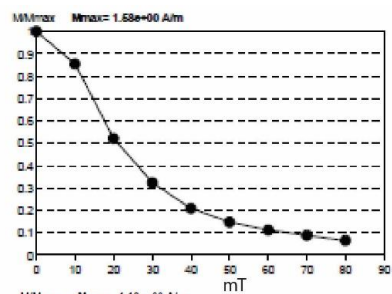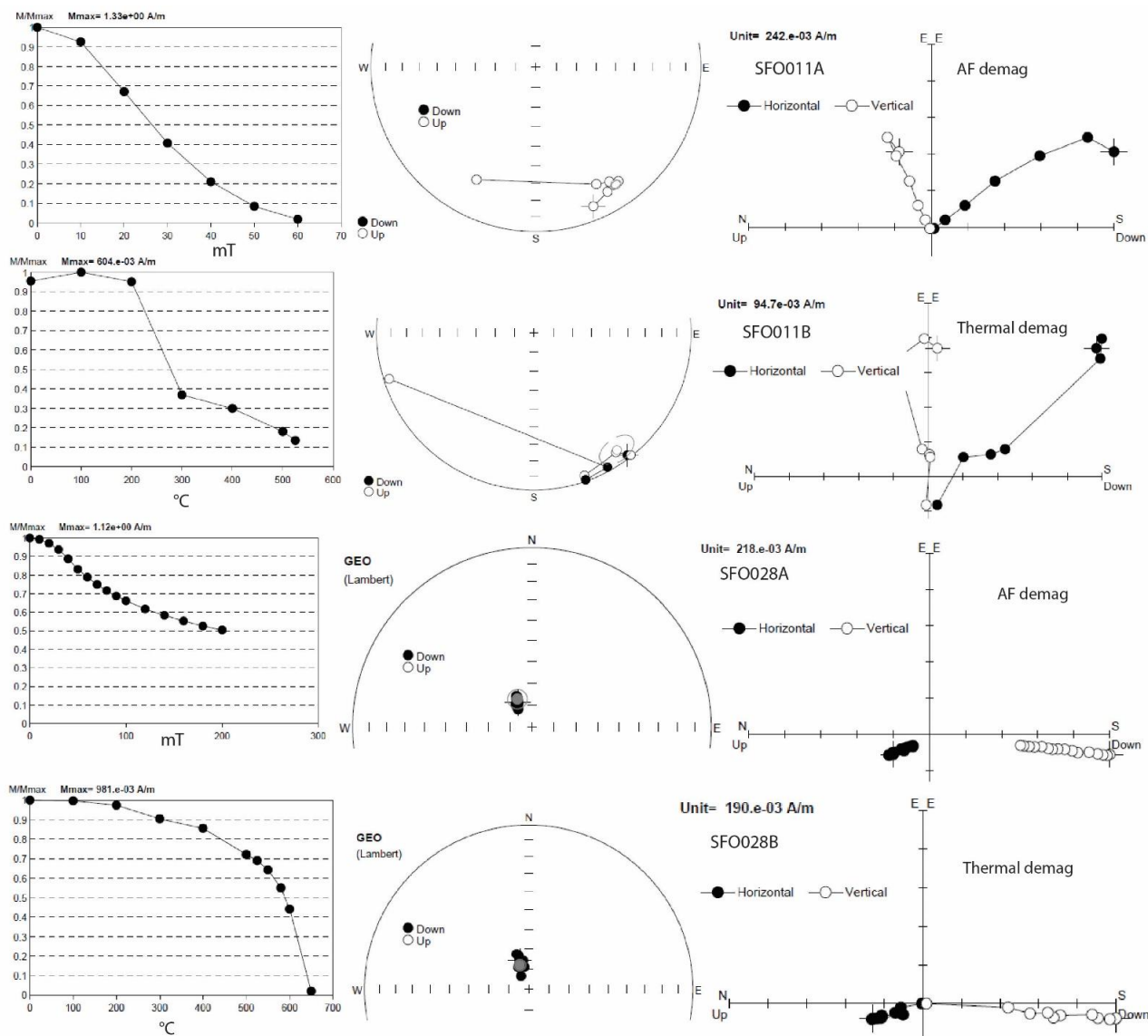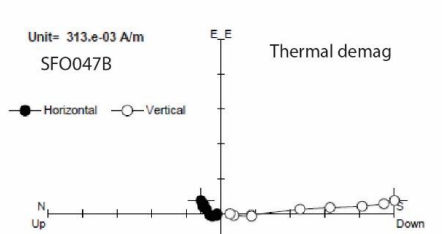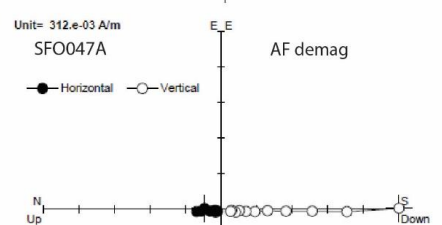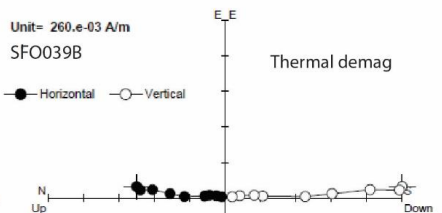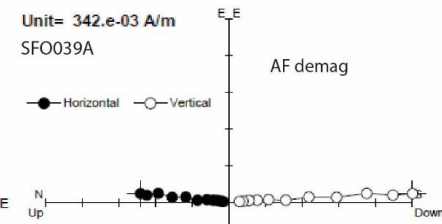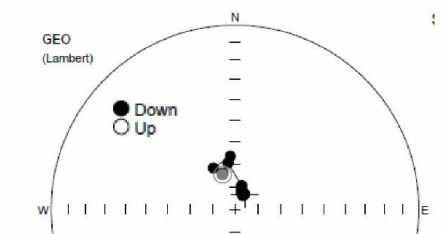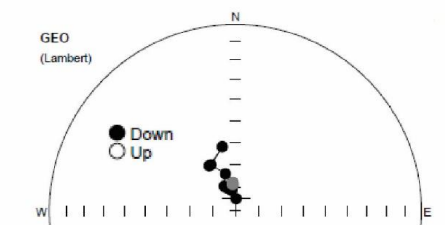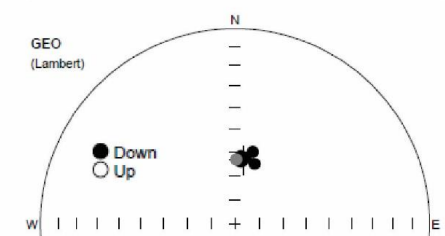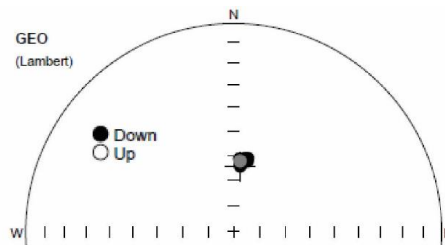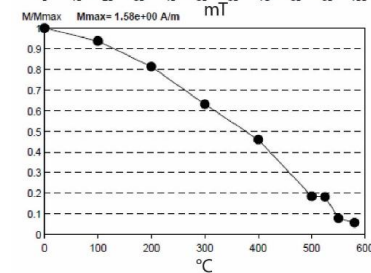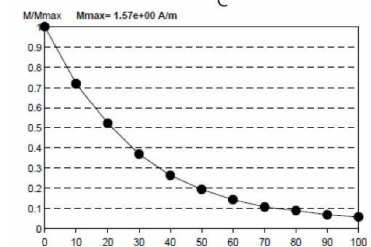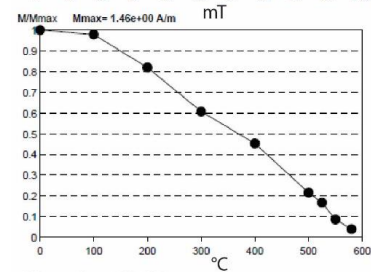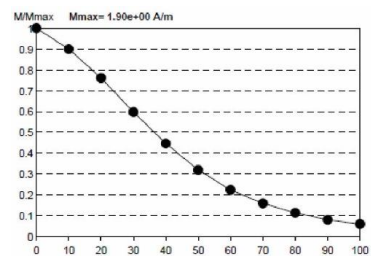
B.3. ^{40}Ar-^{39}Ar age plateau diagrams and summary of radiometric ages for collected paleomagnetic sites at Lillooet Ridge Domain for sites 1 to 4, respectively and Meager Massif Domain sites 1 to 4 respectively. Additionally, detailed preparation, analysis, and data reduction were presented within four Excel Workbook files as supplementary material.

Lillooet Ridge Domain-Site 1
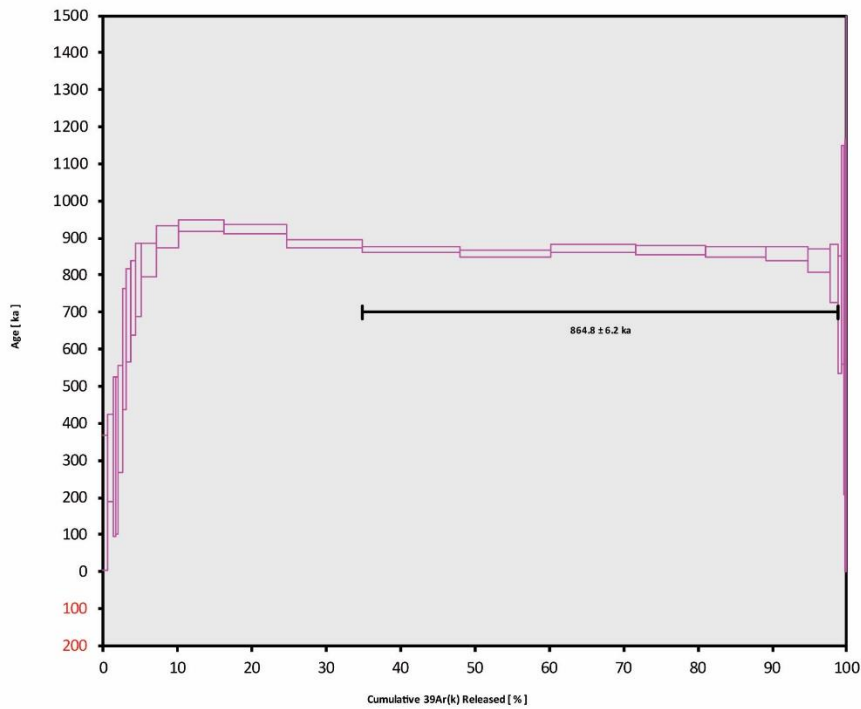
Ar-Ages in ka

WEIGHTED PLATEAU
864.8 ± 6.2
TOTAL FUSION
856.0 ± 5.5
NORMAL ISOCHRON
877.0 ± 15.6
INVERSE ISOCHRON
877.3 ± 15.5

MSWD
(PROBABILITY)
1.62 (12%)

Results	40(a)/36(a) ± 2σ	40(r)/39(k) ± 2σ	Age ± 2σ (ka)	MSWD	39Ar(k) (%,n)	K/Ca ± 2σ
Age Plateau		0.28723 ± 0.00184 ± 0.64%	864.8 ± 6.2 ± 0.71%	1.62 12%	63.91 8	0.302 ± 0.066
		Full External Error ± 45.4		2.07	2σ Confidence Limit	
		Analytical Error ± 5.5		1.2732	Error Magnification	
Total Fusion Age		0.28432 ± 0.00160 ± 0.56%	856.0 ± 5.5 ± 0.64%		27	0.313 ± 0.001
		Full External Error ± 44.8				
		Analytical Error ± 4.8				
Normal Isochron	291.45 ± 8.32 ± 2.85%	0.29130 ± 0.00511 ± 1.75%	877.0 ± 15.6 ± 1.78%	1.32 25%	63.91 8	
		Full External Error ± 48.2		2.15	2σ Confidence Limit	
		Analytical Error ± 15.4		1.1472	Error Magnification	
				21	Number of Iterations	
			0.0000025383		Convergence	
Inverse Isochron	291.39 ± 8.28 ± 2.84%	0.29141 ± 0.00508 ± 1.74%	877.3 ± 15.5 ± 1.77%	1.29 26%	63.91 8	
		Full External Error ± 48.2		2.15	2σ Confidence Limit	
		Analytical Error ± 15.3		1.1355	Error Magnification	
				3	Number of Iterations	
			0.0017704068		Convergence	
				38%	Spreading Factor	

Liliooet Ridge Domain-SITE2
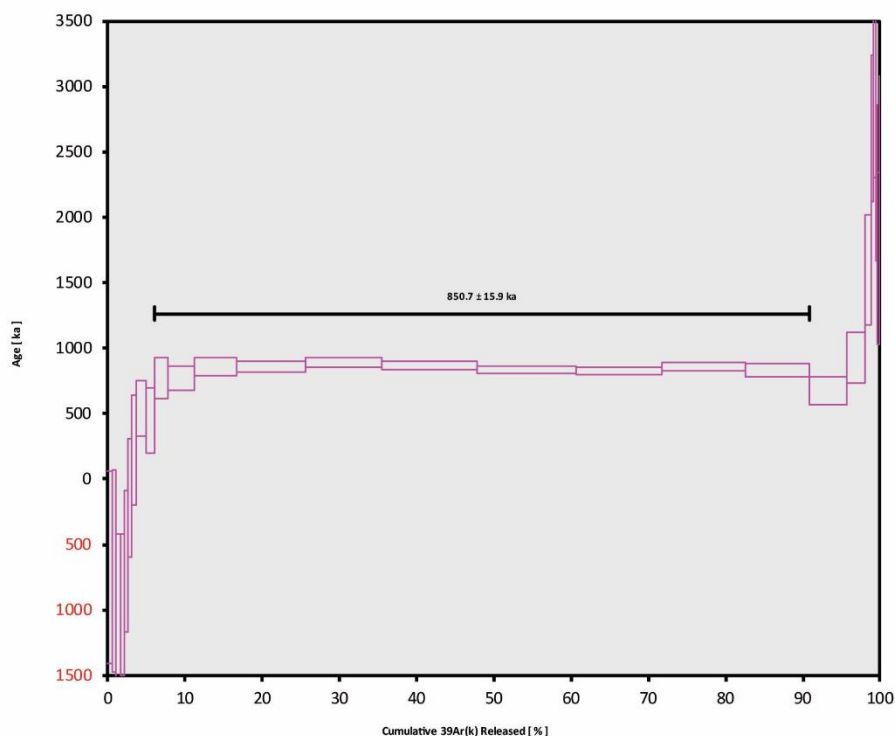
Ar-Ages in ka

WEIGHTED PLATEAU
850.7 ± 15.9
TOTAL FUSION
806.4 ± 16.8
NORMAL ISOCHRON
871.5 ± 40.5
INVERSE ISOCHRON
871.7 ± 40.4

MSWD
(PROBABILITY)
1.58 (12%)

Results	40(a)/36(a) ± 2σ	40(r)/39(k) ± 2σ	Age ± 2σ (ka)	MSWD	39Ar(k) (%,n)	K/Ca ± 2σ
Age Plateau		0.28271 ± 0.00519 ± 1.84%	**850.7** ± **15.9** ± **1.86%**	1.58 12%	84.76 10	0.394 ± 0.043
		Full External Error ± 47.0		1.94	2σ Confidence Limit	
		Analytical Error ± 15.6		1.2558	Error Magnification	
Total Fusion Age		0.26797 ± 0.00553 ± 2.06%	**806.4** ± **16.8** ± **2.09%**		27	0.316 ± 0.001
		Full External Error ± 45.2				
		Analytical Error ± 16.6				
Normal Isochron	297.62 ± 1.67 ± 0.56%	0.28960 ± 0.01342 ± 4.63%	**871.5** ± **40.5** ± **4.64%**	1.79 7%	84.76 10	
		Full External Error ± 60.7		2.00	2σ Confidence Limit	
		Analytical Error ± 40.4		1.3380	Error Magnification	
				3	Number of Iterations	
			0.0000010105		Convergence	
Inverse Isochron	297.62 ± 1.68 ± 0.56%	0.28969 ± 0.01340 ± 4.63%	**871.7** ± **40.4** ± **4.64%**	1.79 7%	84.76 10	
		Full External Error ± 60.7		2.00	2σ Confidence Limit	
		Analytical Error ± 40.3		1.3386	Error Magnification	
				2	Number of Iterations	
			0.0012604862		Convergence	
			12%		Spreading Factor	

Lilooet Ridge Domain-SITE3
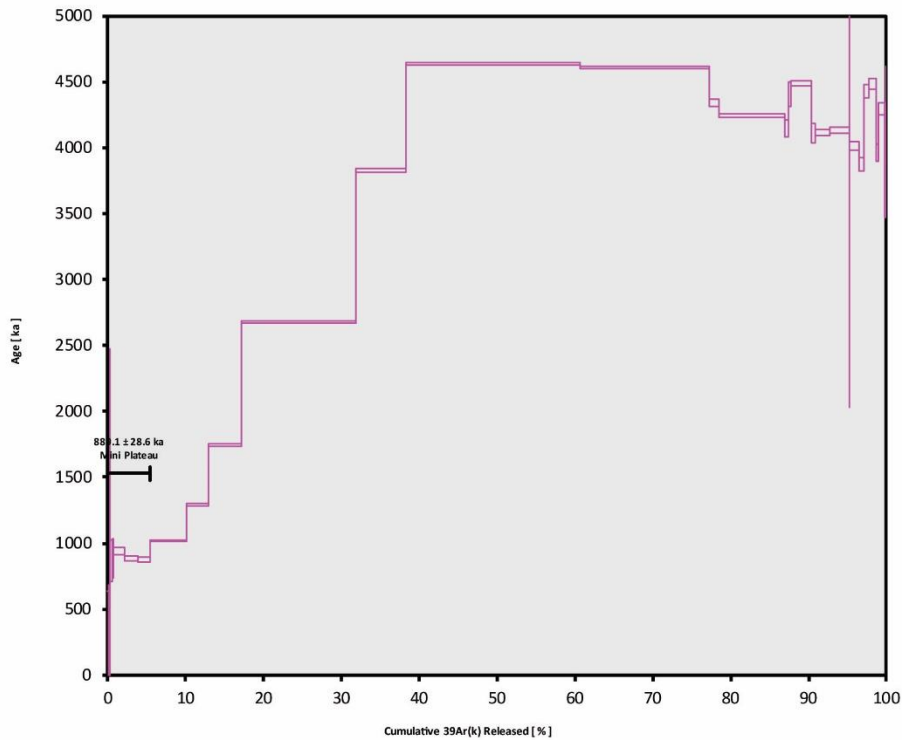
Ar-Ages in ka

WEIGHTED PLATEAU
889.1 ± 28.6
TOTAL FUSION
3614.7 ± 12.0
NORMAL ISOCHRON
896.3 ± 33.3
INVERSE ISOCHRON
897.8 ± 34.1

**MSWD
(PROBABILITY)**
5.21 (0%)

Results	40(a)/36(a) ± 2σ	40(r)/39(k) ± 2σ	Age ± 2σ (ka)	MSWD	39Ar(k) (%,n)	K/Ca ± 2σ
Age Plateau		0.29563 ± 0.00946	**889.1** ± **28.6**	5.21	5.35	19.1 ± 6.3
Error Mean		± 3.20%	± 3.21%	0%	8	
		Full External Error ± 54.3		2.07	2σ Confidence Limit	
		Analytical Error ± 28.4		2.2832	Error Magnification	
Total Fusion Age		1.20275 ± 0.00131	**3614.7** ± **12.0**		33	18.2 ± 0.3
		± 0.11%	± 0.33%			
		Full External Error ± 188.2				
		Analytical Error ± 3.9				
Normal Isochron	296.22 ± 4.69	0.29803 ± 0.01105	**896.3** ± **33.3**	5.43	5.35	
Error Chron	± 1.58%	± 3.71%	± 3.72%	0%	8	
		Full External Error ± 57.3		2.15	2σ Confidence Limit	
		Analytical Error ± 33.2		2.3296	Error Magnification	
				23	Number of Iterations	
			0.0000022759		Convergence	
Inverse Isochron	296.35 ± 4.74	0.29852 ± 0.01130	**897.8** ± **34.1**	5.47	5.35	
Error Chron	± 1.60%	± 3.79%	± 3.80%	0%	8	
		Full External Error ± 57.8		2.15	2σ Confidence Limit	
		Analytical Error ± 34.0		2.3381	Error Magnification	
				3	Number of Iterations	
			0.0002570487		Convergence	
				66%	Spreading Factor	

Lilooet Ridge Domain–SITE4

ASSUMED TRAPPED 40Ar/36Ar RATIO
Low 40/36 = 286.26 ± 1.11 (%SD)

Age [Ma]

Cumulative 39Ar(k) Released [%]
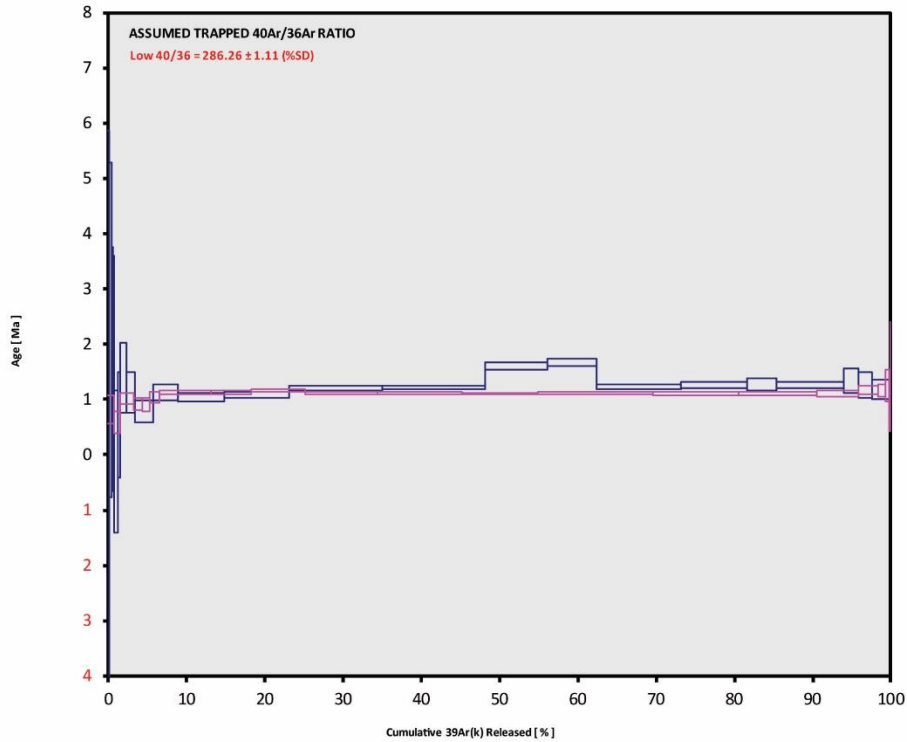
Ar-Ages in Ma

WEIGHTED PLATEAU
1.14 ± 0.02
TOTAL FUSION
1.14 ± 0.01
NORMAL ISOCHRON
1.13 ± 0.03
INVERSE ISOCHRON
1.13 ± 0.04

MSWD
(PROBABILITY)
6.05 (0%)

Results	40(a)/36(a) ± 2σ	40(r)/39(k) ± 2σ	Age ± 2σ (Ma)	MSWD	39Ar(k) (%,n)	K/Ca ± 2σ
Age Plateau		0.37786 ± 0.00573	**1.14 ± 0.02**	6.05	86.88	0.358 ± 0.139
Error Mean		± 1.52%	± 1.55%	0%	24	
		Full External Error ± 0.06		1.59	2σ Confidence Limit	
		Analytical Error ± 0.02		2.4596	Error Magnification	
Total Fusion Age		0.37935 ± 0.00280	**1.14 ± 0.01**		44	0.217 ± 0.000
		± 0.74%	± 0.80%			
		Full External Error ± 0.06				
		Analytical Error ± 0.01				
Normal Isochron	285.29 ± 9.83	0.37466 ± 0.01049	**1.13 ± 0.03**	7.52	86.88	
Error Chron	± 3.45%	± 2.80%	± 2.82%	0%	24	
		Full External Error ± 0.07		1.60	2σ Confidence Limit	
		Analytical Error ± 0.03		2.7421	Error Magnification	
				31	Number of Iterations	
				0.0000033367	Convergence	
Inverse Isochron	284.16 ± 11.70	0.37722 ± 0.01225	**1.13 ± 0.04**	10.89	86.88	
Error Chron	± 4.12%	± 3.25%	± 3.26%	0%	24	
		Full External Error ± 0.07		1.60	2σ Confidence Limit	
		Analytical Error ± 0.04		3.3007	Error Magnification	
				4	Number of Iterations	
				0.0003564529	Convergence	
				55%	Spreading Factor	

■ Age Plateau and Total Fusion Ages assume Trapped Low 40/36 = 286.26 ± 1.11 (%SD)

Meager Massif Site 1(MM1)

Results	40(a)/36(a) ± 2σ	40(r)/39(k) ± 2σ	Age ± 2σ (ka)	MSWD	39Ar(k) (%,n)	K/Ca ± 2σ
Age Plateau		0.61721 ± 0.02302 ± 3.73%	1906.4 ± 71.1 ± 3.73%	0.36 94%	61.11 9	0.116 ± 0.006
			Full External Error ± 106.8	2.00	2σ Confidence Limit	
			Analytical Error ± 71.1	1.0000	Error Magnification	
Total Fusion Age		0.57028 ± 0.02449 ± 4.29%	1761.5 ± 75.6 ± 4.29%		15	0.112 ± 0.002
			Full External Error ± 105.5			
			Analytical Error ± 75.6			
Normal Isochron	290.35 ± 22.81 ± 7.86%	0.63275 ± 0.05244 ± 8.29%	1954.4 ± 161.9 ± 8.28%	0.35 93%	61.11 9	
			Full External Error ± 181.3	2.07	2σ Confidence Limit	
			Analytical Error ± 161.9	1.0000	Error Magnification	
Inverse Isochron	290.50 ± 22.76 ± 7.84%	0.63390 ± 0.05179 ± 8.17%	1957.9 ± 159.9 ± 8.17%	0.35 93%	61.11 9	
			Full External Error ± 179.6	2.07	2σ Confidence Limit	
			Analytical Error ± 159.9	1.0000	Error Magnification	
				38%	Spreading Factor	
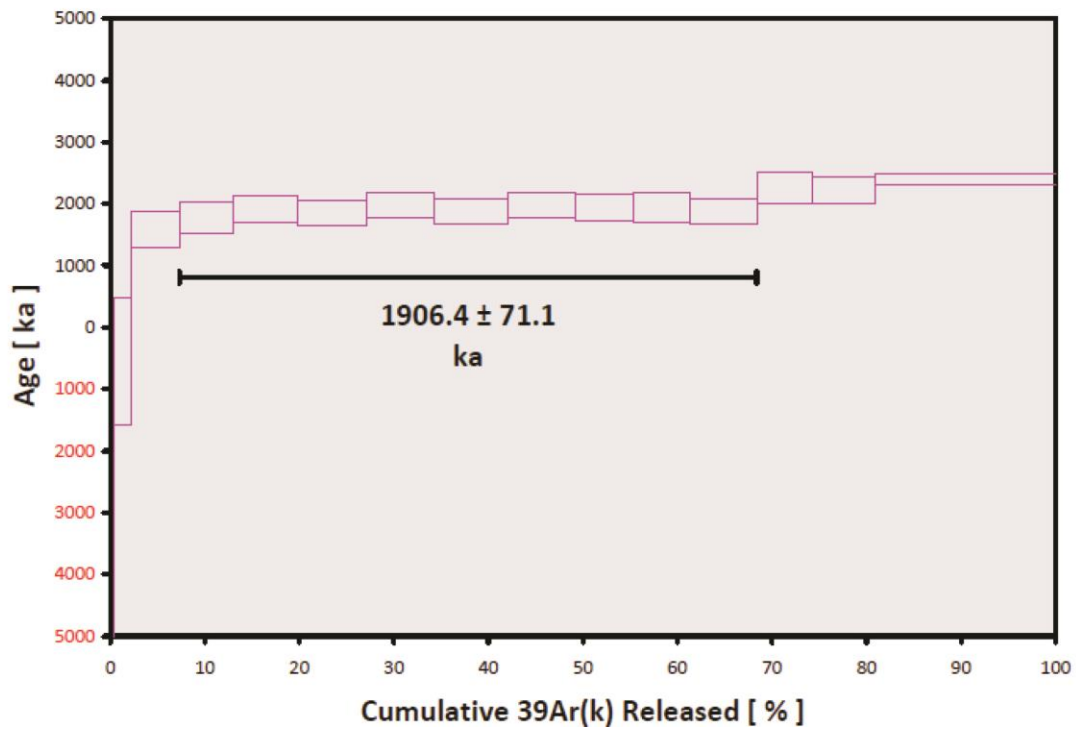
Meager Massif Site 2(MM2)

Results	40(a)/36(a) ± 2σ	40(r)/39(k) ± 2σ	Age ± 2σ (ka)	MSWD	39Ar(k) (%,n)	K/Ca ± 2σ
Age Plateau		0.02116 ± 0.02272 ± 107.36%	65.8 ± 70.6 ± 107.36%	1.35 19%	79.12 12	0.0578 ± 0.0046
		Full External Error ± 70.6		1.85	2σ Confidence Limit	
		Analytical Error ± 70.6		1.1611	Error Magnification	
Total Fusion Age		0.04478 ± 0.01921 ± 42.90%	139.1 ± 59.7 ± 42.90%		16	0.0576 ± 0.0004
		Full External Error ± 60.0				
		Analytical Error ± 59.7				
Normal Isochron	294.00 ± 6.65 ± 2.26%	0.03624 ± 0.03261 ± 89.98%	112.6 ± 101.3 ± 89.98%	1.25 25%	79.12 12	
		Full External Error ± 101.4		1.89	2σ Confidence Limit	
		Analytical Error ± 101.3		1.1190	Error Magnification	
Inverse Isochron	293.94 ± 6.55 ± 2.23%	0.03985 ± 0.01983 ± 49.75%	123.8 ± 61.6 ± 49.74%	1.23 27%	79.12 12	
		Full External Error ± 61.8		1.89	2σ Confidence Limit	
		Analytical Error ± 61.6		1.1089	Error Magnification	
					8%	Spreading Factor

65.8 ± 70.6 ka
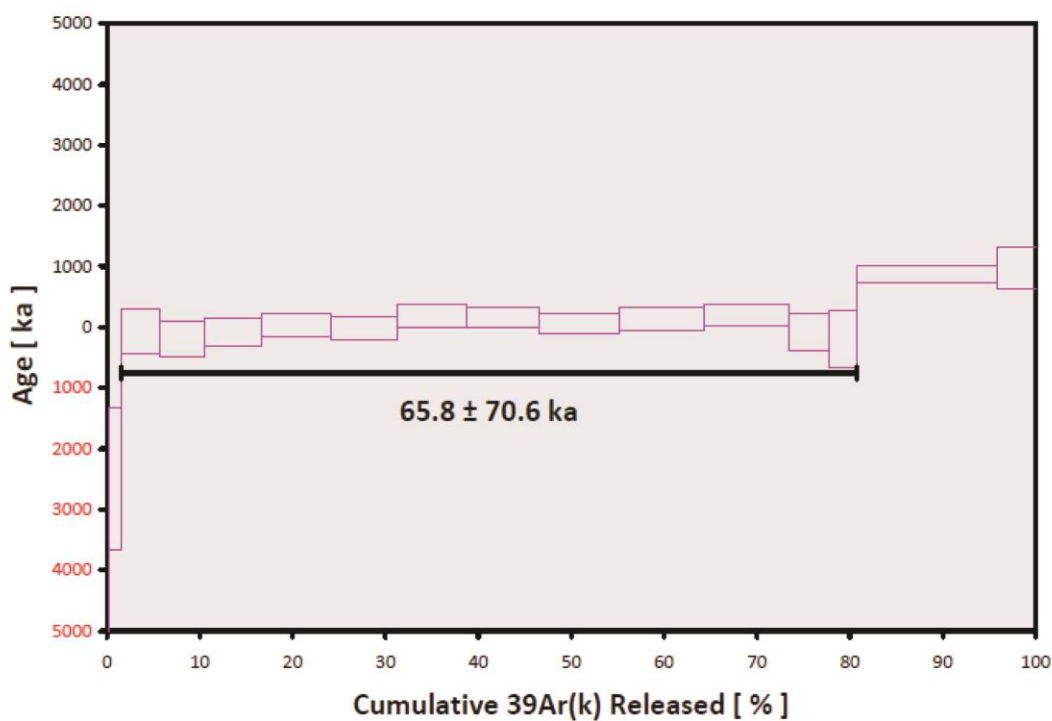
Meager Massif Site 3(MM3)

Results	40(a)/36(a) ± 2σ	40(r)/39(k) ± 2σ	Age ± 2σ (ka)	MSWD	39Ar(k) (%,n)	K/Ca ± 2σ
Age Plateau		0.17278 ± 0.05426 ± 31.41%	535.4 ± 168.1 ± 31.40%	1.59 15%	83.39 7	0.0523 ± 0.0017
			Full External Error ± 169.6	2.15	2σ Confidence Limit	
			Analytical Error ± 168.1	1.2613	Error Magnification	
Total Fusion Age		0.00536 ± 0.05484 ± 1022.25%	16.6 ± 169.9 ± 1022.25%		12	0.0528 ± 0.0003
			Full External Error ± 169.9			
			Analytical Error ± 169.9			
Normal Isochron	276.28 ± 30.57 ± 11.06%	0.27359 ± 0.15180 ± 55.48%	847.7 ± 470.2 ± 55.47%	1.29 26%	83.39 7	
			Full External Error ± 471.6	2.26	2σ Confidence Limit	
			Analytical Error ± 470.2	1.1377	Error Magnification	
Inverse Isochron	272.19 ± 30.76 ± 11.30%	0.30059 ± 0.13117 ± 43.64%	931.3 ± 406.3 ± 43.63%	1.31 26%	83.39 7	
			Full External Error ± 408.2	2.26	2σ Confidence Limit	
			Analytical Error ± 406.3	1.1429	Error Magnification	
				21%	Spreading Factor	

535.4 ± 168.1 ka
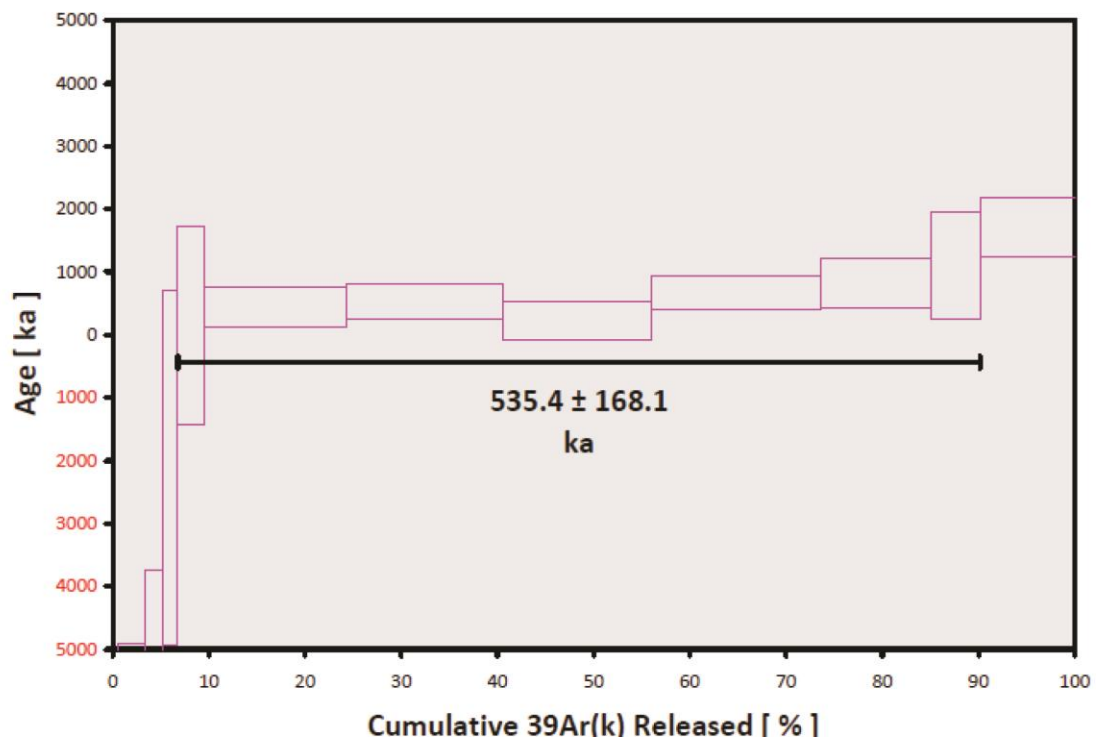
Meager Massif Site 4(MM4)

Results	40(a)/36(a) ± 2σ	40(r)/39(k) ± 2σ	Age ± 2σ (ka)	MSWD	39Ar(k) (%,n)	K/Ca ± 2σ
Age Plateau		0.07888 ± 0.01141 ± 14.47%	245.4 ± 35.5 ± 14.47%	0.92 46%	80.69 6	0.0664 ± 0.0158
		Full External Error ± 37.0		2.26	2σ Confidence Limit	
		Analytical Error ± 35.5		1.0000	Error Magnification	
Total Fusion Age		0.14668 ± 0.01088 ± 7.42%	456.3 ± 33.9 ± 7.42%		10	0.0594 ± 0.0004
		Full External Error ± 38.9				
		Analytical Error ± 33.8				
Normal Isochron	299.22 ± 7.75 ± 2.59%	0.07689 ± 0.01970 ± 25.62%	239.2 ± 61.3 ± 25.61%	1.12 35%	80.69 6	
		Full External Error ± 62.1		2.41	2σ Confidence Limit	
		Analytical Error ± 61.3		1.0566	Error Magnification	
Inverse Isochron	299.09 ± 7.94 ± 2.66%	0.07800 ± 0.01953 ± 25.03%	242.7 ± 60.7 ± 25.03%	1.16 33%	80.69 6	
		Full External Error ± 61.6		2.41	2σ Confidence Limit	
		Analytical Error ± 60.7		1.0774	Error Magnification	
				14%	Spreading Factor	

245.4 ± 35.5 ka
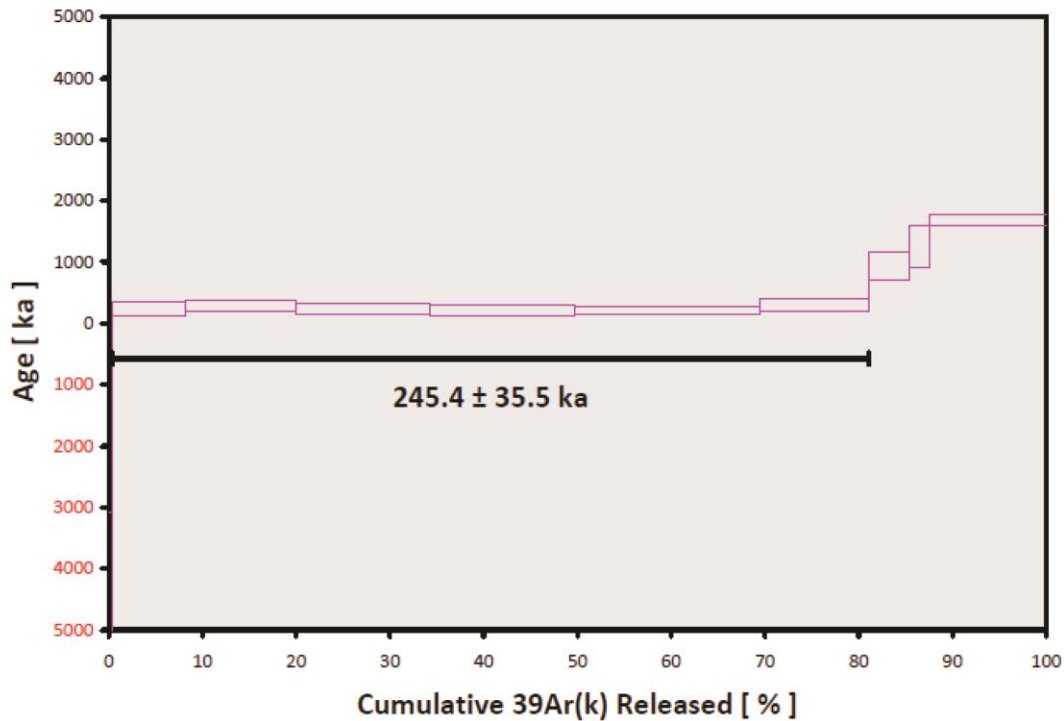
Appendix C. Supplementary Materials for Chapter 4

C.1. Geotechnical Kinematic Analysis Supplementary Data

Table S4.1. Sensitivity analysis data for experimenting Factor of Safety vs Friction Angle for Different Cohesion and Water Pressure Conditions.

Friction angle (degrees)	Cohesion (MPa)	Key Block Factor of safety	Shear strength (MPa)
0	0	0	0
2	0.02	0.145	0.22
4	0.04	0.29	0.44
6	0.06	0.435	0.66
8	0.08	0.582	0.88
10	0.10	0.729	1.11
12	0.12	0.878	1.34
14	0.14	1.029	1.57
16	0.16	1.181	1.8
18	0.18	1.336	2.04
20	0.20	1.494	2.28
22	0.22	1.655	2.53
24	0.24	1.819	2.79
26	0.26	1.987	3.05
28	0.28	2.16	3.32
30	0.30	2.338	3.6

32	0.32	2.522	3.9
34	0.34	2.713	4.2
36	0.36	2.911	4.52
38	0.38	3.118	4.85
40	0.40	3.334	5.2
42	0.42	3.561	5.57
44	0.44	3.8	5.97
46	0.46	4.053	6.39
48	0.48	4.323	6.84
50	0.50	4.612	7.32

Table S4.2. Sensitivity analysis data for experimenting Cohesion, Key Block Factor of Safety, and Shear Strength vs Friction Angle.

Friction angle	Factor of safety							
	Cohesion=0 MPa, dry condition	Cohesion =0.1 MPa, dry condition	Cohesion =0.2 MPa, dry condition	Cohesion =0.3 MPa, dry condition	Cohesion =0.4 MPa, dry condition	Cohesion =0.5 MPa, dry condition	Cohesion=0 MPa water pressure =0.3 MPa	Cohesion =0.5 MPa water pressure =0.3 MPa
0	0	0.18	0.36	0.54	0.72	0.90	0	0.78
10	0.549	0.72	0.91	1.09	1.27	1.45	0.4	1.19
20	1.133	1.31	1.49	1.674	1.85	2.03	0.85	1.63
30	1.798	1.97	2.158	2.33	2.51	2.69	1.35	2.13

40	2.61	2.79	2.973	3.15	3.33	3.5	1.96	2.74
50	3.71	3.89	4.071	4.25	4.43	4.6	2.79	3.57
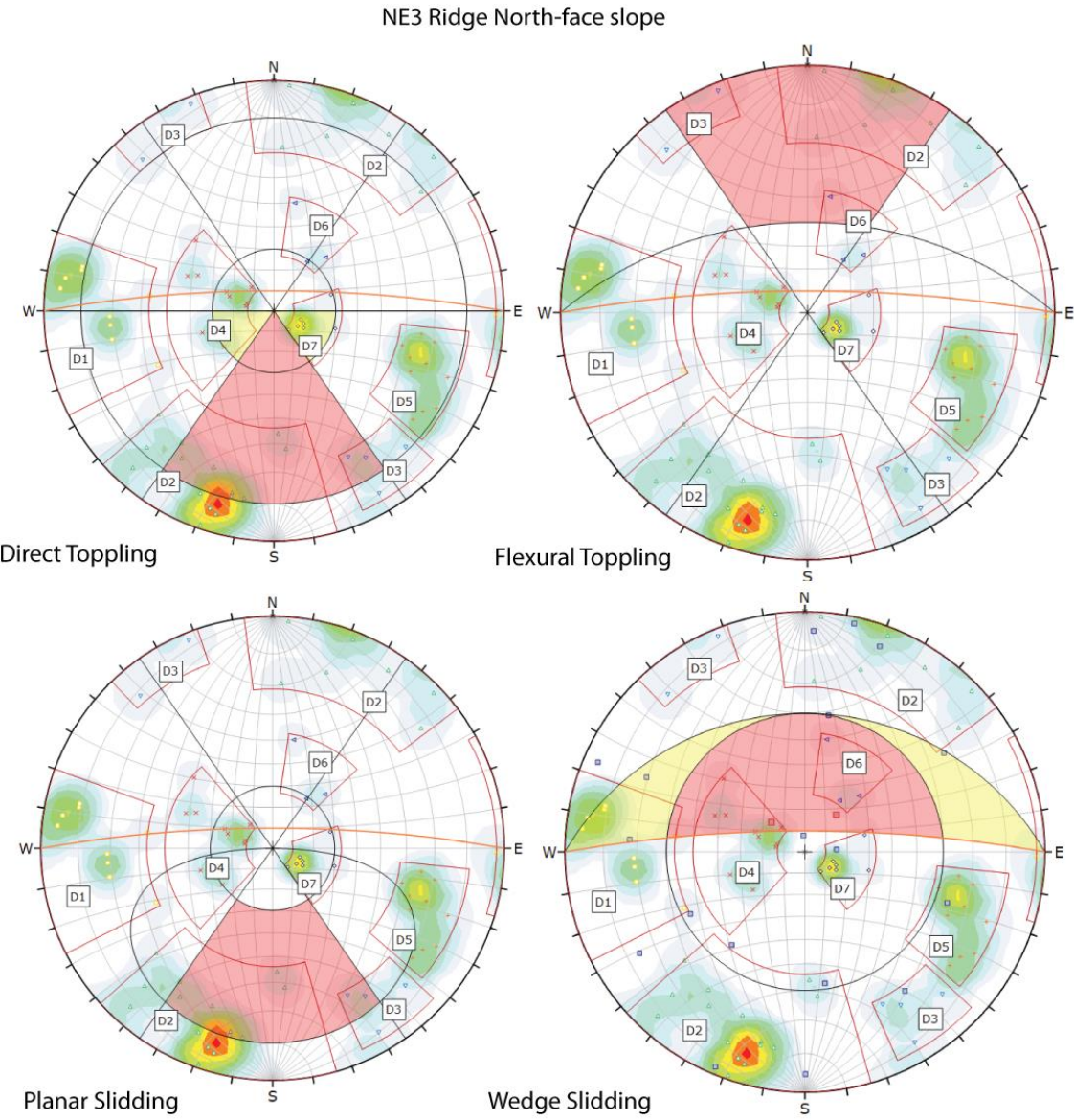
Plate 1: Two-dimensional geotechnical kinematic analysis of discontinuities for field measurements at North Slope in Domain 1

NE3 Ridge south-face slope

Direct Toppling

Flexural Toppling

Planar Slidding

Wedge Slidding
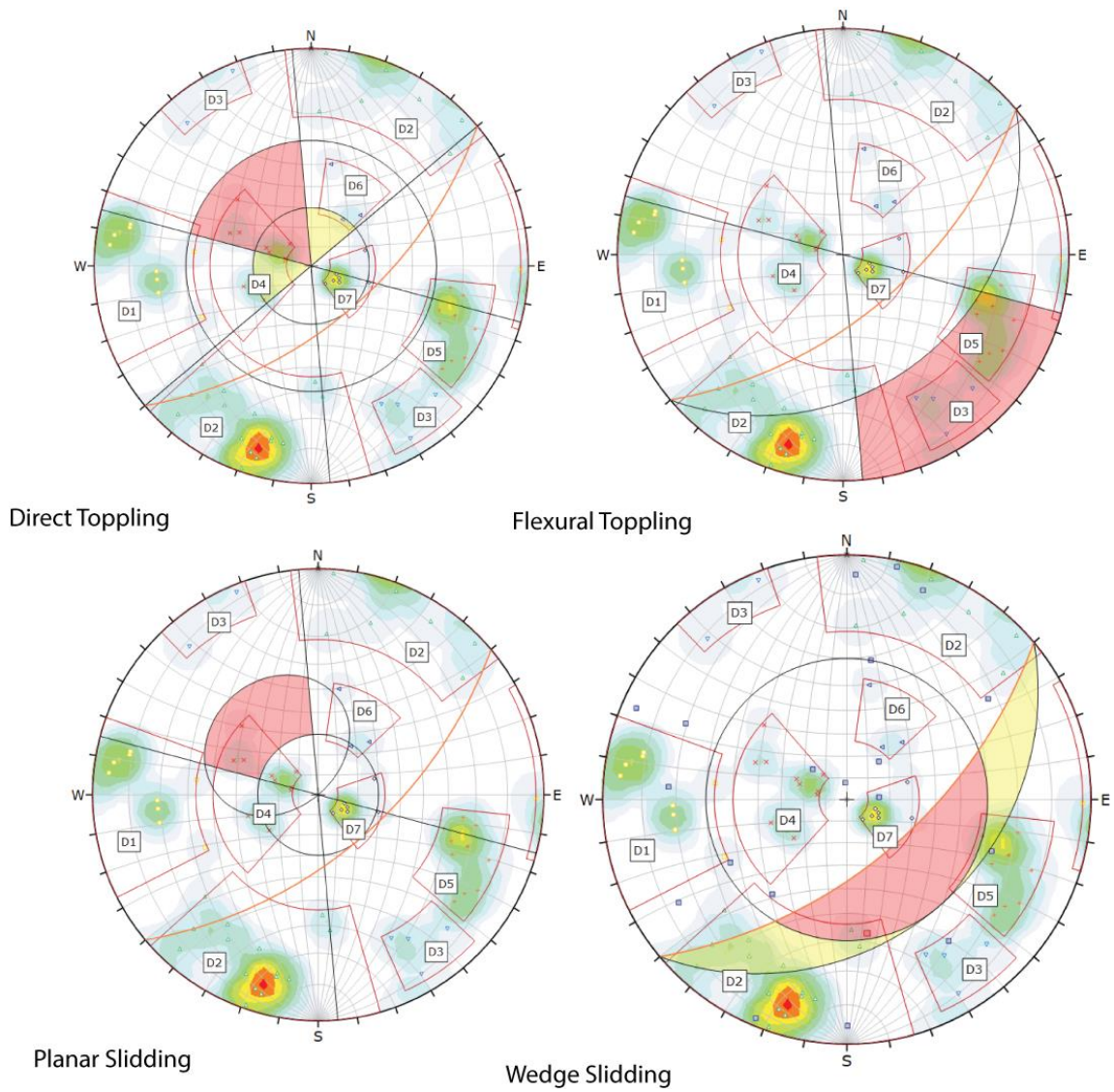
Plate 2: Two-dimensional geotechnical kinematic analysis of discontinuities for field measurements at South Slope in Domain 1.
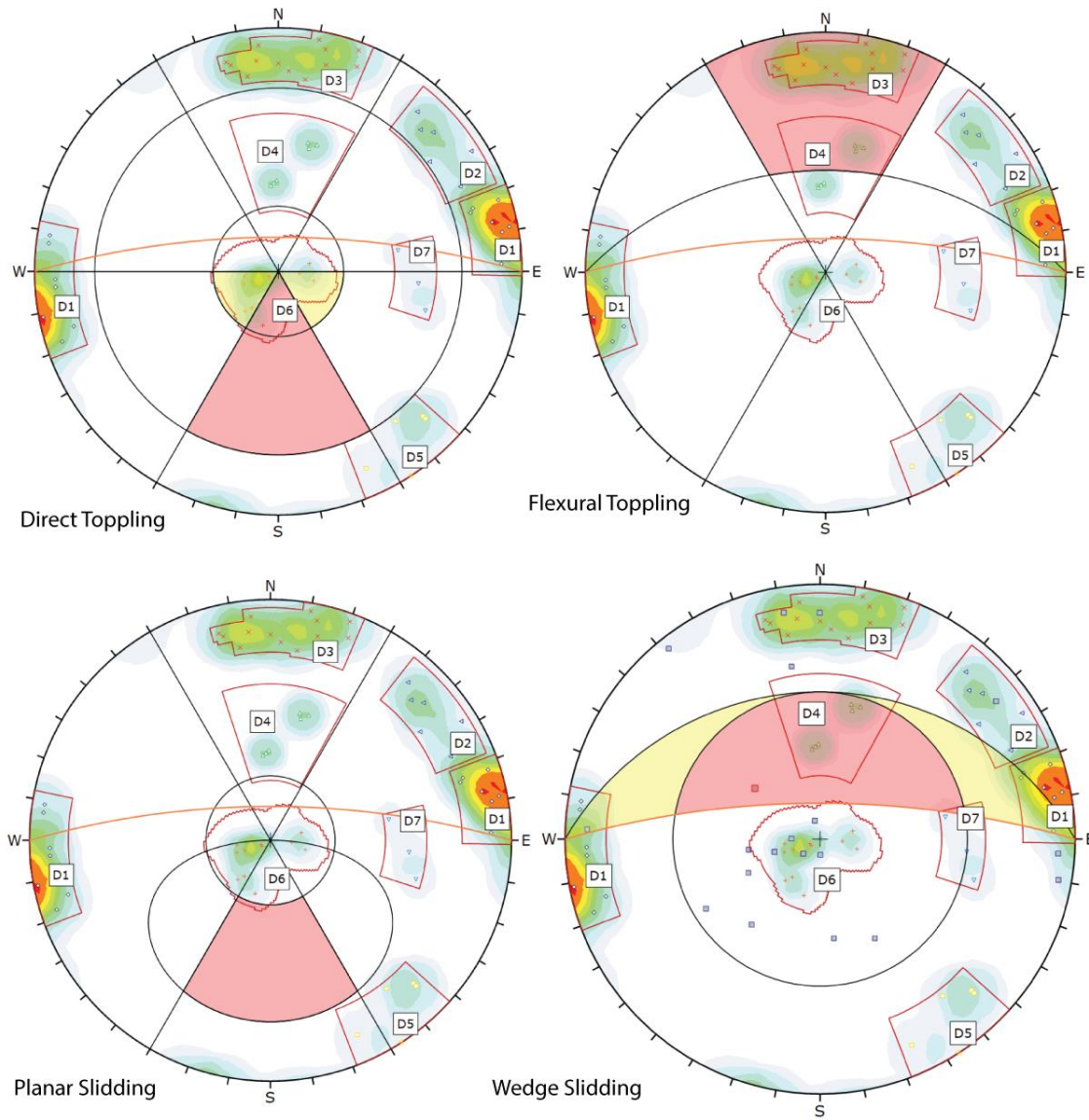
Plate 3: Two-dimensional geotechnical kinematic analysis of discontinuities for field measurements at North Slope in Domain 2

NW-1 Ridge south-face slope
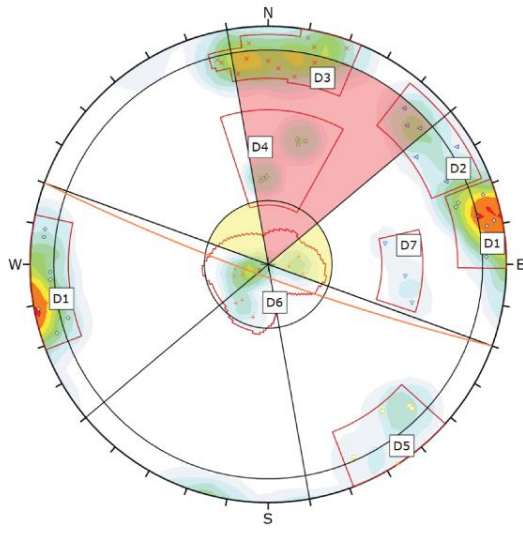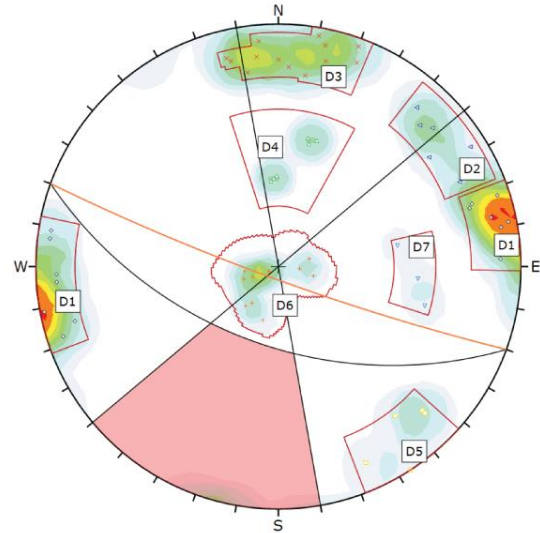
Direct Toppling

Flexural Toppling
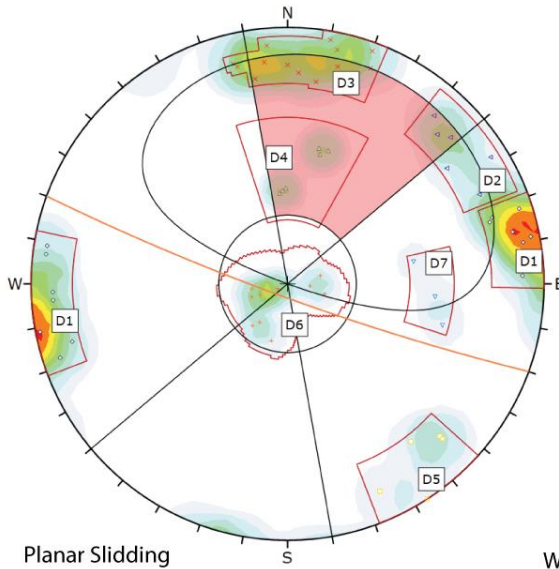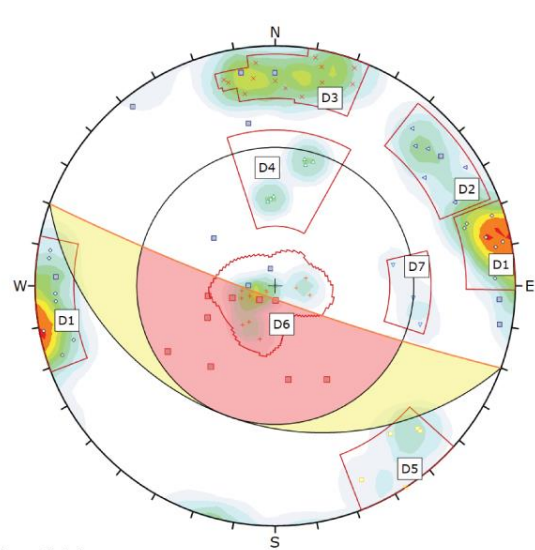
Planar Slidding

Wedge Slidding

Plate 4: Two-dimensional geotechnical kinematic analysis of discontinuities for field measurements at South Slope in Domain 2
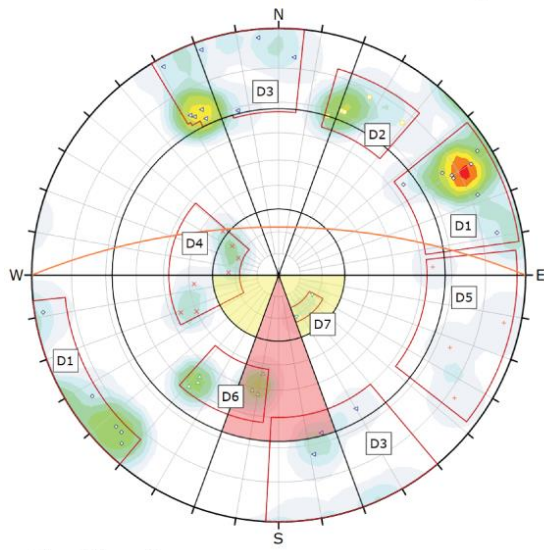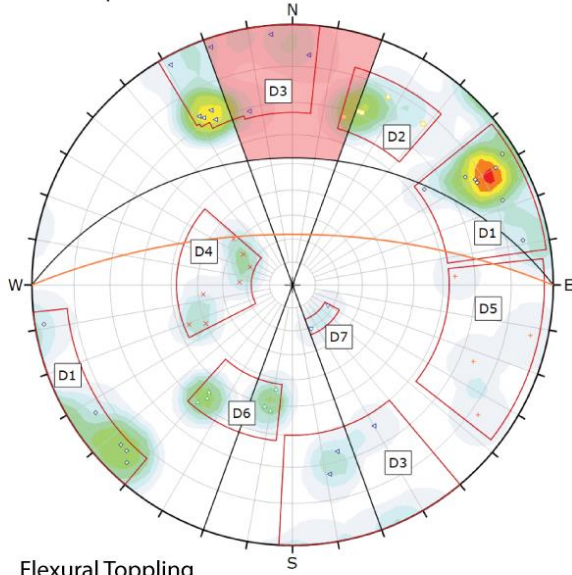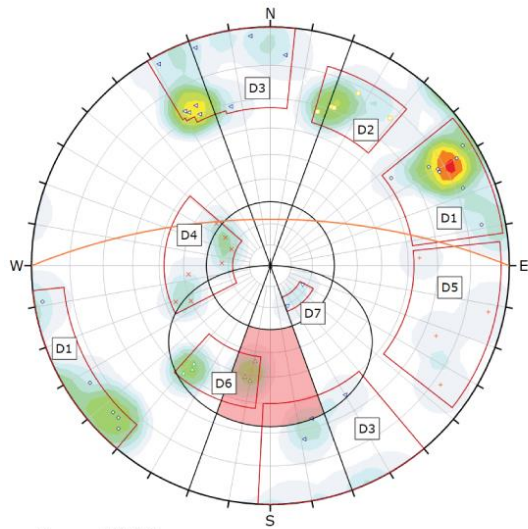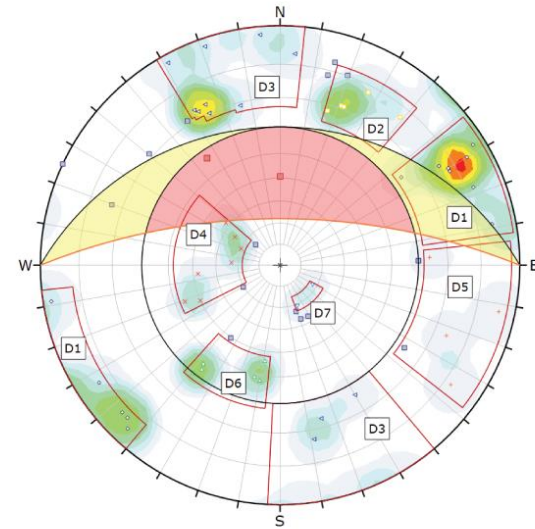
Plate 5: Two-dimensional geotechnical kinematic analysis of discontinuities for field measurements at North Slope in Domain 2
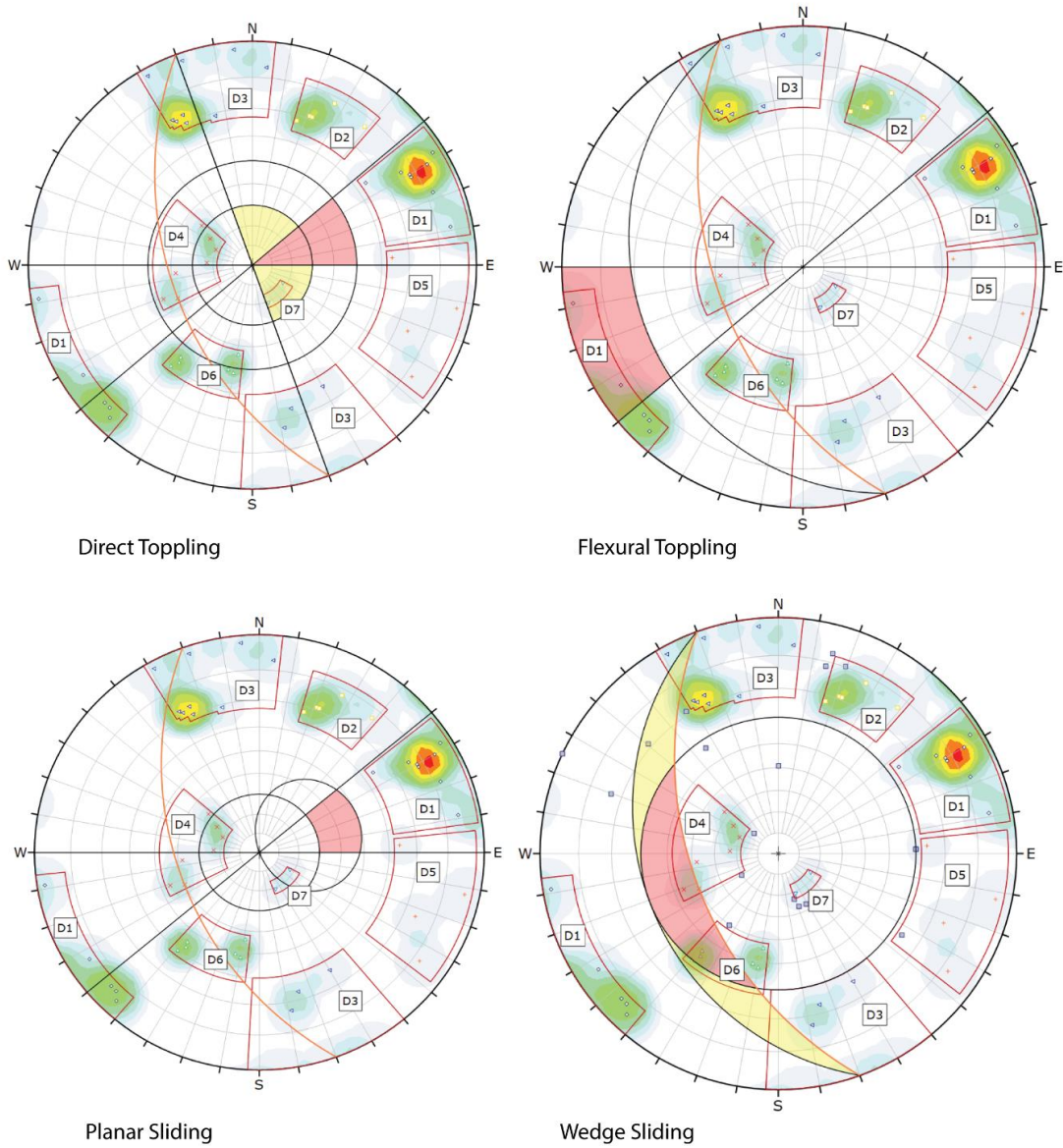
Plate 6: Two-dimensional geotechnical kinematic analysis of discontinuities for field measurements at South Slope in Domain 2

C.2. Field Data

Geotechnical Discontinuity Survey Mapping Data

Below are descriptions of the codes used in Table S1 and Table S3

Persistence

1. Very low persistence   <1 m
2. Low persistence   1–3 m
3. Medium persistence   3–10 m
4. High persistence   10–20 m
5. Very high persistence   >20 m

Spacing

1. Extremely close spacing   <20 mm
2. Very close spacing   20–60 mm
3. Close spacing   60–200 mm
4. Moderate spacing   200–600 mm
5. Wide spacing   600–2000 mm
6. Very wide spacing   2000–6000 mm
7. Extremely wide spacing

Surface Roughness
See Tables S2 and S4

Aperture/width

1. Very tight (<0.1 mm)
2. Tight (0.1–0.25 mm)
3. Partly open (0.25–0.5 mm)
4. Open (0.5–2.5 mm)
5. Moderately wide (2.5–10 mm)
6. Wide (>10 mm)
7. Very wide (1–10 cm)
8. Extremely wide (10–100 cm)
9. Cavernous (>1 m)

Nature of filling

1. Clean
2. Surface staining
3. Non-cohesive
4. Inactive clay or clay matrix
5. Swelling clay or clay matrix
6. Cemented
7. Chlorite, talc or gypsum
8. Other — specify

Surface shape

1. Stepped
2. Undulating
3. Planar

Termination

0. Neither end visible
1. One end visible
2. Both ends visible
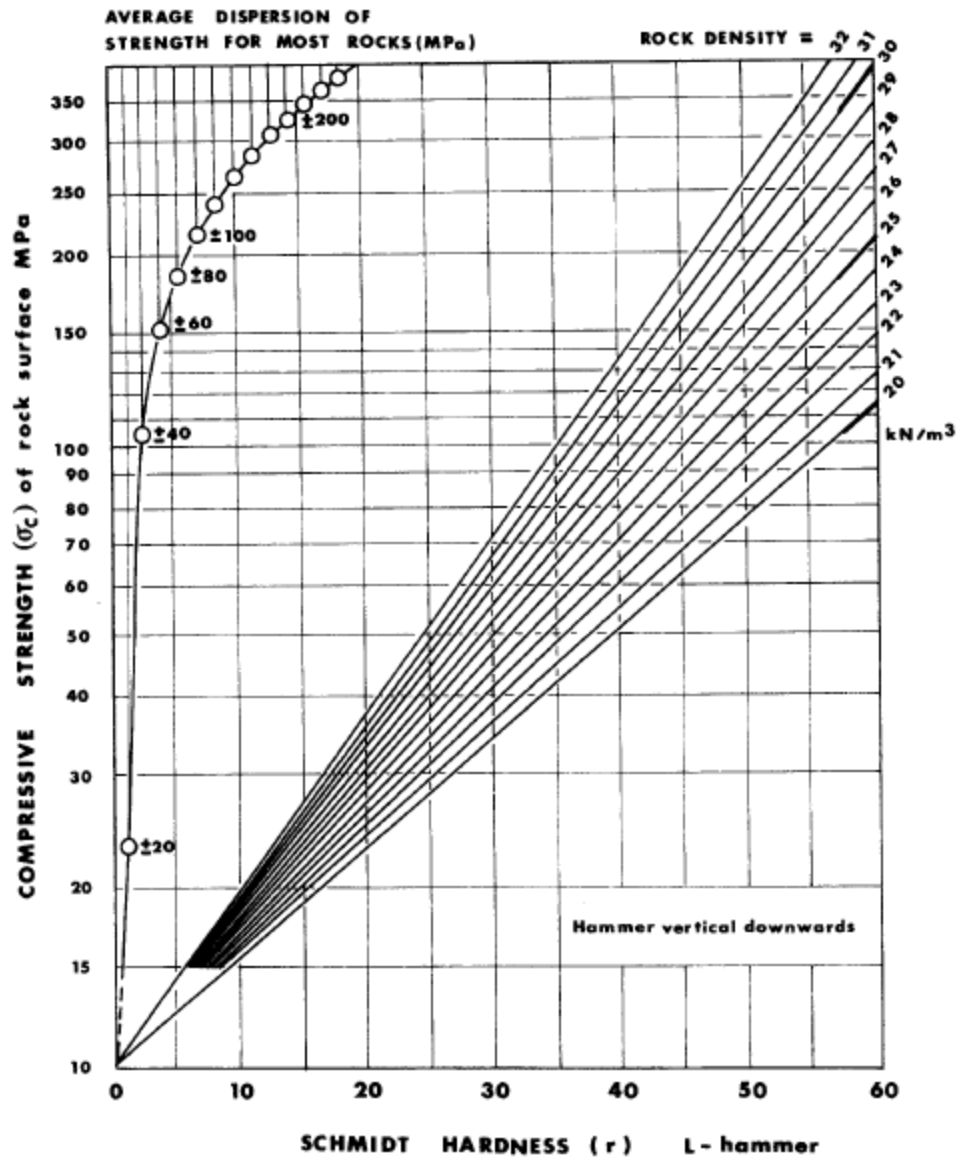
Figure S4.1. Correlation chart for Schmidl (L) hammer, relating rock density, compressive strength, and rebound number (ISRM,1978)

Table S4.3: Discontinuity survey data and descriptions within domain 1.

Station NO	Dip Direction	dip	Lat	Long	Roughness	surface shape	Persistence	Termination	Aperture	Filling	joint spacing	Rock Strength (No. of hits by hammer)
1	280.821	71.3721	50.26265	-122.758	3-18.jpg	2	3	2	6	4	3	5
	327.967	74.327	50.26262	-122.758	3-21.jpg	2	3	2	6	4	3	
	307.677	75.2583	50.26261	-122.758	3-21.jpg	2	3	2	6	4	3	
	225.903	88.4579	50.26263	-122.758	3-25.jpg	2	2	1	6	4	5	
	230.551	79.2494	50.26261	-122.758	3-26.jpg	2	1	2	5	1	5	
	73.3485	36.4996	50.2626	-122.758	3-28.jpg	2	1	2	5	1	5	
	80.4897	71.0933	50.2626	-122.758	3-29.jpg	2	2	2	5	1	5	
	85.258	70.5302	50.26259	-122.758	3-29.jpg	2	2	2	5	1	5	
2	20.9093	72.1498	50.26374	-122.759	3-31.jpg	1	5	0	8	5	3	8
	32.0927	74.0405	50.26373	-122.759	3-31.jpg	1	5	0	8	5	3	
	48.2288	68.2147	50.26375	-122.759	3-31.jpg	1	5	0	8	5	3	
	288.666	63.9649	50.26376	-122.759	3-34.jpg	1	1	1	7	1	5	
	284.968	59.6437	50.26374	-122.759	3-34.jpg	1	1	1	7	1	5	
	315.908	79.4458	50.26375	-122.759	3-34.jpg	1	1	1	7	1	5	
	106.033	14.2458	50.26373	-122.759	3-37.jpg	3	1	2	3	4	4	
	107.937	23.2326	50.26376	-122.759	3-37.jpg	3	1	2	3	4	4	
	99.0069	13.7768	50.26376	-122.759	3-37.jpg	3	1	2	3	4	4	
	112.214	43.8564	50.26375	-122.759	3-41.jpg	3	1	2	1	1	2	
	115.174	40.2254	50.26375	-122.759	3-41.jpg	3	1	2	1	1	2	
	132.23	48.6697	50.26374	-122.759	3-41.jpg	3	1	2	1	1	2	
3	13.0678	77.771	50.2643	-122.76	3-44.jpg	3	5	0	1	1	3	40
	17.5348	83.959	50.26429	-122.759	3-44.jpg	3	5	0	1	1	3	

	9.16527	79.3553	50.26431	-122.759	3-44.jpg	3	5	0	1	1	3	
	78.9202	30.1471	50.26432	-122.759	3-47.jpg	3	5	0	1	1	4	
	58.9891	27.4854	50.26429	-122.759	3-47.jpg	3	5	0	1	1	4	
	53.993	29.7636	50.26433	-122.76	3-47.jpg	3		0	1	1	4	
	288.585	70.2174	50.26441	-122.76	3-50.jpg	3	2	1	5	1	6	
	294.284	65.9018	50.26438	-122.76	3-50.jpg	3	2	1	5	1	6	
	278.844	65.7652	50.26437	-122.76	3-50.jpg	3	2	1	5	1	6	
4	34.868	70.1076	50.26481	-122.762	3-55.jpg	3	5	1	7	1	4	5
	43.1714	77.7053	50.26481	-122.762	3-55.jpg	3	5	1	7	1	4	
	330.247	84.5573	50.26484	-122.762	3-59.jpg	2	2	1	8	1	4	
	157.763	87.9385	50.26482	-122.762	3-59.jpg	2	2	1	8	1	4	
	285.59	30.5511	50.26481	-122.762	3-61.jpg	3	2	0	1	1	4	
	254.38	29.0508	50.26482	-122.762	3-61.jpg	3	2	0	1	1	4	
5	42.3492	85.28	50.26499	-122.759	3-61.jpg	1	5	1	2	4	4	5
	21.9903	80.8467	50.26503	-122.759	3-61.jpg	1	5	1	2	4	4	
	16.0186	84.7102	50.26502	-122.759	3-61.jpg	1	5	1	2	4	4	
	293.431	15.6495	50.26505	-122.759	3-61.jpg	3	5	1	2	4	4	
	287.709	14.2959	50.26507	-122.759	3-61.jpg	3	5	1	2	4	4	
	87.7899	71.3102	50.2652	-122.759	3-68.jpg	3	5	0	5	4	5	
	64.857	57.6021	50.26522	-122.759	3-70.jpg	3	5	0	5	4	5	
	97.4983	57.0237	50.26516	-122.759	3-70.jpg	3	5	0	5	4	5	
6	223.653	35.9835	50.26548	-122.759	3-70.jpg	3	5	0	7	1	4	8
	190.613	51.4393	50.26548	-122.759	3-70.jpg	3	5	0	7	1	4	
	213.973	29.3237	50.26551	-122.759	3-70.jpg	3	5	0	7	1	4	
	138.776	81.5234	50.26551	-122.759	3-70.jpg	2	5	1	6	1		
	101.989	81.2801	50.2655	-122.759	3-70.jpg	2	5	1	6	1	3	
	271.161	88.3041	50.26549	-122.759	3-77.jpg	2	5	1	6	1	3	
	332.917	70.873	50.26549	-122.759	3-78.jpg	3	5	1	6	1	3	

	355.008	61.7524	50.2655	-122.759	3-78.jpg	3	5	1	6	1	6	
	358.197	56.3123	50.26549	-122.759	3-78.jpg	3	5	1	6	1	6	
7	196.92	77.3766	50.26324	-122.757	3-78.jpg	3	2	1		1	4	Weathered rock 7 and unweathered rock (fresh) >50
	182.856	71.4772	50.26324	-122.757	3-91.jpg	3						
	18.5668	88.7789	50.26324	-122.757	3-91.jpg	3	2	1	7	1	4	
	212.598	85.0631	50.26324	-122.757	3-91.jpg	3	2	1	7	1	4	
	290.761	78.376	50.26326	-122.757	3-91.jpg	3	5	0	7	1	4	
	300.591	79.4544	50.26323	-122.757	3-91.jpg	3	5	0	7	1	4	
	304.243	75.7072	50.26324	-122.757	3-91.jpg	3	5	0	7	1	4	
	135.607	15.6506	50.26327	-122.757	3-91.jpg	3	5	0	7	1	3	
	112.005	24.8068	50.26337	-122.757	3-91.jpg	3	5	0	7	1	3	
8	299.729	17.443	50.26414	-122.757	3-91.jpg	3	5	1	5	1	4	>50
	302.885	13.5466	50.26418	-122.757	3-91.jpg	3	5	1	5	1	4	
	321.392	12.0225	50.26419	-122.757	3-91.jpg	3	5	1	5	1	4	
	201.099	87.9536	50.26418	-122.757	3-94.jpg	3	5	1	6	1	4	
	12.78	78.931	50.26417	-122.757	3-94.jpg	3	5	1	6	1	4	
	184.331	89.3207	50.26416	-122.757	3-94.jpg	3	5	1	6	1	4	
	95.7304	85.9665	50.26418	-122.757	3-94.jpg	3	5	0	5	1	4	
	102.818	80.86	50.26418	-122.757	3-94.jpg	3	5	0	5	1	4	
	98.7132	85.4814	50.26418	-122.757	3-94.jpg	3	5	0	5	1	4	

Table S4.4: Show discontinuity surface roughness images mentioned in table S1.1.

Image number	Roughness Image	Image number	Roughness Image
3-18.jpg		3-47.jpg	
3-21.jpg		3-50.jpg	
3-25.jpg		3-55.jpg	
3-26.jpg		3-61.jpg	

3-28.jpg	
3-29.jpg	
3-31.jpg	
3-34.jpg	
3-37.jpg	
3-68.jpg	
3-70.jpg	
3-77.jpg	
3-78.jpg	
3-91.jpg	

| 3-41.jpg | | 3-94.jpg | |
| 3-44.jpg | | | |

Table S4.5: Discontinuity survey data and descriptions within domain 2.

Station NO	Dip Direction	dip	Lat	Long	Roughness	surface shape	Persistence	Termination	Aperture	Filling	joint spacing	Rock Strength (No. of hits by hammer)
1	39	60	50.2 4671	-122.798	4-103.jpg	3	5	0	7	4	4	19
	37	57	50.2 4674	-122.798	4-103.jpg	3	5	0	7	4	4	
	38	55	50.2 4676	-122.798	4-103.jpg	3	5	0	7	4	4	
	248	82	50.2 4674	-122.798	4-105.jpg	2	5	1	6	1	4	
	234	64	50.2 4675	-122.798	4-105.jpg	2	5	1	6	1	4	
	238	76	50.2 4674	-122.798	4-105.jpg	2	5	1	6	1	4	
	151	73	50.2 4673	-122.798	4-108.jpg	2	5	0	7	1	4	
	155	70	50.2 4677	-122.798	4-109.jpg	2	5	0	7	1	4	
	161	88	50.2 468	-122.798	4-110.jpg	2	5	0	7	1	4	
2	201	71	50.2 4736	-122.799	4-110.jpg	3	5	0	7	4	5	19
	197	68	50.2 4741	-122.799	4-110.jpg	3	5	0	7	4	5	
	202	71	50.2 4741	-122.799	4-110.jpg	3	5	0	7	4	5	
	175	88	50.2 474	-122.799	4-116.jpg	2	5	0	6	4	3	
	45	84	50.2 4743	-122.799	4-116.jpg	2	5	0	6	4	3	

	151	88	50.2474 4	-122.799	4-116.jpg	2	5	0	6	4	3	
	305	82	50.2474 3	-122.799	4-116.jpg	2	5	0	6	4	3	
	128	32	50.2474 1	-122.799	4-120.jpg	2	5	0	7	1	4	
	122	25	50.2474 2	-122.799	4-120.jpg	2	5	0	7	1	4	
	113	20	50.2474 3	-122.799	4-120.jpg	2	5	0	7	1	4	
	293	74	50.2474 1	-122.799	4-120.jpg	2	5	0	5	1	5	
	282	86	50.2 474	-122.799	4-124.jpg	2	5	0	5	1	5	
	81	88	50.2474 2	-122.799	4-124.jpg	2	5	0	5	1	5	
3	241	78	50.2486 2	-122.799	4-124.jpg	3	5	0	7	1	5	>83
	267	64	50.2486 1	-122.799	4-124.jpg	3	5	0	7	1	5	
	259	84	50.2 486	-122.799	4-124.jpg	3	5	0	7	1	5	
	301	18	50.2485 9	-122.799	4-129.jpg	2	5	0	6	1	6	
	93	23	50.2486 1	-122.799	4-129.jpg	2	5	0	6	1	6	
	337	21	50.2485 6	-122.799	4-129.jpg	2	2	0	6	1	6	
	219	77	50.2485 6	-122.799	4-133.jpg	2	5	0	6	1	4	
	207	78	50.2485 7	-122.799	4-133.jpg	2	5	0	6	1	4	

	184	83	50.2485 6	- 122.799	4-133.jpg	2	5	0	6	1	4	
4	349	73	50.2 496 8	-122.8	4-133.jpg	3	5	0	5	1	4	24
	345	67	50.2 496 6	-122.8	4-133.jpg	3	5	0	5	1	4	
	330	64	50.2 496 5	-122.8	4-138.jpg	3	5	0	5	1	4	
	84	38	50.2 498 3	-122.8	4-138.jpg	3	5	0	4	1	4	
	66	40	50.2 498 4	-122.8	4-138.jpg	3	5	0	4	1	4	
	69	46	50.2 497 5	-122.8	4-138.jpg	3	5	0	4	1	4	
	47	84	50.2 498	- 122.799	4-138.jpg	3	5	0	5	1	4	
	238	87	50.2 497 9	- 122.799	4-138.jpg	3	5	0	5	1	4	
	240	84	50.2 497 9	- 122.799	4-138.jpg	3	5	0	5	1	4	
5	13	51	50.2 502 7	- 122.799	4-145.jpg	2	5	0	4	1	4	24
	9	44	50.2 502 8	- 122.799	4-145.jpg	2	5	0	4	1	4	
	10	52	50.2 503 4	- 122.799	4-145.jpg	2	5	0	4	1	4	
	43	86	50.2 502 7	- 122.799	4-145.jpg	3	5	0	7	1	5	
	240	78	50.2 502 9	- 122.799	4-145.jpg	3	5	0	7	1	5	
	57	84	50.2 502 4	- 122.799	4-145.jpg	3	5	0	7	1	5	
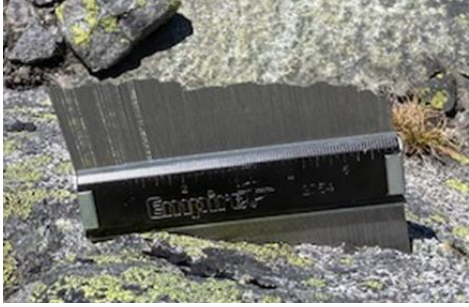
	155	73	50.2 5025	- 122.799	4-155.jpg	2	5	0	4	1	5	
	152	72	50.2 5027	- 122.799	4-155.jpg	2	5	0	4	1	5	
	166	69	50.2 5029	- 122.799	4-155.jpg	2	5	0	4	1	5	
6	65	5	50.2 4385	- 122.789	4-155.jpg	3	5	0	4	1	4	24 only small flakes
	53	5	50.2 4382	- 122.789	4-155.jpg	3	5	0	4	1	4	
	64	5	50.2 439	- 122.789	4-155.jpg	3	5	0	4	1	4	
	252	80	50.2 4386	- 122.789	4-155.jpg	3	5	0	7	1	4	
	257	84	50.2 4389	- 122.789	4-155.jpg	3	5	0	7	1	4	
	238	86	50.2 4389	- 122.789	4-155.jpg	3	5	0	7	1	4	
	180	81	50.2 439	- 122.789	4-155.jpg	3	5	0	5	1	4	
	183	79	50.2 4388	- 122.789	4-155.jpg	3	5	0	5	1	4	
	193	82	50.2 4386	- 122.789	4-155.jpg	3	5	0	5	1	4	
7	36	21	50.2 4931	- 122.786	4-155.jpg	3	5	0	6	1	3	26
	40	24	50.2 4931	- 122.786	4-155.jpg	3	5	0	6	1	3	
	16	26	50.2 4932	- 122.786	4-155.jpg	3	5	0	6	1	3	
	97	87	50.2 4931	- 122.786	4-155.jpg	3	5	0	6	1	2	

	88	85	50.2493	-122.786	4-155.jpg	3	5	0	6	1	2	
	99	87	50.24931	-122.786	4-155.jpg	3	5	0	6	1	2	
	171	78	50.24933	-122.786	4-155.jpg	3	5	0	6	1	2	
	166	83	50.24932	-122.786	4-155.jpg	3	5	0	6	1	2	
	167	82	50.24932	-122.786	4-181.jpg	3	5	0	6	1	2	
8	264	88	50.25132	-122.788	4-181.jpg	3	5	0	6	1	4	<5
	75	82	50.25133	-122.788	4-181.jpg	3	5	0	6	1	4	
	253	79	50.2513	-122.788	4-181.jpg	3	5	0	6	1	4	
	336	83	50.25135	-122.787	4-181.jpg	3	5	0	6	1	4	
	327	90	50.25135	-122.788	4-181.jpg	3	5	0	6	1	4	
	175	86	50.25136	-122.788	4-181.jpg	3	5	0	6	1	4	
	285	17	50.25133	-122.788	4-181.jpg	3	5	0	6	1	4	
	256	15	50.25134	-122.788	4-181.jpg	3	5	0	6	1	4	
	276	10	50.25134	-122.788	4-191.jpg	3	5	0	6	1	4	
9	82	16	50.2519	-122.788	4-191.jpg	3	5	0	6	1	3	<5
	68	13	50.25189	-122.788	4-191.jpg	3	5	0	6	1	3	

	70	17	50.2 518 7	- 122.788	4-191.jpg	3	5	0	6	1	3	
	234	75	50.2 518 9	- 122.788	4-191.jpg	3	5	0	6	1	3	
	245	79	50.2 519	- 122.788	4-191.jpg	3	5	0	6	1	3	
	252	87	50.2 518 9	- 122.788	4-191.jpg	3	5	0	6	1	3	
	188	77	50.2 519 3	- 122.788	4-191.jpg	3	5	0	6	1	3	
	190	88	50.2 519 5	- 122.788	4-191.jpg	3	5	0	6	1	3	
	174	82	50.2 519 5	- 122.788	4-200.jpg	3	5	0	6	1	3	
10	285	64	50.2 529 8	- 122.789	4-200.jpg	3	5	0	6	1	4	<5
	260	53	50.2 529 6	- 122.789	4-200.jpg	3	5	0	6	1	4	
	275	60	50.2 529 4	- 122.789	4-200.jpg	3	5	0	6	1	4	
	197	57	50.2 529 4	- 122.789	4-200.jpg	3	5	0	6	1	4	
	194	55	50.2 529 5	- 122.789	4-200.jpg	3	5	0	6	1	4	
	193	57	50.2 529 4	- 122.789	4-200.jpg	3	5	0	6	1	4	
	86	85	50.2 529 3	- 122.789	4-200.jpg	3	5	0	6	1	4	
	79	89	50.2 529 2	- 122.789	4-200.jpg	3	5	0	6	1	4	
	72	86	50.2 529 2	- 122.789	4-209.jpg	3	5	0	6	1	4	

11	225	79	50.2553	-122.787	4-209.jpg	3	5	0	7	1	4	<5
	228	81	50.2553	-122.787	4-209.jpg	3	5	0	7	1	4	
	221	82	50.25528	-122.787	4-209.jpg	3	5	0	7	1	4	
	315	80	50.2553	-122.787	4-209.jpg	3	5	0	7	1	4	
	322	76	50.25531	-122.787	4-209.jpg	3	5	0	7	1	4	
	315	81	50.25531	-122.787	4-215.jpg	3	5	0	7	1	4	
	60	81	50.25481	-122.788	4-216.jpg		5	0	7	1	4	
	355	43	50.25478	-122.788	4-216.jpg		5	0	7	1	4	
12	259	88	50.25254	-122.79	4-216.jpg	3	5	0	7	1	4	9
	260	86	50.25255	-122.79	4-216.jpg	3	5	0	7	1	4	
	268	85	50.25258	-122.79	4-216.jpg	3	5	0	7	1	4	
	177	40	50.25261	-122.79	4-222.jpg	3	5	0	7	1	4	
	175	39	50.2526	-122.79	4-223.jpg	3	5	0	7	1	4	
	179	41	50.25259	-122.79	4-224.jpg	3	5	0	7	1	4	
	192	86	50.25255	-122.79	4-224.jpg	3	5	0	7	1	4	
	201	84	50.25259	-122.79	4-224.jpg	3	5	0	7	1	4	
	200	88	50.25258	-122.79	4-224.jpg	3	5	0	7	1	4	

Table S4.6: Show discontinuity surface roughness images mentioned in table S4.3.

Image number	Roughness Image	Image number	Roughness Image
4-103.jpg		4-145.jpg	
4-105.jpg		4-155.jpg	
4-108.jpg		4-181.jpg	
4-109.jpg		4-191.jpg	

4-110.jpg		4-200.jpg	
4-116.jpg		4-209.jpg	
4-120.jpg		4-216.jpg	
4-124.jpg		4-222.jpg	

4-129.jpg		4-223.jpg	
4-133.jpg		4-224.jpg	
4-138.jpg			

Appendix D. Supplementary Materials for Chapter 5

Data Prep Stage

This stage includes downloading and gathering the data of interest such as satellite radar, satellite optical or ground-based camera. Additionally, correcting the downloaded raster dataset into the appropriate datatype such as 8-bit unsigned integer raster.

For the current study we download and use radiometrically corrected (RTC) sentinel 1 radar imagery and PlanetScope medium resolution imagery via PlanetLab educational and academic account (Fig. S 5.1). Although, the user can use other datasets such as sentinel 2, Landsat, and other available radar sensor imageries such as ALOS, Radarsat, and so on.

```
akhdefo_functions.Akhdefo_Utilities.download_RTC(username: str = '', password: str = '',
prompt=False, asf_datapool_results_file: str = '', save_dir: str = '', job_name: str =
'rtc-test', dem_matching: bool = True, include_dem: bool = True, include_inc_map: bool =
True, include_rgb: bool = False, include_scattering_area: bool = False, scale: str =
'amplitude', resolution: int = 10, speckle_filter: bool = True, radiometry='gamma0',
dem_name='copernicus', download: bool = False, limit: int = None, path_number: int = None,
frame_number: int = None, RTC: bool = False, autorift: bool = False, insar: bool = False,
max_neighbors: int = 2)                                                          [source]
```

```
async akhdefo_functions.Akhdefo_Utilities.akhdefo_download_planet(planet_api_key='',
AOI='plinth.json', start_date='May 1, 2016', end_date='', limit=5, item_type='PSOrthoTile',
product_bundle='analytic_sr_udm2', clear_percent=90, cloud_filter=0.1,
output_folder='raw_data', clip_flag=True, download_data=False)                   [source]
```

Figure S5.1. Snaph shot of the two functions from AkhDefo library to download radar and optical imagery.

Radar backscatter images originally came with three different scales including power, amplitude, and decibel: representing the strength of the backscatter signal. The power scale represents the raw radar return signal's power and is presented in a linear scale and measures the actual power received by the radar system. Amplitude scale also presented in a linear scale and calculated the square root of power scale. Contrastingly, decibel scale presented in a logarithmic scale.

Similarly, satellite optical imagery comes with various surface reflectance bands with various data ranges for instance, visible bands such as red band covers wavelengths in the range of approximately 600 to 700 nanometers (nm); green band covers wavelengths from about 500 to 600 nm and blue band ranges from around 450 to 500 nm.

We use AkhDefo raster correction algorithm to produce 8-bit unsigned integer raster format (Fig. S5.2). The steps of raster correction include:

Normalization and Scaling:

This step includes logarithmic scaling for radar imagery that comes with power scale. Additionally, applying linear Scaling for radar images that come with amplitude scale. These transformations help in reducing the dynamic range of the data, making features more distinguishable.

Filtering:

Using bilateral filters, gaussian low-pass filter, and Contrast Limited Adaptive Histogram Equalization (CLAHE) filter from OpenCV library. The bilateral filter is a nonlinear method effective in smoothing an image while preserving prominent edges. This filter's capability to break down an image into various scales while avoiding halo effects post-modification has led to its
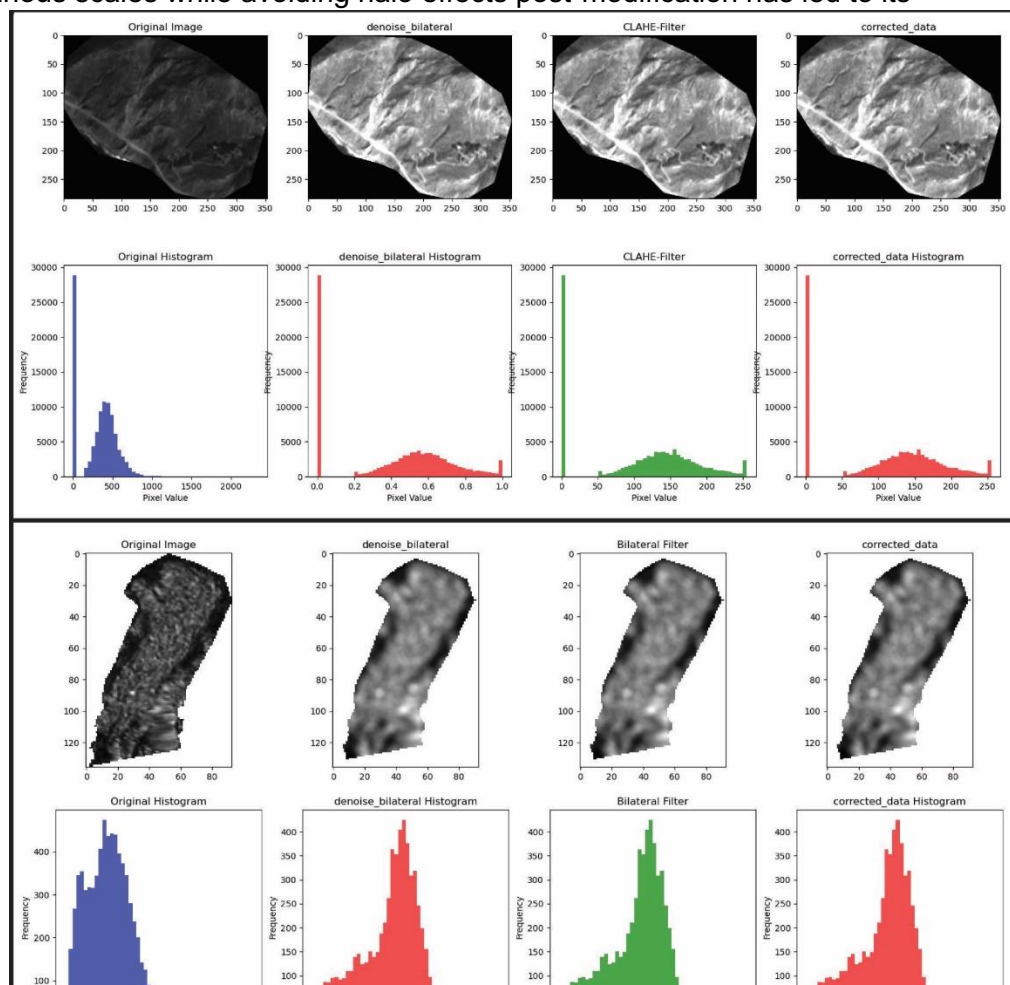
Figure S 5.2. Top panel show optical raster calibration before calculating displacement products. Bottom panel show radar raster calibration before calculating displacement products.

widespread use in computational photography(Paris et al., 2009). It is commonly employed in various applications, including tone mapping, style transfer, relighting, and image denoising(Paris et al., 2009), Gaussian low pass filter also used to remove high frequency noise. Additionally, CLAHE filter is used for optical imagery which improves local contrast and enhances the definitions of edges in regions of an image. CLAHE works by dividing the image into small windows, applying histogram equalization to each window(Muhammad et al., 2022).

Processing stage

Optical flow

The Farneback algorithm (Farnebäck, 2003) is being used from OpenCV library, to determine optical flow for subsequent image sets such as (n1-n2, n2-n3) or (n1-n2, n1-n3, n2-n3, n2-n4, etc.…), where n represents the image number at a given time. This algorithm is capable of handling both minor and major movements through multi-scale approach. It begins by estimating global motion patterns at a rough, low-resolution scale, then progressively refines these estimates at higher resolutions using a pyramid-like method. This approach is particularly effective for large motion detection, as such movements are more easily identified in low-resolution images where finer details are less evident (Farnebäck, 2003; Muhammad et al., 2022).

Once the algorithm has established a baseline motion estimate at the coarse level, it moves to higher resolution levels within the image pyramid. At each level, the optical flow is further refined. This refinement is based on the understanding that large movements are more visible at lower resolutions, while smaller movements become clearer and more accurately measurable at higher resolutions. The algorithm often uses
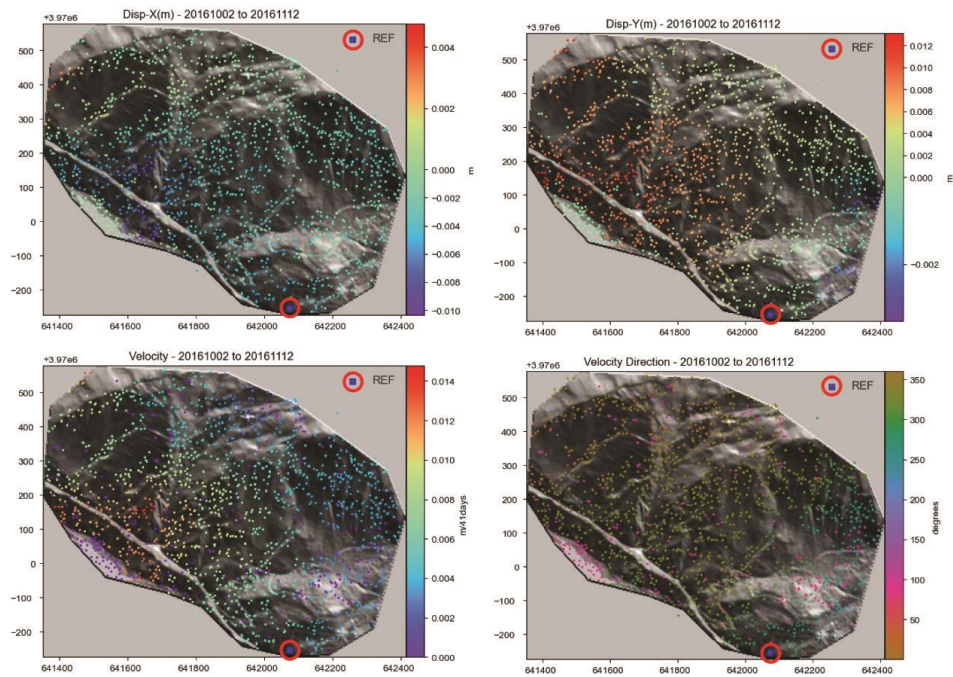
Figure S 5.3. Show optical flow displacement products. Top left displacement in east-west direction, top right displacement in north-south direction. Bottom left two-dimensional horizontal velocity displacement. Bottom right aspect of two-dimensional horizontal velocity displacement. The Blue square inside red circle represents reference point where all the displacement points referenced to that point.

image warping as it transitions from coarser to finer scales. This involves altering one image in the pair using the flow estimated at the coarser scale, aligning it more closely with the first image and aiding in the detection of smaller movements missed at the coarser level (Fig. S 5.3).

The algorithm compiles the flow calculated at each scale to form a cumulative flow. As it progresses up the pyramid, the incremental flow calculated at each finer level is added to the existing flow, creating a comprehensive representation that encompasses both large and small motion displacements.

Scale Invariant Feature Transform (SIFT)

The Scale Invariant Feature Transform (SIFT) represents a significant advancement in computer vision, enabling the extraction of unique, invariant features from images (Fig. S 5.3). These features aid dependable matching across various perspectives of an object or scene. Notably, these features remain consistent regardless of changes in the scale and rotation of the image. Furthermore, they demonstrate strong matching capabilities across a wide array of conditions, including affine distortions, alterations in 3D viewpoints, the introduction of noise, and variations in lighting(Lowe, 2004).

The SIFT algorithm performs the following consecutive steps to match stable features between two images. To understand the detailed mathematical theory behind the development of SIFT algorithm read the paper by (Lowe, 2004).

1. Detection of Scale-Space Extrema: In this initial phase, the algorithm comprehensively searches across all scales and image locations. This process is made efficient through the use of a difference-of-Gaussian function, which helps pinpoint potential points of interest that are unaffected by changes in scale and orientation.
2. Localization of Keypoints: For every potential keypoint, the algorithm develops a detailed model to ascertain its precise location and scale. The selection of keypoints is based on the stability of their characteristics such as elimination of low contrast keypoints and the edge response.
3. Assignment of Orientation: Each keypoint is assigned one or more orientations, determined by the directions of the local image gradients. All subsequent procedures are conducted on the image data that has been modified in

accordance with the keypoint's orientation, scale, and location, ensuring the feature's invariance to these transformations.

4. Construction of Keypoint Descriptor: The algorithm measures local image gradients at the keypoint's scale within the surrounding area. These measurements are then converted into a descriptor that accommodates significant local shape distortions and variations in lighting.

Structural Similarity Index Map (SSIM)

SSIM works like the human visual system's ability to perceive structural information in visual scenes. This method is crucial for assessing image similarity and thus identifying stable pixels with consistent brightness pattern (Fig. S 5.4). It focuses on the preservation and structural distortion of the image and distinguishes between structural and nonstructural distortions. Nonstructural distortions include external factors such as brightness changes, contrast variations, gamma distortion, and pixel shifts(Palubinskas, 2014; Muhammad et al., 2022).

The SSIM measures similarities of images based on the combination of three independent elements i.e., the brightness values, the contrast values, and the structure of the visual image scene. Assuming that x and y are the locations of two areas within two images of the same size, the similarity of brightness value becomes l(x,y), the similarity of contrast is c(x,y), and the similarity of the area structures is s(x, y) (Palubinskas, 2014; Kim et al., 2020):

$$SSIM(\text{x}, \text{y}) = l(\text{x}, \text{y}) \cdot c(\text{x}, \text{y}) \cdot s(\text{x}, \text{y}) = \left(\frac{2\mu_x\mu_y + C_1}{\mu_x^2 + \mu_y^2 + C_1} \right)$$
$$\cdot \left(\frac{2\sigma_x\sigma_y + C_2}{\sigma_x^2 + \sigma_y^2 + C_2} \right) \cdot \left(\frac{\sigma_{xy} + C_3}{\sigma_x\sigma_y + C_3} \right)$$

where μ_x and μ_y are local sample means of x and y areas, respectively. σ_x and σ_y are local standard deviations of x and y areas; σ_{xy} allocates the sample cross-correlation of x and y after removing the means of x and y areas. To avoid numerical instability in calculating sample means, variances and correlations, small positive constants C_1, C_2, and C_3 were introduced. The SSIM map is produced by computing a sliding window moving pixel-by-pixel across the entire image (Palubinskas, 2014; Kim et al., 2020). A single SSIM score for whole image is then calculated by averaging the SSIM values across the entire image.

Figure S5.4 Show the similarity of pixels between two images taken at different dates. Zero means no similarity and one is equal to perfect similarity.

Statistical outlier removal

The Z-score, a standard score, has been employed to filter out anomalous displacement readings. A Z-score of 0 signifies that the data point aligns perfectly with the mean. A Z-score of 1 implies that the data point falls within one standard deviation for 68% of the dataset. Similarly, a Z-score of 2 encompasses 95% of the dataset within two standard

deviations, while a Z-score of 3 covers 99.7% of the dataset within three standard deviations. Users can modify the Z-score threshold to exclude specific measurements.

To calculate the Z-score of a given value X, the formula used is: $Z = (X - \mu)/\sigma$ where X represents the measurement value, μ is the mean of the data and σ is the standard deviation of the data. The above formula adjusts the score of an individual data point relative to the mean of the dataset and scales it in terms of the standard deviation.

Interpolation of displacement Products

A significant challenge in visualizing optical flow displacement lies in selecting an appropriate interpolation method. While interpolating small movements may not pose a significant issue, accurately interpolating datasets that comprise both minor and major displacements can substantially affect the quality of the resulting data points.

The choice of interpolation method in optical flow visualization is crucial because it directly influences the accuracy and clarity of the motion representation. Small motions usually have less variability and are easier to interpolate, but when the data includes a mix of small and large displacements, the complexity increases. This is where Kriging stands out, as it accounts for spatial correlations and can adjust to different scales of motion more effectively than many other methods.

It should be noted that the implementation of Kriging interpolation can be computationally intensive, particularly when utilizing existing open-source Python libraries. In our recent study, AkhDefo package interpolation (Fig. S 5.5) workflow builds upon and enhances the capabilities of the open-source GSTools Python library. This improvement includes the functionality to interpolate datasets in smaller segments, addressing the issue of memory overload that often occurs when performing Kriging interpolation on large datasets.

The selection of an appropriate variogram in Kriging is crucial because it shapes the interpolation process by defining how spatial correlation is quantified and modeled. The variogram represents the degree of spatial dependence between data points, influencing how Kriging weighs nearby versus distant observations in its predictions. A well-chosen

variogram captures the intrinsic characteristics of the spatial data, such as range, sill, and nugget, which are essential for accurate modeling of spatial variability. If the variogram is not representative of the actual spatial relationships, it can lead to inaccurate interpolations, failing to reflect the true underlying patterns in the data. Thus, the careful selection and fitting of the variogram are key steps in ensuring the reliability and precision of Kriging as an interpolation method, directly impacting its effectiveness in diverse applications from environmental science to geostatistics.

The AkhDefo package employs the Auto variogram (Fig. S 5.5) method from GSTools (Müller et al., 2022) to align data with twelve different variogram models, subsequently executing interpolation using the model that demonstrates the optimal fit. This is determined by the highest coefficient of determination (R^2) score. The coefficient of determination is commonly utilized to assess the quality of the fit, with the R^2 value offering an indication of the extent to which the variogram model accounts for the variance observed in the empirical data.
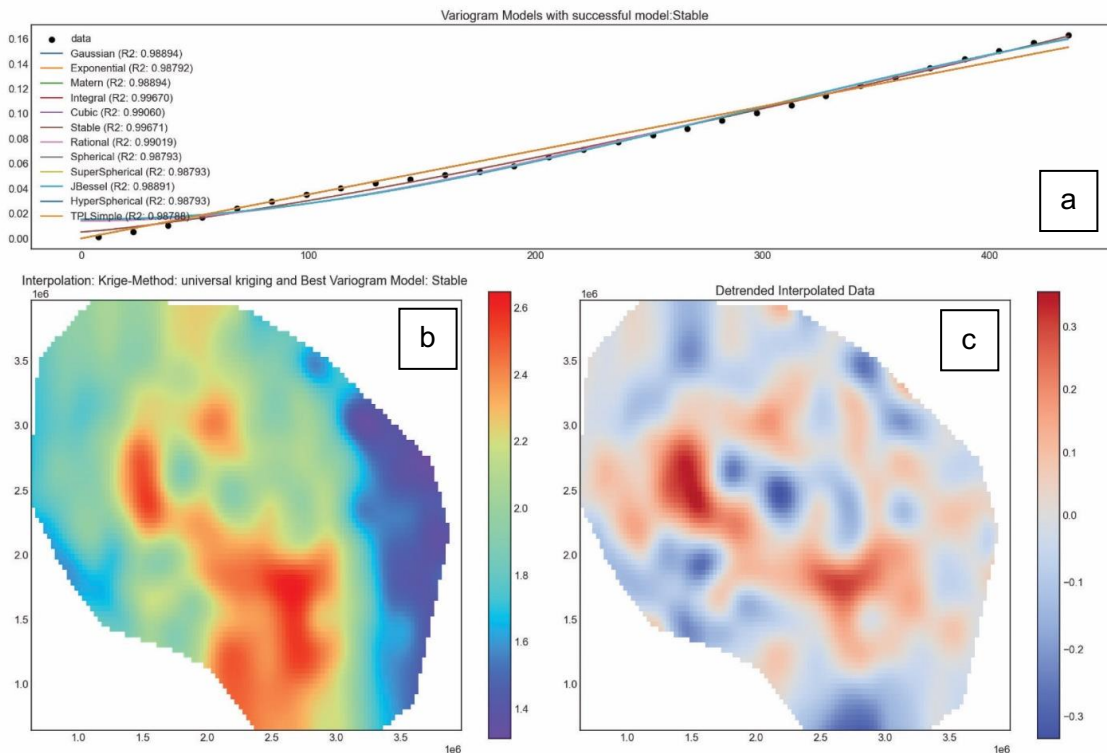
Figure S5.5. (a) show fitted data with 12 variogram models and predicting the best variogram fit model to the data. (b) Universal kriging interpolation with best fitting variogram model. (c) detrended interpolation for further analysis.
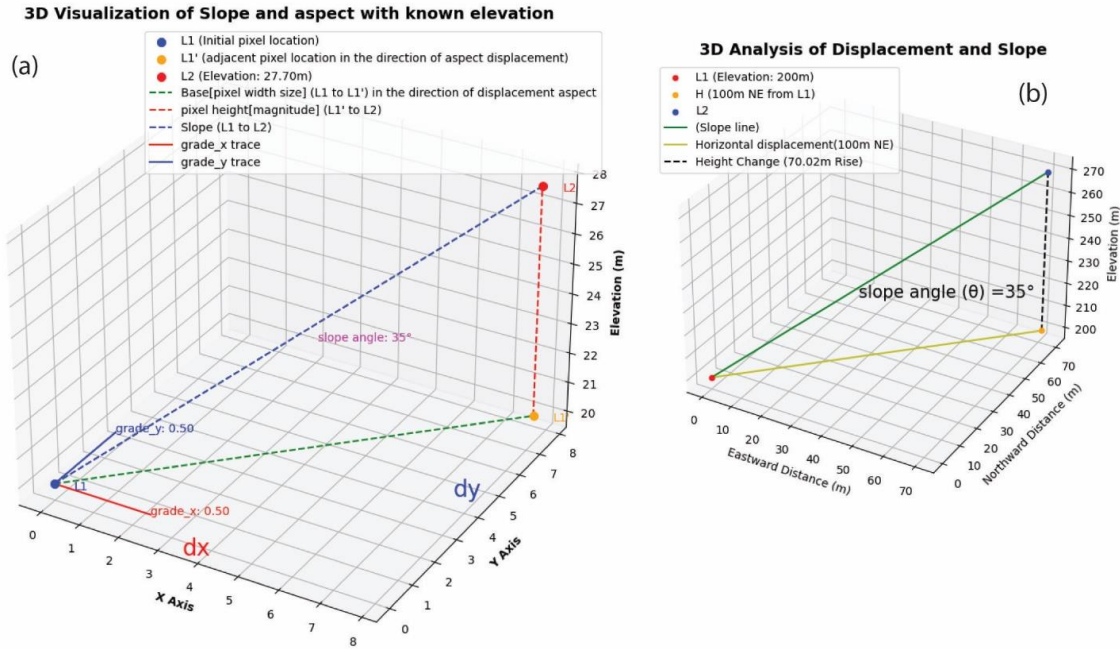
Figure S5.6. Terrain height and volume change from 2D displacement data and pre-landslide digital elevation model (DEM). (a) Calculation of the slope map with aid of two-dimensional displacement aspect map and pre landslide DEM. (b) Explains the use of calculated slope map along with aspect and displacement magnitude to estimate height change.

Volume Estimation

The AkhDefo package uses optical flow to estimate the motion field from a 2D raster array, therefore, the displacement products can only be estimated in east-west and north-south geographical coordinate system and lack the ability to estimate the vertical motion. The vertical change can nevertheless be estimated using trigonometry and the pre-deformation digital elevation model, with the resultant displacement vector calculated from the east-west and north-south displacement components:

The vector magnitude (aspect) $= arctan2(ew\_displacement, ns\_displacement)$ EQ.1

The vector magnitude (aspect) or directional gradient is found by combining the gradient in both the x and y directions. Mathematically, it is expressed using the mathematical equations taken from the NumPy Python library gradient function (Harris et al., 2020).

For a digital elevation model (DEM) or any scalar field represented as a 2D array DEM, with spacing (pixel dimensions) dx in the x-direction and dy in the y-direction (Fig. S 5.6 a), the gradient is computed as follows:

1. grade_x: This is the partial derivative of DEM with respect to x, representing the rate of change of the function along the x-axis. Mathematically, it's expressed as:

$\frac{\partial f}{\partial x} = (f(x\_i + 1, y\_j) - f(x\_i - 1, y\_j)) / (2 * dx)$ where $\text{grade\_x} = \frac{\partial f}{\partial x}$

2. grade_y: This is the partial derivative of DEM with respect to y, representing the rate of change of the function along the y-axis. Mathematically, it's expressed as:

$\frac{\partial f}{\partial y} = (f(x\_i, y\_j + 1) - f(x\_i, y\_j - 1)) / (2 * dy)$ where $grade\_y = \frac{\partial f}{\partial y}$

Given the aspect, gradient in x-direction(grade_x), and gradient in y-direction(grade_y), the directional gradient, representing the rate of change of the scalar field in the direction of the aspect, is given by.

Directional Gradient = cos(θ) * grade_x + sin(θ) * grade_y

For a given pixel, if the elevation and location before and after displacement are known (from L1 to L2), one can calculate the vertical change (rise). This vertical change is the elevation difference between the displaced position (L2) and the original position (L1). The horizontal distance (run) is the pixel dimension, which is the distance between L1 and the projected position L1' on the horizontal plane directly beneath L2.

The slope angle at pixel p is then calculated by taking the arctangent of the ratio of the rise to the run. The arctangent function yields the angle in radians between the line representing the rise and the horizontal distance (run), which is the angle of the slope. It is expressed as:

$$slope\ angle = arctan(Directional\ Gradient)$$

This process is repeated across the entire DEM to produce a slope angle map, which is a representation of the terrain's steepness at every point (pixel).

Once the slope angle relative to the resultant displacement aspect has been calculated, we can incorporate it to find the vertical change for the resultant horizontal displacement magnitude relative to the aspect and slope angle map.

Given that the slope angle (θ), aspect and the horizontal displacement (the distance from L1 to h) are known (Fig. S 5.6 b), we can use these to find the elevation difference, which is the rise in the right triangle formed by the displacement from L1 to L2. The tangent of the slope angle is the ratio of the rise (elevation change) over the run (horizontal displacement), expressed as:

$$tan(\theta) = \frac{Rise}{Run}$$

Where "Run" is the horizontal distance from L1 to H (resultant two-dimensional horizontal displacement magnitude). and the "Rise" (elevation change, from H to L2) is calculated using the formula below.

$$Rise = tan(\theta) \times Run$$

Appendix E. Products out of this thesis

Journal Articles

- **Mahmud Muhammad**, Glyn Williams-Jones, and René W. Barendregt. 2024. Structural geology of the Mount Meager Volcanic Complex, BC, Canada: implications for geothermal energy and geohazards. *Canadian Journal of Earth Sciences*. **61**(2): 158-186. https://doi.org/10.1139/cjes-2023-0077

- **Muhammad, M**., Williams-Jones, G., Stead, D., Tortini, R., Falorni, G., & Donati, D. (2022). Applications of image-based computer vision for remote surveillance of slope instability. *Frontiers in Earth Science*, *10*, 909078.

- **Mahmud Muhammad**, Glyn Williams-Jones, and Doug Stead, 2024, Integrated Assessment of Rock Slope Stability Incorporating Structural Geology, Kinematic Analysis, and Satellite Remote Sensing: A Case Study of Mount Currie, British Columbia, Canada. Landslide Journal (Ready for submission to the Journal)

- **Mahmud Muhammad**, Glyn Williams-Jones, Douglas Stead, Maqsad Suriev, 2024, Optical Flow: A Multifaceted Approach for Analyzing and Observing Rockfalls and Landslides through Optical and Radar Images Landslide Journal (Ready for submission to the Journal).

Conference Paper

- **Mahmud Muhammad**, René W. Barendregt, Glyn Williams-Jones, René W. Barendregt, Structural Geology Constraints and Its Influence on Geothermal Systems At Mt. Meager, British Columbia, 2nd Canadian Geothermal Students' Days 2021At: University of Manitoba, Winnipeg. 2021

Technical Reports

- **Muhammad, M.**, Williams-Jones, G., Barendregt, R.W, Applications of structural geology to the exploration of geothermal systems, Mt. Meager, within Garibaldi Geothermal Energy Project - Phase 1, Geoscience BC Report 2021-08.

- **Mahmud Muhammad**, Glyn Williams-Jones, Doug Stead, Davide Donati, Mount Currie 2020 Geology Fieldwork Report: Key Geological Parameters Controlling Main Mount

Currie Scarp Structure, Squamish-Lillooet Regional District (SLRD)-Simon Fraser University (SFU), Mount Currie Hazard Assessment -Year 1-Geological Investigation.

- Martin Harris, **Mahmud Muhammad**, Glyn Williams-Jones, James Kelly Russell, Bedrock mapping for Mount Meager Geothermal Research Initiative: In the Garibaldi Volcanic Belt Geothermal Energy Project – Mount Meager 2019 Field Program, Geoscience BC Report 2020-09. DOI: 10.13140/RG.2.2.15103.64169.

Conference Presentations

- **Mahmud Muhammad**, Glyn Williams-Jones, Doug Stead, AkhDefo Software: A tool for land deformation Monitoring using daily satellite optical imagery,6th world landslide Forum, held in Florence (Italy) from 14 to 17 November 2023.

- **Mahmud Muhammad**, Glyn Williams-Jones, Doug Stead: Measuring 3D Surface Displacement of Landslides Using Combined Optical and SAR Imagery, GSA Connects 2022 Meeting in Denver, Colorado, Geological Society of America Abstracts with Programs. Vol 54, No. 5, doi: 10.1130/abs/2022AM-380889.

- **Mahmud Muhammad**, Martin Harris, Glyn Williams Jones, and James K. Russell: Structural and Tectonic activity of Mount Meager Complex: Implications for quality of Geothermal Exploration, AME-Roundup 2020 poster sessions, Vancouver, January 2020.

Bedrock Mapping and Geology Mapping

- **Mahmud Muhammad**, Glyn Williams-Jones, and René W. Barendregt. Structural geology of the Mount Meager Volcanic Complex, BC, Canada: implications for geothermal energy and geohazards. Canadian Journal of Earth Sciences. [Detailed geology map of MMVC, GVB, British Columbia, Canada at a scale 1:30 000](#)

- Harris, M., Russell, J. K., **Muhammad, M**. & Williams-Jones, G. (2022). Mount Meager Volcanic Complex, Garibaldi Volcanic Belt, British Columbia: expanded bedrock map including Cracked Mountain, north Lillooet Ridge, and west Mount Meager. *Geological Survey of Canada, Open File*, 8881. https://doi.org/10.4095/329886